Interplay of Spin-Orbit Interaction and Two-Dimensional Superconductivity in Al/InAs Heterostructures

Dissertation

zur Erlangung des Doktorgrades der Naturwissenschaften

(Dr. rer. nat.)

der Fakultät für Physik

der Universität Regensburg

vorgelegt von

Lorenz Fuchs

aus Vilsbiburg

im Jahr 2021

Das Promotionsgesuch wurde am 08.04.2021 eingereicht.
Die Arbeit wurde von Prof. Dr. Christoph Strunk angeleitet.
Das Promotionskolloquium fand am 20.09.2021 statt.

Prüfungssausschuss:

Vorsitzende:	Prof. Dr. M. Grifoni
1. Gutachter:	Prof. Dr. C. Strunk
2. Gutachter:	Prof. Dr. J. Fabian
Weiterer Prüfer:	Prof. Dr. S. Ganichev

Contents

1. Introduction

All fields of society, economy and science are thriving for resource saving methods to make human existence sustainable. One way to save time, energy and essential materials in science is to simulate possible outcomes of experiments, chemical reactions or weather and climate forecasts. Life science is more and more dominated by bio-informatics [1]. Vaccines e.g. against SARS CoV-2 are mainly developed virtually on the computer before they are realized in the laboratory. The computational power that is needed for such simulations, however, grows faster than the development of new and more efficient, classical computers that are usually built from silicon based computational units. The need for energy saving and by magnitudes larger computational powers is evident. Quantum computers (QC's) could be one possible candidate for solving these problems. The smallest computing units of QC's according to classical bits are called quantum bits (qubits). These can be realized as low dimensional devices of semiconducting material that is in proximity to a superconductor [2]. While bits as a classical object can only represent one state at a time, qubits behave as a quantum object. This means it can represent both states or any linear combination of both states at the same time. Combining more qubits to a quantum circuit the number of states represented simultaneously grows exponentially. A big challenge, however, of such solid state qubits is its usually very short decoherence time, which describes the average time after which coherence and therefore information is lost. Thermal or external electromagnetic noise leads to a disturbance of the quantum state and hence to its breakdown. Good shielding, filtering and very low temperatures are necessary to create states with large enough decoherence times. A very elegant type of qubits that are expected to reach such high stabilities are realized by Majorana zero modes (MZM). In topological superconductors like Al-covered InAs nanowires in parallel magnetic fields states at zero energy emerge at the edges of the wire. Due to the spatial separation of these Majorana zero modes they are very stable and only decay in an exponentially small overlap region [3]. In two dimensions braiding operations such as winding one Majorana zero mode around another one can be used to perform logical operations.

In order to establish stable MZM's in superconducting devices unconventional p-wave superconductivity is the key ingredient. Confirmed p-wave superconductivity, however, has been so far only be reported in Sr_2RuO_4. But even in this compound, there is still debate whether there is enough evidence to call it p-wave. Another elegant approach to induce unconventional superconductivity is to use the combined effects of spin-orbit coupling (SOC) effects, ordinary superconducting s-wave pairing and external magnetic fields to break time-reversal symmetry [4][5].

The hunt for MZM's has triggered a lot of effort in material development and theoretical understanding of the underlying mechanisms, that lead to the fascinating physics of 2D superconducting/semiconducting hybrids. In such kind of materials many, much more fundamental effects take place, which give a prospect to possible future, technological application in superconducting electronics. In a recent work, Ando et al. [6] have impressively shown for the first time, that the interplay of Rashba SOC and superconductivity in a layered, bulk structure can be used to build a superconducting diode, which is able to rectify supercurrent analog to the current rectification in classic diodes. As diodes are one of the most important basic components in an electrical circuit, a superconducting analogue to the classic one can be seen as a big step towards superconducting electronics. Their findings have triggered very recent theoretical work describing the ability of superconductors with SOC to rectify supercurrent in an external magnetic field [7][8].

In this work the phenomenology of supercurrent transport in 2-dimensional Al/InAs heterostructures in external magnetic fields with different relative orientations is investigated. Although the investigated system is considered very clean, strong indications for an unexpected BKT-like transition are found. A strong inductive response of the superconducting condensate is measured in the presence of an out-of-plane field, which is attributed to the motion of weakly pinned vortices in the superconductor. It will be shown, that the interplay of superconductivity provided by the thin film of Al and spin-orbit-coupling arising from the asymmetric AlInAs/InAs/AlInAs 2DEG leads e.g. to unexpected, anisotropic vortex pinning enhancement in in-plane magnetic fields so far not reported in literature. Furthermore, a polarity dependent critical current and resistance is found in these kind of superconducting/semiconducting hybrids, when they are exposed to magnetic fields perpendicular to the current direction. In such a heterostructure supercurrent rectification and non-reciprocal resistance could be expected due to the interplay of Rashba SOC and an in-plane field orthogonal to the current direction

[7][8]. There is, however, also a strong indication towards an anisotropic out-of-plane spin-orbit field texture, which may arise from a broken crystal symmetry at the Al/InAs interface. Such spin-textures have so far also not been reported in literature.

The different techniques, most importantly a revised version of a resonator technique first introduced by Meservey and Tedrow already in 1969 [9] to measure the tiny kinetic inductance of superconductors will be demonstrated and its dynamics calculated theoretically. This work is also intended to work as a guideline for following researchers working with similar techniques and to draw attention to artifacts and systematic errors that can occur in the course of daily life lab work. Therefore, possible sources of artifacts and deviations of the measured quantities from the expected results will be discussed.

Chapter 2 will give a theoretical background of the basic concepts of the complex impedance of thin film superconductors, SOC related supercurrent rectification processes and a novel theory on pinning enhancement in SOC superconductors. In chapter 3 methods of sample fabrication and the different measurement techniques and related complications are discussed. Chapter 4 will give a short overview over the most important, physical parameters of the investigated samples. Results of inductance measurements performed on long superconducting meander structures in a RLC circuit are shown in chapter 6. Chapter 7 polarity dependence of supercurrent and resistance in a straight wire of Al/InAst in external magnetic fields will be demonstrated. In chapter 7 the presented results will be summarized and discussed together with an outlook towards possible directions for future research. In the appendix, practical challenges and additional interesting measurement results, which are beyond of the scope of this work are presented and discussed briefly.

2. Theoretical Background

2.1. Phenomenology of Superconductivity

Most metals and other conducting materials have a temperature dependent resistance. For metallic specimen resistivity decreases linearly with decreasing temperature due to suppression of electron-phonon scattering. At very low temperatures some materials undergo a phase transition into a different state, which is described by a single collective wavefunction. This state was first observed by Heike Kamerlingh Onnes in 1911 when he measured the resistivity of mercury at low temperatures. He found a sharp drop of resistance to an immeasurably small value below 4.2 K. In addition in 1938 Meissner and Ochsenfeld [10] found out that superconductors also expel external magnetic fields and therefore are perfect diamagnets. In the center of the superconductor the magnetic field vanishes. Within the surface the external field is suppressed exponentially with a characteristic length λ_L, the so called London penetration depth. The London equations describing electric fields $\mathbf{E}$ and magnetic fields $\mathbf{B}$ as well as supercurrent density $\mathbf{j_s}$ are the basis for most calculations.
The first London equation reads

$$\mathbf{E} = \Lambda \frac{\partial}{\partial t} \mathbf{j_s}, \tag{2.1}$$

where $\Lambda = \mu_0 {\lambda_L}^2$ is the so-called London parameter. The second London equation can be written as

$$-\mathbf{B} = \Lambda \nabla \times \mathbf{j_s}. \tag{2.2}$$

2.1.1. Kinetic Inductance

Based on the first London equation it is possible to define a reactance associated to the inertia of Cooper pairs in a superconductor. For a rectangular superconducting wire of width w, length l and thickness d the electric field that is produced by a voltage U along

l is

$$E = U/l, \tag{2.3}$$

while the current through the wire is defined via

$$\frac{I}{wd} = |\vec{j}|. \tag{2.4}$$

Inserting these two expressions into the first London equation 2.1 and multiplication with wd on both sides leads to a voltage drop across the wire

$$U = -\frac{l}{w}\frac{\Lambda}{d}\dot{I}, \tag{2.5}$$

where the ratio $\frac{l}{w}$ describes the number of squares of the conductor over the length l. The result is a voltage produced by a temporal change of current, which can be interpreted as an inductance and is called kinetic inductance. The inductance per square is then defined as

$$L_{s,\square} = \frac{\Lambda}{d} = \mu_0\frac{\lambda^2}{d}. \tag{2.6}$$

In order to calculate the dependence of the kinetic inductance on external parameters such as temperature, current or magnetic field it is necessary to solve the Usadel equations for the investigated sample geometry within the Eilenberger-Usadel formalism. Highlighted should be a work by Kubo [11], where dependencies of superconducting parameters like Δ, λ or j_c on external parameters are calculated.

For thin film superconductors the corresponding Usadel equation reads

$$\left(\Delta - \frac{s}{\sqrt{1+\cot^2(\phi)}}\right)\cot(\phi) = \hbar\omega_n + \Gamma, \tag{2.7}$$

where Γ is the Dynes pair-breaking scattering rate and $\hbar\omega_n = 2\pi k_B T(n + 1/2)$ the Matsubara frequency and s a parameter describing the supercurrent. Δ needs to fulfill the self-consistent equation

$$\ln(\frac{T_{c0}}{T}) = 2k_B T \sum_{\omega_n>0}\left(\frac{1}{\hbar\omega_n} - \frac{\sin(\phi)}{\Delta}\right). \tag{2.8}$$

The superfluid density n_s and consequently λ are given by

$$\frac{n_s(s,\Gamma,T)}{n_{s0}} = \frac{{\lambda_0}^2}{\lambda(s,\Gamma,T)^2} = \frac{4k_BT}{\Delta_0}\sum_{\omega_n>0}\sin^2(\phi). \tag{2.9}$$

For the zero bias limit ($s \to 0$) and in absence of any pair breaking ($\Gamma \to 0$) this equation can be solved and leads to the well-known formular for the penetration depth

$$\frac{\lambda^{-2}(T)}{\lambda^{-2}(0)} = \frac{\Delta(T)}{\Delta(0)}\tanh\left[\frac{\Delta(T)}{2k_BT}\right]. \tag{2.10}$$

The temperature dependence of the total inductance of a real sample in series with an external inductance L_0 is then given by

$$L(T) = L_0 + N\mu_0\frac{\lambda^2(0)}{d}\left[\frac{\Delta(T)}{\Delta(0)}\tanh\left[\frac{\Delta(T)}{2k_BT}\right]\right]^{-1}, \tag{2.11}$$

where N is the number of squares in series and d the film thickness. The superconducting gap $\Delta(T)$ can in principle be determined by solving eq. 2.7 and 2.8. For simplicity in this work an approximation is used for the temperature dependence of the normalized gap

$$\frac{\Delta(T)}{\Delta(0)} \approx \left[\cos\left(\frac{\pi T^2}{2{T^2}_c}\right)\right]^{1/2}. \tag{2.12}$$

Using eqs. 2.11 and 2.12 allows to fit experimental $L(T)$ data. The absolute value of $L_{s,\square}(0)$ and $\lambda(0)$ can be estimated from the normal state resistance as

$$L_{s,\square}(0) = \frac{R\hbar}{\pi\Delta(0)} = 0.18\frac{R_\square\hbar}{k_BT_{c0}} \tag{2.13}$$

$$\lambda(0) = \sqrt{\frac{L_{s,\square}(0)d}{\mu_0}} = \sqrt{0.18\frac{R_\square\hbar}{k_BT_{c0}}\frac{d}{\mu_0}} \tag{2.14}$$

2.1.2. Ginzburg-Landau Theory

On the basis of Landau's work on second order phase transitions, he together with Ginzburg established a theory describing superconductivity near the transition temperature by introducing a complex order parameter ψ, whose square of the absolute value represents the density of cooper pairs being zero above and larger than zero below the transition. In their theory, free energy can be expressed in terms of an expansion in ψ as

$$F = F_n + \alpha|\psi|^2 + \frac{\beta}{2}|\psi|^4 + \frac{1}{2m}|(-i\hbar\nabla - 2e\vec{A})\psi|^2 + \frac{|B^2|}{2\mu_0}, \tag{2.15}$$

where F_n is the free energy in the normal phase. Minimizing free energy regarding order parameter and vector potential leads to the so-called Ginzburg-Landau equations

$$\alpha\psi + \beta|\psi^2|\psi + \frac{1}{2m}(-i\hbar\nabla - 2e\vec{A})^2\psi = 0 \tag{2.16}$$

$$\vec{j} = \frac{2e}{m}\Re\{\psi^*(-i\hbar\nabla - 2e\vec{A})\psi\}. \tag{2.17}$$

Calculation of the rotation of the current density delivers the second London equation

$$\mathrm{rot}\vec{j} = -\frac{n_s e^2}{m}\vec{B}, \tag{2.18}$$

where $n_s = |\psi^2|$. Considering a superconducting material in an external field (Fig. 2.1), where the magnetic flux is parallel to the z-direction, the resulting differential equation follows from introducing eq. 2.18 into the Maxwell equation $\mathrm{rot}\vec{B} = \mu_0\vec{j}$:

$$\frac{\mathrm{d}^2 B\,(x)}{\mathrm{d}x^2} - \frac{\mu_0 n_s e^2}{m} B\,(x) = 0. \tag{2.19}$$

This equation is solved by

$$B\,(x) = B_0 \mathrm{e}^{-x/\lambda_L}, \tag{2.20}$$

where the London penetration depth is defined as

$$\lambda_L = \sqrt{\frac{m}{\mu_0 n_s e^2}}. \tag{2.21}$$

As the cooper pair density is dependent on temperature, this is also the case for the penetration depth. In the Ginzburg-Landau theory this dependence is given by:

$$\lambda_L\,(T) = \frac{\lambda_L\,(0)}{\sqrt{1 - T/T_c}}. \tag{2.22}$$

An empirical expression approximately valid over a larger T-range has been found, which provides the temperature dependence of λ_L known as 'two-fluid model' as [13]

$$\lambda_L\,(T) \approx \frac{2\lambda_L\,(0)}{\sqrt{1 - (T/T_c)^4}}. \tag{2.23}$$

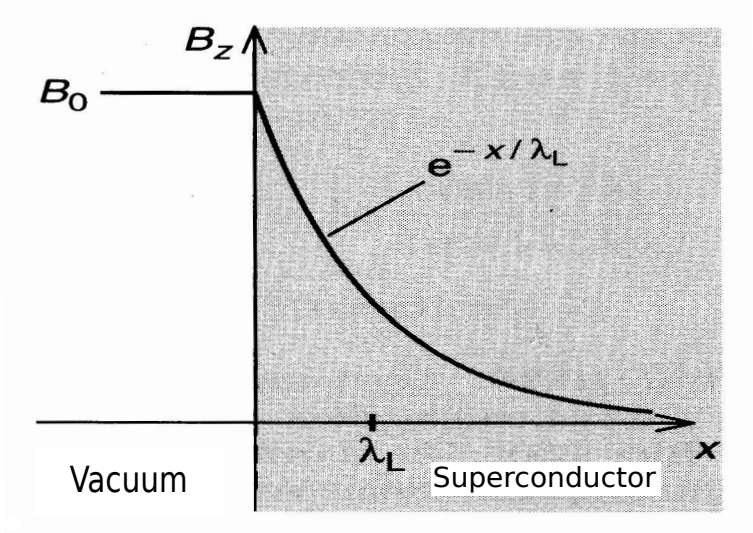

Fig. 2.1: Magnetic field in a superconductor. Due to screening currents the magnetic field in a superconductor is suppressed. The external field decreases exponentially towards the center of the material (adapted from [12]).

Near T_c this is equivalent to the temperature dependence of λ_L in the Ginzburg-Landau theory (Eq. 2.22). As a consequence the density of Cooper pairs, which is proportional to λ^{-2} is expected to behave like $n_s \propto 1 - \frac{T^4}{T_c^4}$.
Together with the Ginzburg-Landau coherence length ξ, which is a reference for the length over which the density of Cooper pairs can vary, and the related coherence length ξ_0, which describes the extension of single Cooper pairs, this is the most important parameter describing superconductivity.

2.1.3. Superconductivity in Thin Films

Thin metallic films show a very different superconducting behavior than bulk materials. In their work *Ivry et al.* have collected data of the past 50 years, which show that in most cases a reduced film thickness and therefore enhanced disorder leads to a smaller transition temperature and increased resistivity compared to its bulk value [14]. For thin Al films, however, T_c increases with disorder as well as for smaller thickness. This is in contradiction to Anderson's theorem, which predicts independence of T_c from disorder up to a certain degree [15]. Deviations from characteristic bulk parameters may also be a consequence of the fabrication process. The structural quality of thin films strongly depend on the conditions during deposition.
In a type II or also in thin film type I superconductors flux vortices may appear once the field exceeds the lower critical field B_{c1}. Further increase of the field strength above the upper critical field B_{c2} eventually leads to an overlap of vortex cores and thus to

destruction of the dissipationless charge transport. In thin films, however, it is possible that even in absence of an external field flux vortices are created by thermal fluctuations [16]. Below the so-called Berezinskii-Kosterlitz-Thouless transition temperature T_{BKT} these vortices are bound in vortex-antivortex pairs and a state of zero resistance is the consequence. Above T_{BKT} vortices can move freely and generate a finite resistance. One significant feature of a BKT transition is the discontinuous drop of the superfluid density n_s at T_{BKT} in contrast to a smooth transition in bulk material [17].
Pearl has shown that in thin films ($2d \ll \lambda$) the transverse penetration depth is thickness dependent as $\lambda_\perp \approx 2\lambda^2/d$ [18]. Thus, a reduced film thickness results in a larger penetration depth perpendicular to the surface. Additionally he stated that the long-range falloff of the circulating sheet current density is only proportional to a power law in the distance of the core center instead of an exponential decay in bulk.

2.1.4. Vortex Dynamics

Pinning

In a very intuitive picture, vortices can lower their energy by occupation of a sample volume, where the superconducting order parameter is already lowered by some defects. In reality a vortex can gain energy from more than one small pinning center. These pinning sites can be for example crystal defects, impurities, grain boundaries or interfaces, provided they suppress the superfluid density . The energy of a vortex, which has a normal core with a superconducting order parameter equal to zero at the center is reduced if it is placed at a position, where the superconductor is in the extreme case normal anyways. In this case less condensation energy has to be paid to break Cooper pairs in the center of the vortex. The energy of a vortex in a pinning potential can be calculated as a convolution of a pinning potential $U_{pin}(\mathbf{r})$ and a term describing the vortex structure $|\Psi(\mathbf{r})|^2$ [19]

$$\epsilon(\mathbf{u}, z) = \int \mathrm{d}^2 R U_{pin} |\Psi(\mathbf{r} - \mathbf{u})|^2. \tag{2.24}$$

In this case the vortex can save free energy of the order of $\delta F \approx \frac{B_{c,th}^2}{2\mu_0} \frac{4}{3} \pi r_0^3$, where r_0 is the defect radius [20]. This energy corresponds to the condensation energy density multiplied with the volume of the defect. For the case of defects very small compared with the extension of a vortex core ξ, which should be the case in relatively clean thin film superconductors, this energy gain can be rather small. In addition, as Anderson pointed

out, small non-magnetic defects should not even reduce the local order parameter at all. Thus this effect alone could not explain the high pinning forces that were measured e.g. in irradiated superconductors [21].
It was found that there is a second mechanism that produces an effective pinning force, which is related to a non-local effect of a scattering center on Cooper pairs in its vicinity [22]. In order to nucleate a vortex, a superconductor has to locally suppress the absolute value of the order parameter at its core. In that case the defect "helps a superconductor to sustain deformations of the order parameter up to distances on the order of the zero-temperature coherence length" [20]. This leads to an effective pinning energy that is larger than that of the elementary pinning mechanism by a factor of $\frac{\xi}{r_0}$, which is an enhancement of some orders of magnitude for defects of $r_0 \sim$ Å. For relatively clean samples this effect should be the main contribution to the pinning force and strongly dependent on the microscopic nature of the defects.

(Pinned) Vortices in a superconductor with supercurrent flow $j_y = \rho_s v_y$ are subject to a Lorentz force, that is for a parabolic potential in first approximation compensated by a viscous force and a linear restoring force

$$\phi_0 j_y = \eta v_x - k_p x, \tag{2.25}$$

where $\phi_0 j_y$ is the driving Lorentz force (Fig. 2.2), ηv_x is a friction force caused by the vortex viscosity η and $F_p(x) = k_p x$ is the restoring pinning force. In this approximation the mass of the vortex is neglected.

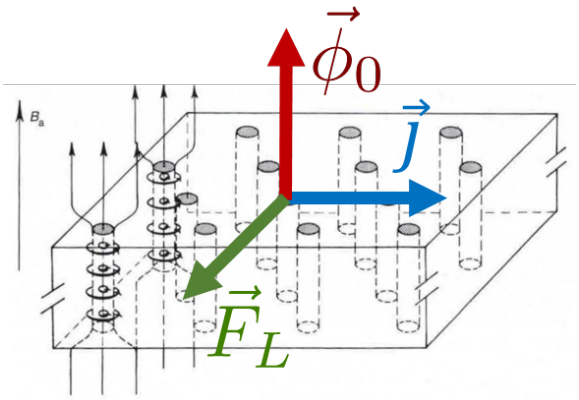

Fig. 2.2.: Flux line lattice in a type II superconductor. Vortices are subject to a Lorentz force when a supercurrent is applied. This causes the vortices to move perpendicular to the current direction. Picture adapted from [13].

In elementary core pinning model, the pinning energy is simply proportional to the condensation energy $\sim \frac{B_c^2}{2\mu_0}$ times the volume of the defect [20]. As the thermodynamical

critical field $B_c(T)$ empirically follows a $\left(1-\frac{T^2}{T_c^2}\right)$ dependence and $k_p(T) \propto \frac{B_c^2(T)}{2\mu_0}$ is defined as the curvature at the center of the pinning potential, $k_p(T)$ can be written as

$$k_p(T) = k_{p0}\left(1-(T/T_c)^2\right)^2. \tag{2.26}$$

In high-T_c superconductors this temperature dependence of k_p was confirmed experimentally [23]. For moderate out-of-plane fields the pinning constant is assumed to be field-independent. In this case each vortex occupies one single pinning site. For higher fields i.e. larger vortex concentrations, however, each pinning site can host many vortices. In the collective pinning regime k_p is smaller than in the individual pinning case and field-dependent [24].

Static Case

For a constant current, there will be equilibrium between Lorentz force and pinning restoring force as long as the supercurrent j_y is small enough, so that vortices are still confined in their pinning potential. Vortices will only be displaced from its original position without motion ($v_v = 0$). For currents that exceed the sample characteristic depinning current density $\mathbf{j}_c$ vortices are no longer pinned and can move freely ($v_v \neq 0$). In this case one can easily see that energy will be dissipated, which can be measured as a finite resistance. This resistance is known as flux flow resistance

$$\rho_{FF} = \frac{\phi_0 B_z}{\eta}. \tag{2.27}$$

Dynamic Case

In the case of an alternating current density $j_y = j_{y,0}\cos\omega$ the solution of equation 2.25 leads to the expression for the complex resistivity

$$\rho = \rho_{FF}\left(\frac{\omega}{\omega - i\omega_0}\right), \tag{2.28}$$

where $\omega_0 = k_p/\eta$ is the depinning frequency. From this equation two limits can be identified. For $\omega \gg \omega_0$ the resistivity is simply ρ_{FF} and real. In the low frequency limit $\omega \ll \omega_0$ the impedance is imaginary and equals

$$\rho = -i\frac{\phi_0 B_z}{k_p}\omega. \tag{2.29}$$

From this equation a vortex associated inductance per square can be deduced by substituting the complex resistivity with a reactance $\rho = X_L d$, where $X_L = -i\omega L_v$

$$L_v = \frac{\phi_0 B_z}{k_p d}. \tag{2.30}$$

For a typical pinning constant of 100 N/m in 150 nm thick Al [25] a vortex inductance of 141 pH/T per square is expected. This can for moderate fields compete with the sheet kinetic inductance. The pinning constant in a thin film itself is proportional to the length of a vortex line and therefore to the film thickness. Hence L_v can exceed L_s by orders of magnitude in very thin films.

2.1.5. Complex Conductivity

Superconductors show a finite reactance in AC fields. In thin films often the complex surface impedance $Z_s = R_s + iX_s = i\omega\mu_0\tilde{\lambda}$ is used. Clem and Coffey in detail describe the surface impedance of type II superconductors [26][27]. They investigated the influence of excited quasiparticles, vortex pinning and flux creep on the complex resistivity by generalizing the magnetic penetration depth to a complex valued length $\tilde{\lambda}$ that includes the classic field-dependent penetration depth λ_s, the normal-fluid skin depth $\delta_{nf} = (2\rho_{nf}/\mu_0\omega)^{1/2}$ and an effective skin depth that results from vortex motion $\tilde{\delta}_v = (2\phi_0 B\tilde{\mu}/\mu_0\omega)^{1/2}$. They find a self-consistent solution for the generalized penetration depth

$$\tilde{\lambda}(\omega, B, T) = \left[\frac{\lambda_s^2(B,T) - (i/2)\tilde{\delta}_v^2(B,T,\omega)}{1 + 2i\lambda_s^2(B,T)/{\delta_{nf}}^2(B,T,\omega)}\right]^{1/2}. \tag{2.31}$$

In a more convenient notation this reads [28]

$$\tilde{\lambda} = \left[\frac{{\lambda_s}^2 + {\lambda_v}^2}{1 + 2i{\lambda_s}^2/{\delta_{nf}}^2}\right]^{1/2}, \tag{2.32}$$

where λ_s is the condensate penetration depth, δ_{nf} the normal fluid skin depth and λ_v the vortex penetration depth. B describes a magnetic field perpendicular to the film surface which induces vortices in the superconductor. In most cases apart from very near T_c, δ_{nf} is much larger than all other length scales and therefore the denominator reduces to 1. For thin films the complex penetration depth is renormalized by the film thickness d such that $\tilde{\lambda}$ is replaced by $\tilde{\lambda}^2/d$ and therefore $Z_s = R_s + iX_s = i\omega\mu_0\tilde{\lambda}^2/d$ This allows to separate real and imaginary parts of the resistivity

$$R_s = \omega\mu_0 \mathrm{Im}(\tilde{\lambda}^2)/d = \omega\mu_0/d \frac{\phi_0 B}{\omega_0 \eta \mu_0} \frac{\omega/\omega_0}{1+(\omega/\omega_0)^2} \left[1 + \chi\left(\frac{\omega_0}{\omega}\right)^2\right] \tag{2.33}$$

$$X_s = i\omega\mu_0 \mathrm{Re}(\tilde{\lambda}^2)/d = i\omega\mu_0/d \left[{\lambda_s}^2 + \frac{\phi_0 B}{\omega_0 \eta \mu_0} \frac{1-\chi}{1+(\omega/\omega_0)^2}\right], \tag{2.34}$$

where ω_0 is the so called depinning frequency and χ is the flux creep factor, describing the strength of flux hopping from one pinning site to another. ω_0 is related to the vortex viscosity η and the pinning constant k_p via $\omega_0 = \frac{k_p}{\eta}$. Associating the reactance X_s to an inductance $L = iX_s/\omega$ the total inductance of a thin film superconductor in absence of vortex creep results in a sum of kinetic inductance $L_s = \mu_0 {\lambda_s}^2/d$ and vortex inductance $L_v = \frac{\phi_0 B}{k_p d} \frac{1}{1+(\omega/\omega_0)^2}$. For small λ_s and large δ_{nf} eq. 2.32 reduces to

$$\tilde{\lambda}^2 = {\lambda_s}^2 + {\lambda_v}^2. \tag{2.35}$$

Thus from an electrical point of view the simultaneous presence of kinetic and vortex inductance can be described as a series connection of resistors and inductors. For frequencies far below ω_0 the sheet inductance is independent of ω

$$L(\omega \to 0) = \mu_0 {\lambda_s}^2/d + \frac{\phi_0 B}{k_p d} = \frac{1}{d}\left(\mu_0 {\lambda_s}^2 + \frac{\phi_0 B}{k_p}\right). \tag{2.36}$$

Both components are only in first approximation independent from each other as the pinning constant k_p is related to the superfluid density $1/\lambda_s^2$ but also very much to microscopic details as defect type and size.

The temperature dependence of the total inductance can by using eqs. 2.10, 2.30 and 2.26 in approximation be written as

$$L(T) = L_s(0) \frac{\Delta(T)}{\Delta(0)} \tanh\left[\frac{\Delta(T)}{2k_B T}\right] + L_v(0)\left(1 - \frac{T^2}{{T_c}^2}\right)^{-2} \tag{2.37}$$

In the case of pair-breaking, e.g. by an external parallel magnetic field the superfluid density $1/{\lambda_s}^2$ is reduced and hence L_s is increased. The reduction of superfluid stiffness leads to a reduction of the pinning potential energy and therefore also increases the vortex inductance. Vortices contribute to the total inductance with a power-law dependence in T(see eq. 2.26). In unconventional superconductors with nodes in the gap also the change of the kinetic inductance $\Delta L_s(T) = L_s(T) - L_s(0)$ follows a power-law. Therefore it is challenging to discriminate a vortex-associated inductance from a kinetic inductance in unconventional superconductors. For the measurement of a purely kinetic

inductance it is extremely important to minimize external out-of-plane fields across the whole sample. This is especially necessary for samples with weak pinning as in this case the vortex inductance can exceed the kinetic contribution by orders of magnitude.

2.1.6. AC Impedance

The frequency dependent complex conductivity of superconductors in the absence of vortices in the limit of $\omega\tau_n \ll 1$, where τ_n is the elastic scattering time, can be written as [29]

$$\begin{aligned}\sigma_1(\omega) &= (\pi n_s/2m)\,\delta(\omega) + n_n e^2\tau_n/m \\ \sigma_2(\omega) &= n_s e^2/m\omega\end{aligned} \tag{2.38}$$

In the two-fluid model the quasiparticle density can be approximated by $n_n = n_0 \exp(-\Delta(T)/k_B T)$, the Cooper pair density by $n_s = n_0(1 - \exp(-\Delta(T)/k_B T)$. It can be shown that the dissipative component of the complex impedance then can be calculated as

$$R_S = \delta^{-1}\sigma_1/\sigma_2^2 = R_N {\tau_n}^2 \omega^2 \frac{\exp(-\Delta(T)/k_B T)}{(1 - \exp(-\Delta(T)/k_B T))^2}, \tag{2.39}$$

where δ is a skin depth, that can be neglected in thin films. For $\tau_n \sim 10^{-14}\,\mathrm{s}$ and $\omega \sim 10^7\,\mathrm{Hz}$ the resulting R_S for temperatures not too close to T_c is only of the order of $10^{-14} R_N$, which is not measurable in most experiments. As a consequence, whenever a dissipative resistance is measured in the frequency range of up to 5 MHz used in this work it cannot be attributed to a Bogoliubov quasiparticle AC resistance, but must have a different origin.

2.2. Two-Level System Loss

Microwave resonators with large Q-factors are usually built from superconducting materials in order to minimize losses caused by charge carrier scattering. At low temperatures, however, the electromagnetic fields of the resonator can couple to two-level systems (TLS) in the substrate or other insulating parts in the vicinity of the superconductor [30]. These TLS can for example result from single atoms that can tunnel between two crystal sites. These states have electric dipole moments that couple to the electric driving field. This coupling effectively changes the dielectric constant of the microwave resonator. This leads to losses and therefore a reduction of the quality factor

as well as to a shift of the resonance frequency. For weak fields, i.e. driving currents, the internal quality factor of a microwave resonator is given by [31]

$$\frac{1}{Q_i} = F\delta^0_{TLS} \tanh\left(\frac{hf}{2k_BT}\right), \tag{2.40}$$

where F is called the filling factor of the TLS system in the material close to the resonator. It is a measure of the ratio of the electric energy stored in the TLS to the total energy in the resonator [32]. δ^0_{TLS} describes the loss tangent of the medium containing the TLS. It is defined as the ratio of the dissipative reaction of a medium with complex permittivity $\epsilon = \epsilon' - i\epsilon''$ to a electromagnetic wave propagating inside of it. For an insulating material with small losses the loss tangent can be written as

$$\tan(\delta) \approx \delta = \epsilon''/\epsilon'. \tag{2.41}$$

For frequencies $f \ll \frac{2k_BT}{h} \sim$ GHz for a temperature $T = 0.1\,\mathrm{K}$ the internal quality factor limited by the TLS is barely changed. The change of resonance frequency for weak driving can be calculated as

$$\frac{f_r(T) - f_r(0)}{f_r} = \frac{F\delta^0_{TLS}}{\pi}\left[\mathrm{Re}\Psi\left(\frac{1}{2} + \frac{hf}{2\pi i k_BT}\right) - \ln\left(\frac{hf}{2\pi k_BT}\right)\right]. \tag{2.42}$$

For low frequencies the first term reduces to $\Psi(\frac{1}{2}) \approx -1.96$ and hence the temperature dependence results entirely from the second term. f in the ln-term can be set to f_0 as the temperature varies much stronger than f_0. From equations 2.40 and 2.42 it follows, that for low frequencies the quality factor is nearly unchanged by the TLS but there is a small shift of the resonance frequency.

Eq. 2.42 is valid for microwave resonators, where all the energy is stored in the superconductor. In this work the resonator consists of a superconductor in series with an external copper coil with inductance L_0 much larger then the kinetic inductance L_s. Hence most of the energy will be stored in the coil. The characteristic prefactor $F\delta^0_{TLS}$ in eq. 2.42, in contrast, depends only on the energy in the superconductor. The resonance frequency $f_0(T)$, however depends on the total inductance $L_{total} = L_s + L_0$ of the sample. A fit of the measured $f_0(T)$ data to eq. 2.42 will give a fitting parameter $F\delta^0_{TLS}$ that is too small by a factor of L_s/L_{total}. Fitting parameters for $F\delta^0_{TLS}$ in this work will therefore be multiplied by the factor L_{total}/L_s and only the corrected number will be given.

The main structure under investigation consists of a thin Al film that is grown epitaxially on a high mobility 2DEG made from a InGaAs/InAs/InGaAs quantum well. The Al

layer is terminated by a native oxide (AlOx) layer that forms upon controlled oxidation at low oxygen partial pressures. Most of the supercurrent is flowing in the Al layer due to its much larger supferfluid stiffness and therefore coupling via electromagnetic fields should occur mainly at the Al/AlOx interface. Oxygen vacancies at the Al/AlOx interface can produce TLS and therefore change the resonance frequency of the system [33][34][35]. Single crystalline Al_2O_3 dielectrics have been shown to produce much less two-level fluctuations than amorphous AlOx [36], which either forms by evaporation of Al in an oxygen atmosphere or by oxidation of Al surfaces by diffusion of oxygen atoms into the crystal. The latter mechanism forms the oxide layer on top of the Al films in this work.

2.3. Spin-Orbit Coupling

Spin-orbit coupling (SOC) is a relativistic effect arising from the motion of an electron in an electric field. A basic example is a free atom, where electrons move in the potential of a positively charged core [37]. An electron that moves in the Coulomb field of the atom with velocity $\mathbf{v}$ experiences a magnetic field $\mathbf{B}$

$$\mathbf{B} = \gamma(\mathbf{v} \times \mathbf{E})/c^2, \tag{2.43}$$

where $\gamma = (1-v^2/c^2)^{-1/2}$. The spin of the electron σ is coupled to this magnetic field via the Zeeman effect, which leads to an energy contribution to the standard Hamiltonian of

$$H_{SOC} = \frac{\mu_B}{2c^2}(\mathbf{v} \times \mathbf{E}) \cdot \sigma. \tag{2.44}$$

In atoms each orbital can be filled with either spin-up or spin-down electrons. Therefore the energetical degeneracy of the two electrons is lifted because of the energy shift originating from SOC. In free atoms the electric field is produced by the positive charge of the nucleus. As the effective charge of the atom core is proportional to the atom number this effect becomes more pronounced for heavier atoms.

This concept can also be translated into solid state physics. From Eq. (2.44) it follows that in order to have a splitting due to SOC a finite electric field $\mathbf{E} = -\nabla\Phi(\mathbf{r})$ has to be present in the crystal. For bulk and centrosymmetric crystals the electric environment is relatively isotropic and hence SOC is typically weak. Materials that lack inversion symmetry in the bulk, however, produce a non-symmetric potential and lead to the

intrinsic so called Dresselhaus-SOC with the Dresselhaus parameter β [38]. Also surfaces, asymmetric heterostructures like 2DEG's embedded between two different materials or also gate voltages lead to finite electric fields in the crystal. Splitting of bands due to such macroscopic anisotropy is called Rashba-SOC [39] with associated Rashba parameter α_r. Of course it is possible that both effects appear at a time. In that case the associated spin-orbit (SO) field vectors have to be added in order to calculate the total spin-orbit field

$$\Omega = \sqrt{\alpha_r^2 + \beta^2 + 2\alpha_r\beta\cos(2\theta)}, \tag{2.45}$$

where θ is the angle between Rashba and Dresselhaus fields. The associated energy splitting is calculated as

$$\Delta E = 2\Omega k_F, \tag{2.46}$$

with k_F being the Fermi wavevector. One example of crystals with Dresselhaus SOC are Zincblende struktures like InAs, InGaAs, GaAs. If such compounds are grown in [001]-direction their spin-orbit fields lie in the [001] plane. The absolute value of the Rashba fields are isotropic in the plane with direction their direction perpendicular to the momementum. Dresselhaus fields have a more complicated $\vec{k}$-dependence (see Fig. 2.3).
Dresselhaus SO-fields can therefore induce anisotropy in 2-dimensional systems. Park et al. [41] directly measured the $\vec{k}$-dependence of the total SOC strength. SOC leads to a beating pattern when SdH-oscillations are measured. From the position of nodes of the pattern the total SO parameter can be extracted (Fig. 2.4). In the range of operation they estimated that the Dresselhaus field was just 5% of the Rashba field. Anisotropies originating from the Dresselhaus $\vec{k}$-contribution therefore should be small but detectable.

2.3.1. Nonreciprocal Transport

In systems where spatial and time-reversal symmetry is broken non-linearities in the electrical properties emerge. Rikken et. al. [42][43][44] measured this effect, which is generally known as magnetochiral anisotropy, in resistive systems. Spatial inversion is broken either an electric field perpendicular to the current direction by charging gate electrodes or making use of intrinsic electric fields that occur in systems with SOC. Time-reversal symmetry is broken by application of a magnetic field perpendicular to

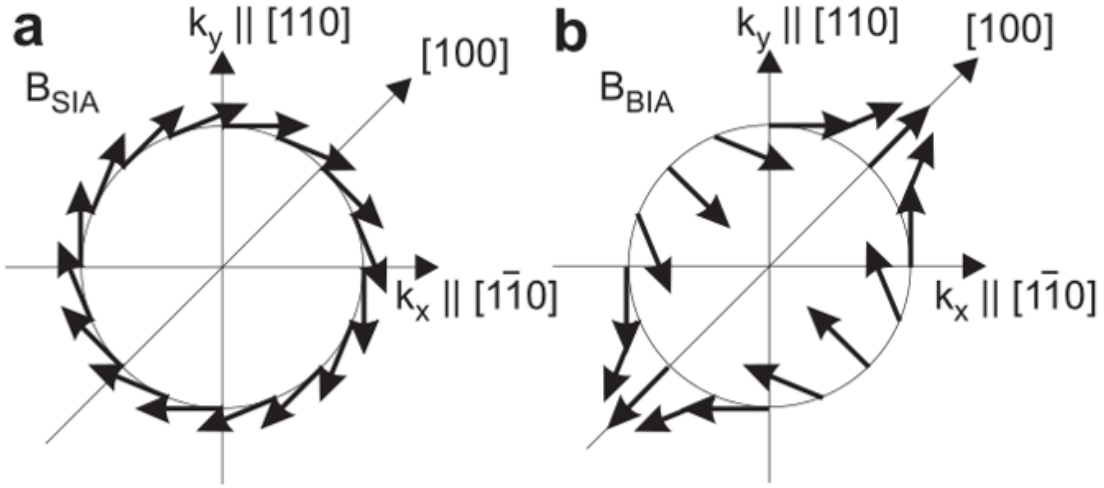

Fig. 2.3.: Spin-Orbit fields in Zincblende GaAs/InGaAs quantum wells. The growth direction is [0 0 1]. a) Rashba SO-field vector in the plane of the quantum well is always perpendicular to **k**. b) Dresselhaus SO-field vector is parallel/antiparallel to **k** in [1 0 0] / [0 1 0] directions. The total SO-field is calculated as vector sum over the different contributions. Taken from [40]

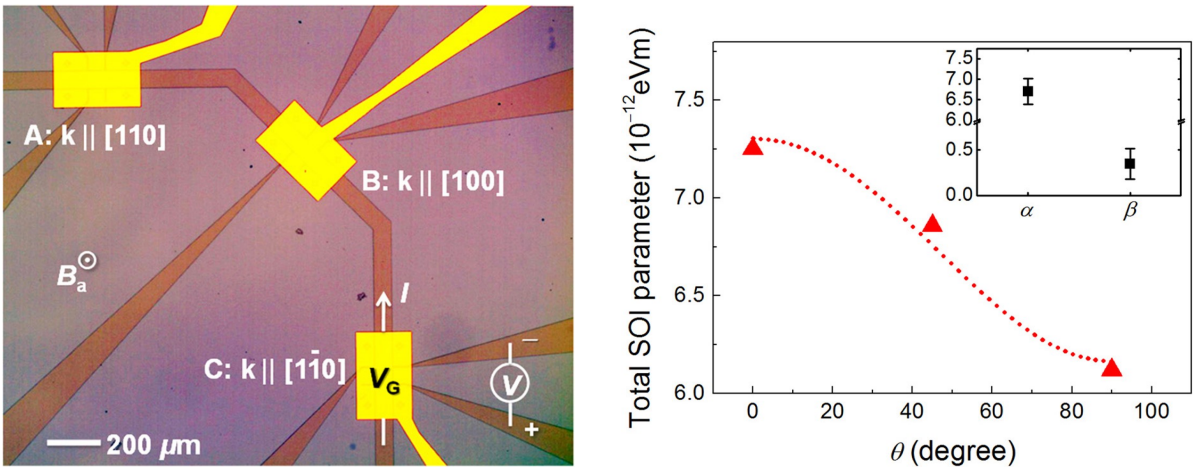

Fig. 2.4.: left: ion milling patterned structure (red) defines the dominating $\vec{k}$-direction of the 2DEG for three different current (momentum) orientations. With additional gate-electrodes (yellow) the Rashba SO parameter can be tuned. right: Total SO parameter determined from beating pattern of SdH-oscillations as a function of momentum direction. For $\theta = 0$ ($\vec{k} \parallel [110]$) the SOC strength is highest. Pictures from [41]

the current and electric field direction. In normal metals this effect is rather small as it depends on the ratio of energy scales of the involved quantities, i.e. Zeeman energy $E_z = \mu_B B$ and SOC strength $\Delta_{SO} = k_F \Omega$ with Ω being the total spin-orbit parameter. Compared to the Fermi energy E_F, E_z and Δ_{SO} are small. Therefore the observed

magnetochrial asymmetry will be small.
Such an anisotropy, however, can also be measured in superconductors. In this case the relevant energy is the superconducting gap Δ, which is orders of magnitudes smaller and therefore small Zeeman and SOC energies can lead to a significant magnetochiral effect in the fluctuation and BKT regime. Ando et. al [6] demonstrated non-reciprocal transport in an artificially layered SOC superconductor in an in-plane magnetic field perpendicular to the current direction. They could show that not only resistance was dependent on the current direction, but also the critical current. This can be viewed as a pendant to a classical diode, which rectifies normal current. The resistance in the regime of non-reciprocal transport in such systems can be heuristically written as

$$R = \frac{V}{I} = R_0 \left(1 + \gamma_s \left(\vec{B} \times \vec{z}\right) \cdot \vec{I}\right), \tag{2.47}$$

where $\vec{z}$ is a unit vector pointing out of the surface and γ_s is a parameter, that describes the magnetochiral anisotropy, which depends on the SOC strength. γ_s can elegantly be determined by measuring the first and second harmonic resistance in a low-frequency AC experiment (see also section 3.3.2). γ_s can then be calculated as

$$\gamma_s = \frac{2R_{2\omega}}{R_\omega B_\parallel I}, \tag{2.48}$$

where R_ω and $R_{2\omega}$ are the first and second harmonic resistance, B is the magnetic field and I the current through the sample.

Fluctuation Regime of Superconductors

Hoshino et al. [45] made a comprehensive derivation of various mechanisms that can lead to non-reciprocal transport in superconductors with spin-orbit coupling. One important domain, where non-reciprocal transport occurs, is the fluctuation (or paraconductivity) regime of the superconducting transition in 2D Rashba superconductors. In this regime an additional contribution to the conductance is produced by thermal fluctuations of the order parameter. Pure intraband pairing will occur for $\Delta \ll \Delta_{SO} \ll E_F$, where Δ is the superconducting gap. In that regime even and odd parity interactions lead to mixed parity of the superconducting order parameter. The explicit form of the $W\gamma_S$-value (W : width of sample) corresponding to the parity mixing contribution to the non-reciprocal charge transport is

$$W\gamma_S = \frac{\pi r_{t,s} S_3 E_F \alpha}{e S_1 T_0 E_{FR}}. \tag{2.49}$$

The parameter $r_{t,s}$ describes the parity mixing and can have both signs depending on the signs of singlet and triplet pairing interactions. All of the numeric factors in eq. 2.49 are positive and depend on sample parameters. This means that γ_S can have both signs depending on the actual pairing interactions. From the current $j = \sigma_1 E + \sigma_2 E^2$ the temperature dependence of $\gamma_S(T)$ can be calculated by replacing σ_1 with the fluctuation conductivity $\sigma_1 + \sigma_n$, where σ_n is the normal state conductivity. Using the Aslamazov-Larkin contribution to the conductivity the temperature dependence of $\gamma_S(T) \propto \sigma_2/(\sigma_1 + \sigma_n)^2$ is given by

$$\gamma_S(T) = \gamma_{S0} \left[1 + \frac{1}{c_0} \frac{\sigma_n}{e^2/h} \frac{T - T_{c0}}{T_{c0}} \right]^{-2} \tag{2.50}$$

BKT Regime

In 2D superconductors the transition from the dissipationless to the dissipative state is of the Berezinskii-Kosterlitz-Thouless type [46] [47]. This means that above a critical temperature T_{BKT} thermally activated vortex-antivortex pairs become unbound and can move freely when driven by a supercurrent. The result is a finite resistance already below the mean-field critical temperature T_{c0}. In the temperature range $T_{BKT} < T < T_{c0}$, an in-plane magnetic field leads to non-reciprocal transport in a Rashba superconductor.

The following derivation follows closely the work by Hoshino et al. [45]. In superconducting Rashba systems an in-plane magnetic field renormalizes the superfluid density isotropically as [45]

$$\tilde{n}_s = n_s \left(1 + 4\Lambda' B v_{s0} \right), \tag{2.51}$$

where v_{s0} is the vortex velocity, which depends on the externally applied current and $\Lambda' \sim -\frac{\sqrt{m}}{|E_F^{3/2}|}$ with $m \sim m*$. At the BKT transition point the attractive force that acts on the two constituent vortices (antivortices) of a bound pair separated by distance r are balanced by an entropic force proportional to the temperature

$$e^2 \tilde{n}_s \frac{1}{m^* r} \phi_0 = \frac{4 k_B \tilde{T}^{KT}}{r}. \tag{2.52}$$

This means that the effective BKT transition temperature is modified by the external current and the in-plane magnetic field and depends on the relative orientation of the two quantities [48].

$$\tilde{T}_{BKT} = T_{BKT}\,(1 + \alpha BI) \tag{2.53}$$

Furthermore an in-plane field leads to an anisotropic renormalization of the vortex viscosity

$$\eta = \eta_0\,(1 + d_0 \Lambda' B v_{s0}) \tag{2.54}$$

with $d_0 = \text{const.}$ and $\eta_0 \simeq \pi\sigma_n e^4 \xi^2$. These two effects lead to asymmetric IV-characteristics at fixed bath temperatures resulting in a finite γ_S. Surprisingly this can lead - with the right choice of parameters - to a *decreasing* linear resistance $R = V/I$ when the current is *increased*. In standard superconductors the linear resistance usually only increases with current due to pair breaking, depinning or heating effects. The temperature dependence of γ_S in the limit $T \to T_{BKT}$ is given by

$$\gamma_S \propto (T - T_{BKT})^{-3/2}\,. \tag{2.55}$$

This means that in the vicinity of T_{BKT} a diverging non-recirprocal signal could be expected. Near the mean-field critical temperature $T \to T_{c0}$ the temperature dependence reads

$$\gamma_S \propto (T - T_{c0})^{-1}\,. \tag{2.56}$$

γ_S-values resulting from non-reciprocal transport in the BKT-regime always have a positive sign. In the fluctuation regime, however, γ_S can have both and negative sign depending on the sign of the $r_{t,s}$-parameter. This means that a sign change in the $\gamma_S(T)$ curve can give an indication of the nature of the pairing interactions. As a superconducting system will upon cooling or heating pass through the fluctuation and BKT regime in a continuous manner, the different contributions to γ_s will partly overlap and make it hard to differentiate if the superconducting transition is sharp.

2.3.2. Field-Induced Pinning Enhancement in Superconductors with Rashba SOC

Out-of-plane field introduce vortices in thin film superconductors. As will be seen, the inductive response of a superconductor in presence of pinned vortices can be by orders of magnitude larger than the pure kinetic inductance, that is measured in zero field. Therefore the impact of an in-plane field on the vortex the pinning potential of a vortex in a system with strong Rashba SOC is of particular interest.

Dr. Denis Kochan from the University of Regensburg has proposed a model which estimates the effect of an in-plane field on the order parameter near a vortex core in a 2D system with SOC. At the time of writing a manuscript was being prepared for later publishment. What follows is a direct quote from this work in progress contributed by Dr. Denis Kochan.

"On the phenomenological level non-centrosymmetric quasi-2D superconductors with Rashba spin orbit coupling and external magnetic field can be described by the extended Ginzburg-Landau functional:

$$F[\Psi, \mathbf{A}] = a(T)|\Psi|^2 + \frac{b}{2}|\Psi|^4 + \frac{1}{4m}(\mathbf{D}\Psi)^* \cdot \mathbf{D}\Psi + F_L[\Psi, \mathbf{A}] \tag{2.57}$$

that apart of the conventional terms includes also the so called (isotropic) *Lifshitz invariant*:

$$F_L[\Psi, \mathbf{A}] = -\frac{1}{2}\kappa(\mathbf{n} \times \mathbf{B}) \cdot \mathbf{Y}_\Psi \tag{2.58}$$

$$= -\frac{1}{2}\kappa(\mathbf{n} \times \mathbf{B}) \cdot \Big[(\Psi)^* \mathbf{D}\Psi + \Psi(\mathbf{D}\Psi)^*\Big]. \tag{2.59}$$

In the above expressions Ψ stands for the condensate (Cooper pair) wave function, $\mathbf{A}$ for the vector potential, $\mathbf{B} = \mathrm{rot}\,\mathbf{A}$, and $\mathbf{D} = \frac{\hbar}{i}\nabla - 2e\mathbf{A}$ for the covariant momentum operator. The non-centrosymmetry of the quasi-2D film is captured by the isotropic Rashba Hamiltonian $H_R = \alpha_R(\mathbf{k} \times \mathbf{n}) \cdot \boldsymbol{\sigma}$, where the unit vector $\mathbf{n}$ is normal to the plane of the superconducting film and the parameter κ reads

$$\kappa \simeq 3\alpha_R \mu_B / p_F^2, \tag{2.60}$$

therein μ_B is the Bohr magneton, and p_F Fermi momentum. For the full derivation based on the microscopic theory including the exact expression for the numerical prefactor of κ (that is T_c dependent) see [49]. Adding to $F[\Psi, \mathbf{A}]$ also the energy density of the

magnetic field, $\mathbf{B}^2/\mu_0$, one can derive in a standard way the 1st and 2nd Ginzburg-Landau equations in the presence of non-centrosymmetry:

$$0 = \frac{1}{4m}\Big[\mathbf{D} - 2m\kappa(\mathbf{n}\times\mathbf{B})\Big]^2\Psi + \Big[a(T) - m\kappa^2(\mathbf{n}\times\mathbf{B})^2\Big]\Psi + b|\Psi|^2\Psi, \tag{2.61}$$

$$0 = \mathrm{rot}\,\left[\frac{1}{\mu_0}\mathbf{B} - \frac{1}{2}\kappa\,\mathbf{n}\times\mathbf{Y}_\Psi\right] - \frac{e}{2m}\mathbf{Y}_\Psi + 2\kappa e|\Psi|^2\mathbf{n}\times\mathbf{B}. \tag{2.62}$$

They are given in SI units, where e is elementary charge, m mass of the electron, and μ_0 magnetic permeability.

In what follows we assume the superconducting film is laying in xy-plane, i.e. its unit normal $\mathbf{n} = \hat{z}$ points along the z-axis, the vortex-generating magnetic field induction $\mathbf{B}_z$ is perpendicular to the film, i.e. $\mathbf{B}_z = B\hat{z}$, and the in-plane magnetic field induction $\mathbf{B}_{ip}$ is pointing along the y-axis, i.e. $\mathbf{B}_{ip} = H\hat{y}$. We assume quasi-2D geometry without crystallographic anisotropies, meaning, Ψ, B and H are functions of the in-plane coordinates only and there aro not preferential in-plane directions. As a comment, B and H are local fields at the spot and differ from laboratory values $B_\perp$ and $B_\parallel$. Moreover, looking for the vortex solution we assume $\Psi \simeq fe^{i\varphi}$, where f is a complex-valued function (with zero a winding number around the origin) that is varying on the range of the Ginzburg-Landau coherence length ξ. This is an excellent approximation if the magnetic penetration depth λ of the film is much larger than the Ginzburg-Landau coherence length ξ (assumed tacitly from now). Moreover, we are interested in Ψ inside the vortex core, i.e for radius $r \lesssim \xi$ where $|\Psi|^2 = |f|^2 \ll n_s \equiv |a(T)|/b$—the superconducting density far away the vortex center. Within these assumptions the second Ginzburg-Landau equation (or more precisely "rot" applied to its left and right sides what is liberating us from the vector potential $\mathbf{A}$) determines the magnetic field $\mathbf{B} = \mathbf{B}_{ip} + \mathbf{B}_z$ in terms of $|\Psi|^2 = |f|^2 = n_s\frac{|f|^2}{n_s}$:

$$\partial^2_{xy}H = 0 \tag{2.63}$$

$$\partial^2_{xx}H = \frac{H}{\lambda^2}\,\frac{|f|^2}{n_s}\,\frac{1}{1+2\kappa^2 m\mu_0|f|^2} \tag{2.64}$$

$$\Delta B = \frac{B}{\lambda^2}\,\frac{|f|^2}{n_s} - \frac{\Phi_0}{\lambda^2}\delta(x)\delta(y), \tag{2.65}$$

wherein $\Phi_0 = h/(2e)$ is the superconducting flux quantum, $\lambda^{-2} = 2e^2\mu_0 n_s/m$ is the inverse square of the magnetic penetration length and $\delta(x)\delta(y)$ represents 2D Dirac

delta-function centered in origin. Since inside the vortex core $|f|^2/n_s \ll 1$, we can safely set in the above equations $|f|^2/n_s$ to zero, doing so we get the following approximate solutions: (1) a constant H, whose value is tunable by the laboratory field (with a partially screened value), and (2) "logarithmically singular" $B(r) \simeq -\frac{\Phi_0}{2\pi\lambda^2} \ln r/r_{\text{cut-off}}$. This singularity is unphysical and a more involved treatment [50] gives for $r = 0$ and the vortex core region a finite value, something of the order of

$$B(0) \simeq \frac{\Phi_0}{2\pi\lambda^2} \ln\left(\frac{\lambda}{\xi}\right). \tag{2.66}$$

Since our discussion is qualitative we keep B inside the core as a fixed constant not far from $B(0)$, and determine its low temperature value later.

Knowing H and B that are effectively constants we can proceed further and linearize the 1st Ginzburg-Landau equation assuming T far below T_c, i.e. $a(T = 0) = -|a_0| < 0$, magnetic field $|\mathbf{B}_z|$ close B_{c2}, and the non-linear term $b|\Psi|^2\Psi \simeq 0$. To make a fully quantitative theory for $|\mathbf{B}_z|$ close B_{c1} is beyond the scope of this paper while it requires a numerical solution of the non-linear partial differential equation (lacking rotational symmetry) what makes a serious complications. The linearized 1st Ginzburg-Landau equation is gauge invariant, and in order to avoid any z dependence we employ the vector potential in the Coulomb gauge that depends just on the in-plane coordinates, particularly $\mathbf{A} = (-y\,B/2, x\,B/2, -x\,H)$. Plugging $\mathbf{A}$ into the linearized Eq. (2.61) and shifting the origin of coordinates from $(0,0)$ to $(0, -\frac{2m\kappa H}{eB})$, we get for Ψ (already with respect to such shifted origin) the following equation:

$$\begin{aligned} 0 = &-\frac{\hbar^2}{4m}\Delta\Psi + \frac{e^2B^2}{4m}\left[\left(1 + \frac{4H^2}{B^2}\right)x^2 + y^2\right]\Psi \\ &+ \frac{eB}{2m}\hat{L}_z\Psi - \left(|a_0| + m\kappa^2H^2\right)\Psi, \end{aligned} \tag{2.67}$$

where $\hat{L}_z$ is the zth component of the angular momentum operator $\hat{\mathbf{L}}$. To have the vortex solution we seek Ψ in the following form:

$$\Psi(x,y) = N\,(x + i\delta\,y)\,\exp\left[-\alpha\,\frac{x^2}{2} - i\beta\,xy - \gamma\,\frac{y^2}{2}\right], \tag{2.68}$$

where α, β, γ, δ and N are unknown real parameters. A direct calculation gives:

$$\alpha = \frac{2eB}{\hbar}\,\delta(H), \qquad \beta = \frac{eB}{\hbar}, \tag{2.69}$$

$$\gamma = 0, \qquad \delta(H) = \sqrt{1 + \frac{H^2}{B^2}}, \tag{2.70}$$

along with a constraint on the magnitude of B (aka upper critical field):

$$\frac{\hbar e}{2m}\sqrt{B^2 + H^2} \simeq |a_\kappa(H)| \equiv |a_0| + m\kappa^2 H^2. \tag{2.71}$$

To obtain N one needs to return to the non-linearized 1st Ginzburg-Landau equation, Eq. (2.61), however as already mentioned due to the lack of the rotational symmetry (coefficients in front of x^2 and y^2 in Eq. (2.67) differ) the problem is hard to tackle analytically. Since we are gliding on a semi-quantitative level we limit ourselves to the well-known solution for N in the conventional (rotationally symmetric) case, which can be found, for example, in [50]. To account for the non-centrosymmetry we only change in those standard formulas $|a_0|$ by $|a_\kappa(H)|$. Based on that "poor-man approach" we can estimate

$$N^2 \simeq \frac{4m}{\hbar^2}\frac{|a_\kappa(H)|^2}{b}. \tag{2.72}$$

Combining results expressed by Eqs. (2.68)-(2.72) and ignoring terms in higher order than κ^2 we can estimate the in-plane-field dependencies of the *superconducting stiffness curvatures* k_x and k_y, defined for the corresponding directions by the Taylor expansion of $|\Psi|^2$ around the vortex center, i.e.

$$|\Psi|^2(x,y) \simeq N^2\,x^2 + (N\,\delta(H))^2\,y^2 \equiv k_x\,x^2 + k_y\,y^2. \tag{2.73}$$

Looking only at magnetic field scaling one gets:

$$k_x(H) \propto |a_\kappa(H)|^2 \simeq c_1 + c_2\,H^2, \tag{2.74}$$

$$k_y(H) \propto \Big[\,|a_\kappa(H)|\,\delta(H)\,\Big]^2 \simeq (c_1 + c_2\,H^2)(1 + c_3 H^2/B^2), \tag{2.75}$$

where the coefficient $c_2 \propto \kappa^2$ quantifies an "amount of the non-centrosymmetry" of the Rashba 2D superconductor. It is obvious that $k_x(H) < k_y(H)$ for $H \neq 0$ and that both grow with growing H. As a consequence, if the probing in-plane current is perpendicular [parallel] to $\mathbf{B}_{ip} = H\hat{y}$, then one probes the inductance proportional to $1/k_y(H)$ $[< 1/k_x(H)]$. Moreover, if c_2 would be zero then the inductance proportional to $1/k_x$

would not depend on the in-plane field.“

Parameters k_x and k_y represent the curvature of the order parameter $|\Psi(x,y)|^2$ at the center of the vortex in the two orthogonal in-plane directions. Pinning energy can be calculated as a convolution of defect form factor and the order parameter itself. For δ-like defects the pinning energy as a function of dislocation (x,y) is equivalent to the order parameter in the vortex. In essence an in-plane field changes the shape of the order parameter in the vortex by reducing its core width depending on direction and strength of $B_\parallel$. Depending on the direction of the driving current (and therefore the vortex motion), different directions of the pinning potentials are probed, which will be seen in the measurement.

Initially eq. 2.75 only had two free coefficients c_1 and c_2. In order to be able to fit our data a third free parameter c_3 had to be added. The vortex inductance $L_v = \frac{\phi_0 B_\perp}{k_p d}$ (see eq. 2.30) resulting from motion of vortices in a pinning potential that is described by eq. 2.75 should be written in a more convenient way.
In the following B_t defines an in-plane field transverse to the current, B_p refers to an in-plane field parallel to the current. $L_{v,p}$ therefore defines the vortex inductance in a parallel in-plane field. $L_{v,pt}$ represents a vortex inductance in a transverse field. $L_{v,p}$ is then given by

$$L_{v,p}(B_\perp, B_p) = \frac{\Phi_0}{d}\frac{B_\perp}{k_x(B_p)} = \frac{\Phi_0}{d}\frac{B_\perp}{k_{p,0}\left(1+\frac{B_p^2}{\tilde{B_\parallel}^2}\right)}, \tag{2.76}$$

where c_1 is absorbed in a pinning constant $k_{p,0}$ at $B_\parallel = 0$. c_2 is absorbed in a characteristic in-plane field $\tilde{B}_\parallel$. For a fixed $B_\perp$ eq. 2.76 can be written as

$$L_{v,p}(B_p) = \frac{\Phi_0}{d}\frac{B_\perp}{k_x(B_p)} = \frac{L_{v,0}}{1+\frac{B_p^2}{\tilde{B_\parallel}^2}}, \tag{2.77}$$

where $L_{v,0}$ is the vortex inductance for $B_p = 0$.

$L_{v,t}$ in the case, where the in-plane field is perpendicular (transverse) to the current can be written as

$$L_{v,t}(B_\perp, t) = \frac{\Phi_0}{d}\frac{B_\perp}{k_y(B_t)} = \frac{\Phi_0}{d}\frac{B_\perp}{k_{p,0}\left(1+\frac{B_t^2}{\tilde{B_\parallel}^2}\right)\left(1+c_3\frac{B_t^2}{B_\perp^2}\right)}, \tag{2.78}$$

For fixed $B_\perp$ eq. 2.78 is simplified to

$$L_{v,t}(B_t) = \frac{\Phi_0}{d}\frac{B_\perp}{k_y(B_t)} = \frac{L_{v,0}}{\left(1+\frac{B_t^2}{\tilde{B_\parallel}^2}\right)\left(1+c_3\frac{B_t^2}{B_\perp^2}\right)}, \tag{2.79}$$

where c_3 scales the strength of the anisotropy of k_p.

$L_{v,p}(B_\perp)$ (eq. 2.76) is linear in $B_\perp$ with a reduced slope $\propto \left(1+\frac{B_p^2}{\tilde{B_\parallel}^2}\right)$ for $|B_\parallel| > 0$. For $B_\parallel = 0$, eq. 2.78 predicts also a linear $L_{v,t}(B_\perp)$ similar to eq. 2.30. Taylor expansion of $L_{v,t}(B_\perp)$ in $B_\perp$ (eq. 2.78), however gives a leading term that is cubic in $B_\perp$ for a non-zero B_t. The truth probably lies somewhere between these two limits as will be seen in section 6.2.4.

2.4. Unconventional Superconductivity

2.4.1. Pairing States

Cooper pairs are particles that are composed of two spin s = 1/2 particles that follow Fermi-Dirac statistics. The wave function of a two particle system consisting of two fermions needs to by antisymmetric upon exchange of the two constituents. The total wavefunction of a Cooper pair can be written by decomposing it into an orbital (l = 0,1,2...) and a spin component. Cooper pair wave functions that have a symmetric orbital component thus need to have an antisymmetric spin component. This means that in this case the two particles have opposite spin (s = 0 singlet). In the simplest case (l=0) this represents s-wave pairing, which is isotropic in k-space. Spin singlet inversion symmetric superconductors siwith higher order orbital angular momentum wave functions are e.g. called d-wave(l = 2). For superconductors with antisymmetric orbital wave function the spin component needs to be symmetric under exchange (S = 1 triplet). The pairing states for different odd orbital angular momentum are called p-wave (l = 1) or f-wave (l = 3). In the present samples under investigation, inversion symmetry is broken, and therefore p-wave admixtures to the order parameter can be expected [51].

2.4.2. Measureable Signatures of p-Wave Superconductors

Knight Shift

One hallmark that can be used to determine, whether Cooper pairs are spin singlet or triplet states is the temperature dependence of the Knight shift, which probes spin susceptibility by using NMR [52]. Magnetic fields produced by charge carriers (mostly due to its spin) shift the NMR frequency of the nuclei of metallic materials [53]. Spin singlet superconductors (s-wave, d-wave) show a decrease of the spin susceptibility below T_c, whereas in triplet paired superconductors (p-wave, f-wave) the measured susceptibility is constant [54]. For NMR measurements, however, high magnetic fields are crucial. Hence only superconductors that can sustain such high fields can be measured in this way. Thin films generally have much higher critical in-plane fields than their bulk counterpart due to the reduced orbital pair breaking effects, but very accurate alignment of field and film plane have to be assured. This makes Knight-shift measurements as a probe for unconventional superconductivity challenging.

Suppression of T_c by Impurity Scattering

In conventional, isotropic s-wave superconductors scattering with non-magnetic impurities does not lead to a suppression of T_c. This is commonly known as Anderson's theorem [15]. For Cooper pairs with finite angular momentum and therefore broken time-reversal symmetry, Anderson's theorem is not valid anymore. This leads to a significant reduction of the critical temperature for increasing concentrations of non-magnetic impurities. It was shown theoretically that even in anisotropic (l = 0) s-wave superconductors non-magnetic impurities lead to a reduction of the transition temperature [55]. Experimentally this effect was shown to be present in the f-wave triplet superconductor UPt_3 [56], in the triplet superconductor $K_2Cr_3As_3$ [57] and in the iron based superconductor $Ba_{0.8}K_{0.2}Fe_2As_2$ [58].

Temperature Dependence of n_s at Low T

Unconventional superconductors can have nodes in the superconducting gap for certain directions in momentum space. Therefore thermally excited quasiparticles persist down to low temperature. The exponential suppression of thermally excited quasiparticles in isotropic s-wave superconductors is replaced by a power-law T-dependence in superconductors, that have nodes in the excitation spectrum. Experimentally this can be addressed by measuring the temperature dependence of the change of kinetic inductance $L_s(T) - L_s(0)$, which is inversely proportional to the superfluid stiffness.

Parallel Field Tunability

In two-dimensional superconductors SOC mixes spin-singlet and -triplet states as Rashba and Gor'kov pointed out [51]. Considering p-wave pairing, SOC strengthens influences the superconducting order parameters for both singlet and triplet states [59][60]. The ratio of singlet and triplet state therefore depends on SOC strength. An external parallel magnetic field induces Zeeman splitting in the SOC-split quasiparticle bands. Whereas the Zeeman field lowers the singlet energy gap, the triplet gap for a fixed SOC strength stays rather constant (see Fig. 2.5)[61]. Triplet pairing therefore should be favored in an external parallel field [61]. This would make it possible to field-tune the ratio of the singlet-triplet mixed order parameter of a p-wave superconductor. The ratio of the two as observable quantity then of course has to be determined by measurement of some observable quantity (see other signatures).

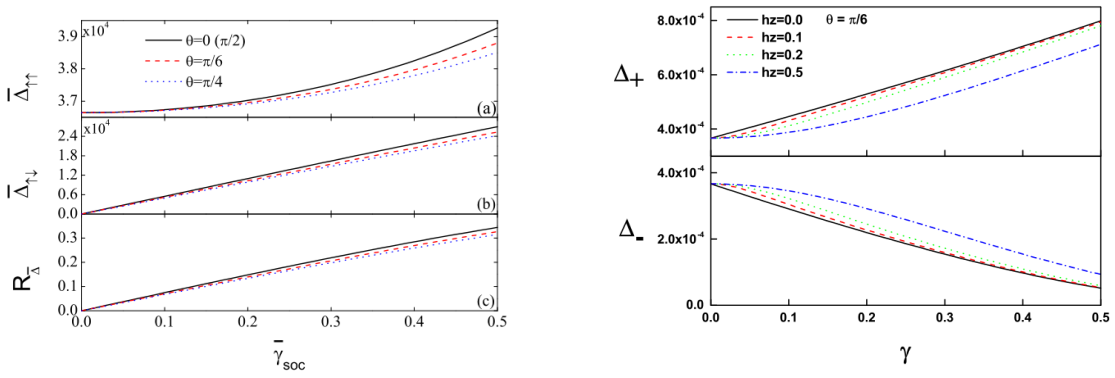

Fig. 2.5.: left: dependence of spin-singlet and triplet energy gaps on SOC strength in p-wave superconductors [59]. The interplay of Rashba and Dresselhaus SOC can lead to anisotropies depending on the relative orientation of both components. right: dependence of the quasiparticle energies on SOC and Zeeman fields (colored lines). For increasing fields $|\Delta_+|$ and $|\Delta_-|$ get closer and therefore the singlet energy gap $|\Delta_{\uparrow\downarrow}| = \frac{1}{2}(|\Delta_+| - |\Delta_-|)$ decreases, whereas the triplet gap $|\Delta_{\sigma\sigma}| = \frac{1}{2}(|\Delta_+| + |\Delta_-|)$ stays rather constant. Picture is taken from [61].

Enhancement of Vortex Pinning Potential in p-wave Superconductors

Another signature of a field-tunable p-wave superconductor could be the enhancement of the vortex pinning potential in a Zeeman field. For chiral p-wave superconductors $p_+ = (p_x + ip_y)$, the order parameter around a vortex is isotropic, if the in-plane field is zero. In finite fields the order parameter turns from the chiral p_+ state into a non-chiral p_x-state depending on the magnetic field direction (p_x for $B \parallel \hat{e}_x$) [62]. This also leads to a deformation of the vortex core. Its initially circular shape turns into a more elliptic form with anisotropy of the order parameter. For isotropic pinning centers this also leads to anisotropy of the pinning potential [63]. It can be investigated by measurement of the pinning potential for different displacement directions. The displacement of a vortex under a driving supercurrent is always perpendicular to the current direction. Therefore, by changing the relative orientations of in-plane field and current the symmetry of the pinning potential and hence the underlying pairing symmetry can be probed.

As mentioned earlier a Zeeman field can tune the ratio of singlet (s-wave) and triplet (p-wave) components of the superconducting order parameter for a p-wave pairing interaction. Hayashi and Kato have shown that the vortex pinning potential depends on the pairing state of the superfluid [64][65]. In s-wave superconductors vortices can reduce their energy by sticking to defects where the order parameter is reduced due to pair breaking effects or by quasiparticle scattering that helps the superconductor to sustain

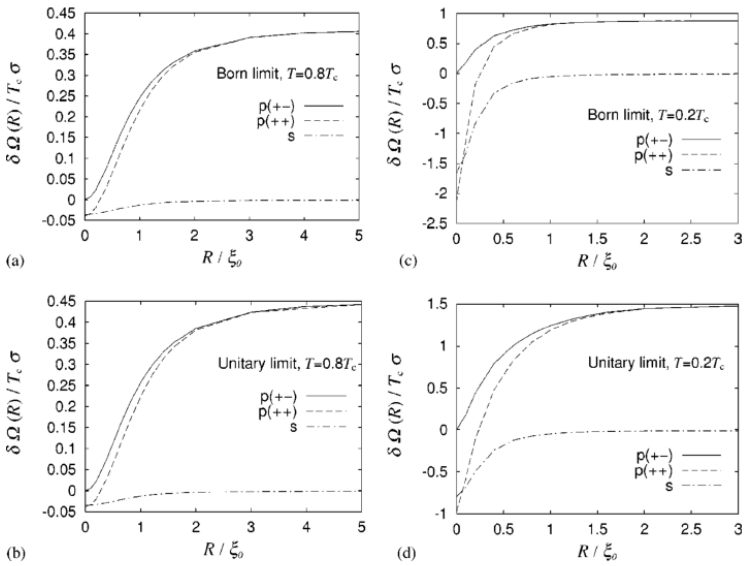

FIG. 1. The vortex pinning potential as a function of the distance R between the vortex center and the defect. Solid lines $[p(+-)]$ correspond to the case of the p-wave pairing with the chirality antiparallel to the vorticity (case I). Dashed lines $[p(++)]$ correspond to the case of the p-wave pairing with the chirality parallel to the vorticity (case II). Dot-dashed lines correspond to the case of the isotropic s-wave pairing. T_c is the superconducting critical temperature. The distance R is normalized with the coherence length $\xi_0 = v_F/\Delta_{BCS}(T=0)$.

Fig. 2.6.: Dependence of the vortex pinning potential on the dislocation of a vortex from a defect for different pairing states. Figure taken from [64].

local deformations of the order parameter. Far away from the vortex center Anderson's theorem applies and small defects do not change the superconducting order parameter. For p-wave superconductors exactly the opposite is true. In this case Anderson's theorem does not apply in the bulk and a defect located at a vortex center also leads to non-local pair breaking at a distance $\sim \xi_0$ away from the vortex core. This loss of condensation energy contributes to the vortex pinning potential. p-wave pairing therefore leads to enhanced vortex pinning that could be determined by measurement of the depinning current or the vortex inductance of such a system. Furthermore it was stated that at high temperatures the difference between the vortex pinning energy for s-wave and p-wave superconductors becomes even larger compared with low temperatures (see Fig. 2.6) [64]. Measurement of the parallel field dependence of the pinning constant at low and high temperatures offers another approach to acquire information on the underlying pairing mechanism.

3. Methods

3.1. Sample Structure and Fabrication

The following section will give a short overview over the crystal growth, structural properties and lithography of the measured samples. The three different crystal structures investigated in this work consist of thin Al films grown either on top of an insulating GaAs substrate or on top of a semiconducting InAs 2DEG with large Rashba spin-orbit coupling. From the Al/InAs heterostructure samples Al/InAs-M (meander), Al/InAs-S (strip), Al/InAs-C (circle) and 1D_JJ1 (Josephson junction array) were fabricated. From the Al/GaAs crystals two meander samples Al/GaAs-M15 and Al/GaAs-M7 were measured as a reference without spin-orbit coupling to sample Al/InAs-M.

3.1.1. Al/InAs Heterostructure

The material which was mainly investigated in this thesis is an Al/InAs heterostructure which was grown and provided by the group of Michael Manfra at Purdue University. The layer stack of the material is depicted in Fig. 3.1. The growth starts from an InP substrate on which a graded buffer layer is grown in order to produce a virtual InAlAs substrate. On this virtual substrate a 7 nm thick, asymmetric InGaAs/InAs/InGaAs 2DEG is grown. As a thin surface layer of Al oxidizes rapidly in air $2 - 2.5$ nm is subtracted from the nominal thickness in the quantitative analysis. The asymmetry of the confinement potential assures Rashba SOC. On top of the 2DEG a two monolayer thick GaAs layer is grown which acts as an etch stop. The last layer consists of 7 nm thick Al that grows epitaxially on the GaAs.

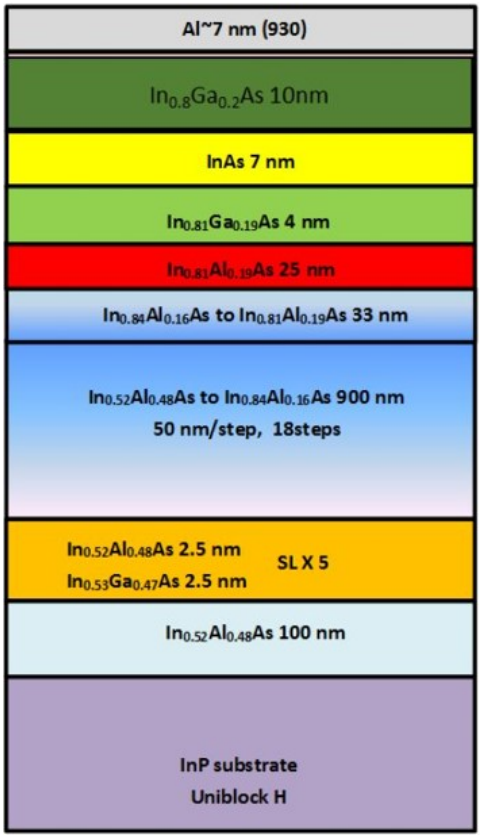

Fig. 3.1: Layer stack of wafer M10-08-18.2. The 7 nm thick Al layer is grown epitaxially on top of an InGaAs/InAs/InGaAs structure, which hosts a high mobility 2DEG (yellow). The layers are separated by a two monolayer thick GaAs sheet which acts as an etch and oxidation barrier. The heterostructure is on top of an InAlAs virtual subtrate. From top to bottom the In content is increased for the first 33 nm from 0.81 to 0.84 before it decreases again from 0.84 to 0.52 over a thickness of 900 nm. The whole stack is grown on a commercial InP wafer.

3.1.2. Crystal Lattice Matching in Al/InAs

In the following the symmetries of the two different crystal structures and their relative position relative to each other are discussed. If certain crystal directions are mentioned in this work section, they are always to be understood relative to its host lattice. This means, that the same expression for the crystal direction (e.g. [110]) corresponds to different directions in real space for the two lattices.
The substrate and the 2DEG are grown in the [001] direction. With the presented atomic composition ratios and most importantly a GaAs terminated surface the Al was shown to grow in the fcc [111] direction [66][67]. A top view of the two crystal surfaces is shown in Fig. 3.2. Zincblende (001) plane has a two fold symmetry and two mirror axes in the directions $[\bar{1}10]$ and [110] (left side of Fig. 3.2). Therefore thin chips of these crystals usually break along these directions when they are cleaved. The fcc (111) surface of the Al on top of the semiconductor has a threefold symmetry with three mirror axes (right side of Fig. 3.2). One of the in-plane mirror axes of the fcc (111) plane is $[\bar{1}\bar{1}2]$.

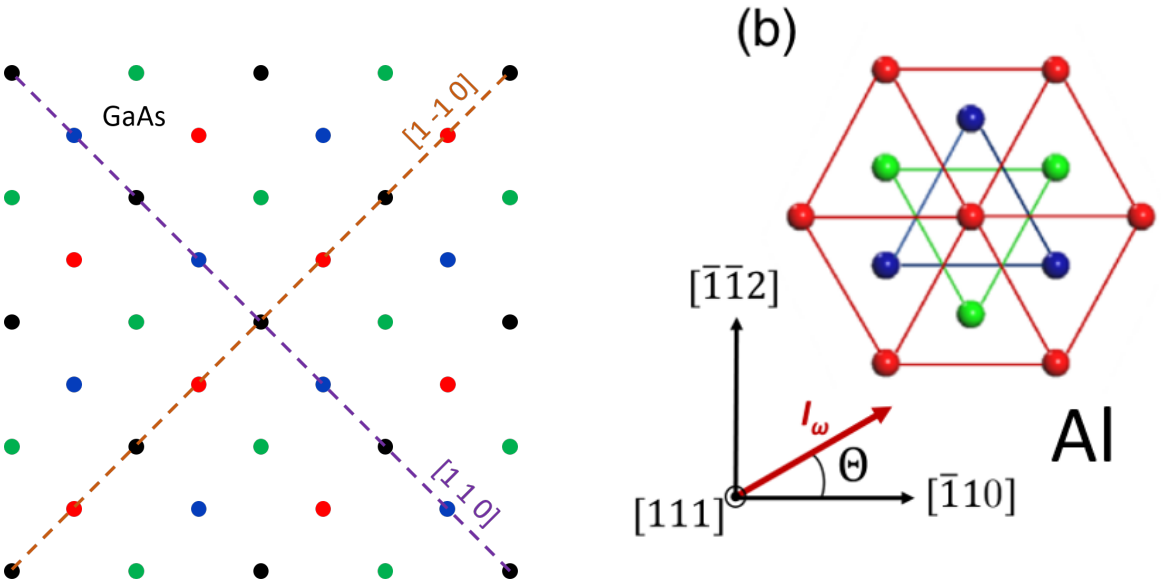

Fig. 3.2.: left: top view of the Zincblende (001) surface of the semiconductor. Different colors correspond to different atomic layers: black -> As atom in first layer, blue -> Ga atom in second layer, green -> As atom in third layer, red -> Ga atom in fourth layer. There are two mirror symmetric crystal directions $[1\bar{1}0]$ and [110]. right: Top view of the fcc (111) plane of the Al layer. There is a threefold symmetric structure. The Al $[\bar{1}\bar{1}2]$ axis is one of the three mirror symmetry axes, whereas the $[\bar{1}10]$ axis lacks mirror symmetry. Depending on the current direction (red arrow I_ω) Cooper pairs experience spin-orbit fields with threefold symmetry. Right picture taken from [68]

The orientation of the Al in-plane $[\bar{1}\bar{1}2]$ axis was reported to be either parallel to the

[110] [67] or the [1$\bar{1}$0] [66] axis of the semiconductor. The two possible stackings are shown in Fig. 3.3. This means that along one of the two Zincblende mirror axes also the Al has a mirror axis, whereas along the other main Zincblende axis, Al fcc lacks symmetry. The mismatch of the two lattice structures of the different lattices then breaks the symmetry of the system at the interface not only in the [001]-direction but also in the interface plane. Maybe this leads to strain in the structure and therefore electric fields in the plane. As a consequence, possibly a spin-orbit texture perpendicular to such fields i.e. out-of-plane is introduced at the Al/GaAs interface (see section 2.3).

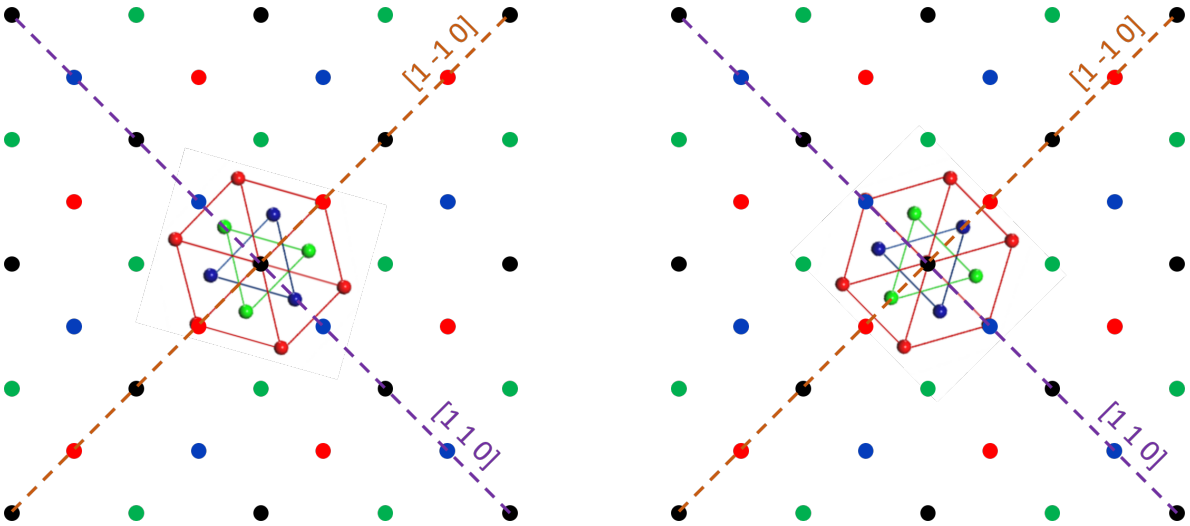

Fig. 3.3.: Possible stackings of the Al fcc (111) (dots with lines) and the (001) GaAs (dots) surface. The semiconductor In the left sketch the fcc [$\bar{1}\bar{1}$2] mirror axis is parallel to the zincblende [110] mirror axis. In the right picture fcc [$\bar{1}\bar{1}$2] mirror axis is parallel to the zincblende [1$\bar{1}$0] mirror axis. Note that these sketches only show the possible relative orientations of the rotational symmetries of the two lattices. The interatomic distances are not shown true to scale.

From this point on crystal directions are always to be understood as relative to the Zincblende lattice. For example, "current is flowing in the [110]-direction" means, that the current flow in real space is parallel to the Zincblende [110]-direction.

3.1.3. Lithography

The investigated samples all were either structured by means of optical or electron beam lithography (EBL). The provided wafer was successively broken into small pieces of some mm length and width always taking care that the crystallographic main axes were known. After a cleaning procedure in an ultrasonic Acetone bath and successive washing in Propanol the clean samples were blown dry with nitrogen. Afterwards the small rectangular pieces were spin coated with either optical or EBL resist. The samples were then heated in order to evaporate the solvent of the resist. Lithography was then performed either with an electron beam in a scanning electron microscope (SEM) or with UV radiation in a mask aligner setup. After the writing process the samples were put into resist developing chemicals. In the case of the optical lithography in the development step at the same time the desired structure was already etched into the Al layer, because the developer was based on NaOH, which dissolves Al. In the EBL case the commercially available etchant Transene D was used to selectively remove the Al layer from the resist-free regions. Afterwards a wet etching solution (orthophosphoric acid : citric acid : hydrogen peroxide : distilled water = 1.2 : 22 : 2 : 88) was used to etch deep into the substrate of the layer stack.

3.2. Measurement Setups

Probing superconducting dynamics deep in the superconducting state is featureless in DC resistance experiments because of the vanishing resistance at low temperatures. In order to investigate changes of the superconducting properties far away from the phase boundaries it is necessary to use AC techniques for measurement of the inductive response of a superconductor. In this next chapter two techniques that allow the measurement of the complex impedance of a superconducting thin film are introduced. The first approach was to measure the mutual inductance of two axially symmetric coils with the thin superconducting film sandwiched in between them. Although reliable results could be achieved for films with large dimensions, it turned out, that this method was not suitable for measuring small, patterned devices with high enough resolution. This made it necessary to establish a second technique based on the measurement of a frequency shift of a cold RLC circuit incorporating the superconducting structure.

3.2.1. Mutual Inductance Setup

Design Theoretical Description

The mutual inductance technique was introduced for the first time by Hebard and Fiory in 1980 [69]. Lemberger et al. [70][71][72] have used this technique to determine λ for thin Nb films and many other materials and came up with almost the same results as measured by ubin et al. [73] with a microwave resonance technique. Validity of the procedure therefore can be stated. In the course of this work two variants of the two coil setup have been constructed.
The setup of the first generation is sketched in Fig. 3.4. Photographs of the setups are shown in Figs. 3.5 to 3.7. The two coils wound from 50 μm thick copper wire are always kept at the same distance D from each other. The top part consists of a standard ceramic chip carrier, in which holes had been burnt in the center and on two corners with a laser from the electrical workshop of the chemistry department. One of the coils has then been glued into this hole and the leads put through the two outer holes and soldered on two contact pads on the inside of the chip carrier. The second coil has been connected with 4 spring loaded contacts as to be seen in Fig. 3.6, which should make contact with the gold pads inside of the chip carrier when mounted. In practice contact problems occurred at these points and the second coil was eventually contacted by simply soldering wires on two contact pads inside of the chip carrier and connecting them with two of the springs.

By sending a defined AC current with frequency f through one of the coils, called 'drive coil', a magnetic field is generated, which induces a voltage in the second, the 'pickup coil'. The complex mutual inductance between the two coils is then defined as

$$M = M_1 + iM_2 = \frac{U_{ind}}{I\omega}, \tag{3.1}$$

where I is the current through the drive coil and $\omega = 2\pi f$ the angular frequency of the drive current. M_1 represents the out-of-phase and therefore inductive part of the response function, M_2 the dissipative in-phase component caused by vortex friction, respectively.
As the direct measurement of the inductance of a superconductor by a standard transport measurement is challenging at low frequencies, one can make use of the magnetic response of a superconductor in an external magnetic field. By comparison of measured and simulated mutual inductances, λ can be computed. The model calculation of M follows

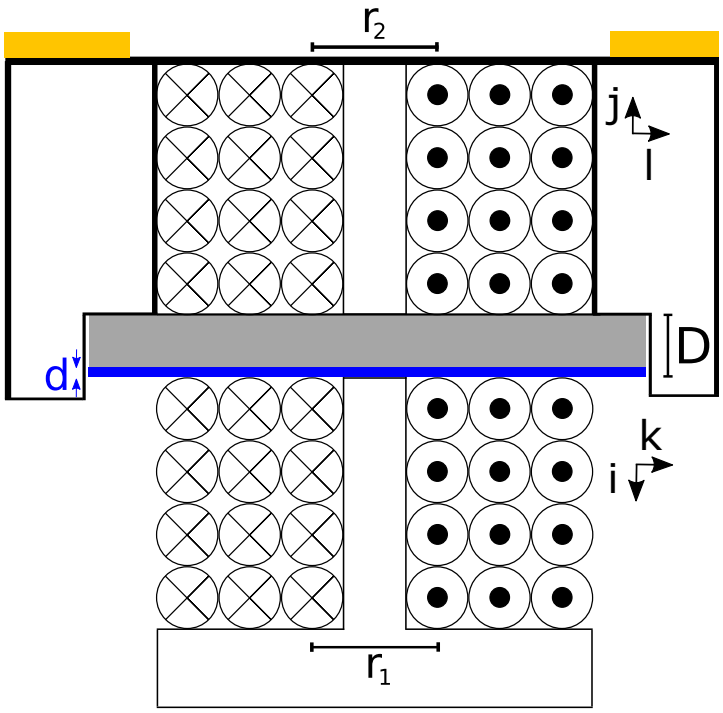

Fig. 3.4: Schematic view of the measurement setup. Two axially aligned coils are located on opposite sides of the sample of thickness D consisting of a substrate indicated by the grey bar and a thin superconducting film with thickness d, depicted as a black bar. Crosses in the loops are describing currents flowing into the drawing plane, dots indicate currents coming out of the plane.

Biot-Savart's law, which allows to compute the magnetic field at each point induced by a current density $\vec{J}(\vec{r})$ in the film:

$$\vec{B}(\vec{r}) = \frac{\mu_0}{4\pi} \int_V \vec{J}(\vec{r'}) \frac{\vec{r} - \vec{r'}}{\mid \vec{r} - \vec{r'} \mid} \mathrm{d}\vec{r'}. \tag{3.2}$$

Clem and Coffey [74] have shown that the mutual inductance between two single, coaxial coils with radii r_1 and r_2 on opposite sides of a thin film separated by a distance D in absence of vortex motion is given by

$$M_{sl} = \pi \mu_0 r_1 r_2 \int_0^\infty \frac{\Lambda}{1+\Lambda} e^{-Dq} J_1(qr_1) J_1(qr_2) \mathrm{d}q, \tag{3.3}$$

where $\Lambda = 2\lambda^2/d$ is Pearl's effective penetration depth. $J_1(x)$ represents the Bessel function of the first kind. The total mutual induction between the two coils is then computed by taking the sum over all possible pairs of single loops of both coils. For the given geometry this leads to

$$M(\lambda) = \sum_i \sum_j \sum_k \sum_l 2\pi \mu_0 r_{1,k} r_{2,l} \int_0^\infty \frac{q\frac{\lambda^2}{d}}{1+q\frac{\lambda^2}{d}} e^{-D_{i,j}q} J_1(qr_{1,k}) J_1(qr_{2,l}) \mathrm{d}q, \tag{3.4}$$

where $r_{1k} = (0.45 + k \cdot 0.08)$ mm, $r_{2l} = (0.45 + l \cdot 0.08)$ mm are distances from the symmetry axis and $D_{ij} = (1.261 + i \cdot 0.088 + j \cdot 0.065)$ mm the distance between a specific

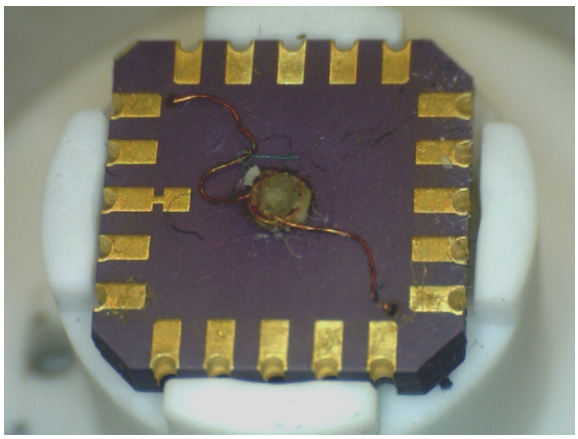

Fig. 3.5.: Top view of the two-coil setup. The pick-up coil is fixed into a standard chip carrier and connected with the contact pins. The chip is then pressed against the bottom part of the setup (right picture).

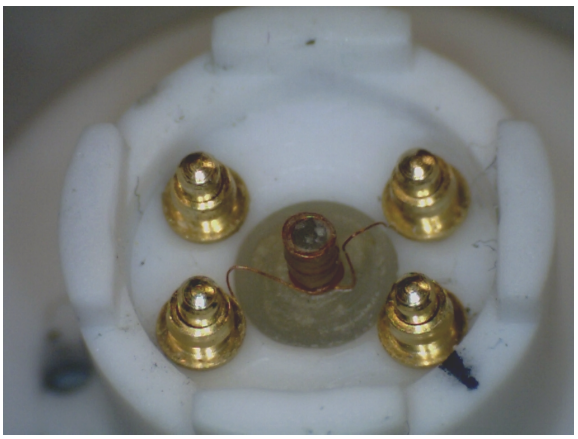

Fig. 3.6.: Drive coil and spring loaded contacts. The drive coil is connected with the springs which lead to the top of the setup.

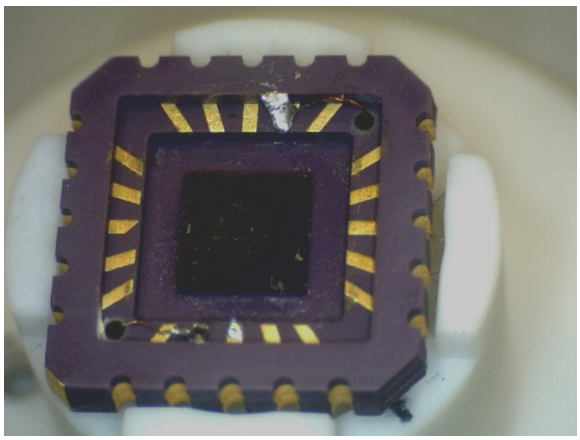

Fig. 3.7.: Sample (black square) inside the bottom side of the chip carrier. In the course of the measurement process a stencil has been cut with inner sizes of the films to center them within the setup. In the top and bottom row of contact pads, there are two solder joints for contacting the primary coil.

pair of loops. i and j represents the number of turns in the vertical, k and l those in the horizontal direction. These parameters lead to a calculated mutual inductance of $\sim 28\,\mathrm{nH}$ in the limit of infinite penetration depth in absence of superconductivity, which is in good accordance to the measured value in absence of a superconducting film of $\sim 28.6\,\mathrm{nH}$ (Fig. 3.8). This small difference does not much influence the actual results, as only normalized values are compared. For small λ, $M(\lambda)$ is approximately quadratic (see inset of Fig. 3.8).

The summation over single pairs of loops in eq. 3.4 requires the assumption that on the one hand single loops lie in planes parallel to the sample surface and turns in the horizontal direction are perfectly ordered next to each other as sketched in Fig. 3.4, on the other hand. Furthermore it is necessary to assume the single turns to lie in a strictly

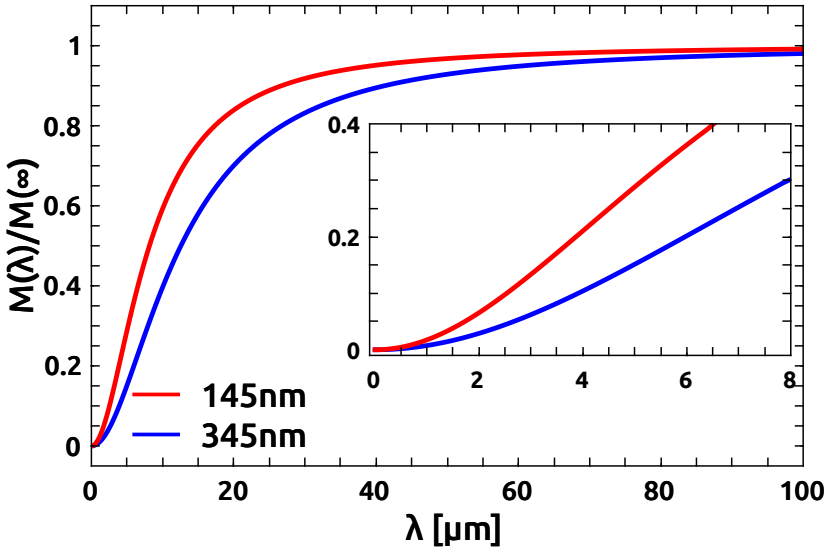

Fig. 3.8.: Simulated dependence of mutual inductance on magnetic penetration depth for the two investigated diamond films. M(λ) is normalized by the value calculated from eq. 3.4 for a sample with infinite penetration depth ($\sim 28\,\mathrm{nH}$). For $\lambda \to \infty$ the drive field can penetrate the superconductor without any suppression.

horizontal plane, although the coils have more or less helical shape. For simplicity the diameter of the wire is neglected. Therefore in the simulation all current flows in the center of the wire. In the vertical direction 30 loops in 3 layers are wound over a total length of 2 mm, so the distance between a pair of coils is just a sum over D plus the number of the vertical turns i and j times the average length per turn.

λ is then determined by solving $M_{meas}(T) = M(\lambda)$ for each point using a numerical solver included in Scientific Python. As mentioned, this simulation only holds in absence of vortices. For superconductors in the vortex state a second term, which describes vortex motion in the film caused by AC fields has to be added to the response resulting from screening currents

$$M = M_{scr} + M_v. \tag{3.5}$$

The vortex term is proportional to the number of vortices in the sample. Without perfectly zeroed out-of-plane field or near T_{BKT} the number of vortices is unknown. Hence, the vortex contribution is neglected in the calculation. Assuming that there can be a vortex contribution, calculated λ represents an upper limit for the actual value [74].

Calibration Measurement and Exemplary Results

Once the film reaches its critical temperature, the out-of-phase signal measured by the pickup coil is reduced strongly due to the Meissner effect. The dissipative component, on the other hand, is most dominant near the transition temperature, where vortices are excited thermally and can move freely before they become bound or pinned by defects below T_{BKT}. The drive field in all cases was kept small enough of the order of $5\,\mu$T to avoid introduction of vortices.
For $d \gg \lambda$ the film is assumed to completely screen magnetic field lines produced by the drive coil, that would go through the sample. Only field lines leaking around the film then contribute to the signal. As already mentioned, the simulation is only valid for films of infinite lateral extension without any leakage signal. Therefore it is necessary to compensate this offset in the induced voltage. To do so, a calibration measurement is carried out with a 200 nm thick ($d_f \gg \lambda$) aluminum film (Fig. 3.9), which is assumed to screen all of the magnetic flux, that would go through the sample. Measurements with superconducting films of the same cross section are then normalized with these values:

$$\frac{M_{sim}(\lambda)}{M_{sim}(\infty)} = \frac{M_{exp}(T,B) - M_{cal}(0)}{M_{cal}(T \gg T_c) - M_{cal}(0)}. \tag{3.6}$$

If, on the other hand, the penetration depth is in the range of the film thickness, there is still a non-zero contribution of the magnetic flux through the film to the measured voltage. The resulting net signal is then compared with the simulation for the whole setup including all geometric factors. For evaluation all the measured curves are normalized to its magnitude just above T_c and then compared with the simulation mentioned above. This normalization is important to minimize run to run variations.

Fig. 3.11 shows the temperature dependence of the magnetic penetration depth and the DC resistance of a nominally 6.5 nm thick Al film that was grown on top of an InAs 2DEG in the MBE chamber of the workgroup of Dominique Bougeard at UR. The relatively high transition temperature of 2 K and a sheet resistance of $109\,\Omega$ in the normal state hints towards some granularity of the film. Together with a measured penetration depth $\lambda(0) > 1\,\mu$m the Al film quality turned out not to be a possible platform for artificial p-wave superconductivity where high quality films and interfaces between superconductor and 2DEG are needed.

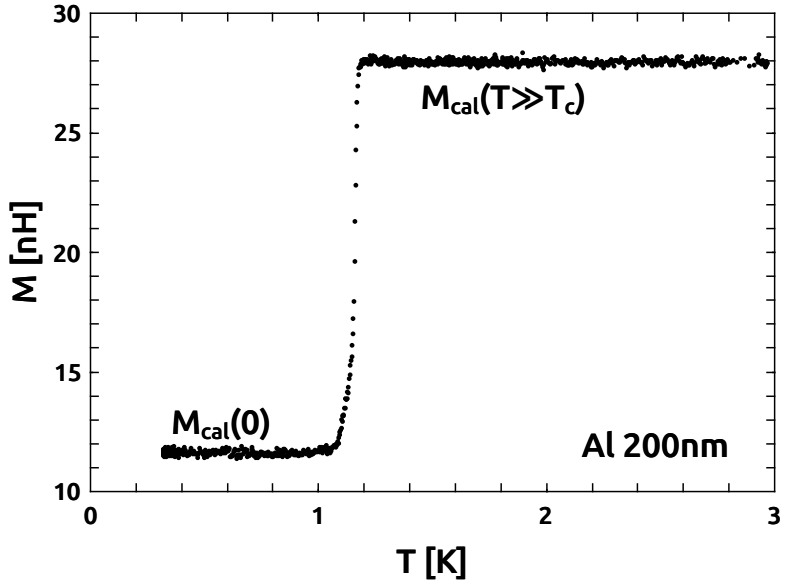

Fig. 3.9.: Calibration curve for samples with a cross section of 3.1 mm × 3.1 mm. $M_{cal}(0)$ shows screening of the thick aluminum film in the superconducting state and is supposed to represent only magnetic flux leaking around the sample. Above and below T_c a constant mutual inductance is measured. The difference between these two constants is the effective, maximum mutual inductance for samples of the same cross section.

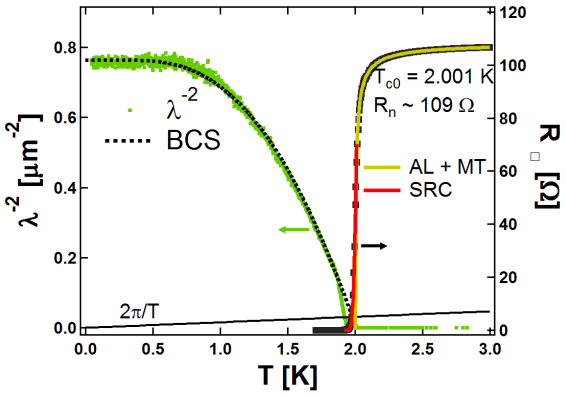

Fig. 3.10.: Temperature dependence of magnetic penetration depth and DC resistance of a 6.5 nm thick Al film grown on top of a InAs 2DEG.

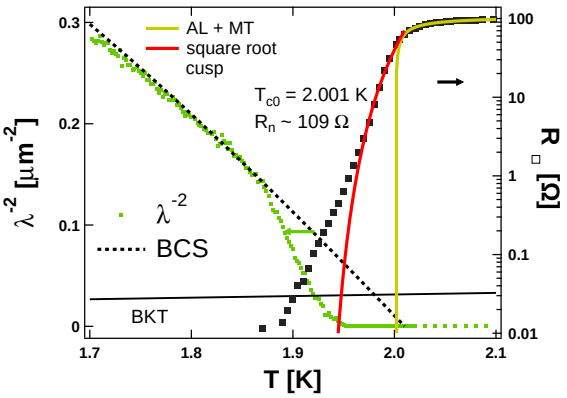

Fig. 3.11.: Zoom near T_c. Resistance is plotted in a logarithmic scale. The temperature where the DC resistance was not measurable anymore fairly coincides with the onset of superfluid density although both measurements were performed in two consecutive cooldowns.

Alternative Setup Designs

Further measurements were performed in the course of a master and state examination thesis. The results are not shown here. The used mutual inductance setups, however,

should be introduced here, as they might be useful for future applications. The coils were all wound by the author. For the measurements in these works a modified version of the above sketched setup was used. Instead of a single pickup-coil an additional, equally but counter-wound coils is connected in series with the first pickup coil. With that compensation pickup of slowly in space varying magnetic AC fields can be reduced and signal-to-noise ratio is increased. For the numerical calculation on the right hand side of eq. 3.4 there will be a sum of contributions from the two coils with different sign. The signal will, however, still be dominated by the first pickup-coil due to the exponential dependence on the distance between drive and pickup-coil. The coils of the second generation are wound from 25 μm thick copper wire. Photographs through the optics of a microscope is shown in Fig. 3.12 and 3.13. As such thin wire are easily torn apart, the winding of such coils is quite challenging.

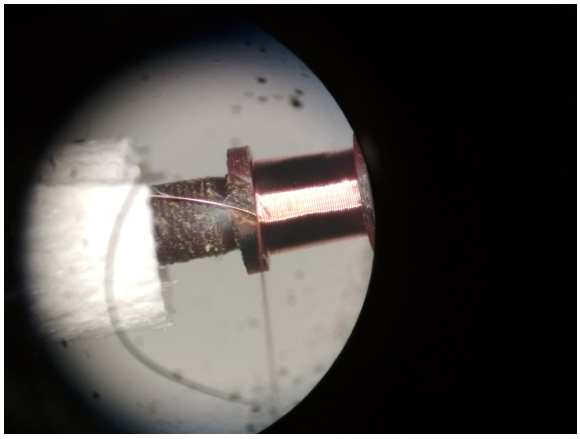

Fig. 3.12.: Photograph of a still unglued drive coil. On the left side the two leads can be seen. The coils are wound from 25 μm thick copper wire. The single turns of the coil align nicely parallel by keeping a small tension in the direction opposite to the feed.

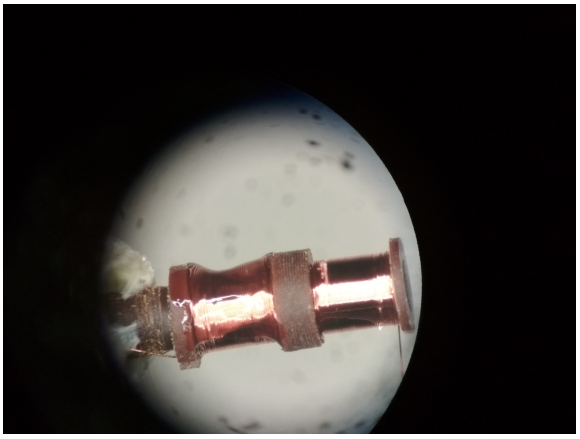

Fig. 3.13.: Photograph of a compensated pair of self-compensated pickup-coils consisting of two counterwound but otherwise similar single coils. The left coil is already glued with second glue. Leads can be seen on the very left and right side of the coils.

The setup used for coil winding is shown in Fig. 3.14. The coil body is clamped in the drill chucks of a cordless drill that can rotate in both directions. The spool with the copper wire is placed on a metal rod under the table. The wire is lead through a constriction of soft foam and finally over a soft edge made from standard duct tape. By that a small, but sufficient tension in the wire could be achieved, that is necessary for a proper arrangement of the windings on the coil body. The first lead is glued with duct tape on the side of the drill chucks before winding. During the winding process the wire is always kept under tension with a small angle away from the feed direction. With that

the single turns of the wire automatically arrange parallel to each other. For coils with more than one layer the wire tension direction has to be adjusted when one end of the coil body is reached before the reversal of the feed direction. The winding progress can be watched through an optical microscope. In that way also the number of turn wound on the coil bodies are counted.

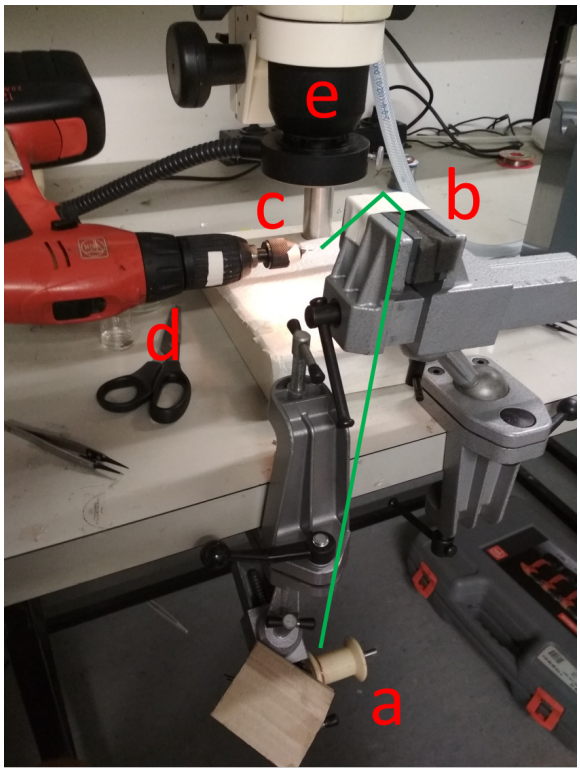

Fig. 3.14.: Setup used for winding of the microcoils. a: Spool with copper wire. b: Soft foam constriction producing finite tension on wire and duct tape changing wire direction. c: drill chuck holding the coil body. d: cordless drill. e: optical microscope. Green line represents the copper wire during the winding process.

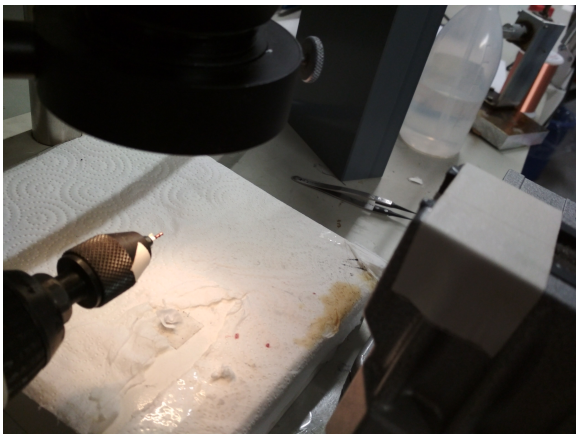

Fig. 3.15.: Photograph of a fully wound pickup-coil still mounted in the drill chucks. On the right side one can see the wire running across the white duct tape before it is bent down towards the coil body.

A third version of such a mutual inductance setup was also tested. In that design both drive and pickup-coil are located at the same side of the superconducting film. The drive coil in this case is glued symmetrically inside a hole drilled in the center of the pair of compensated counterwound coils. The signal above T_c is zero as the two parts of the pickup-coil pick up the same flux from the drive coil which produces equal induction voltages with opposite sign. As a superconductor is placed on one side of the

setup an additional signal is produced by the inductive response of the thin film. The flux resulting from the induced Meissner currents in the superconductor decays over the distance to the film surface. Then a net signal is measured, because the pickup-coil next to the film will detect more flux than the one further away. The calculation of λ from the mutual inductance data is very similar to that already mentioned with slight adjustments. As the signal is nearly zero (depending on the equality of the windings of the two parts of the pickup-coil, proper arrangement of drive coil inside the pickup-coil etc...) above T_c this method is especially well suited for small inductive responses as to be expected in very disordered thin film superconductors. Small voltages allows the use of high amplification for the detection, which gives good signal-to-noise ratio. Furthermore the relative position of drive and pickup-coil does not need to be changed when the sample is changed. With that, the run to run fluctuations can be kept much smaller compared with two separate coils.

At last the self compensated setup gives the possibility to put another coil on the far side of the thin film. This allows the simultaneous measurement of the inductive response on both sides of the sample. In the course of this work with the help of bachelor students Lukas Herrmann, state examine student Christian Gaube and master student Leon Müller efforts were made to directly measure the anisotropy of the Meissner currents of thin film d-wave YBCO superconductors. In principle this technique should work for any superconducting state that has anisotropic Meissner responses to external fields, which is expected in Al/InAs heterostructures.

For that kind of setup, an arrangement of micro coils were produced by means of electron beam lithography and evaporation of gold on a Si/SiO_2 substrate. These gradiometer coils were placed on the far side of the film with the center of the arrangement aligned axially with the drive/pickup-coil. The chip with the microcoils could be rotated in-situ by a room temperature step motor with a transmission to the sample holder of a 4K stick. Fig. 3.16 shows two sets of microcoils. The coils are interconnected by bond wiring in a way that neighboring coils produce opposite voltages so that zero net voltage should be achieved in a radial symmetric excitation field. Asymmetric fields resulting from anisotropic Meissner currents in the sample therefore should produce a finite voltage in the gradiometer coils. By rotating the sample together with drive and pickup-coil relative to the gradiometer coils symmetries of the supercurrent pattern could be investigated. The whole setup was put at the very end of a 4K dip stick (Fig. 3.17)

Although the production and calibration of the gradiometer coils were succesful and

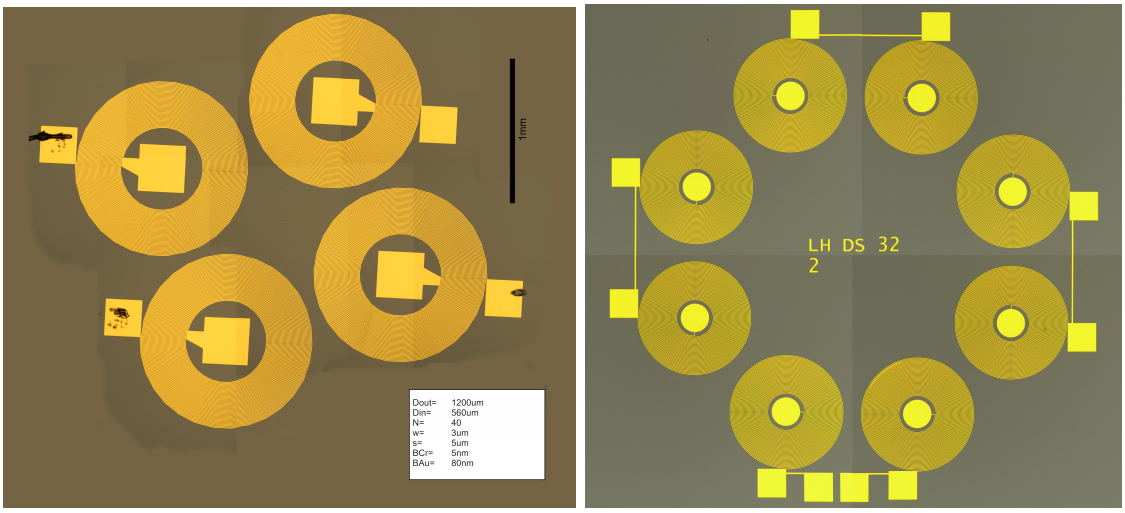

Fig. 3.16.: left: Quadrupol arrangement of on-chip microcoils produced by EBL and gold evaporation. The linewidth of the coils are in the low μm regime. Picture taken from master thesis of Leon Müller, April 2020. Right: Octupol arrangement of microcoils. Picture taken from bachelor thesis of Lukas Herrmann, November 2018.

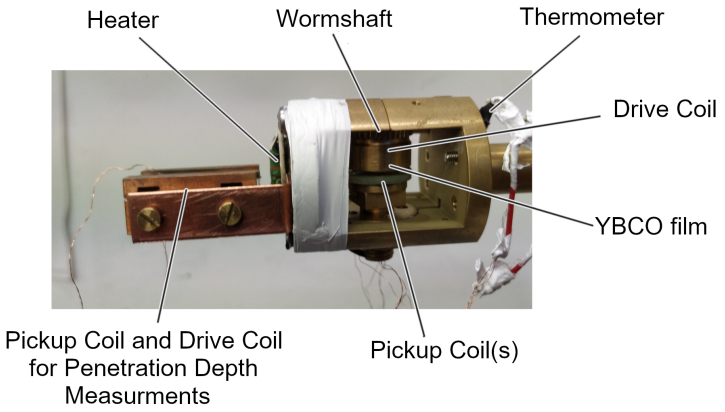

Fig. 3.17: Photograph of the sample holder with the gradiometer setup (center) and a standard two-coil setup (left). Picture taken from master thesis of Leon Müller, April 2020.

induced voltages could be measured there was no clear signature of anisotropic Meissner effects in thin film YBCO. In order to achieve reliable results a more dedicated approach by means of a full-time PhD student working on the topic would be needed to be employed.

Limits of the Mutual Inductance Technique

The mutual inductance technique to determine the inductance of superconducting thin films, although well established, has some limitations, which made it inappropriate for the further use in this work. Firstly, for a good accuracy relatively large (lengthscale cm) and on that scale also clean samples are needed, because the signal strength de-

pends on the dimensions of the pick-up coils. Therefore only averages over the whole sample can be measured. Secondly, it is not possible to simultaneously perform standard DC transport measurements with a good accuracy or to determine the impact of superimposed DC currents of a sample. Thirdly, an inductance measurement of small, structured devices like Josephson junctions or constrictions is not possible. Furthermore, for each sample geometry an individual calibration measurement with an equally sized, thick superconducting reference sample is needed. At last, the use of a setup with moveable parts lead to significant run to run fluctuations. All these disadvantages demand a more dedicated setup for measuring the complex impedance of superconducting microstructures in a reproducible manner.

3.2.2. RLC Circuit

The above mentioned limitations of the two-coil method demanded a different setup, better suited to measure the complex impedance of superconducting microstructures. The setup design used for that purpose is based on the work of Meservey and Tedrow from 1969 [9]. They determined the kinetic inductance of long superconducting meanders by measuring the resonance frequency of an RLC circuit, in which the sample was incorporated. They used an analog counter to determine the frequency of the damped oscillation after application of a DC puls to the resonator. From the oscillation frequency they were able to determine the kinetic inductance of the structure. By counting oscillations instead of absolute voltages, the signal-to-noise ratio can be enhanced significantly.

There are some advantages in using resonators in the MHz regime for probing superconducting dynamics instead of a microwave experiment performed with a superconducting stripline resonator. Mhz frequencies are usually far away from the range, where thermally excited Bogoliubov quasiparticles produce a significant resistance, which would damp the resonance, as it is the case in microwave resonators. Also the vortex depinning frequency, at which pinned vortices start to dissipate under an AC current, is usually in the GHz regime. Free vortex motion significantly reduces the quality factor of microwave resonators, whereas in the present RLC circuit dissipation due to vortex motion is small. This allows to measure vortex dynamics of weakly pinned vortices in rather high out-of-plane fields by using MHz frequencies. In a superconducting microwave experiment, great care needs to be taken to reduce losses caused by quasiparticles. This is achieved partly by decoupling the microwave resonator from the leads by with small capacitors in series at the input and output of the stripline. This prevents DC and low-frequency noise from spoiling the quality factor. This, however, also makes it impossible to study the impact of DC currents on the superconductor, which is a crucial parameter when measuring polarity dependent impedances. For a precise measurement of the dynamics of the complex impedance of superconducting structures, a RLC-resonator in the low MHz regime is therefore very well suited. The modified version of the resonance technique of Meservey and Tedrow used in this work and the corresponding electrodynamics are discussed in the following sections.

Circuitry and Electrodynamics

The basic principle of measuring the kinetic inductance and therefore the superfluid stiffness of a superconductor used in this work is to incorporate the sample into a parallel, resonant RLC circuit (Fig. 3.18). The sample is placed in series with a constant inductor L_0 and parallel to a constant capacitor C. The inductor is a self-wound coil made from copper wire. In the superconducting state of the sample, where damping of the resonator is small and mostly due to the resistance of the coil, the resonator shows a sharp peak at the resonance frequency f_0. f_0 and the width of the resonance δf can then be extracted by fitting the recorded data to a standard resonance curve. From these two quantities, the complex impedance of the sample can be calculated. Photographs of the two RLC resonators that were used in this work are shown in Fig. 3.19.

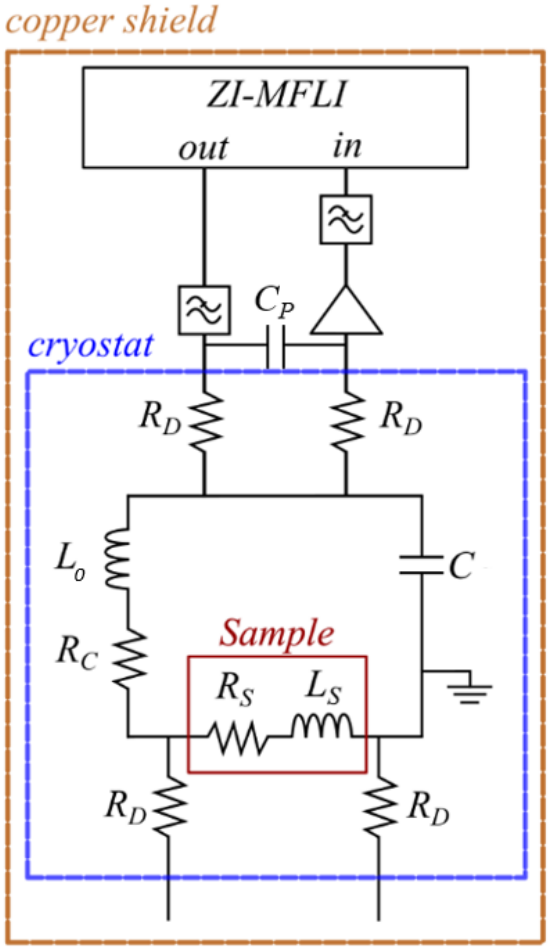

Fig. 3.18: left: Schematic picture of the RLC resonator. The setup is isolated from the rest of the cryostat by four resistors R_D. In the RLC parallel resonant circuit the superconducting sample is connected in series with a constant inductor L_0 and parallel to a constant capacitor C. Sample resistance R_s and inductance L_s are varied by external parameters. C_P represents a stray capacitance between the measurement leads. The resonator is driven and the preamplified returned signal read out by a digital lock-in amplifier working in the low MHz regime. Room temperature π-filters reduces high frequency noise in the system.

The circuit is isolated from the rest of the cryostat with four resistors R_D with a resistance larger than the characteristic circuit resistance at the resonance $Z_m = \frac{L}{CR_s}$. For

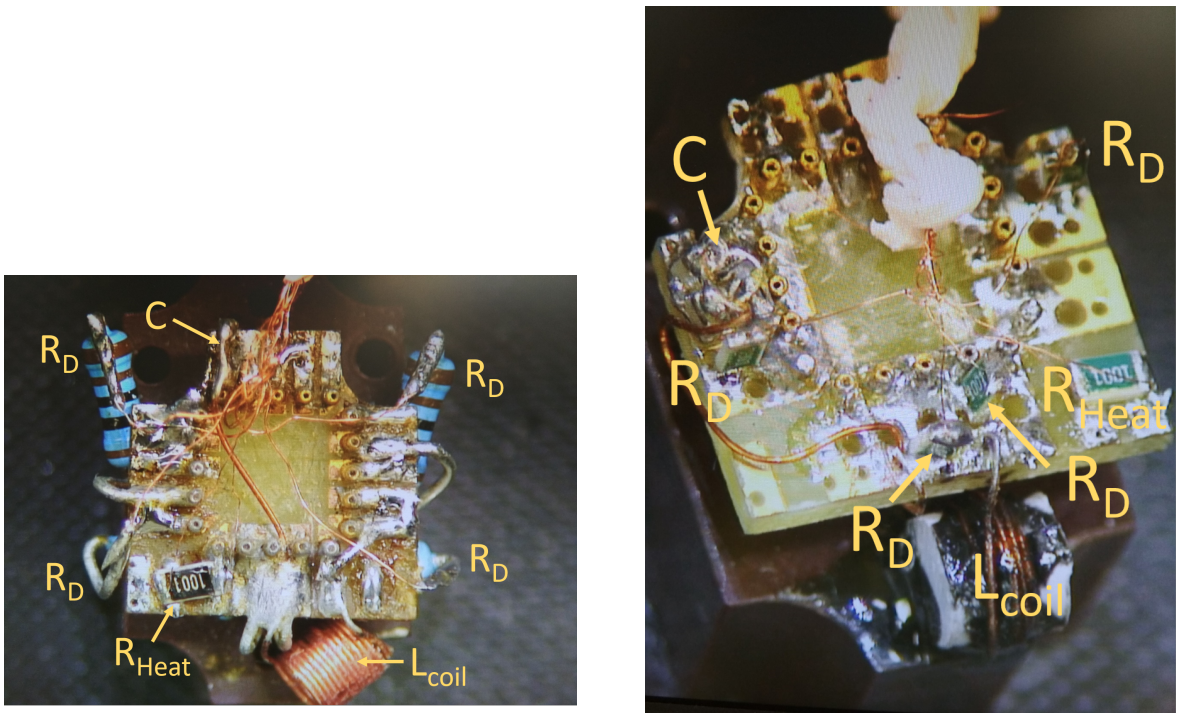

Fig. 3.19.: Left: RLC resonator of first generation used for parts of the measurements. Decoupling resistors R_D are standard 1 kΩ cylinder resistors with nearly constant resistance down to low temperatures. The air filled coil was wound from 100 μm thick copper wire and has an inductance of $L_{coil} \approx 320$ nH. The capacitance C consists of two parallel 2.2 nF SMD capacitors with a total capacitance of 4.42 nF. R_{Heat} is a 1 kΩ SMD resistor, that can be used to locally heat the sample holder without warming up the mixing chamber. Right: RLC resonator used for the major part of the inductance measurements. The decoupling resistors and the heater are 1 kΩ SMD resistors. The capacitance consists of four 1 nF SMD capacitors in parallel with a total $C = 4$ nF. The inductor is a coil wound from copper wire on a small rod of PVC with an approximate inductance of 396 nH, which is fixed on the sample holder with epoxy. With this unwanted changes of inductance due to accidental bending of the coil leads during sample exchange can be prevented, which gives good reproducibility.

films and resonators in this work this resistance is of the order of $\sim 300\,\Omega$. If this is fulfilled the circuit can in good approximation be considered a series circuit with resonance frequency

$$f_0 = \frac{1}{2\pi}\sqrt{\frac{1}{LC}}, \tag{3.7}$$

where $L = L_0 + L_s$. L_0 is the inductance of the small coil in series with all stray inductances coming from self-inductances of bond wires, cables or loops of conducting lines.

Quality factor Q of the resonator can be calculated as

$$Q = \frac{1}{R_s}\sqrt{\frac{L}{C}} = \frac{f_0}{\delta f}. \tag{3.8}$$

Spectra are taken at constant external parameters such as temperature, magnetic field or DC current through the sample. With an inductance of typically several hundred nH of the coil and a capacitance of some nF, a resonance frequency in the low MHz is achieved, which can be detected with a 5 MHz lock-in amplifier. Spectra are fitted using a Fano resonance function

$$|V|^2 = {V_0}^2 + A\frac{\left(q\frac{\delta f}{2} + f - f_0\right)^2}{\left(\frac{\delta f}{2}\right)^2 + (f - f_0)^2}, \tag{3.9}$$

where δf is the full width at half maximum and f_0 is the center frequency. From the two fitting parameters f_0 and δf, L and $Q = \frac{f_0}{\delta f}$ and via eq. 3.8 R_s can be determined. Fano resonances arise from an interference of a continuous spectrum or background with a discrete one. The continuous spectrum can result from parasitic transmission paths like stray capacitances between leads or to ground, while the discrete on in the present case comes from a RLC resonator [75]. The resulting transmission coefficient S_{21} can be written as [76]

$$S_{21} = \frac{a}{1 + 2i\frac{f - f_0}{\delta f}} + ib, \tag{3.10}$$

where the first term describes the RLC resonator while the latter corresponds to an imaginary background transmission resulting from a stray capacitance or mutual inductance that connects the input resistors R_D and the lock-in output and the preamplifier, respectively. The transmitted power is calculated as

$$\begin{aligned} |S_{21}|^2 = |\frac{a}{1 + 2i\frac{f - f_0}{\delta f}} + ib|^2 = |\frac{a + (1 + 2i\frac{f - f_0}{\delta f})ib}{1 + 2i\frac{f - f_0}{\delta f}}|^2 = \frac{(a - 2b\frac{f - f_0}{\delta f})^2 + b^2}{1 + (2\frac{f - f_0}{\delta f})^2} = \\ \frac{(\frac{\delta f}{2}a - b(f - f_0))^2 + (b\frac{\delta f}{2})^2}{(\frac{\delta f}{2})^2 + (f - f_0)^2} = \frac{(\frac{\delta f}{2})^2(a^2 + b^2) - 2ab\frac{\delta f}{2}(f - f_0) + (b(f - f_0))^2}{(\frac{\delta f}{2})^2 + (f - f_0)^2} \end{aligned} \tag{3.11}$$

Comparison of coefficients in formulas 3.11 and 3.9 gives

$$\begin{aligned} Aq^2 &= a^2 + b^2 \\ 2Aq &= -2ab. \end{aligned}$$

Solving this equation for A and q leads to

$$q = -\frac{a^2 + b^2}{ab}$$
$$A = \frac{a^2 b^2}{a^2 + b^2}.$$

In the limit of $b \ll a$ (small parasitics), this gives

$$q = -\frac{a}{b}$$
$$A = b^2 = \frac{a^2}{q^2}.$$

In this limit eq. 3.11 is equivalent to eq. 3.9.
A change of inductance and/or resistance of the sample changes the resonance conditions and therefore the shift or broaden the measured spectra in frequency. In Fig. 3.20 a set of resonance curves measured in zero magnetic field are shown. The depicted curves are exemplary for all datasets from which inductance and resistance values are extracted but not shown.

From the center frequency and the width of the resonance inductance and resistance values can be determined by using eq. 3.9 and eqs. 3.7 and 3.8. A fit of the data at $T = 0.05\,\mathrm{K}$ to eq. 3.11, where no approximations are applied, delivers a ratio of $\frac{b}{a} = 0.057$. This shows that the approximation formular 3.9 is valid. The small perturbation b is an effective value that can result from various sources like capacitances to ground, between the leads or inductive transmission. The fit only delivers transmission parameters for a and b, not for a concrete circuit element. Extraction of the real values depend strongly on the used circuit model. Furthermore, the use of circuit elements with input and output resistance different from $50\,\Omega$ would make the calculation very complex. In most cases a voltage divider was used at the input with an output resistance of $10\,\Omega$. A concrete value for the stray transmission in form of an effective capacitance is therefore not easily accessible.

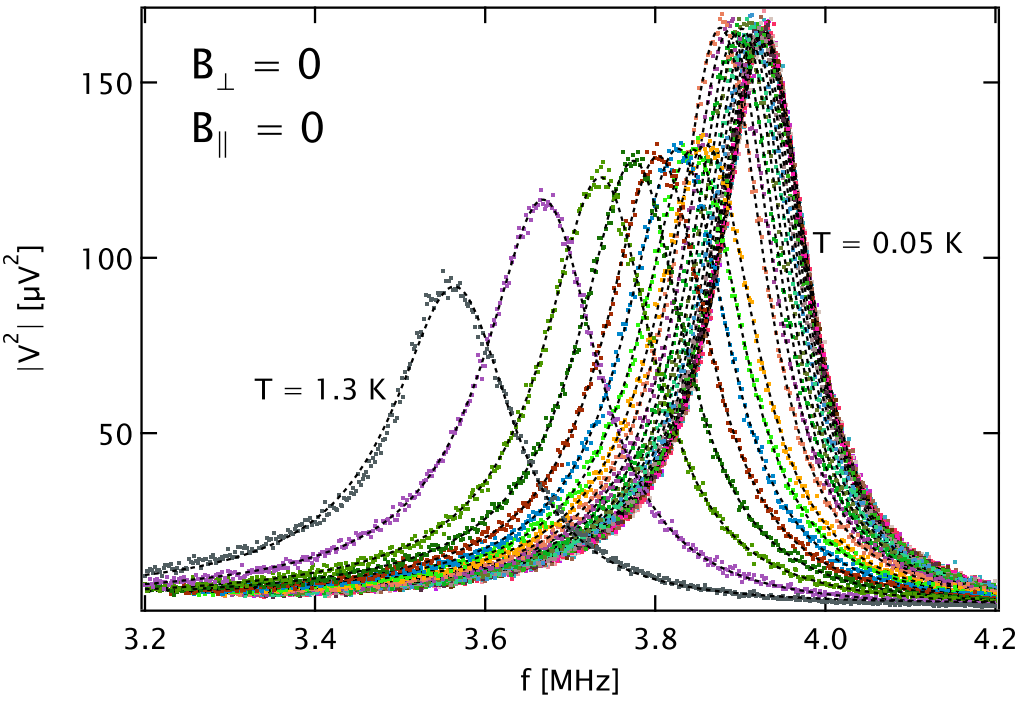

Fig. 3.20.: Exemplary resonance spectra measured in zero magnetic field for temperatures from 0.05 K (highest resonance frequency) to 1.3 K (lowest resonance frequency) in temperature steps of 0.05 K. Increased temperature leads to a reduction of the resonance frequency as well as to a damping of the resonance because of pair breaking effects caused by the finite temperature. Dashed lines represents a fit to a Fano-like resonance curve (eq. 3.9) from which center frequency and width of the transition can be extracted.

Given by the setup layout, a DC voltage on top of the probing AC voltage applied to the input resistor leads to a DC current that flows through the inductor and the sample. With this setup it is possible to probe the DC current dependence of the inductance, which is in general not possible in microwave experiments. This is because in standard GHz measurements the superconducting resonators are coupled to the measurement leads capacitively, which blocks DC currents. A voltage applied to the setup always produces Joule heating at least of the order of $P = \frac{{V_0}^2}{R_D}$, where V_0 is the voltage to ground at the input resistor R_D. As there is a thermal resistance between the sample holder and the mixing chamber, this can lead to a significant heating of the whole setup and has to be taken into account. The AC current I_0 that is flowing through the RLC circuit to the cold ground is nearly constant and primarily determined by the input resistor. The circular current, however, that is flowing back and forth in the RLC circuit and therefore through the sample is frequency dependent and has a maximum at the resonance

$$I_{max} = QI_0 = QV_0/(R_D + Z_m). \tag{3.12}$$

This can lead to a distortion of the spectra if there are non-linear terms in the current-inductance dependence, as it is the case for superconductors at high currents. Pair breaking or depinning effects can lead to such non-linearities and have to be taken into account in the analysis. If not mentioned otherwise, measurements were always performed at AC bias voltages, where non-linear effects can be neglected.

Simulation

A symbolic circuit simulator was used for an approximate calculation of the transfer function of the circuitry. For that also cable resistances and capacities of the cryostat and room temperature filters were taken into account. A schematic picture of the circuit is depicted in Fig. 3.21. With measured values for the π-filter capacities of 6.3 nF and 8.2 nF and reasonable estimated guesses of some hundred pH for the line capacities it is possible to reproduce the measured spectrum of the resonator with a superconducting sample placed in series with the inductor. The analytical expression calculated with the circuit simulator consists of hundreds of terms in the numerator and denominator. Performing a fitting procedure to extract exact values is therefore not easily possible.
The presented circuitry is of course a relatively simplified version of the real circuit. The main features, however, can be captured qualitatively. This design was used for early measurements. In later experiments a 100:1 ($R_1 = 1\,\mathrm{k\Omega}$ and $R_2 = 10\,\Omega$) voltage divider was inserted between the output of the lock-in amplifier and the input π-filter in order to increase the cutoff frequency at the ingoing side by a factor of 5. This led to a much flatter spectrum in the whole frequency range of 0 to 5 MHz. With this voltage divider also noise as well as DC offset voltages of the lock-in amplifier were divided by a factor of 100. This was especially useful, because the DC offset voltages of the lock-in amplifier have been on the order of some hundreds of μV and hence produced currents through the sample of the order of some hundreds of nA. Without this voltage divider it was necessary to remove the DC offset at the beginning of each session and also to check from time to time whether the offset was still properly compensated by a finite bias set in the instrument. By suppressing the small offset by a factor of 100 this compensation was not needed anymore, because some finite DC currents of some nA did not alter the inductive response of the sample.

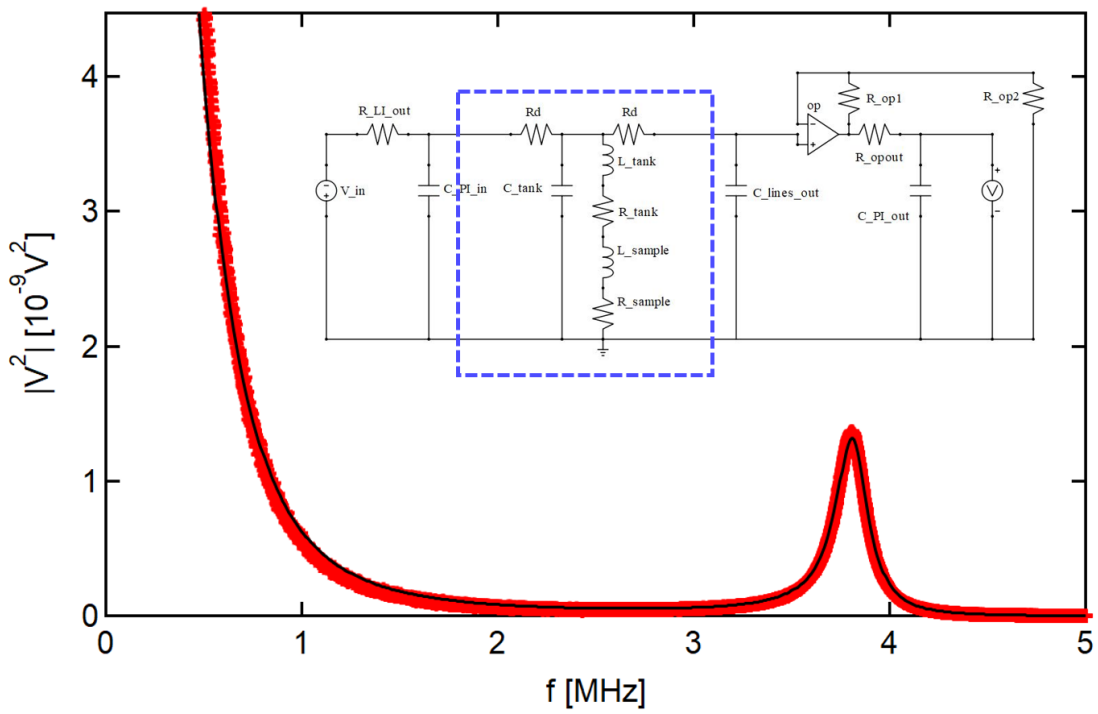

Fig. 3.21.: Simulated (black line) transfer function and measured spectrum (red points) of a typical RLC resonator setup used in this work. The part which is highlighted with the blue dashed box is located inside of the cryostat. The inductance L_{tank} and the resistance R_{tank} of the copper coil are in series with the superconducting sample with inductance L_{sample} and resistance R_{sample}. The inductors together with a parallel capacitor C_{tank}, form the RLC circuit. The strong low-pass-like background is caused by capacities of room temperature *pi*-filters at the input and outputs of the cryostat (C_Pi_in, C_Pi_out). Additionally, measurement leads in the cryostat also have a capacity to ground (C_lines_out). At the ingoing side the $R\_LI\_out = 50\,\Omega$ output resistance of the lock-in amplifier together with the capacity of a room temperature filter form a RC low-pass with a cutoff frequency in the high kHz regime. On the other hand, the decoupling resistors R_d on the outgoing side together with the outgoing line capacity (C_lines_out) also form a low-pass-like element with a cutoff-frequency in the low MHz regime. At the output of the cryostat a 56 dB preamplifier is used to amplify the voltage signal. Numbers for the different circuit elements are: $R\_LI\_out = 50\,\Omega, C\_Pi\_in = 6.3\,\text{nF}, Rd = 1\,\text{k}\Omega, L\_tank = 347\,\text{nH}, C\_tank = 4.418\,\text{nF}, R\_tank = 0.32\,\Omega, L\_sample = 0, R\_sample = 0, C\_lines_out = 100\,\text{pF}, R\_op1 = 31500\,\Omega, R\_op2 = 50\,\Omega, R\_opout = 50\,\Omega, C\_Pi\_out = 8.2\,\text{nH}$.

3.2.3. Setup for Measurement of Critical Current

In superconductors charge flow is carried by Cooper pairs. At high currents the sum of the kinetic energy of the two constituent electrons can overcome the superconducting gap Δ, which leads to a breakup of the Cooper pair into two single particles. The current, at which the Cooper pairs are destroyed, is called the depairing current. In out-of-plane

magnetic fields vortices are introduced in the system. When a vortex is pinned at a defect, small currents do not lead to significant vortex motion. At currents high enough to overcome the maximal pinning force of a vortex, a finite resistance appears due to the vortex friction. The current needed to push a vortex out of its pinning potential is called depinning current and is always smaller than the depairing current. Depairing and depinning current are usually both called critical current.
Reproducible measurements of critical currents of superconducting structures are very challenging. In presence of a dc-bias current electrical noise, flux jumps in the structure and other external sources like fast varying magnetic fields can lead to a spontaneous transition to the normal state. Such events become more and more likely the weaker the superconducting condensate. At high DC currents a superconductor becomes more and more fragile and therefore subject to stochastic switching. Hence, slow measurements of the current-voltage characteristics usually lead to critical currents that are much lower than the true critical current. Furthermore, the current at which a superconductor switches to the normal states can vary strongly from run to run. Although averaging over many runs gives more reproducible average values, the measured switching current is still smaller than the true critical current.

Very fast ramping of the bias current and simultaneous measurement of the voltage drop across a superconducting structure can resolve this problem. For ramp times that are much smaller compared to the time scale between stochastic switching events extracted critical currents come much closer to the true critical current. Measurements of the critical current in this work were performed using a Rigol5352 Arbitrary Waveform Generator as a source for fast DC current ramps and a Tektronix TBS1000C Digital Oscilloscope for recording IV-traces. Ramp times were usually in the low ms range and chosen to be fast enough to overcome the problem of stochastic transitions but slow enough to get enough temporal and therefore current resolution. For each single point of the parameter space a number of traces are recorded and averaged to reduce noise. Due to the relatively low 256 points of resolution of the used oscilloscopes, it is only possible to resolve the jumps to the normal state but, e.g. no vortex dynamics producing voltage signals below the minimal resolution of the instrument.

3.2.4. Cryostat

The different devices were mounted in a dilution cryostat with a base temperature below 40 mK. A mu-metal shield can be placed around the dewar containing the cryostat to

reduce stray magnetic fields from nearby magnets and/or orther sources of slowly varying fields. A superconducting magnet coil can produce vertical, bidirectional fields up to 8 T. The RLC-circuit and hence the sample plane is aligned parallel with the vertical magnetic field (from here on z-) direction. In the course of this work a pair of self-wound superconducting coils was designed and assembled inside of the superconducting magnet, which can produce magnetic fields with a perpendicular orientation with respect to the sample plane. The field constant was determined by a calibration measurement, in which a Hall probe was placed into the center field at the very same location as the samples under investigation. A theoretical calculation using the geometry and number of turns delivered an estimated field constant of $\sim 0.105\,\mathrm{T/A}$ with a field inhomogeneity of 0.2% at a distance of $\pm 1\,\mathrm{mm}$ in radial direction from the symmetry axis of the coils (see Fig. 3.22). Later measurements, however, showed that the field is supposedly much more inhomogeneous. As shown in Fig. 3.25 two parts of a sample with a distance of 1 mm showed a difference in the compensation field of a few %. One reason could be that the center of the sample is not perfectly positioned in the center of the compensation coil in the radial direction which makes the field more inhomogeneous. Measurement of the field strength with a hall probe at the position of the sample delivered a field constant of only $\sim 0.089\,\mathrm{T/A}$, which could also hint towards a non-optimal arrangement of the sample in the center of the compensation field.

The measurement setup is mounted on a rotatable disc driven by a piezo slip-stick rotor that allows for orientation of the sample plane with respect to the vertical field. For the wiring 50 μm thick copper wire was used, which is flexible enough to not exert too much force on the piezo rotator during motion. Due to the wiring and the anisotropic mass distribution on the rotator, the force needed to rotate the disc by a fixed angle is not constant. Hence pulse trains with equal numbers of voltage pulses of equal height do not rotate the system by the same angle. This problem is overcome by using a 3 point readout line at the back of the rotator which allows the determination of the absolute angle in most directions. Only in the region between the nominal angle of 335 ° and 20 ° readout was not possible due to the design of the readout circuit. In this "blind window" the angle however, could be estimated by comparing compensation fields at a fixed vertical field in that region (see next paragraph) with compensation fields measured at both ends of the visible region.

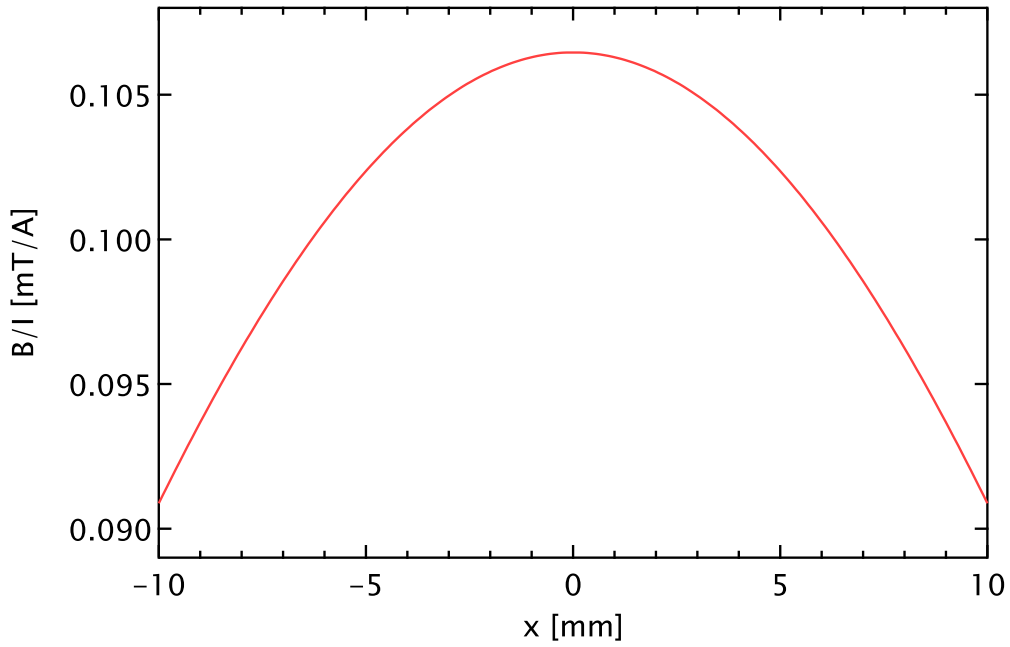

Fig. 3.22.: Calculated field constant of the compensation coils as a function of radial distance from the symmetry axis. Especially for large samples not positioned perfectly in the center of the field inhomogeneities can play a role as they increase with the distance to the center.

3.3. Measurement Procedures

In the following section two important measurement procedures are discussed, that have been used very often in this work. The first part describes a method that allows to eliminate out-of-plane field components arising from a misalignment of the sample plane and z-field. This is done by application of an additional magnetic field perpendicular to the sample plane produced by a pair of superconducting coils. Typical values for the misalignment angles are estimated and shown as a function of rotator angle. The second part explains 2^{nd} harmonic resistance measurements, which are used to determine the magnetochiral anisotropy in the Rashba Al/InAs. Also influence of a DC offset current on the second harmonic resistance of superconducting samples near the transition is discussed.

3.3.1. Compensation of Out-of-Plane Field Components

Due to small misalignments of the different parts of the cryostat, the different setups can never be mounted in such a way, that the sample plane is perfectly parallel to the z-axis. Magnetic fields, orientated in z-direction then lead to small out-of-plane magnetic field

components on the sample. For measurements that demand zero out-of-plane magnetic fields, these small field components have to be manually compensated using the small pair of magnet coils. A procedure to find the smallest possible perpendicular field is to look for a physical feature that is sensitive to absolute perpendicular fields, such as the magnetic field dependence of resistance near the superconducting transition. In Fig. 3.23 a typical compensation measurement is depicted. In this case the low frequency and therefore resistive response of a superconductor sample slightly above the critical temperature is measured, where the resistance is strongly dependent on the perpendicular field. Perpendicular field sweeps are always performed back and forth to ensure that the resistive response is non-hysteretic to exclude e.g. flux trapping. The perpendicular field needed to compensate for a misalignment of the sample with respect to the vertical magnetic field depends on the angle and the field strength of the in-plane field

$$B_{comp}(B_{\parallel}) = \sin(\alpha) B_{\parallel}, \tag{3.13}$$

where α is the angle between the film plane and the in-plane field. α depends on the rotator position and is typically $< 2\,^{\circ}$.
The field minimum is determined by finding the minimum of a parabolic fit of the data. With that an uncertainty of the field minimum better than $5\,\mu$T could easily be achieved. The compensation coils can produce magnetic fields up to 0.5 T in zero in-plane field. As the critical current of the compensation coils decreases with increasing in-plane field, the maximal perpendicular field is limited. Therefore it is not always possible to compensate perpendicular field components completely. For this reason some high-field measurements are cut-off at an in-plane field, where the compensation was just possible. Fig. 3.24 shows compensation fields needed to null the out-of-plane field component of an in-plane field of 0.5 T for different rotator positions which set the relative angle of in-plane field and film plane. Rotating the setup back and forth shows some hysteresis of the compensation field indicating some long-term drift. The most probable explanation for this drift would be, that trapped flux in the large magnet creeps upon application of the compensation field. The difference between compensation fields in the back- and forth-direction can be of the order of 10 %. Therefore it is not possible to once characterize the misalignment of the in-plane fields relative to the sample plane and then rely on linearity and long term stability. In measurement, where $B_{\perp} = 0$ is demanded, it is therefore necessary to carry out a compensation procedure after each change of angle and/or in-plane field. This makes measurements, where rotator angles or in-plane fields are changed very lengthy and challenging.

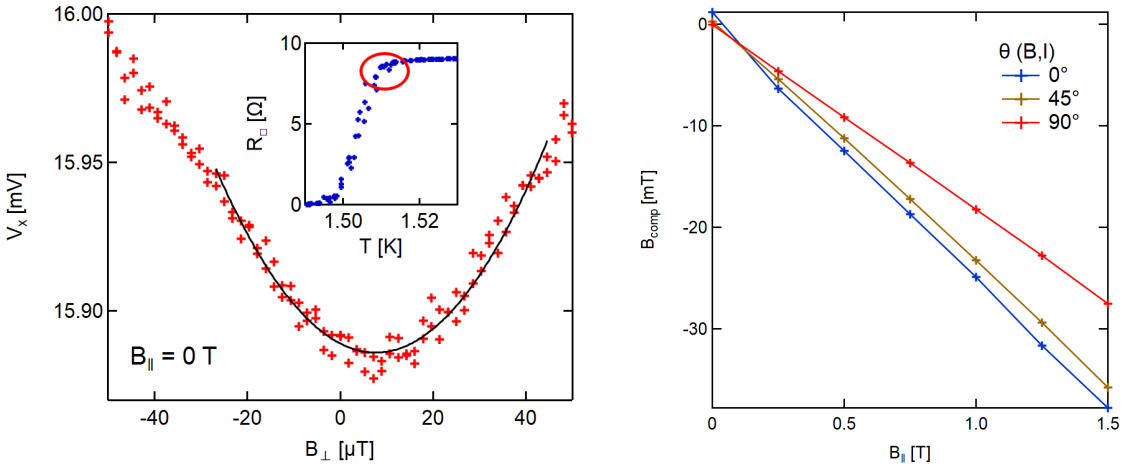

Fig. 3.23.: left: Typical measurement for determination of the zeroes of the perpendicular field. Low frequency resistance of a superconducting sample is measured as a function of perpendicular field at a temperature slightly above the superconducting transition. The measurement was performed at a nominally absence of a vertical field. A finite offset of the perpendicular field minimum that results from stray fields of a small residual field in the z-Magnet, can be observed. The red ellipse in the inset indicates the regime in the $R(T)$-curve where the compensation procedure is performed. right: Horizontal compensation field as a function of the vertical field for three different relative orientations of vertical field an sample plane. The misalignment angles calculated via $\alpha = \arcsin(\frac{dB_{comp}}{dB_{\parallel}})$ are: red -> $\alpha = 1.03\,°$, yellow -> $\alpha = 1.34\,°$, blue -> $\alpha = 1.41\,°$

It turned out that the compensation field was not entirely homogeneous across the whole sample dimensions of some mm in width. In Fig. 3.25 the compensation field in an in-plane field of 1.2 T for two wires in sample Al/InAs-S (see Fig. 7.1), which are roughly 1 mm apart from each other, is shown as a function of rotator angle. The relative difference of the two fields $\delta B = \frac{B_{comp.1-10} - B_{comp.110}}{1/2(B_{comp.1-10} + B_{comp.110})}$ is also shown. It can be seen that the compensation fields needed to null the out-of-plane field component at the two different regions of the sample deviate by some percent. For high compensation fields, sample parts that are apart from each other on the mm scale, are subject to some finite out-of-plane field component of the order of uo to some hundred μT. Measurements that are extremely sensitive to very small out-of-plane fields are hence difficult when the sample dimensions are large. This was in fact the case for the zero-perpendicular field measurements in the Al/InAs meander as well as in sample Al/InAs-S.
If not stated otherwise, from this point on curves with no explicit perpendicular field present have always been measured with a compensated out-of-plane field component. Explicit numbers for $B_{\perp}$ always mean field strength relative to the beforehand determined minimum if not stated otherwise.

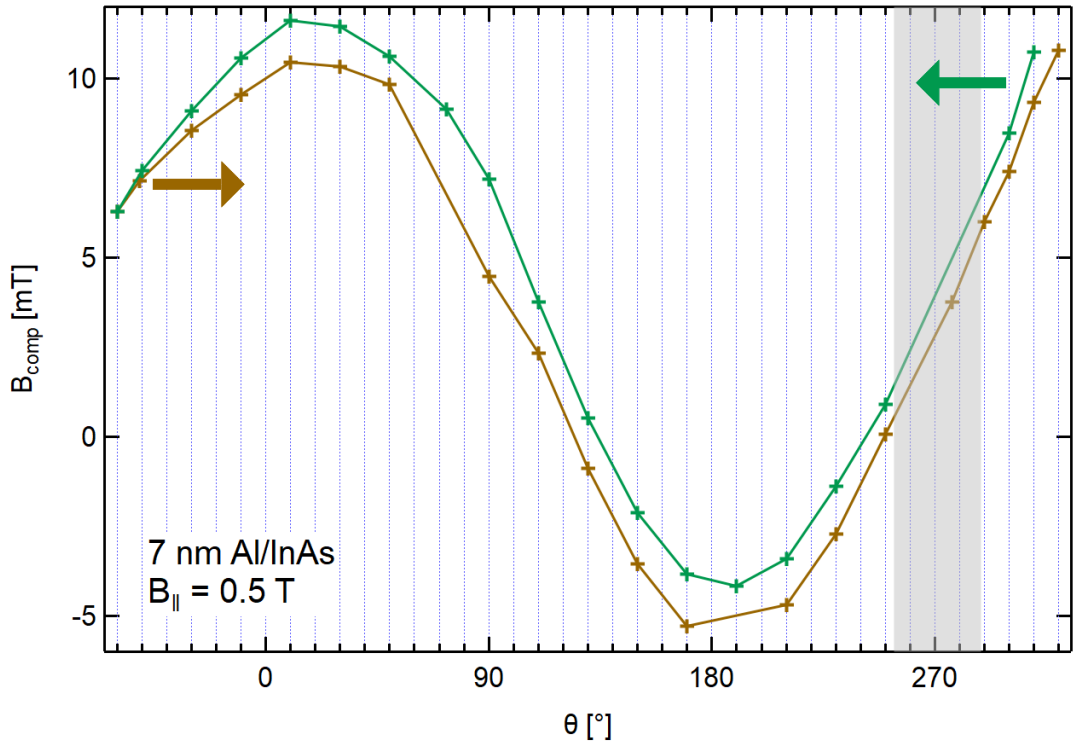

Fig. 3.24.: Typical angle dependence of the horizontal field needed to compensate the perpendicular component of an in-plane field of 0.5 T. The angle θ was swept from 320 ° to −60 ° and back. The different colors mark different sweep directions and the points where sweep direction was reversed coincide naturally. A small long time drift can be observed by the fact that both traces are systematically shifted with respect to each other. The grey region marks the blind window, where readout is not possible. In this regime the angle θ was estimated by comparison of the measured compensation field at a fixed unknown angle with an interpolated line between points of the trace on both sides of the shaded area, where readout was possible.

Fig. 3.25: Absolute values and relative difference of compensation fields at two different regions of sample Al/InAs-S in an in-plane field of 1.2 T as a function of the rotator angle. The relative difference of the compensation fields are shown on the left axis and are of the order of some % of the absolute value.

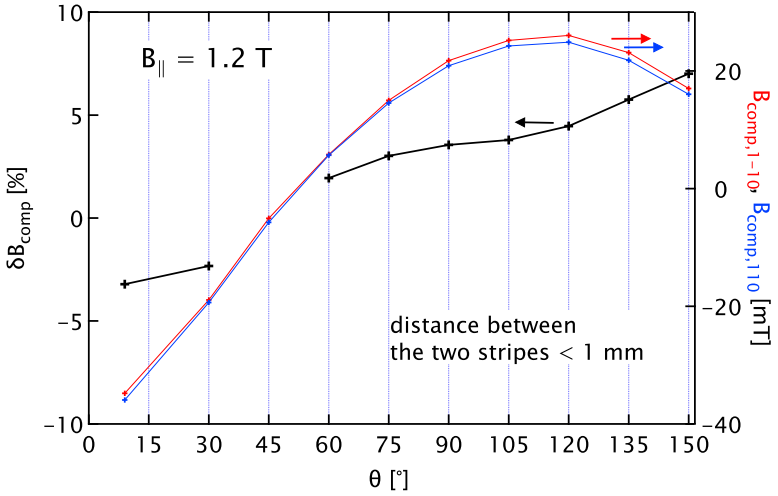

3.3.2. Second Harmonic Resistance Measurements

Equation 2.47 shows that for systems with non-reciprocal transport properties the ohmic contribution to the voltage drop, which is linear in the current I, is complemented by a quadratic in I term. γ_s, which defines the strength of non-reciprocity can elegantly be measured in a low-frequency resistance measurement, where besides the linear resistance R_ω also its second harmonic $R_{2\omega}$ is recorded. The relation between γ_s (see eq. 2.48) and first and second harmonic resistance is not obvious and will be derived in the following.

Starting from the heuristic expression for the resistance

$$R = R_0 \left(1 + \gamma_s B I\right), \tag{3.14}$$

where the first and second terms correspond to the linear and the non-reciprocal resistance, a voltage drop in the presence of a driving current I can be calculated as

$$V = R_0 \left(I + \gamma_s B I^2\right). \tag{3.15}$$

By applying an AC current $I = I_0 \sin(\omega t)$ with amplitude I_0 and frequency ω the voltage drop is

$$\begin{aligned} V &= R_0 I_0 \sin(\omega t) + R_0 \gamma_s B I_0^2 \sin^2(\omega t) \\ &= R_0 I_0 \sin(\omega t) + \frac{1}{2}\gamma_s R_0 B I_0^2 \left[1 + \sin(2\omega t - \frac{\pi}{2})\right]. \end{aligned} \tag{3.16}$$

In this equation first harmonic

$$R_\omega = \frac{V_\omega}{I_0} = R_0 \tag{3.17}$$

and second harmonic resistance

$$R_{2\omega} = \frac{V_{2\omega}}{I_0} = \frac{1}{2}\gamma_s R_0 B I_0 \tag{3.18}$$

can be identified. Inserting eq. 3.17 into eq. 3.18 then leads to

$$\gamma_s = \frac{2R_{2\omega}}{R_\omega B I}. \tag{3.19}$$

This is a powerful method as it allows to determine possible magnetochiral anisotropy

with an AC experiment, which has a much better signal-to-noise ratio then DC measurements. It should be noted, that eq. 3.16 implies that in the experiment the quadrature component of the second harmonic voltage signal is the relevant one, because the measured second harmonic voltage has a phase shift of π with respect to the driving current. It is important to compensate small DC current offsets, that pass through the superconducting sample, as they produce artifacts in AC transport experiments. For instance near T_c the $V(I)$-dependence of a superconductor is typically of power 3. If a current $I = I_0 \sin(\omega t) + I_{DC}$ is applied, the resulting voltage drop is

$$\begin{aligned} V(I) \propto I^3 &= (I_0 \sin(\omega t) + I_{DC})^3 \\ &= I_0^3 \sin^3(\omega t) + I_0^2 I_{DC} \sin^2(\omega t) + I_0 I_{DC}^2 \sin(\omega t) + I_{DC}^3. \end{aligned} \tag{3.20}$$

Using trigonometric relations and sorting the terms according to its frequencies it follows

$$\begin{aligned} V(I) \propto I^3 = &-\frac{1}{4} I_0^3 \sin(3\omega t) \\ &- \frac{1}{2} I_0^2 I_{DC} \cos(2\omega t) \\ &+ \left(\frac{3}{4} I_0^3 + I_0 I_{DC}^2\right) \sin(\omega t) \\ &+ \frac{1}{2} I_0^2 I_{DC} + I_{DC}^3. \end{aligned} \tag{3.21}$$

In the second line of eq. 3.21 one can find again a 2ω signal phase shifted by π with respect to the current. When driven by an AC current with a small DC offset V(I)-terms that have a power of 3 or greater always produce signals with double the excitation frequency and hence can overshadow even terms in the V-I-characteristic resulting from the magnetochiral effect.

In principle it should be possible to find a true zero of I_{DC} in absence of a magnetic field by finding experimentally the minimum of $\overline{V_\omega(I_{DC})} = \frac{3}{4} I_0^3 + I_0 I_{DC}^2$ or the current, where in absence of magnetochiral anisotropy the second harmonic becomes zero. This should be done at a temperature where there is a significant cubic component in the V-I-characteristic. Fig. 3.26 shows the fundamental in-phase signal and the second harmonic out-of-phase signal of a superconducting sample in zero parallel field near the critical temperature. A linear dependence of the 2ω-signal is evident.

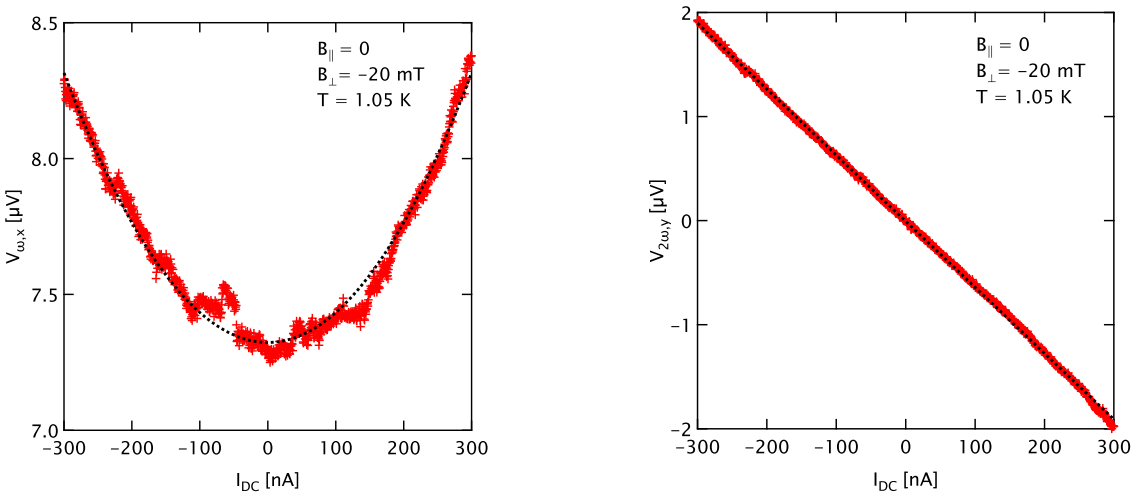

Fig. 3.26.: left: Fundamental AC voltage signal for a superconductor near the critical temperature as a function of DC current. Low frequency noise is mainly caused by temperature fluctuations. right: Second harmonic signal as a function of DC current.

In the case of a finite zero-bias resistance an ohmic contribution $V(I) = R_0 I_0$ with $R_0 = 3.8\,\Omega$ has to be added to the cubic contribution. In Fig. 3.27 the AC-current dependence of the fundamental signal is depicted for zero DC bias current. After subtraction of the ohmic contribution one finds a clear I_0^3 dependence as given by eq. 3.21.

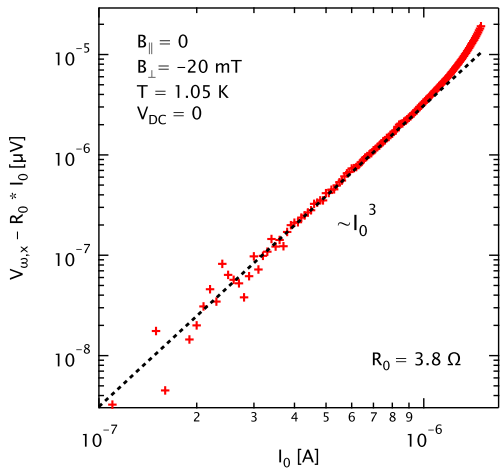

Fig. 3.27: Dependence of $V_\omega - R_0 I_0$ with $R_0 = 3.8\,\Omega$ as a function of AC current I_0 near the superconducting transition. Higher order terms in the IV characteristic lead to a $\sim I_0^3$ contribution to the measured first harmonic signal, which can for higher I_0 be of the order of $R_0 I_0$.

4. Important Parameters

In this section the most important parameters for the three investigated wafers are tabulated.
Sample fabricated from the 15 nm Al/GaAs wafer:

- Al/GaAs-M15 (meander)

Sample fabricated from the 7 nm Al/GaAs wafer:

- Al/GaAs-M7 (meander)

Samples fabricated from the 7 nm Al/InAs wafer:

- Al/InAs-M (meander)
- Al/InAs-S (strip)
- Al/InAs-C (circle)
- 1D_JJ1 (Josephson junction array)

Samples Al/InAs-M, Al/InAs-S and Al/InAs-C are fabricated from the same, nominally 7 nm Al/InAs wafer. The values for electrical and superconducting parameters differ slightly as the different samples have been produced on pieces from different position on the wafer. The deviations, however, are small and therefore the values given in the table for 7 nm Al/InAs can be used.

Table 4.1.: Table with the most important parameters for the different samples

	15 nm Al/GaAs	7 nm Al/GaAs	7 nm Al/InAs
$d[nm]$	13	7	4.5
$R_{\square}[\Omega]$	14.7	3.86	9.22
$l_{el}[nm]$	2.1	14.8	5.0
$\lambda_{R_{\square}}(0)[nm]$	351	147	174
$T_{c0}[K]$	1.576	1.4	1.502
$\Delta_0[\mu eV]$	239	210	228
$\lambda_s(0)[nm]$	456	167	227
$\Lambda(0)[\mu m]$	33.4	7.96	19.8
$B_{c2}(0)[mT]$	100	37	61
$\xi(0)[nm]$	50	91	74
$L_{\square}(0)[pH]$	17.1	5.0	9.2
$B_{c\parallel}(0)[T]$	3	2.9	2.7
$F\delta^0_{TLS}$	0.0048	0.019	0.012
$k_p[N/m^2]$	8.31	91.0	14.9

Description of parameters:
d: effective Al film thickness
$R_{\square}$: normal state resistance for $T \gg T_{c0}$
l_{el}: electric mean free path, calculated via $R_{\square} d l_{el} = 4 \times 10^{-16}\,\Omega\mathrm{m}^2$ [77]
$\lambda_{R_{\square}}(0)$: expected magnetic penetration depth at $T = 0$ from eq. 2.14
T_{c0}: critical temperature, defined as temperature, where $R = 0.5 R_n$
Δ_0: superconducting gap at low temperature $\Delta(0) = 1.76 k_B T_{c0}$
$\lambda_s(0)$: penetration depth measured with RLC resonator at low temperatures in zero field
$\Lambda(0)$: Pearl penetration depth calculated via $\Lambda = 2\frac{\lambda_s^2(0)}{d}$
$B_{c2}(0)$: critical out-of-plane field measured at low T
$\xi(0)$: coherence length calculated as $\xi = \sqrt{\frac{\Phi_0}{2\pi B_{c2}}}$
$L_{\square}(0)$: sheet kinetic inductance at low T, $L_{\square} = \mu_0 \frac{\lambda_s^2}{d}$
$B_{c\parallel}$: critical in-plane field measured at low T
F: filling factor in TLS
δ^0_{TLS}: loss tangent in TLS
k_p: pinning constant calculated at small $B_{\perp}$ via $k_p = \frac{\Phi_0}{d}\left(\frac{\Delta L}{\Delta B_{\perp}}\right)^{-1}$

5. Reference Samples Without SOC

In this chapter the inductive response of two superconducting thin Al films without SOC will be discussed. These measurements were performed in order to characterize the used RLC setup. The two samples that lack SOC also provide a reference to the later discussed heterostructure with strong SOC. Also DC resistance characterization measurements will be shown. Different contributions to the total inductance of the setup will be introduced and quantified. Apart from the kinetic inductance there can be geometric contributions from the sample structure and bond wires. Pinned vortices provide another source of inductance. TLS can change the resonance frequency of the RLC circuit, which leads to a non-saturating behavior of $f_0(T)$ at low temperatures. It will be shown that the subtraction of a TLS-correction δf_{TLS} from $f_0(T)$ leads to a saturating behavior, which follows BCS prediction.

5.1. 7 nm Al/GaAs Meander

The first superconductor investigated is a 7 nm thick Al film with a 1.5 nm thick AlO_2 terminating layer, which was grown on top of an insulating GaAs substrate by the group of Mike Manfra at Purdue University. The film was then patterned into a meander structure in order to be able to measure a decent amount of squares in series to get a proper signal-to-noise ratio (see Fig. 5.1). The current flow has a preferred direction and should from now on be called "current direction". The inductive response will therefore mainly come from the long sections of the meander. The very same geometry was used for the other two meander samples that will be treated later.

5.1.1. DC Characterization

DC resistance measurements were carried out upfront and compared afterwards with inductance measurements. In Fig. 5.2 R(T)-curves are shown for zero parallel field and in a field of 1.5T for different relative alignments of the field with current direction. In

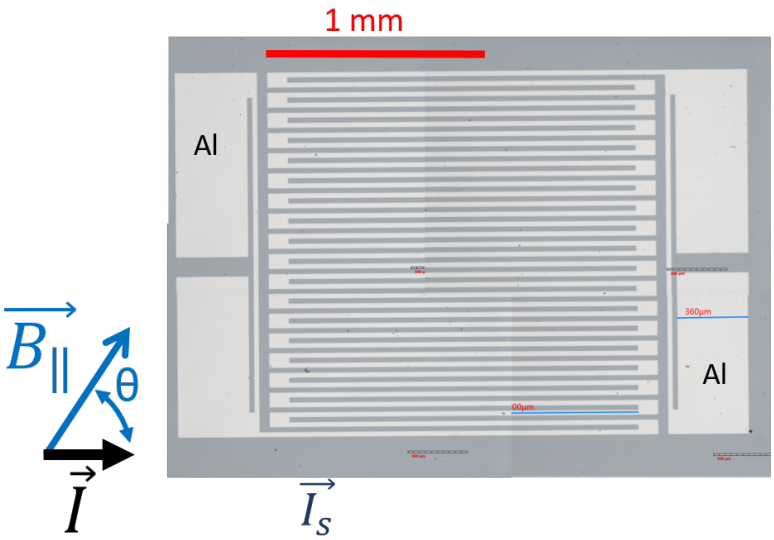

Fig. 5.1.: Sample geometry of the Al/GaAs sample. The meander consists of ca. 3074 squares of Al in series (bright part) with a width of 24 μm. The Al on the darker part was etched away. On the right and left side there are four bondpads for applying bias voltage and voltage probes. The current has a preferred direction parallel to the long sections. The long sections are roughly 1.8 mm long. The turning points were designed broader in order to reduce the current density at these points. This is to ensure that the critical current in the long sections is much higher compared to the critical current perpendicular to the main direction. Therefore non-linear effects of the inductive response under high AC or DC bias will mainly arise in the long sections.

zero field the residual resistance was determined to $R = 3.86\,\Omega$. The critical temperature $T_{c0} = 1.40\,\mathrm{K}$ is defined as the temperature where $R = 0.5R_n$. In an in-plane field of $B_{\parallel} = 1.5\,\mathrm{T}$ there is a small difference between the reduced transition temperature for different angles θ between $B_{\parallel}$ and current. The highest T_c can be observed if field and current are aligned parallel to each other. Rotating the field leads to a monotonic decrease of T_c. With the given T_{c0} the expected sheet inductance calculated via eq. 2.13 is $L_{\square} = 3.77\,\mathrm{pH}$ and the total inductance $L = 11.5\,\mathrm{nH}$.

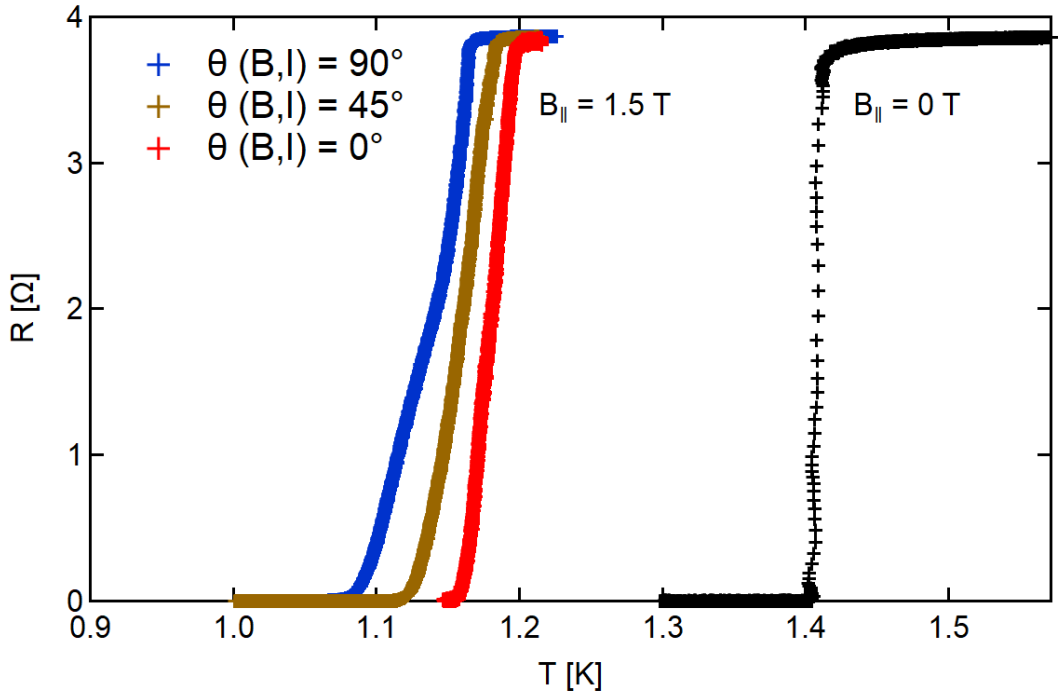

Fig. 5.2.: R(T)-curves in for $B_{\parallel} = 0\,\mathrm{T}$ (black) and $B_{\parallel} = 1.5\,\mathrm{T}$ (colors). The reduced critical temperature in finite field is slightly different for different field alignments.

5.1.2. Contributions from Geometric Inductance

After DC characterization inductance measurements were performed. The total inductance L_{total} is a sum of kinetic inductance L_s, the coil inductance and geometric inductances from the sample and wiring. Inductances not originating from the superconductor will be called L_0. The constant inductance of the copper coil was measured in a separate cooldown with a short circuit replacing the superconductor. This measurement delivered an inductance $L_{0,cal} = 398\,\mathrm{nH}$ of the coil. It turned out that this values is slightly smaller than L_0 measured in the meander samples. The discrepancy can be understood by taking into account geometric contributions to the total inductance of the RLC resonator resulting from the long meander structure and the cylindrical bond wires. The geometric inductance of a straight rectangular wire can be calculated as [78]

$$L_{g,rect} = 2l\left[\ln(\frac{2l}{w+t}) + 0.5 + 0.2235\left(\frac{w+t}{l}\right)\right]\mathrm{nH}, \tag{5.1}$$

with l being the length, t the thickness and w the width of the wire. For instance one segment of the meander with a length of $\sim 1.8\,\mathrm{mm}$, width of $24\,\mu\mathrm{m}$ and thickness of 7 nm would have a geometric inductance of 1.98 nH. As the single segments are

located parallel next to each other, most of the magnetic field between them are probably eliminated due to the pairwise counterflowing currents. Furthermore the internal field in the Al should be screened partly due to the diamagnetism of the superconductor. The largest contribution to the total inductance will therefore be provided by the most outer segments where the magnetic field produced by the current flow is not compensated entirely by the neighboring segments.
Another source of geometric inductance are the cylindrical Al bond wires. The geometric inductance of a round, straight wire far away from a ground plane is given by [79]

$$L_{g,round} = 2l\left[\ln\left((\frac{2l}{d})(1+x)\right) - x + \mu/4 + \frac{d}{2l}\right]\,\mathrm{nH}, \tag{5.2}$$

where $x = \sqrt{1+(d/2l)^2}$, l being the length, d the diameter and μ the permeability of the wire. A wire with diameter of 25 μm and lengths of around 1 mm will each have a geometric inductance of ~ 0.86 nH. Mostly 4 or even more bond wires are used for each contact, thus the parallel inductance of more wires should be smaller. Also mutual inductance between the single bond wires have to be taken into account, however.
The calculations show that a geometric inductance of some nH can be expected. The value for $L_{0,cal}$ can therefore be seen as a lower limit for L_0. As the exact knowledge or even control of the geometric inductance in the system is challenging and even different for different samples the values for L_0 are always extracted from a BCS fit to the zero field $L(T)$ data for each sample separately.

5.1.3. Resonance Shift by Two-Level-Systems

In the low temperature regime RLC measurements show, that the resonance frequency $f_0(T)$ in most cases slightly increases with increasing temperature. In contrast, BCS theory would predict a saturating behavior at low temperatures. As the sample has to cool down from higher temperatures before the T-sweep is started from low temperatures, the simplest explanation would be that the sample has not reached the starting temperature before the measurement. Control measurements on a different sample, however, show that waiting times of ~ 30 min before the measurement and ~ 5 min between two temperatures were long enough to exclude artifacts from incomplete thermalization.
The reason for initial increse of $f_0(T)$ at low T is most probably due to the influence of two-level systems (TLS) either in the InAlAs substrate or the AlOx layer on top of the Al [31]. TLS change the resonance frequency of the system due to coupling of the electric field in the superconductor to dipole moments in the aluminum oxide layer. Fig.

5.3 shows $f_0(T)$ data measured in zero field. Approaching low temperatures TLS lead to a small reduction of the resonance frequency. To account for the small correction due to TLS, a fit of $f_{0,meas}(T)$ to eq. 2.42 is performed, which gives a value for the uncorrected resonance frequency f_r at low temperatures and the characteristic strength of the TLS $F\delta^0_{TLS}$. The small correction $\delta f_{TLS}(T)$ is then subtracted from $f_{0,meas}(T)$ data. This subtraction then leads to a saturating behavior of $f_0(T)$ at low temperatures. Due to the weak dependence of $\delta f_{TLS}(T)$ on T the impact of the TLS correction on the temperature dependence of the resonance frequency is small at higher temperatures.

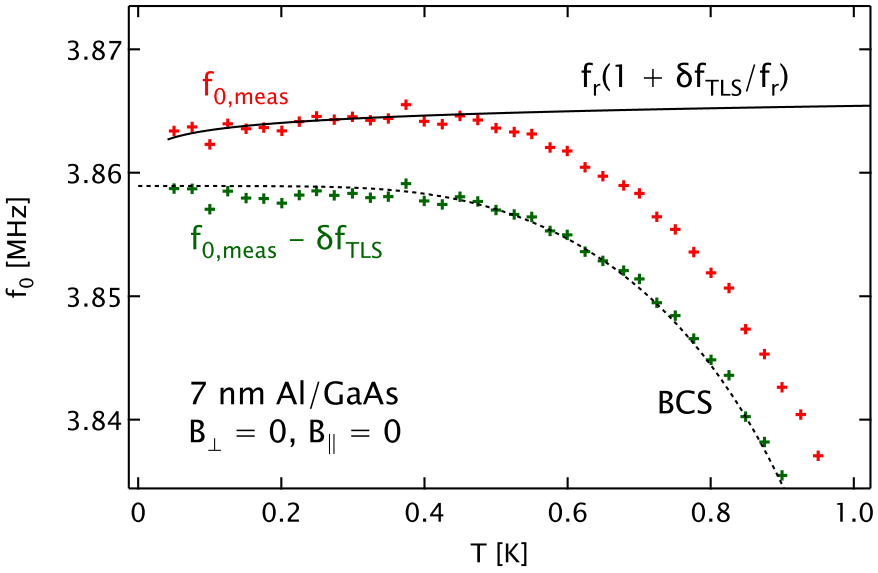

Fig. 5.3.: Resonance frequency as a function of temperature in zero field. Red markers represent measured resonance frequency extracted from Fano fits (eq. 3.9) of spectra measured at different temperatures. Solid line is a fit to eq. 2.42 with fitting parameters $f_r = 3.8582\,\mathrm{MHz}, F\delta^0_{TLS} = 0.019$. The green crosses show the corrected resonance frequency after subtraction of δ_{TLS} from $f_{0,meas}$. The dashed line represents a BCS-fit to the corrected data using eqs. 2.11, 2.12 and eq. 3.7 with three fitting parameters $L_0 = 409.8\,\mathrm{nH}$, $T_{c0} = 1.387\,\mathrm{K}$ and $\lambda(0) = 167\,\mathrm{nm}$.

The extracted $F\delta^0_{TLS} = 0.019$ is rather high compared to values reported for e.g. Nb resonators on a sapphire subtrate, where $F\delta^0_{TLS} \sim 10^{-5}$ [80] or for Nb resonators with amorphous AlOx grown on top by evaporation of Al in a reactive oxygen atmosphere at room temperature, where $F\delta^0_{TLS} \sim 10^{-3}$ [31]. The absolute value of $F\delta^0_{TLS}$ strongly depends on the interface and defect concentration of the amorphous dielectric, formed by oxidation of the Al film at low oxygen pressure. As the AlOx-Al interface forms within an Al single crystal the electromagnetic coupling may be stronger than in the investigated AlOx-Nb interfaces.

5.1.4. BCS T-Dependence of Kinetic Inductance

From the corrected $f_0(T)$ data in Fig. 5.3 the total inductance of the sample can be calculated. The resulting $L_{total}(T)$ curve is shown in Fig. 5.4. The curve nicely follows a standard BCS temperature dependence (eq. 2.11). The extracted value for $\lambda(0) = 167\,\text{nm}$ coincides roughly with the predicted value of $\lambda_R(0) = 147\,\text{nm}$ (eq. 2.14).

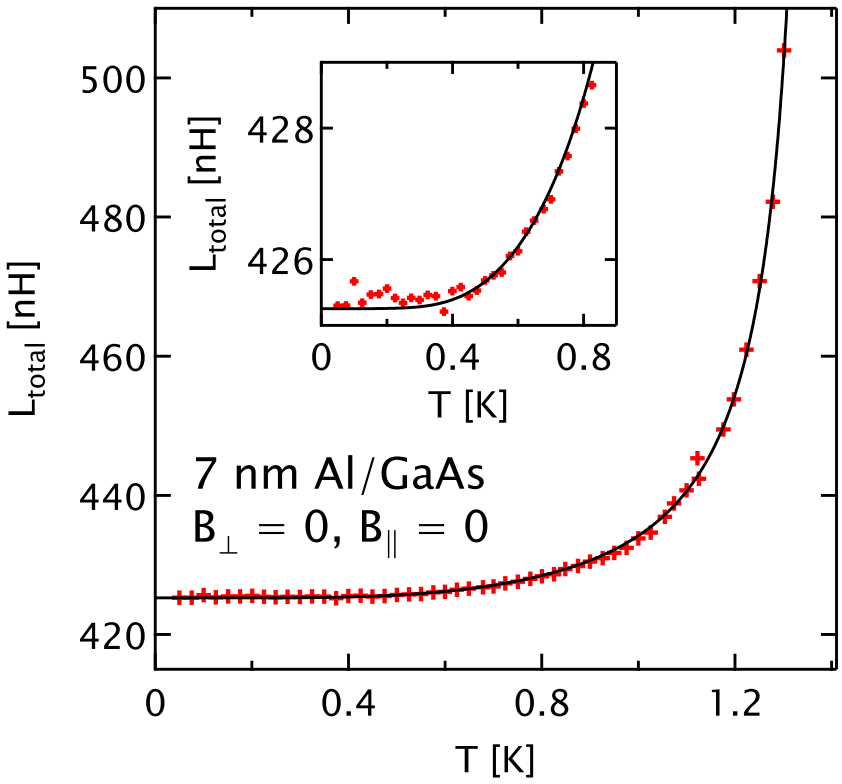

Fig. 5.4.: L(T)-curves in zero field. The solid line represents a 3-parameter fit BCS-fit (eq. 2.10) delivers values for $L_0 = 409.8\,\text{nH}$, $T_{c0} = 1.387\,\text{K}$ and $\lambda(0) = 167\,\text{nm}$.

Fig. 5.5 shows the change of inductance $\Delta L_s = L_{total} - L_{sat}$ as a function of temperature defined as the difference of L_{total} and the low temperature saturation value L_{sat} of the BCS fit in Fig. 5.4. $\Delta L_s(T)$ shows the expected exponential dependence.

In zero field a standard, exponential BCS-like temperature dependence could be shown in sample Al/GaAs-M7 with reasonable agreement of estimated $\lambda_R(0)$ and measured $\lambda(0)$. This shows that with the RLC resonator technique it is possible to produce reliable results for the kinetic inductance, when the corrections of TLS and contributions from geometric inductances are taken into account.

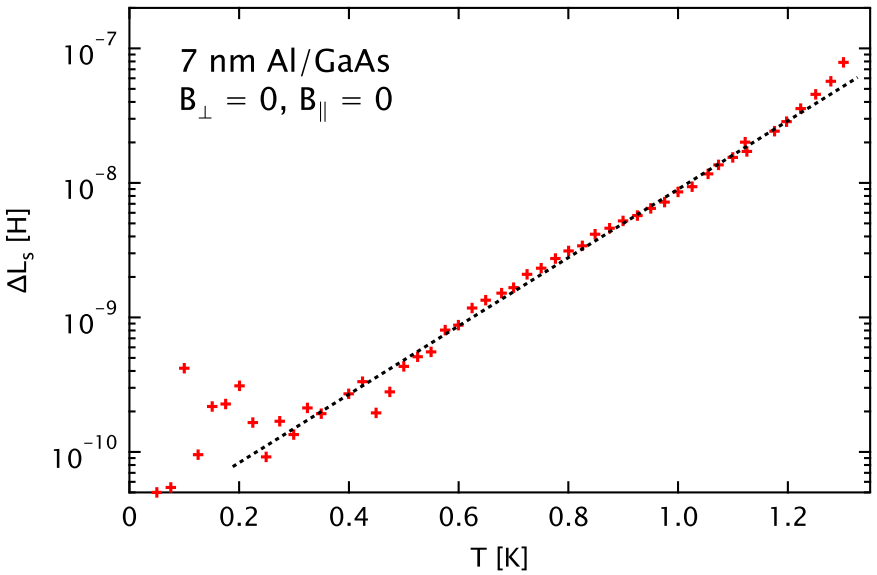

Fig. 5.5.: $\Delta L_s = L_{total} - L_{sat}$ as a function of temperature in zero field. Data show an exponential dependence.

5.1.5. Vortex Motion and Pair Breaking in Magnetic Fields

Besides the temperature dependence of L, the behavior of the inductive response of thin film superconductors in external magnetic fields is of peculiar interest. Therefore measurements in in-plane, out-of-plane and combined in- and out-of-plane fields were performed. In out-of-plane fields vortices are introduced, that will be pinned at structural defects at low temperatures. Vortices can store energy when they are disclocated from their equilibrium position in the pinning potential and hence produce an inductive response. An in-plane magnetic field reduces the superfluid stiffness via orbital pair breaking which also reduces the vortex pinning strength. This means that arbitrary field directions the total inductance is expected to increase monotonically with field strength.

In Fig. 5.6 $L(B_\perp)$ in zero in-plane field is plotted. There is a crossover from a slightly sublinear dependence at small $B_\perp$ to linear for $2\,\mathrm{mT} < B_\perp < 10\,\mathrm{mT}$. For $10\,\mathrm{mT} < B_\perp < 25\,\mathrm{mT}$, $L(B_\perp)$ increases superlinear. There is a kink in $L(B_\perp)$ at $B_\perp \approx 27\,\mathrm{mT}$. For $B_\perp > 30\,\mathrm{mT}$, $L(B_\perp)$ diverges. The divergence is roughly consistent with the critical field value $B_{c2} = 37\,\mathrm{mT}$, reported by Asbjørn Drachman (private communications) for this wafer at low temperatures.
For small $B_\perp$ the total inductance increases almost linearly, which is consistent with the prediction from the individual vortex pinning model, where $L_v = \frac{\Phi_0 B_\perp}{dk_p}$ (see section

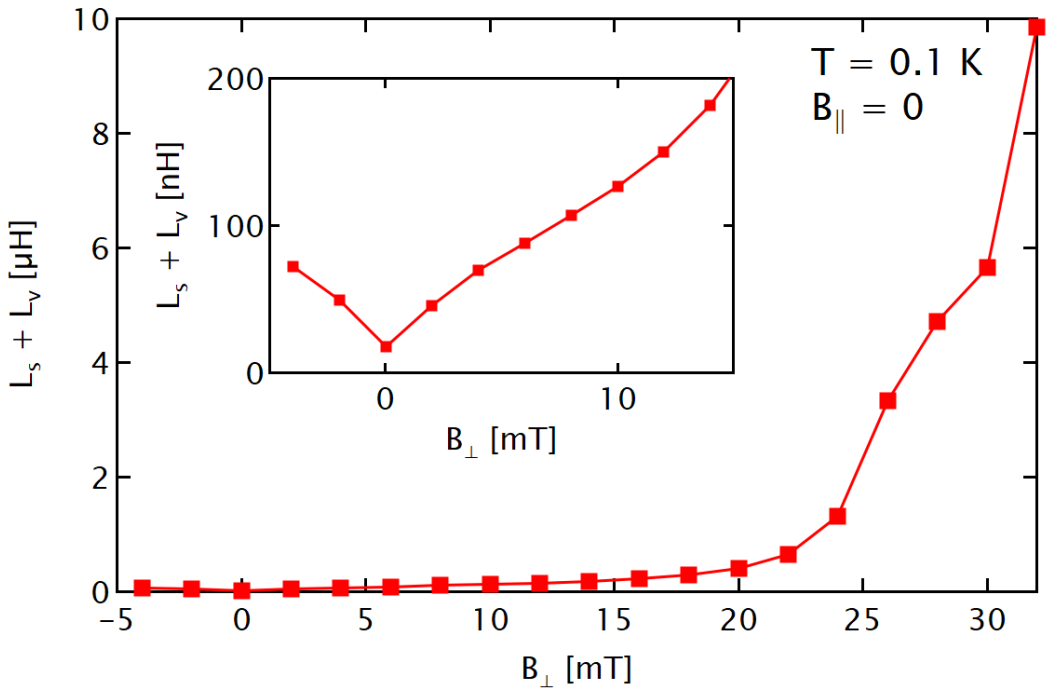

Fig. 5.6.: Total inductance as a function of $B_\perp$ in zero in-plane field at low temperature. For moderate fields (inset) there is a linear dependence suggesting equal contributions from each single vortex. At $B_\perp \approx 26\,\mathrm{mT}$ a kink indicates a crossover to a different pinning regime as will be seen later also in other samples. For $B_\perp > 32\,\mathrm{mT}$ no resonance could be observed anymore.

2.1.4). At higher $B_\perp$ a non-linear behavior is found, which is discussed in section A.1.4. Near B_{c2} superconductivity breaks down and hence $L(B_\perp)$ diverges.

In the next step, in-plane magnetic fields are applied to the superconductor either in absence or presence of vortices. Fig. 5.7 shows the sum of kinetic and vortex inductance as a function of $B_\parallel$ for the same three relative angles of in-plane field and current/crystal as in Fig. 5.2. In zero perpendicular field the pure kinetic inductance $L_s(B_\parallel)$ increases slightly with increasing $B_\parallel$. Introduction of vortices in small perpendicular field leads to an increase of the inductance at $B_\parallel = 0$. $L(B_\parallel)$ shows a crossover from linear ($B_\perp = 0$) to super-linear ($B_\perp \neq 0$). There is a small anisotropy of $L(B_\parallel)$ for the three different angles, which is consistent with different critical temperatures in an in-plane field, measured in DC transport (Fig. 5.2). All curves show a strictly increasing dependence of $L(B_\parallel)$. This is consistent with pair breaking effects. On the one hand suppression of the order parameter leads to increased kinetic inductance while on the other hand reduction of the pinning energy results in an increased vortex inductance.

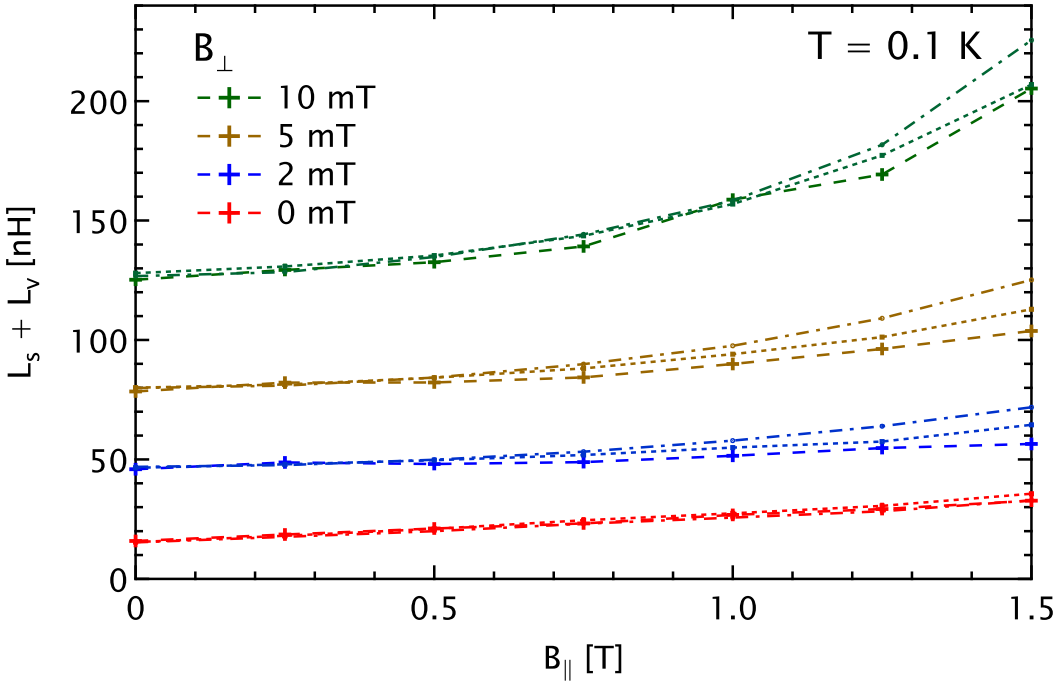

Fig. 5.7.: L as a function of in-plane field for out-of-plane fields of $0, 2, 5, 10\,\mathrm{mT}$ measured for three different orientations of in-plane field an film plane. The angles between the main current direction and in-plane field are $0\,^\circ$ (crosses), $45\,^\circ$ (squares) and $90\,^\circ$ (circles). For all out-of-plane fields and angles L increases with increasing in-plane field.

For all measured field configurations and relative orientations of the in-plane field inductance strictly increases with field strength. As will be seen later the situation changes for heterostructures with broken inversion symmetry.

5.2. 15 nm Al/GaAs Meander

In addition to the epitaxial 7 nm thick Al/GaAs film measurements have been performed on a weakly disordered 15 nm thick Al film that was grown in a metal MBE chamber by Matthias Kronseder at UR. Sample Al/GaAs-M15 has a normal state resistance of 13.6 Ω, which is a rather high value for Al of this thickness [81]. This hints towards a certain disorder in the system. Fig. 5.8 shows R(T) curves for different in-plane fields.

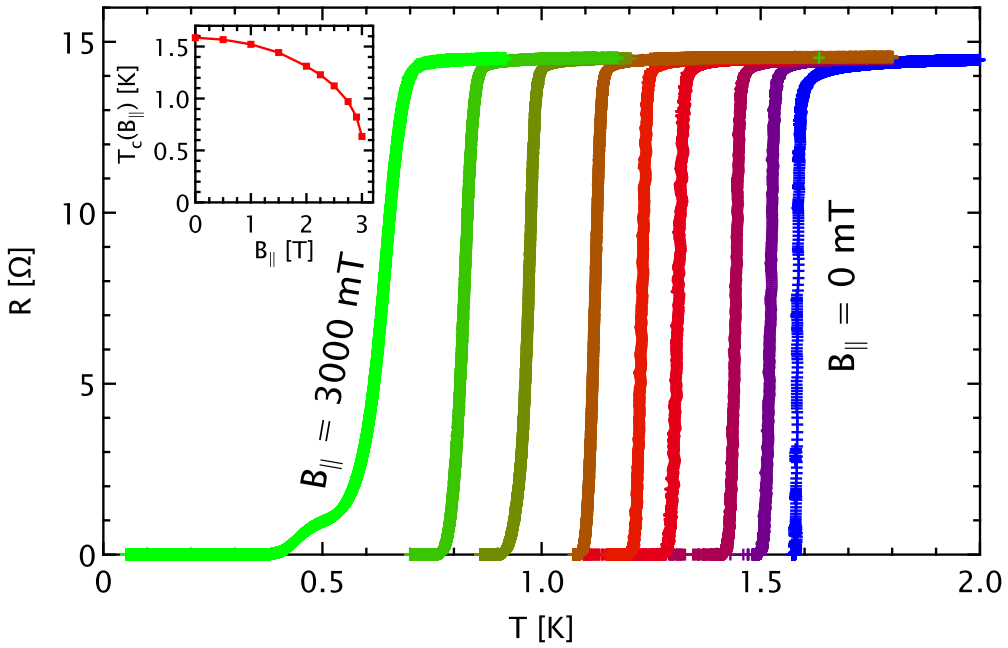

Fig. 5.8.: R(T) for $B_\parallel = 0, 1, 1.5, 2, 2.25, 2.5, 2.75, 2.9, 3$ T (right to left). Orbital pair breaking effects reduce the critical temperature. Inset shows $T_c(B_\parallel)$ determined from the midpoint of the transition.

Increasing magnetic field reduces the critical temperature due to orbital pair-breaking. $T_c(B_\parallel)$ is shown in the inset of Fig. 5.8. A zero resistance state could be observed for $B_\parallel \leq 3.1$ T. The effective sheet thickness of the Al layer is estimated to $d = 13$ nm.

5.2.1. BCS Dependence and Corrections from TLS

Similarly as in the case of sample Al/GaAs-M7 temperature dependence of the kinetic inductance was studied by recording resonance spectra at different temperatures. This sample was measured in a different RLC resonator as the previously discussed one. A calibration measurement with a short circuit replacing the sample delivered a coil inductance $L_{0,cal} = 331\,\mathrm{nH}$. Fig. 5.9 shows the resonance frequency of the RLC as a function of temperature. The measured $f_{0,meas}$ data are fitted with eq. 2.42. The corresponding parameters are $f_r = 3.805\,\mathrm{MHz}, F\delta^0_{TLS} = 0.0048$. The resulting $\delta f_{TLS}(T)$ is then subtracted from $f_{0,meas}(T)$. Whereas $f_{0,meas}(T)$ does not saturate at low temperatures the corrected $f_0(T) = f_{0,meas}(T) - \delta f_{TLS}(T)$ does.

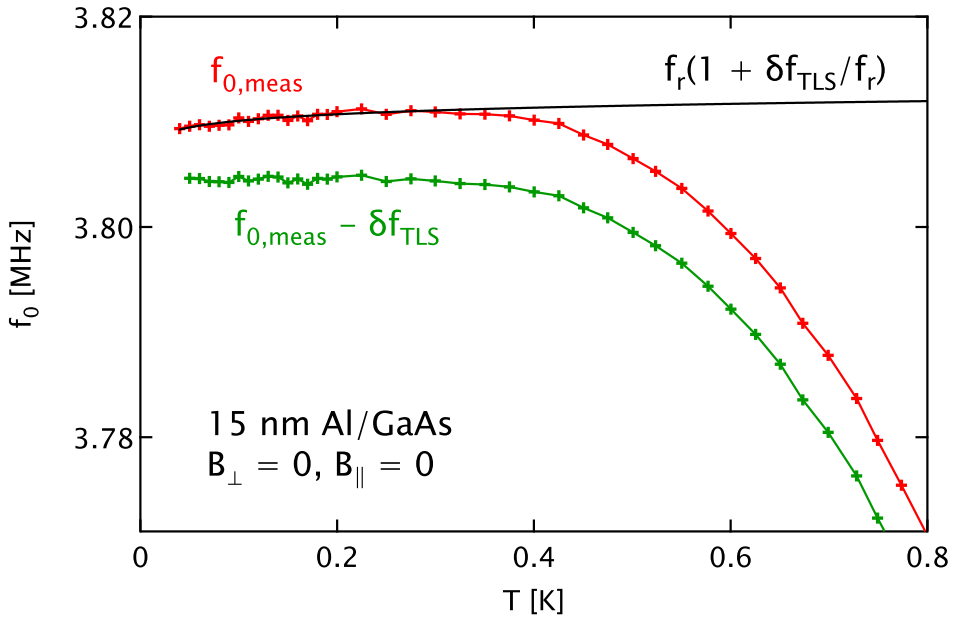

Fig. 5.9.: Resonance frequency as a function of temperature in zero field. Red markers represent measured resonance frequency extracted from Fano fits (eq. 3.9) of spectra measured at different temperatures. Solid line is a fit to eq. 2.42 with fitting parameters $f_r = 3.805\,\mathrm{MHz}, F\delta^0_{TLS} = 0.0048$. The green crosses show the corrected resonance frequency after subtraction of δ_{TLS} from $f_{0,meas}$.

From the corrected resonance frequencies $L(T)$ is calculated. Data are shown in Fig. 5.10. Zero field data (Fig. 5.10) are again fitted using eq. 2.10 and deliver fitting parameters $L_0 = 335\,\mathrm{nH}$ and $\lambda(0) = 456\,\mathrm{nm}$. The corresponding fit reproduces the measured data roughly. At low temperatures there is a small difference between fit and measured data. The fit parameters are very sensible to the data points at higher temperatures, so a deviation at low temperatures can be expected. Also at intermediate

temperature $0.7\,\mathrm{K} < T < 1.1\,\mathrm{K}$ fit and data do not match perfectly. The whole trace takes roughly 12 hours to be measured. Possibly during the measurements magnetic fields or the electromagnetic environment of the sample changed which could affect the inductance of the sample.

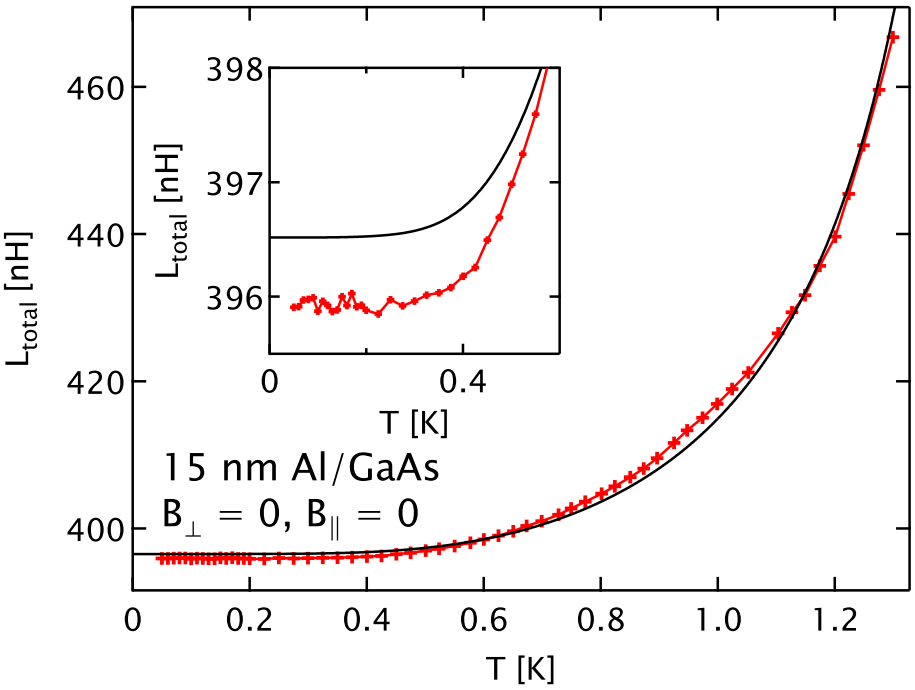

Fig. 5.10.: L(T)-curves in zero field. The solid line is a two-parameter BCS fit with fitting parameters $L_0 = 335\,\mathrm{nH}$ and $\lambda(0) = 456\,\mathrm{nm}$ and a fixed $T_{c0} = 1.585\,\mathrm{K}$. The inset shows a zoom to the low temperature regime, where L saturates. The saturation values for the BCS fit and the measured data are slightly different.

5.2.2. Inductive Vortex Response in Crossed Magnetic Fields

Behavior of the vortex inductance for different in-plane fields was also investigated by measuring resonances at low temperatures with finite $B_\perp$. The results are shown in Fig. 5.11. Again three different regimes can be observed. At low $B_\perp$, $L(B_\perp)$ again shows linear behavior, similar as in sample Al/GaAs-M7 (Fig. 5.6). At higher $B_\perp$ there is again a kink at $B_\perp = 65\,\mathrm{mT} \approx 2/3 B_{c2}$, where $\frac{\mathrm{d}L}{\mathrm{d}B_\perp}$ decreases. The kink position shifts to lower $B_\perp$ with increasing $B_\parallel$, probably due to the decrease of B_{c2} in finite in-plane fields. At the highest in-plane field measured ($B_\parallel = 1.7\,\mathrm{T}$) the normal state is reached without showing a kink structure. At high $B_\perp$ the curves diverge.

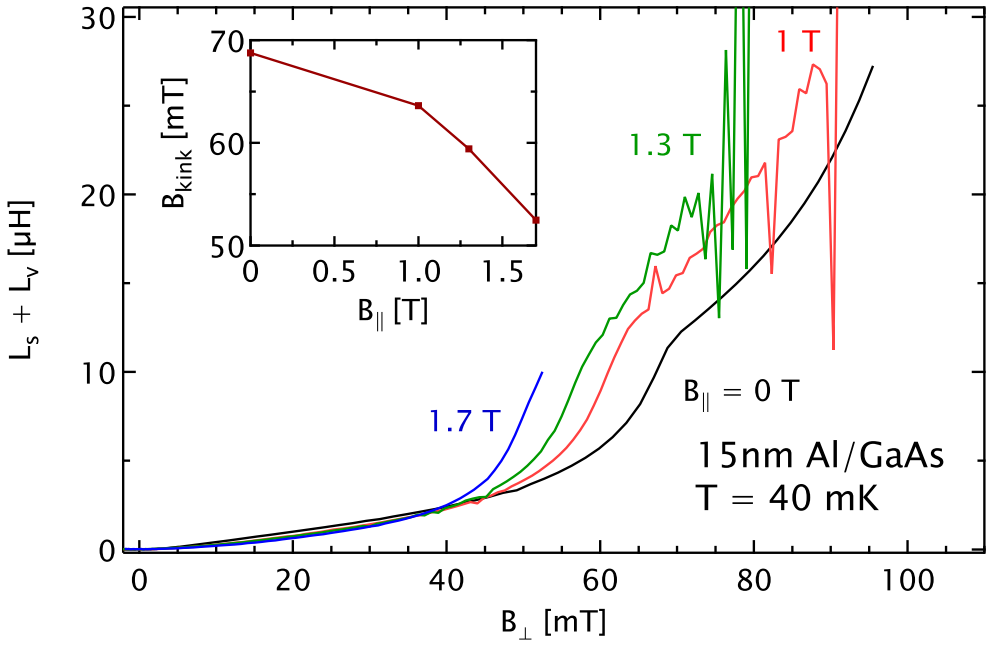

Fig. 5.11.: $L(B_\perp)$ for in-plane fields of $B_\parallel = 0, 1, 1.3, 1.7\,\mathrm{T}$. The inset shows the crossover field B_{kink} as a function of in-plane field.

An in-plane field obviously suppresses the critical out-of-plane field B_{c2}. This is consistent with pair-breaking theory. $B_\parallel$ suppresses the superfluid stiffness of the superconductor via orbital effects. The reduced superfluid stiffness consequently also reduces B_{c2}. The overall characteristic of $(B_\perp)$, however, is unchanged.

6. Spin-Orbit Effects in the Al/InAs Heterostructure

So far only inversion symmetric superconductors have been investigated. In this chapter the dynamics of a 2D superconducting Al/InAs heterostructure will be investigated. As the heterostructure breaks inversion symmetry a possible unconventional admixture to the total order parameter could result in an anisotropic response to an in-plane field depending on the in-plane field direction. Nodes in the order parameter would result in a deviation of the temperature dependence of the kinetic inductance from the standard exponential BCS-dependence. In section 2.3.2 it was further shown that an in-plane field applied to a Rashba superconductor can lead to an anisotropic reduction of the vortex core size. A squeeze of the normal region of a vortex parallel is expected to produce a steepening of the pinning potential. The so increased curvature of the pinning potential in an in-plane field is be measured as a decrease of the vortex inductance. By changing the relative orientation of in-plane field and current also an anistropy of the inductive response of the vortex lattice is observed.

Sample Al/InAs-M was similarly structured as the ones in the previous section by means of optical lithography and wet etching. An optical micrograph is shown in Fig. 6.1. The Wafer was again grown and provided by the group of Michael Manfra at Purdue university. The dominant current direction is parallel to the [110] axis. θ describes the angle between the in-plane magnetic field and the current direction. From TEM measurements on similarly grown Al films with the same nominal thickness an effective Al thickness after oxidation can be estimated to $d = 4.5\,\mathrm{nm}$ [66]. This number will be used for further analysis.
In the following, first DC characterization measurements are discussed from which the most important parameters can be deduced. In the second part results of AC measurements in the RLC circuit are presented.

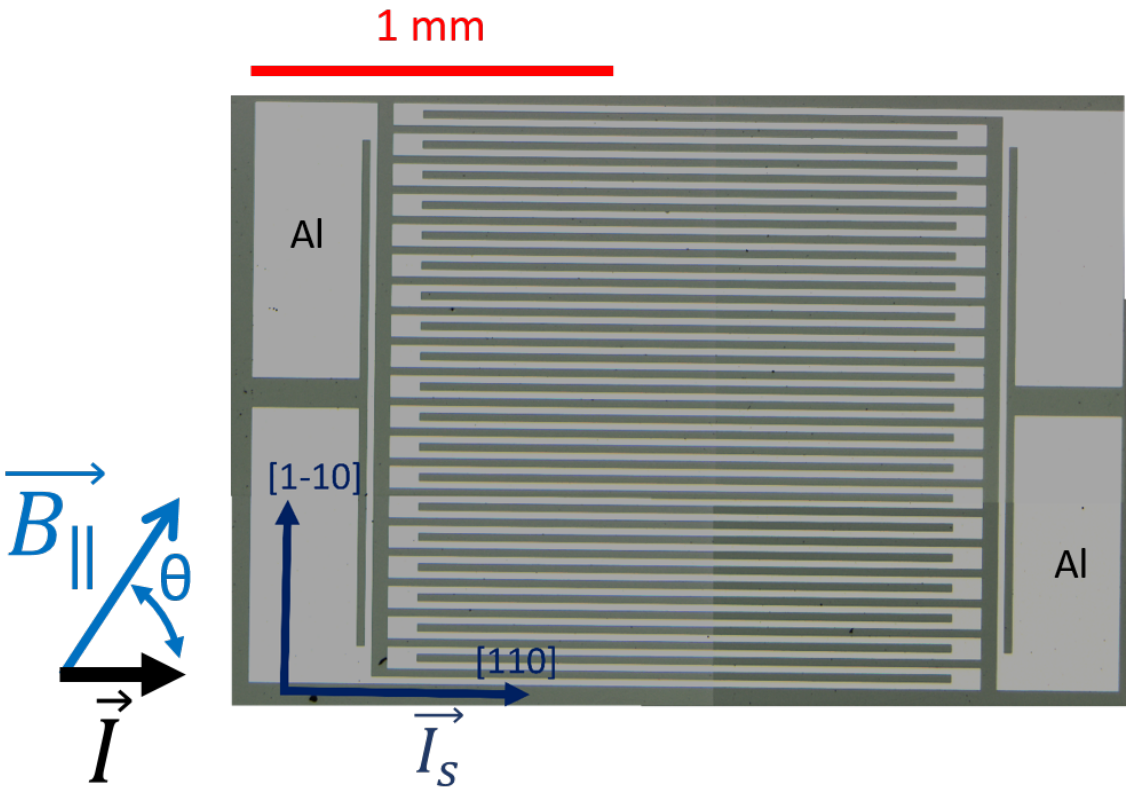

Fig. 6.1.: Sample structure of the Al/InAs meander. The structure consists of 4 contact pads for measuring standard 4-point transport properties. The meander consists of roughly 3000 squares in series with a width of 24 μm. The main current direction is parallel to the [110]-InAs crystal axis. θ is defined as angle between current and in-plane field direction.

6.1. DC-Transport Characterization

Basic transport characterization measurements were performed on sample Al/InAs-M to determine the most important superconducting parameters. In Fig. 6.2, $R(T)$-curves for different in-plane field magnitudes and orientations are shown. All the curves have been measured after compensating out-of-plane field components a best as possible.

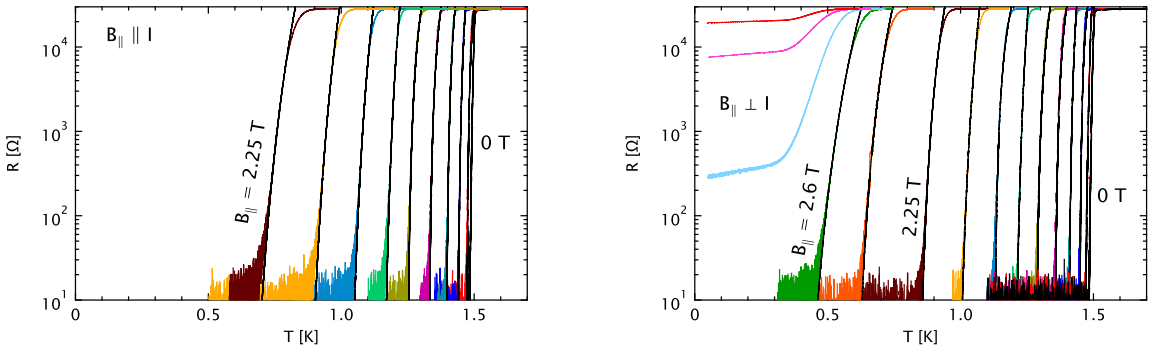

Fig. 6.2.: left: $R(T)$-curves for in-plane fields parallel to the main current direction ranging from 0 T to 2.25 T in steps of 0.25 T. At higher fields the out-of-plane component of the magnetic field could not be compensated anymore, because critical current of the compensation coils were reached. right: R(T)-curves for in-plane fields perpendicular to the current direction ranging from 0 T to 2.5 T in steps of 0.25 T and at high fields of 2.6 T,2.65 T, 2.68 T and 2.7 T. Black lines are fits to the square root cusp formula defined in the main text. At very high $B_{\parallel} > 2.6$ T no zero-resistance state could be observed. At these fields A finite resistance tail emerges.

In zero magnetic field the midpoint of the transition to a dissipationless state is at $T_{c0} = 1.502$ K with a width of the transition of roughly 10 mK. The total resistance above the transition is 28 kΩ leading to a resistance per square of $R = 9.2\,\Omega$. Considering the Al as the main contributor to the conductivity it is possible to calculate the mean free path $l = 8.2$ nm can be determined by using the literature ρl - value for Al $\rho l = 4\,10^{-16}\Omega\mathrm{m}^2$ [77]. In the small resistances regime the curves can nicely be fitted by the square root cusp formula that describes BKT-like transitions [82]

$$R(T) \propto \exp(-b(T/T_{BKT} - 1)^{-1/2}), \tag{6.1}$$

where b is a constant of order unity and T_{BKT} is the Berezinskii–Kosterlitz–Thouless transition temperature. This already shows that the transition to the normal state is probably of a BKT-type. At the highest accessible fields it was not longer possible to achieve a zero resistance state instead a finite resistance tail with a linear slope emerges.

This could be the consequence of vortex motion in parts of the sample where $B_\perp$ is non-zero due to the inhomogeneity of the compensation field (see Fig. 3.25).

From the $R(T)$-curves $T_c(B_\parallel)$ is extracted by defining the temperature of the midpoint ($R(T_c) = 0.5R_n$) of the transition as T_c. From the fits of $R(T)$-data at the low resistance tail to eq. 6.1, $T_{BKT}(B_\parallel)$ can be extracted. $T_c(B_\parallel)$ and $T_{BKT}(B_\parallel)$ are shown in Fig. 6.3. There are two main observations. On the one hand the critical temperatures for the two orientations show slightly different field dependencies showing that one direction is more vulnerable to an in-plane field than the other. On the other hand one can find a broadening of the BKT-transition which indicates that T_{BKT} is suppressed stronger than T_c by the in-plane field.
At low temperatures an out-of-plane critical field $B_{c2} = 61\,\mathrm{mT}$ was determined from an $R(B_\perp)$-sweep (not shown here), corresponding to a coherence length $\xi = 73\,\mathrm{nm}$.

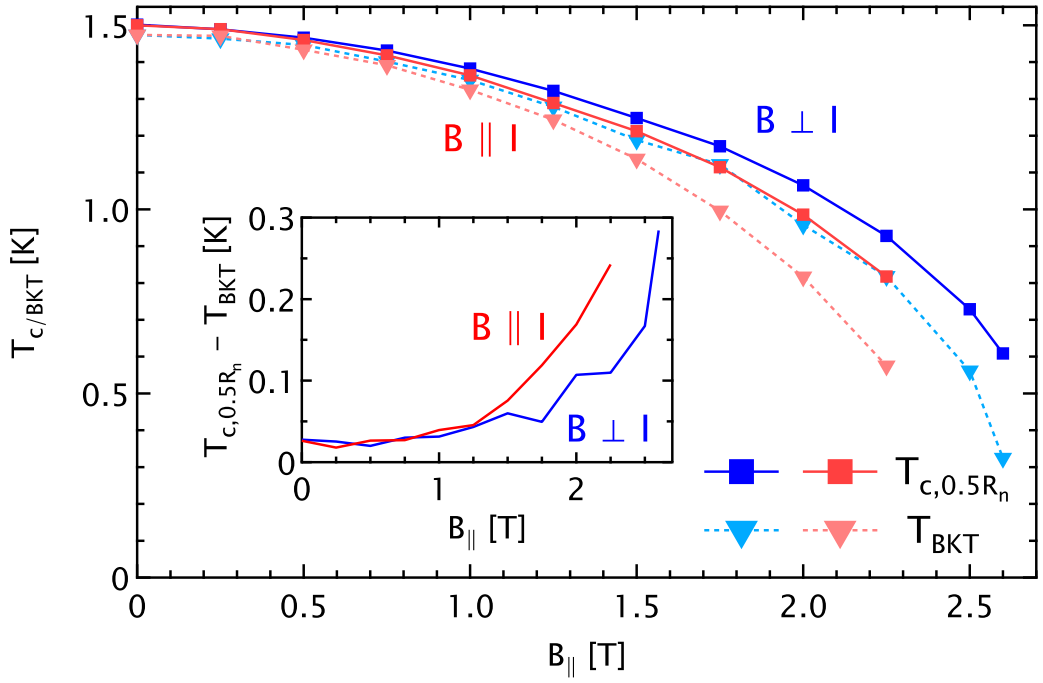

Fig. 6.3.: Critical temperature and BKT transition temperature as a function of the in-plane field for the two main field orientations. Inset: Difference of $T_c(B_\parallel)$ and $T_{BKT}(B_\parallel)$ as a function of field for the two different orientations. Increased in-plane fields lead to a broadening of the BKT-transition.

6.2. Inductive Response of Superfluid

Signatures of an unconventional order parameter are difficult to probe at the phase boundaries with standard DC transport measurements. Therefore it is necessary to investigate the superconducting dynamics deep in the dissipationless regime, which can only be accessed with an AC experiment.
In this chapter the main results of AC measurements performed on sample Al/InAs-M are shown and discussed. The discussion will start with $L(T)$ measurements in zero magnetic field. Afterwards results of inductance measurements in the vortex state for $B_{\parallel} = 0$ will be shown. The impact of a superimposed in-plane field on the vortex dynamics will be discussed in the third section. In the last part of this chapter an unexpected non-linearity of the $L(B_{\perp})$-dependence in in-plane fields perpendicular to the current will be analyzed phenomenologically.

6.2.1. BCS Temperature Dependence and TLS Correction

Of particular interest is the investigation of the temperature dependence of the kinetic inductance. Standard s-wave superconductors exhibit an exponential deviation of $L_s(T)$ from $L_s(0)$, while unconventional superconductors with gaps in the node follow a power-law. In samples Al/GaAs-M7 (Fig. 5.3)and Al/GaAs-M15 (Fig. 5.9) a shift of resonance frequency at low temperatures was found. The same reduction of f_0 for low temperatures is also observed in the Al/InAs heterostructure. Fig. 6.4 shows measured and corrected resonance frequency as a function of temperature in zero magnetic field. At low temperatures the measured resonance frequencies $f_{0,meas}(T)$ can again be fitted by using eq. 2.42. The corresponding fitting parameters are $f_r = 3.800\,\mathrm{MHz}, F\delta^0_{TLS} = 0.012$. The value for $F\delta^0_{TLS}$ is of the same order as the one measured in sample Al/GaAs-M7 ($F\delta^0_{TLS} = 0.019$) with no 2DEG. Both Al films were grown in the same chamber under the same conditions. The good accordance of the two values of $F\delta^0_{TLS}$ indicates that the resonance shift mainly results from TLS in the AlOx layer and less from the substrate. The resulting $\delta f_{TLS}(T)$ is subtracted from $f_{0,meas}(T)$ and leads then to a saturating behavior of $f_0(T)$ at low temperatures after correction. From the corrected resonance frequencies $f_0(T)$, $L(T)$ data are calculated via eq. 3.7.

In Fig. 6.5 the total inductance of the RLC resonator is shown as a function of temperature. $L(T)$ saturates at low temperatures and monotonically increases with increasing temperature. The peak-to-peak noise level is of the order of 0.5 nH.

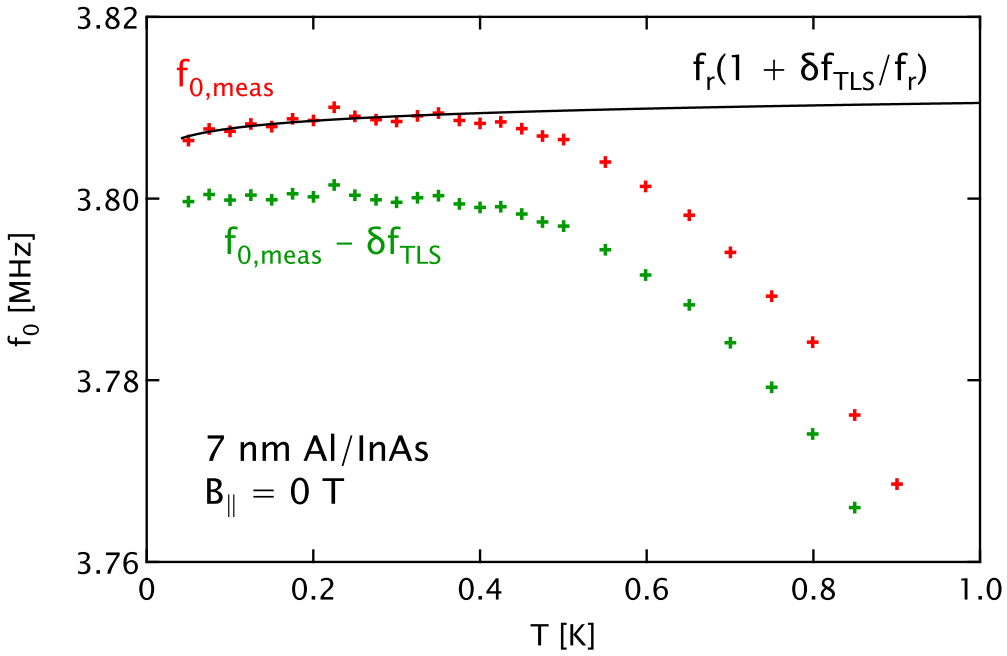

Fig. 6.4.: Resonance frequency as a function of temperature in zero field. Red markers represent measured resonance frequency extracted from Fano fits (eq. 3.9) of spectra measured at different temperatures. Solid line is a fit to eq. 2.42 with fitting parameters $f_r = 3.800\,\mathrm{MHz}, F\delta^0_{TLS} = 0.012$. The green crosses show the corrected resonance frequency after subtraction of δ_{TLS}.

A two-parameter fit of the $L(T)$ data to eq. 2.11 with fitting parameters $L_0 = 394.3\,\mathrm{nH}$ and $\lambda(0) = 227.0\,\mathrm{nm}$ and a fixed $T_{c0} = 1.502\,\mathrm{K}$, which was determined from the DC $R(T)$ curve (Fig. 6.3), describes data reasonably well. The penetration depth $\lambda(0)$ is 25% larger than an estimate from the BCS formular $\lambda_{BCS}(0) = \left(\frac{R_\square d\hbar}{\pi\mu_0\Delta(0)}\right)^{1/2} = 174\,\mathrm{nm}$. In all three samples that were measured in the RLC circuit, the $\lambda(0)$ value from a BCS fit is larger than the expected value from eq. 2.14 and therefore seems to be a systematic problem of the theory.

In zero magnetic field it turns out, that the inductive response of the Al/InAs heterostructure basically behaves similarly as in Al films grown on a GaAs substrate. Although inversion symmetry is broken in sample Al/InAs-M there is so far no clear indication pointing towards a significant triplet component of the order parameter. As one would only expect a small triplet admixture to the singlet order parameter [51] it is not surprising, that $L(T)$ can still be reproduced properly by a standard s-wave BCS T-dependence.

Fano fits to the measured spectra do not only deliver values for the resonance frequency

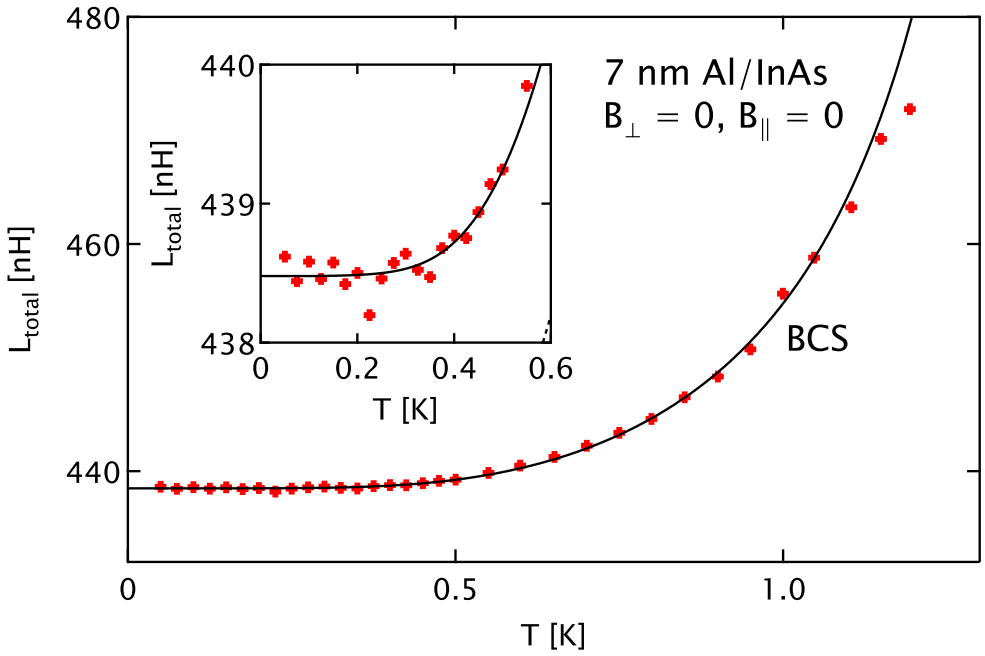

Fig. 6.5.: L(T)-curves in zero magnetic field. The solid line is a two-parameter BCS fit (eq. 2.11) with fitting parameters $L_0 = 394.3\,\mathrm{nH}$ and $\lambda(0) = 227.0\,\mathrm{nm}$ and a fixed $T_{c0} = 1.502\,\mathrm{K}$. $L(T)$ data are in good accordance with a standard BCS theory curve. Inset shows a zoom in the low temperature regime.

f_0, but also for the width of the resonance. Dissipation in the circuit leads to dissipation and hence reduces the quality factor. By using eq. 3.8 the dissipative component R_s of the complex impedance of the circuit can be calculated. Fig. 6.6 shows the temperature dependence of the resistance extracted from both resonator and DC measurements in a logarithmic scale. At the low-temperature end a background resistance of $\sim 0.3\,\Omega$ was substracted, which mainly comes from the copper coil. Resistance data determined from either AC and DC measurements are in good accordance near T_c. This shows that the RLC technique is well suited for expanding the range of resistance measurements by at least 3 orders of magnitude. In the low temperature regime there is a finite slope indicating already a resistance far below T_c. A quasiparticle contribution can be excluded due to the low frequency used in this measurement (see section 2.1.6). The reason for this is unclear so far.

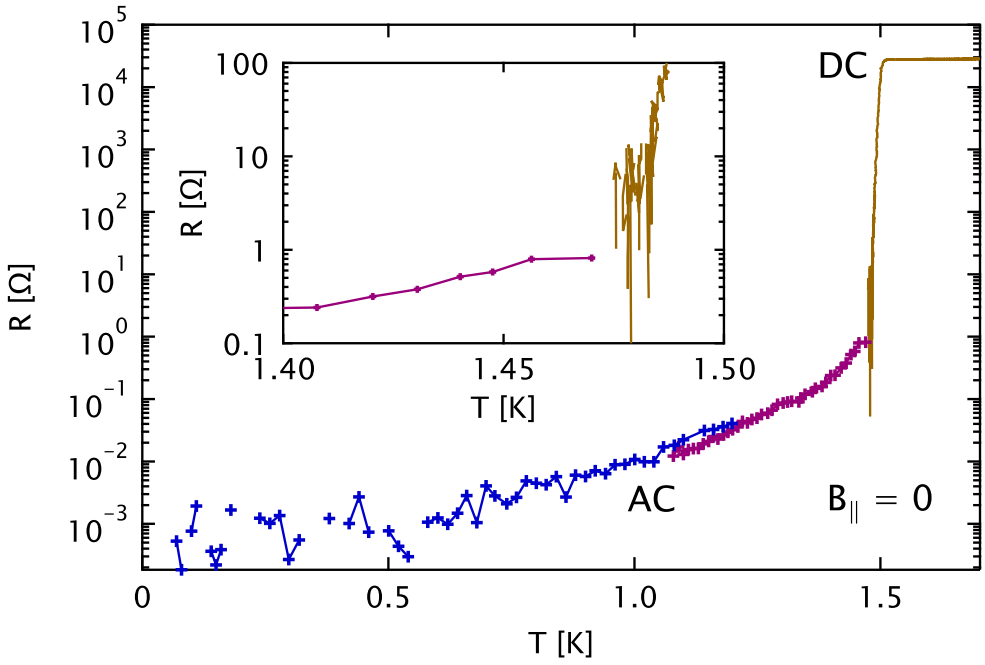

Fig. 6.6.: Combined resistance data as a function temperature. Dark yellow points are measured in a standard 4 point DC measurement. Blue and purple curves are extracted from AC measurements. Both datasets nearly overlap near the critical temperature. Inset shows a zoom in the overlap region of the DC and AC experiment. The resistance already starts to increase for $T > 0.6\,\mathrm{K}$ well below T_c.

6.2.2. Vortex Inductance

In both reference samples (sections 5.1.5 and 5.2.2) it was shown that for out-of-plane fields of some mT a sizeable inductive response much larger than $L_s(B = 0)$ can be measured. With an out-of-plane vortices are introduced in the film, which contribute to the inductance as in the reference samples. Such an inductance occurs when the vortices are dislocated from the center of their pinning potentials when driven by an AC supercurrent. Out-of-plane fields additionally induce Meissner currents in the sample. As in the vortex state most of the sample is field free, the reduction of the superfluid stiffness due to these currents is mainly relevant at the very edges of the sample [83].

In the following sections, the interpretation of inductance data measured in out-of-plane fields relies on the assumption that the vortices are pinned individually and hence eq. 2.30 ($L_v = \frac{\Phi 0}{dk_p}$) is valid.

Fig. 6.7 shows the out-of-plane field dependence of the inductance at low temperatures. The total inductance for $B_\perp \sim$ mT is of the order μH compared with $L_s \sim$ nH with no perpendicular field present. For small fields the curve is nearly linear suggesting that the inductance is simply proportional to the number of vortices and k_p is constant. The slope for small $B_\perp$ is $\frac{\Delta L}{\Delta B_\perp} = 118\,\mathrm{nH/mT}$. From the slope of $L(B_\perp)$ at small fields pinning constant $k_p = 14.9\,\mathrm{N/m^2}$ can be determined. Compared to samples Al/GaAs-M7 and Al/GaAs-M15 the inductive response in the vortex state is much larger in Al/InAs-M. The pinning of vortices therefore seems to be very weak. At intermediate fields $20\,\mathrm{mT} \leq B_\perp \leq 38\,\mathrm{mT}$ $L(B_\perp)$ increases superlinearly. At $B_\perp \approx 38\,\mathrm{mT}$ a kink structure can be observed, beyond which the slope of $L(B_\perp)$ decreases. At high fields $L(B_\perp)$ diverges as $B_\perp$ approaches B_{c2}. There is a small discontinuity of $L(B_\perp)$ at $B_\perp \approx 10\,\mathrm{mT}$. At two consecutive fields the resonance spectra showed some instabilities, which is reflected in a reduced L. The origin is unknown and therefore will not be analyzed further as the overall behavior seems is not changed.

For $B_\perp \geq 20\,\mathrm{mT}$ the simple linear dependence changes to a more complex behavior. The observed kink structure was also found to be present in both Al/GaAs films, which were grown on top of a GaAs substrate without 2DEG and therefore seems to be generic for thin superconducting Al films of this geometry (see Fig. 5.11 and Fig. 5.6). Vortex dynamics in this regime will be treated in section A.1.4 of the appendix.

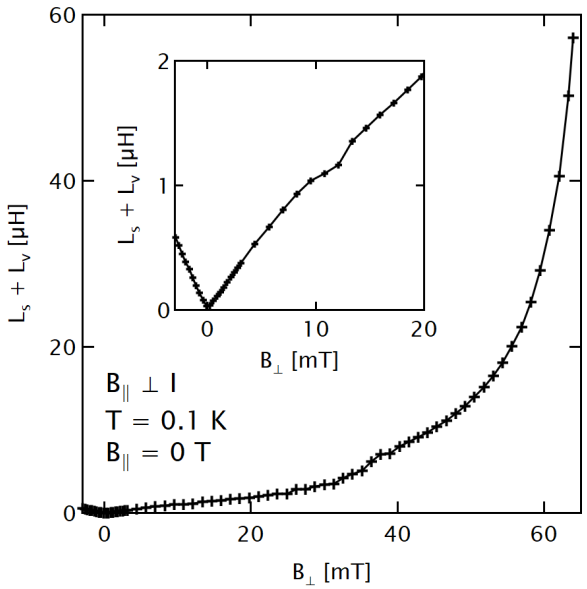

Fig. 6.7: Inductance as a function of the out-of-plane field at low temperature. For small fields $L(B_\perp)$ increases linear with $B_\perp$. Above $\sim 30\,\mathrm{mT}$ the linear dependence evolves into a more than linear function in $B_\perp$. At an intermediate field of $\sim 38\,\mathrm{mT}$ a kink structure is observed. At very high fields the inductance diverges as superconductivity breaks down near the critical out-of-plane field. Inset shows $L(B_\perp)$ in the low field regime $B \leq 20\,\mathrm{mT}$.

The temperature dependence of the vortex inductance in the regime of individual pinning is of peculiar interest. As was shown the pure kinetic inductance $L_s(T)$ follows an exponential dependence. The vortex inductance $L_v(T) \propto \frac{1}{k_p(T)}$ was seen to follow a power law. Eq. 2.26 predicts a $k_p(T)$ dependence $\propto \left(1-(T/T_c)^2\right)^2$.

Fig. 6.8 shows the total inductance as a function of temperature measured in an out-of-plane field of $B_\perp \approx 6.4\,\mathrm{mT}$. As the vortex contribution exceeds the kinetic inductance by at least two orders of magnitude, the kinetic contribution is neglected in the analysis. At $T = 0.175\,\mathrm{K}$ there is a small jump in $L(T)$. For $T \geq 0.2\,\mathrm{K}$ $L(T)$ monotonically increases with a divergence for $T \geq 1.2\,\mathrm{K}$. For temperatures higher than 1.2 K no resonance could be measured anymore. For $0.2\,\mathrm{K} \leq T \leq 0.55\,\mathrm{K}$ inductance roughly follows a $L(T) = L_0\left(1-(T/T_c)^2\right)^{-2}$ power-law matching with eq. 2.26. The saturation value at low temperature is $L_0 = 0.92\,\mu\mathrm{H}$ and T_c was changed to $\left(1-\frac{B_\perp}{B_{c2}}\right)T_{c0} \approx 1.36\,\mathrm{K}$ with $B_{c2} = 61\,\mathrm{mT}$. Above 0.55 K data rather suggest a $L(T) = L_0\left(1-(T/T_c)^2\right)^{-1}$ dependence with the same T_c but slightly larger $L_0 = 1.15\,\mu\mathrm{H}$, which increases weaker than eq. 2.26.

In the inset, there is a small jump to a slightly lower L at $T \approx 0.175\,\mathrm{K}$. The reason for this discontinuity is most probably attributed to a rearrangement of the vortex lattice due to thermal fluctuations in the presence of a driving current. As the vortex inductance is large, the pinning potentials are very shallow. In systems with such

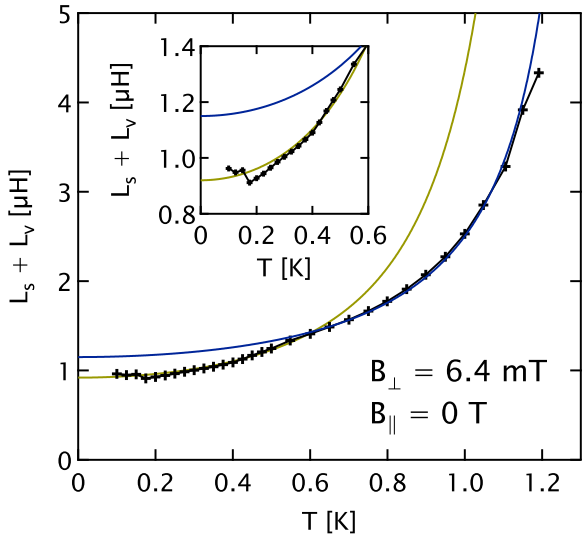

Fig. 6.8: Sum of kinetic and vortex inductance as a function of temperature in an out-of-plane field of 6.4 mT. For $T > 0.2\,\mathrm{K}$ L increases monotonically and finally diverges for $T > 1.2\,\mathrm{K}$. Blue and yellow curves are fits to power-law functions described in the main text. Inset shows a zoom in to the low temperature regime. At $T = 0.175\,\mathrm{K}$ a small jump to a lower inductance value is found.

weak potentials vortices can relatively easy hop from one potential to the other. After cooldown vortices initially do not only occupy the pinning sites with lowest energy, but also partly pinning sites with even smaller curvature at the bottom of the potential. At elevated temperatures or higher currents some vortices move to pinning sites with slightly deeper pinning potential. This interpretation is supported by measurements performed with an additional DC current in the same field and temperature regime (see section A.1.5 in the appendix). As will be seen later, in zero in-plane field the inductive response of the vortex lattice is very unstable. At higher in-plane fields the measured inductance for fixed out-of-plane field is much more stable (see Figs. A.13, A.14 and A.15).

As mentioned before, for $T \leq 0.55\,\mathrm{K}$, $L(T)$ is in good accordance with the predicted temperature dependence for individual vortex pinning [23]. Similar to Fig. 6.7, where a kink structure was observed in the $B_\perp$-dependence of L_v, also $L_v(T)$ measured in a fixed $B_\perp$ shows some kink structure at $T = 0.55\,\mathrm{K}$. The slope $\frac{\mathrm{d}L_v(T)}{\mathrm{dT}}$ is reduced at this temperature. The change of characteristic $L_v(T)$ dependence may again to point towards a crossover to a different pinning regime that can be reached either by increasing the temperature for a given $B_\perp$ or by increasing $B_\perp$ at a fixed temperature.

In the Al/InAs heterostructure pinning seems to be much weaker than in the Al films grown on GaAs. The resulting vortex inductance in an out-of-plane field is at least 2 orders of magnitude larger than the pure kinetic inductance. The precise values of the kinetic inductance L_s and hence also the interpretation of its dependencies on in-

plane fields or temperature strongly depend on a very accurate knowledge of the external inductance L_0. In out-of-plane fields where L is largely dominated by L_v, the uncertainty of L_0 is not so relevant. In the following this large gain in signal is used to measure a possible effect of an in-plane field on the vortex pinning and therefore the underlying superconducting order parameter in the presence of Rashba SOC.

6.2.3. Strongly Anisotropic Pinning Enhancement in In-Plane Fields

In sample Al/GaAs-7 it was shown that both in- and out-of-plane fields and the combination of the two lead to an increase of the inductance (see Figs. 5.7 and 5.11). On the one hand an out-of-plane field introduces vortices, which produce an additional inductive response. Moreover, in-plane fields decrease the superfluid stiffness via orbital pair-breaking, which also reduces the pinning. This leads to an increase of kinetic and vortex inductance in the presence of either oriented magnetic fields. In Rashba superconductors the pinning constant k_p is expected to become dependent on $B_\parallel$. The main idea and deduction of the theory is described in section 2.3.2.

The observation of a large vortex inductance as a function of in-plane field offers a good chance to gain insight into the superconducting phenomenology related to SOC. In the following, B_p (parallel) describes an in-plane field applied parallel to the current, while B_t (transverse) defines an in-plane field perpendicular to the current. The analysis and interpretation of data are all based on the assumption that the measured vortex inductance results from individual pinning described by eq. 2.30 ($L_v \propto 1/k_p$).

In Fig. 6.9 total inductance of sample Al/InAs-M is shown as a function of in-plane field for $B_\perp = 2\,\mathrm{mT}$. As the kinetic inductance $L_s(B_\parallel)$ is of the order of $\sim 40\,\mathrm{nH}$ most of the inductance results from the oscillation of pinned vortices under an AC driving current. Therefore the small contribution of L_s will be neglected in the analysis below. The in-plane field is oriented in directions parallel (red curve) and perpendicular to the current (blue curve), as indicated in the graph. Vortices under an AC driving current move perpendicular to the supercurrent. The red curve ($I \parallel B_\parallel \rightarrow B_p$) refers to vortex motion perpendicular to $B_\parallel$, while the blue curve ($I \perp B_\parallel \rightarrow B_t$) to vortices moving parallel to $B_\parallel$.

In the rotator position, where $B_\parallel$ is perpendicular to the current, four consecutive measurements with zero in-plane field have been performed (see inset of Fig. 6.9). Between

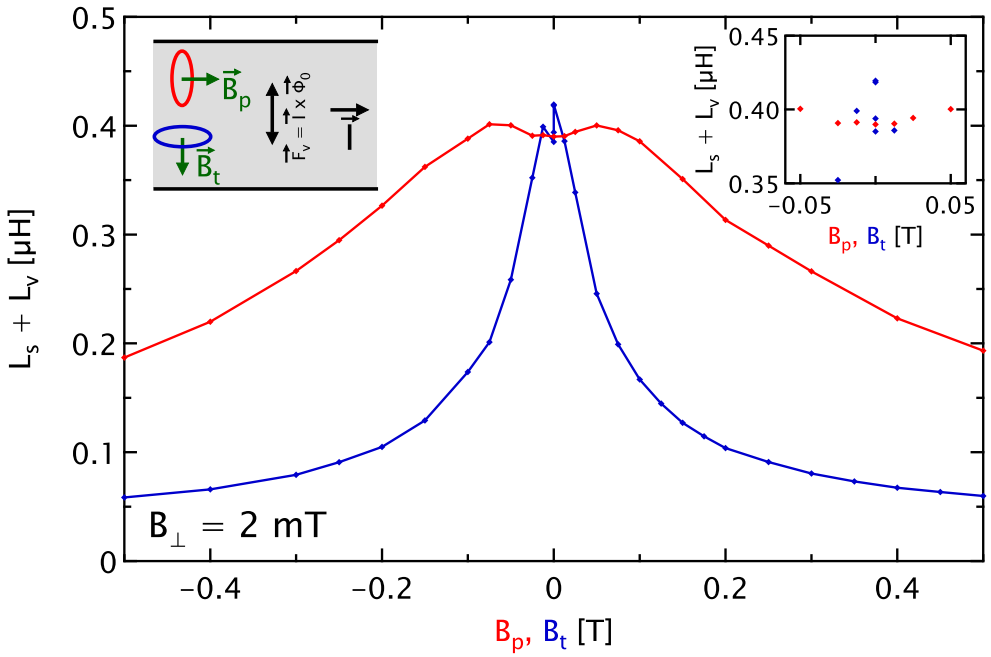

Fig. 6.9.: Inductance in a perpendicular field of 2 mT as a function of in-plane field for a transverse B_t (blue) and parallel in-plane magnetic field B_p (red). Inset shows a zoom in to the low-$B_\parallel$ regime. The sketch in the upper left corner shows definitions of magnetic field and current directions. The vortex motion is perpendicular to the current indicated by the accelerating Lorentz force $\vec{F}_v$. The anisotropic deformation of initially ($B_\parallel = 0$) circular vortex cores in transverse and parallel magnetic fields is indicated by ellipses.

these measurements the sample was heated up above T_c, the field minimum of $B_\perp$ was determined and afterwards a field of $B_\perp = 2\,\mathrm{mT}$ was applied before it was cooled down again. There is a few % scatter of the measured inductance data (inset of Fig. 6.9), which shows again the instability of the vortex lattice for $B_\parallel = 0$.
For a parallel in-plane field B_p (red curve), $L(B_p)$ increases up to a field of $\sim 0.05\,\mathrm{T}$ before it decreases up to the largest applied field of $B_p = 0.5\,\mathrm{T}$. In a transverse field B_t (blue curve), $L(B_t)$ also decreases monotonically with a much steeper decrease than for B_p. Because of the above mentioned instability of $L(B_t)$ at very small B_t it cannot be said, whether there is also an initial increase of $L(B_t)$ as in the red curve. Both curves are mirror symmetric in $B_\parallel$.

There is a strong difference between the $B_\parallel$-dependence of L_v measured in sample Al/GaAs-M7 (see Fig. 5.7) and in the Al/InAs heterostructure. Sample Al/GaAs-M7 showed a strictly increasing inductance when either in- or out-of-plane field or both fields together were applied. This is expected because in a standard s-wave superconduc-

tor $B_\parallel$ leads to orbital pair breaking, which implies a reduction of the pinning constant k_p and hence an increase of L_v. The slight increase of $L_v(B_p)$ for small $B_p \leq 0.05\,\mathrm{T}$ is unlikely to be caused by orbital pair breaking, as this should affect both directions equally and should be negligible for small in-plane fields ($\Delta L_s(B_\parallel) \propto \frac{B_\parallel^2}{B_{c\parallel}{}^2}$). The reason for the anisotropic increase of L_v for small in-plane fields cannot be explained at the moment. At higher $B_\parallel$, $L_v(B_t)$ as well as $L_v(B_p)$ decreases strongly. Furthermore there is a strong difference between the two measured in-plane field directions. The reduction of $L(B_t)$ is much stronger than for $L(B_p)$. If eq. 2.30 ($L_v \propto 1/k_p$) still holds, the individual pinning is enhanced anisotropically in the presence of $B_\parallel$.

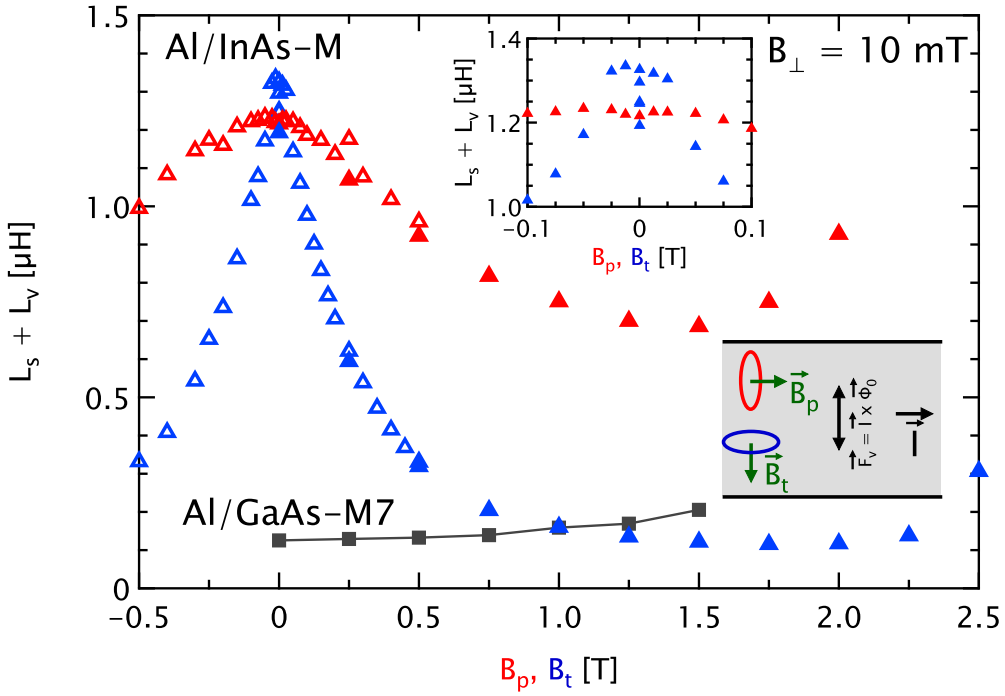

Fig. 6.10.: Inductance for $B_\perp = 10\,\mathrm{mT}$ as a function of transverse (blue) and parallel (red) in-plane magnetic field measured at $T = 0.1\,\mathrm{K}$. Inset shows a zoom in to the low-$B_\parallel$ regime. Definition of the different directions of field and vortex motion is shown in the small sketch on the lower right similar to Fig. 6.9. Black squares are data measured in sample Al/GaAs-M7 for $B_\perp = 10\,\mathrm{mT}$.

Fig. 6.10 show similar data as Fig. 6.9 at higher $B_\perp = 10\,\mathrm{mT}$ in an expanded $B_\parallel$-range. In addition $L_v(B_\parallel)$ measured in sample Al/GaAs-M7, which has no 2DEG, is shown for comparison. Data are taken at $T = 0.1\,\mathrm{K}$. Triangles refer to data taken on sample Al/InAs-M. Open and filled triangles represent data that were measured in separate cooldowns. The black squares show $L(B_\parallel)$ measured on sample Al/GaAs-M7 for only

one $B_\parallel$ direction as there is only very small dependence on the field direction in this sample. Red triangles refer to parallel in-plane magnetic field, blue triangles are taken in a transverse in-plane field. Ellipses again indicate the shape of a vortex core relative to in-plane field (green arrows) and current direction (black arrows).

In a parallel in-plane field, $L(B_p)$ (red curve) increases only very little at small $B_p < 25\,\mathrm{mT}$ (inset of Fig. 6.10). The red curve intersects the blue curve and then decreases until a minimum is reached at $B_p = 1.5\,\mathrm{T}$. Afterwards $L(B_p)$ increases up to the highest field of 2 T. At higher in-plane fields the resistance of the sample and hence the damping was too high to measure a resonance.

In a transverse magnetic field B_t, four consecutive measurements with individual compensation were performed for $B_t = 0$. In that regime (blue curve in inset of Fig 6.10) there is again a $\sim 15\%$ scattering of data points. In a small field range of $0.025\,\mathrm{T}$ $L_v(B_t)$ slightly increases and lies above the red curve. The red curve is much stabler in the small $B_\parallel$ regime. The blue curve intersects the red one for an in-plane field $B_t \approx 25 - 50\,\mathrm{mT}$. For $B_t > 0.025\,\mathrm{T}$, $L(B_t)$ decreases strongly and reaches a minimum at $B_t = 2\,\mathrm{T}$. At very high $B_t > 2\,\mathrm{T}$, $L(B_t)$ increases again. For $B_\parallel > 2.5\,\mathrm{T}$ no resonance could be measured anymore as the sample was too resistive to measure a resonance.

The pinning for small in-plane fields is weaker by roughly one order of magnitude in the heterostructure than in sample Al/GaAs-M7. This can only party explained by the weaker superfluid stiffness, which is only smaller by a factor of 2-3. The pinning energy not only depends on the superfluid stiffness but also on microscopic details like defect size (see section 2.1.4). However, as the Al films in both structures are grown in the very same chamber under the same conditions, similar defect concentrations and sizes could be expected. Maybe the descrepancy is related to the 2DEG.

For $B_t > 1\,\mathrm{T}$, $L(B_t)$ is reduced even below the value measured in sample Al/GaAs-M7. A minimum of inductance is observed as a consequence of two competing effects. On the one hand pinning is enhanced by the in-plane field, on the other hand orbital pair-breaking reduces the superfluid stiffness and hence also weakens pinning. Once $B_\parallel$ approaches $B_{c\parallel}$ superconductivity breaks down and $L_v(B_\parallel)$ diverges. The pinning enhancement, at least for small $B_\parallel$ can be explained as a consequence of a deformation of the vortex core from a circular shape to an ellipsoid produced by the interplay of SOC and in-plane field (see section 2.3.2). The vortex core is squeezed anisotropically by the in-plane magnetic field. The pinning potential is modeled as a convolution of the order

parameter $|\Psi|^2(r)$ and a delta like defect. Convolution of an arbitrary function $f(x)$ with $\delta(x)$ reproduces the shape of $f(x)$. k_p therefore describes the inverse curvature of $|\Psi|^2(r)$ at $r \to 0$ and hence increases with $B_\parallel$. In the direction of $B_\parallel$ the increase of k_p was shown to be enhanced by a factor $(1 + c_3 B_\parallel^2 / B_\perp^2)$ (eq. 2.75) with respect to the zero in-plane field value. The anisotropic, increased k_p in an-in-plane field manifests itself in a decreased, anisotropic inductive response of the vortex lattice.

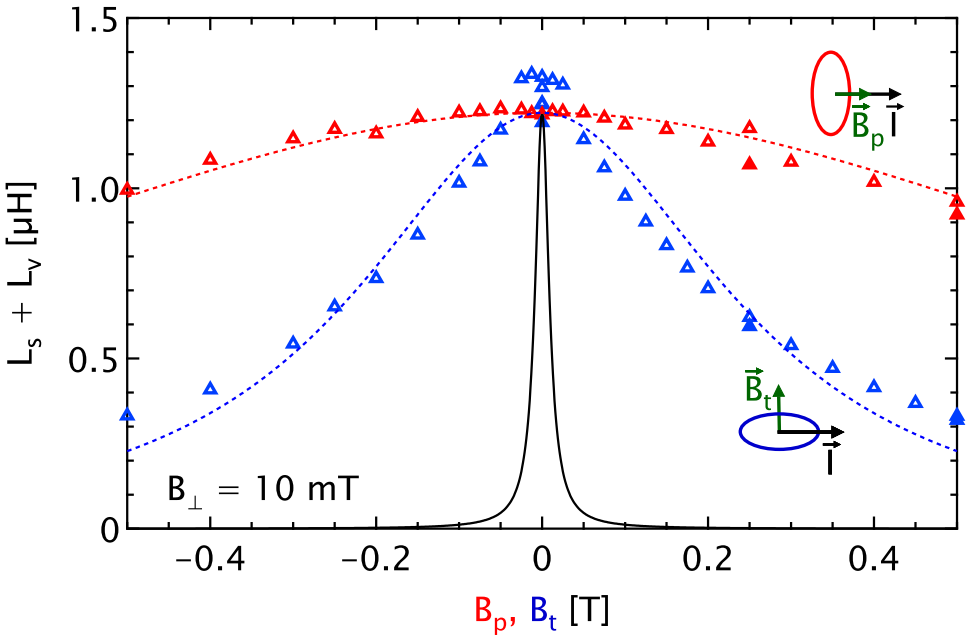

Fig. 6.11.: $L(B_\perp)$ in an out-of-plane field of 10 mT and theoretically expected reduction of L as a function of B_t (blue) and B_p (red). Ellipsoids again indicate the squeezed normal core of a vortex in the presence of an in-plane field. Red dashed line is a fit of $L_v(B_p)$-data to eq. 2.77, blue dashed line refers to a fit of $L_v(B_t)$ to eq. 2.79.

Fig. 6.11 shows the same experimental data as Fig. 6.10 together with fits to eq. 2.75. The red dashed line refers to a fit to eq. 2.77, blue line is a fit to eq. 2.79. At first the red curve is fitted and gives the fitting parameters $L_{v,0} = 1.22\,\mu$H and characteristic field $\tilde{B}_\parallel = 0.99\,$T. Then the blue curve is fitted with $L_{v,0}$ and $\tilde{B}_\parallel$ and gives the anisotropy parameter $c_3 = 0.0013$. For $0.05\,\text{T} \leq B_\parallel \leq 0.3\,\text{T}$ the fit curves agree reasonably well with measured data. The black solid line is calculated similar as the blue curve with the same $L_{v,0}$ and $\tilde{B}_\parallel$ but with $c_3 = 1$. The additional free parameter c_3 is needed to be able to properly fit the measured data. It was introduced because the simple theory described in section 2.3.2 strongly overestimates the impact of a transverse field on the

vortex pinning. The initial increase of $L(B_\parallel)$ for $B_\parallel \leq 0.025\,\mathrm{T}$ is not described by the theory and stays an open question at this point. For large $B_\parallel$, fits deviate from the measured data as orbital pair breaking leads to a decrease of the superfluid stiffness and hence to an increase of kinetic and vortex inductance which is not considered in the theory.

By dividing eq. 2.77 by eq. 2.77 one finds the theoretical ratio of $L_{v,p}$ and $L_{v,t}$, which is quadratic in $B_\parallel$ for a fixed $B \perp$

$$L_{v,p}(B_\parallel)/L_{v,t}(B_\parallel) = \left(1 + c_3 \frac{B_\parallel^2}{B_\perp^2}\right). \tag{6.2}$$

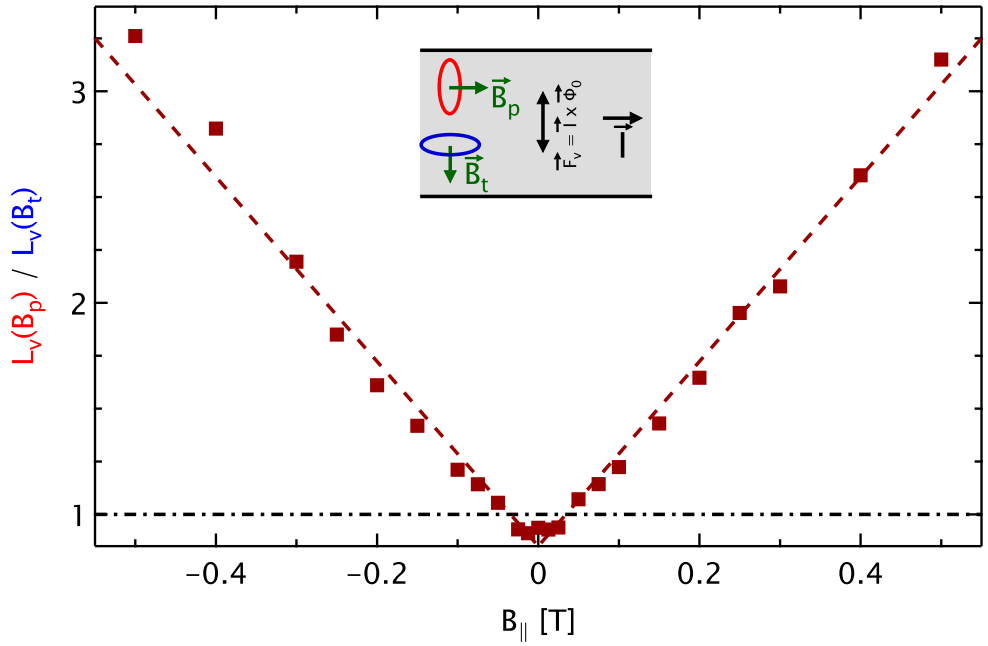

Fig. 6.12.: $L_v(B_p)/L_v(B_t)$ as a function of in-plane field. The anisotropy of the observed vortex inductance in an in-plane field increases linearly with $B_\parallel$

This is in contradiction to the experimental data shown in Fig. 6.12. A linear increase of $L_v(B_p)/L_v(B_t)$ with $|B_\parallel|$ is found in the measurement. This indicates, that although qualitatively the simple theory is in accordance with the data, the theoretically predicted quadratic dependence cannot reproduce experimental data and should be reviewed.

To further study the dependence of $L(\theta)$ on the angle θ between $B_\parallel$ and current the

sample was rotated by the piezo rotator in a constant in-plane field. In Fig. 6.13, $L(\theta)$ in an in-plane field of 0.5 T is shown for $B_\perp = 0$ (left graph) and for finite $B_\perp = 2, 5, 10\,\mathrm{mT}$ (right graph).

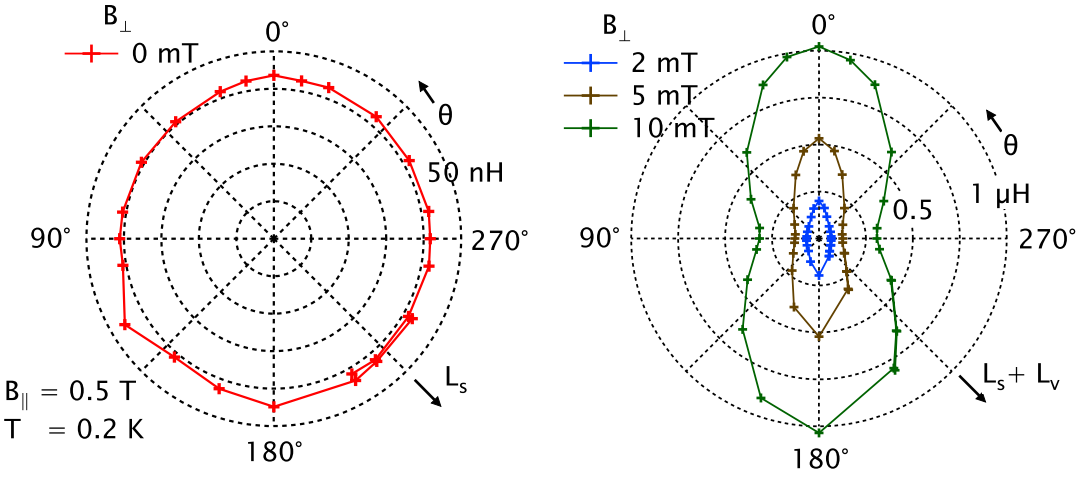

Fig. 6.13.: left: Kinetic inductance $L_s(\theta)$ as a function of relative field orientation for an in-plane field of 0.5 T. On the radial axis inductance is plotted. θ is defined as the angle between $B_\parallel$ and current. right: Polar plot of the total inductance $L_s + L_v$ for $B_\perp = 2, 5, 10\,\mathrm{mT}$. Note the different scalings of the radial axis in the two graphs.

For $B_\perp = 0$, $L_s(\theta)$ is almost independent of θ. Already for $B_\perp = 2\,\mathrm{mT}$, however, $L(\theta)$ strongly varies with θ. A two-fold symmetry can be found. $L(\theta)$ has maxima for $B_\parallel \parallel I$ and minima for $B_\parallel \perp I$. This is in accordance with eq. 2.75, which predicts the strongest enhancement of k_p in the direction of $B_\parallel$. It turns out, that the vortex inductance is a suitable measure in order to measure the symmetry of the order parameter in systems with broken time- and inversion-symmetry.

6.2.4. Fundamental Change of Pinning Mechanism in In-Plane Fields

So far it was shown, that for a fixed $B_\perp$ the total inductance is strongly reduced by an in-plane field. It turns out, however, that also the $L(B_\perp)$-dependence changes dramatically when a tranverse in-plane fields is applied. A linear dependence of $L(B_\perp)$ at small $B_\perp$ reflects the fact, that each introduced vortex contributes a constant amount of inductance. Orbital effects of the field or interaction of single vortices are negligible in that pinning regime. While in zero in-plane field (Fig. 6.7) linearity for small out-of-plane fields could be shown the situation strongly changes when an in-plane field is

applied.

Fig. 6.14 shows $L(B_\perp)$ for different transverse in-plane fields. For $B_t \leq 0.1\,\mathrm{T}$, $L(B_\perp)$ is more or less linear. At higher B_t, $L(B_\perp)$ increases super-linearly, but starting with a smaller slope as for small B_t. The measured data are not mirror symmetric with respect to $B_\perp = 0$. The absolute slope of $L(B_\perp)$ is higher for negative fields. This is probably related to hysteresis effects. $B_\perp$ was swept from negative to positive $B_\perp$ without heating procedure between each single $B_\perp$. $B_\perp$-sweeps, where a heating step was performed after each $B_\perp$, delivered symmetric results (not shown here).

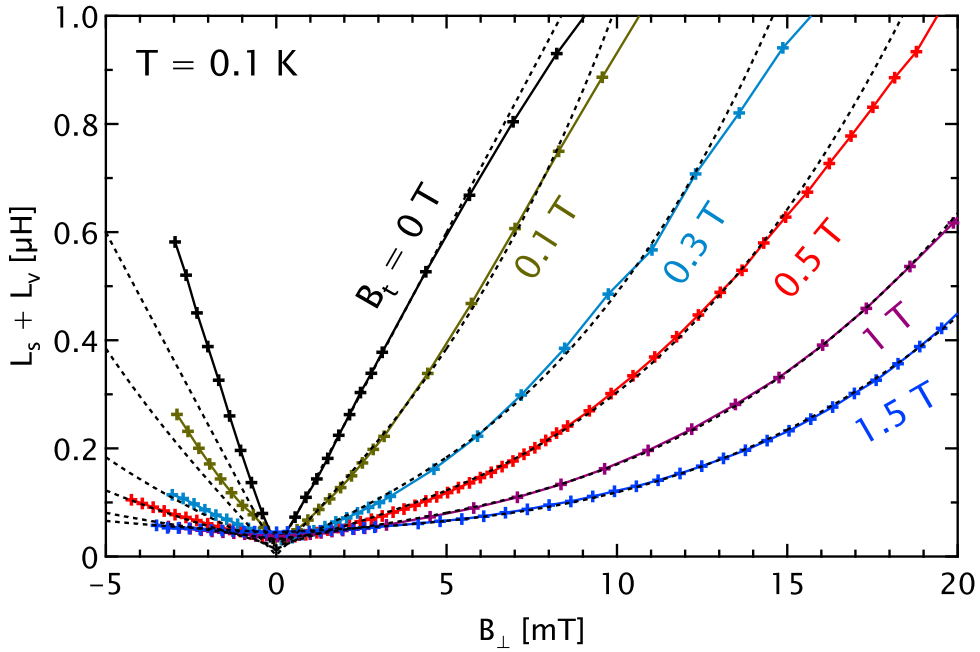

Fig. 6.14.: $L(B_\perp)$ for $B_t = 0, 0.1, 0.3, 0.5, 1, 1.5\,\mathrm{T}$. For $B_t \leq 0.1\,\mathrm{T}$, $L(B_\perp)$ is nearly linear. At higher B_t, $L(B_\perp)$ increases super-linearly, but starting with a smaller slope as for small $B_\parallel$. Dashed lines are fits to eq. 6.3.

The data are fitted to a phenomenological, polynomial function with constant, linear and cubic in $B_\perp$ terms

$$L(B_\perp) = a + b|B_\perp| + c|B_\perp|^3. \tag{6.3}$$

Parameter a represents the pure kinetic inductance L_s measured for $B_\perp = 0$. $b \propto \frac{1}{k_p}$ is a measure of the pinning constant as defined in eq. 2.30. c represents a cubic contribution to $L(B_\perp)$. For $B_t \geq 0.5\,\mathrm{T}$ the experimental $L(B_\perp)$ increases slower than the polynomial

in eq. 6.3. For $B_t = 1\,\mathrm{T}$ and $B_t = 1.5\,\mathrm{T}$ the curves can nicely be reproduced in the range $B_\perp \geq 20\,\mathrm{mT}$.

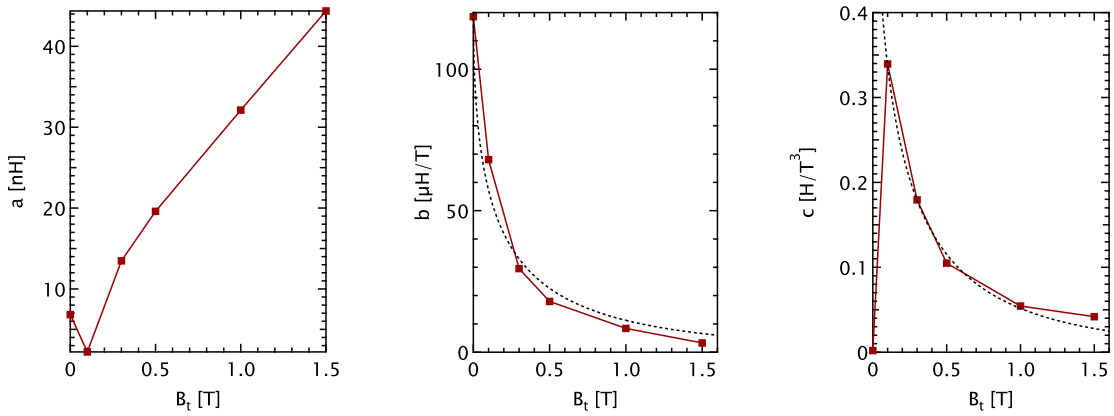

Fig. 6.15.: Fitting parameters of fits to eq. 6.3 of data shown in Fig. 6.14. Dashed lines represent phenomenological fit curves. The fit functions are described in the main text.

The free fitting parameters a, b, c are shown in Fig. 6.15. Because of the large fitting range in $B_\perp$ up to 20 mT, a is mainly determined by the extrapolation to $B_\perp = 0$ and therefore deviates from the measured $L(B_\perp = 0)$. b decreases with B_t and follows roughly a phenomenological, exponentially decreasing function

$$b = b_0 \exp\left(-\frac{B_t}{\tilde{B}_{t,b}}\right), \tag{6.4}$$

where $b_0 = 121\,\mu\mathrm{H/T}$ is the slope of $L(B_\perp)$ for small $B_\perp$ and a characteristic in-plane field $\tilde{B}_{\parallel,b} = 0.177\,\mathrm{T}$. Parameter c can be interpreted as a non-constant, quadratic-in-$B_\perp$ term of the pinning constant, which also decreases with $B_\parallel$. The curve follows roughly the same phenomenological function as 6.4

$$c = c_0 \exp\left(-\frac{B_t}{\tilde{B}_{t,c}}\right), \tag{6.5}$$

with $c_0 = 0.805\,\mathrm{H/T^3}$ and characteristic $\tilde{B}_{\parallel,c} = 0.133\,\mathrm{T}$. $c_(B_\parallel)$ The point at $B_\parallel = 0$ has been excluded from the fit range.

A crossover from slightly sub-linear to a super-linear behavior of $L_v(B_\perp)$ has been found in a transverse in-plane field. As a reference to Fig. 6.14, $L_v(B_\perp)$ measured in a parallel in-plane field is shown together with data measured in the transverse case in Fig. 6.16.

Data in this figure have been recorded in a separate cooldown different from the data shown in Fig. 6.14. Therefore absolute values in the two datasets for similar magnetic fields can slightly deviate.

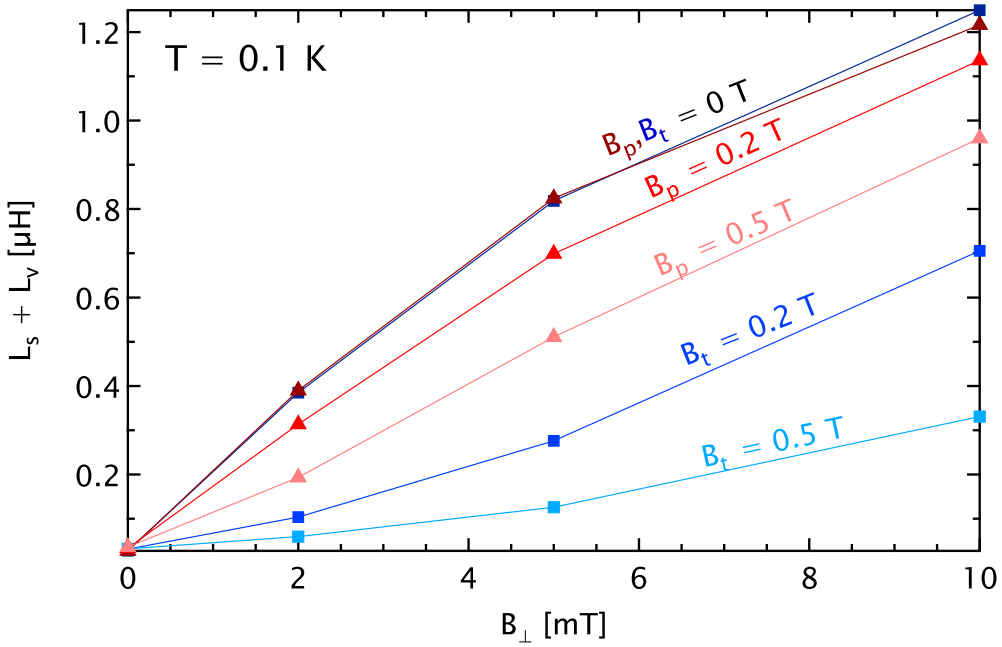

Fig. 6.16.: $L_v(B_\perp)$ for transverse (blue squares) and parallel (red triangles) in-plane fields of $0, 0.2, 0.5\,\mathrm{T}$.

$L(B_\perp)$ in zero in-plane field naturally coincide as time reversal symmetry is not broken for $B_\parallel = 0$. As already seen in Fig. 6.14, increasing the transverse in-plane field from zero to $B_t = 0.5\,\mathrm{T}$ changes the $L(B_\perp)$ dependence from (sub-)linear to superlinear (blue curve). Qualitatively similarly $L(B_\perp)$ in a parallel in-plane field (red curve) changes from (sub-)linear for $B_p = 0\,\mathrm{T}$ to linear for $B_p = 0.5\,\mathrm{T}$.

It was already seen in Fig. 6.9 and Fig. 6.10, that $L_v(B_t)$ decreases strongly with B_t for a fixed $B_\perp$. The crossover to a super-linear behavior of $L(B_\perp)$ for $B_t \geq 0.3\,\mathrm{T}$ is a strong indication towards a fundamental change of the vortex pinning mechanism caused by the in-plane field. For low vortex densities at small B_t all vortices produce on average the same amount of inductance reflected in a linear $L(B_\perp)$-dependence. At higher B_t, $L(B_\perp)$ becomes super-linear in $B_\perp$. For small $B_\perp$, vortices added to the system only contribute with a very small amount to the total inductance. Increasing the number of vortices with $B_\perp$ leads to an increasing average inductance contribution per vortex. This means, that there have to be defects with differently strong pinning potentials. Once

vortices are added to the system, defect sites with the strongest pinning are occupied first. As more vortices are created by increasing $B_\perp$, more shallower pinning potentials are filled. The vortices at weaker pinning sites then contribute with a larger inductance on average. The high-$B_\perp$-field regime is barely affected by the in-plane field (see section A.1.4 in the appendix).

Besides an effect that increases the pinning strength at individual pinning centers according to eq. 2.30, non-linearity of $L(B_\perp)$ in an in-plane field could be a consequence of the orbital effect of the perpendicular field. An out-of-plane field produces Meissner currents at the edges of the sample, which creates potential walls for vortices. Vortices would therefore accumulate at the center of the strip. This eventually could lead to non-linear contributions to the inductance. In-plane fields in Rashba superconductors can lead to additional in-plane anomalous screening currents that flow at the edges of the sample in one direction and return in the center of the strip [84]. Furthermore a spin texture, which rotates in the plane perpendicular to the sample plane when going from one edge to the other, is predicted [84]. The repulsion of vortices by the anomalous edge currents and the magnetic moments resulting from the out-of-plane spin texture could possibly lead to a crowding of vortices on one side of the strip. As a result, non-linearities in $L(B_\perp)$ could arise.

The question whether the non-linear $L(B_\perp)$ arises from supercurrents induced by the in- and out-of-plane fields or from non-linearities in $B_\perp$ of the individual pinning potentials as calculated in section 2.3.2 stays an open question. The exact mechanism responsible for this change of the $L(B_\perp)$-behavior in in-plane fields has still to be determined. The theory elaborated in eq. 2.75 section 2.3.2 captures the qualitative behavior, namely anisotropy and suppression of $L_v(B_t)$ and $L_v(B_p)$ measured in a fixed $B_\perp$ (Fig. 6.11). $L(B_\perp)$-data, however, indicate a polynomial $L(B_\perp)$-dependence with linear and cubic in $B_\perp$ terms for a tranverse in-plane field rather than a purely non-linear dependence as predicted by eq. 2.79. As the theory is based on a Ginzburg-Landau type of approach it should be only valid at the phase boundary, where Δ is small. This is the case for $B \to B_c$ or $T \to T_c$. Data shown in this chapter, however, are measured at low temperatures and low fields. However, the theory should also be at least qualitatively correct further away from the phase boundary. A more detailed, quantitative theory valid deep in the superconducting state, which also takes into account interaction of vortices and orbital effects, would be desirable.

7. Critical Currents and Non-Reciprocal Transport in Al/InAs

In systems with broken inversion symmetry magnetic fields perpendicular to the current direction can produce polarity dependent resistance [45]. External fields can also lead to critical currents that depend on their polarity [6][7][8]. A short introduction into the phenomenology of non-reciprocal transport was given in section 2.3.1. This chapter will shows results of critical current and 2^{nd}-harmonic resistance measurements performed on straight rectangular strips of Al/InAs. An increase of the vortex depinning current in in-plane fields perpendicular to the current directions is found. Furthermore it will be shown that in-plane and unexpectedly also out-of-plane fields lead to polarity dependent resistance and critical current. The role of the crystal direction on non-reciprocal tranport properties will be discussed.

Sample Al/InAs-S was fabricated by electron-beam-lithography and wet etching by Christian Baumgartner. An optical micrograph of the sample is shown in Fig. 7.1. It consists of three straight stripes parallel to different crystal axes ($[110], [1\bar{1}0], [100]$). The strips have a length of $200\,\mu$m and a width of $2.3\,\mu$m resulting in a total number of squares of ~ 87. The fabrication process consists of two lithography and etching steps (see section 3.1.3). In the first step bondpads, leads and 5 nominally equal straight strips are written for each of the three crystal directions. The unexposed areas are then etched deep into the substrate. From the 5 straight lines the one with the least defects is identified with scanning electron microscope. After a second lithography step the other 4 strips are etched away.

The current flow in most measurements is from I^+ to I^-, while the voltage drop across the wires in different crystal directions is measured differentially using the corresponding

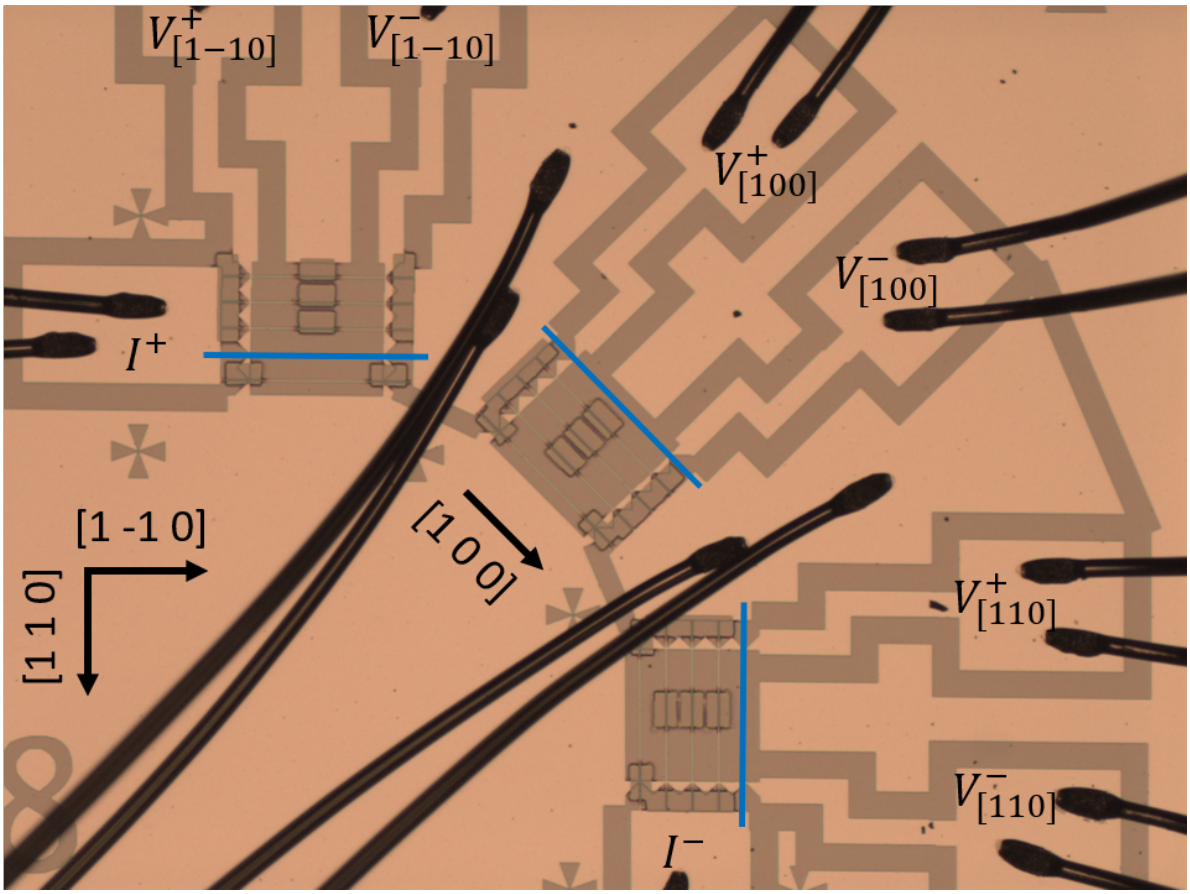

Fig. 7.1.: Optical micrograph of sample Al/InAs-S. Ocher parts are Al/InAs, in the greyish regions the sample was etched deeply into the insulating substrate. The large ocher areas are bondpads and leads for electrical contacts. The single straight sections are 2.3 μm broad and 200 μm long. There are three wires parallel to the different crystal directions [110], [1$\bar{1}$0], [100] indicated by blue lines. Black lines are bond wires attached to the sample. Annotation I and V in the bond pads indicate voltage and current electrodes for the different directions.

voltage contacts. It was shown that there is no mutual heating effects from one segment to the other at high currents. Being able to measure the transport properties of wires with a current flow in different crystal directions simultaneously, allows to efficiently investigate a possibly anisotropic character of the non-reciprocal transport properties.

7.1. Critical Current Measurements

7.1.1. Exemplary IV-Characteristics and Methodology

Inductance measurement on sample Al/InAs-M showed that the vortex pinning is strongly enhanced when an in-plane field perpendicular to the current is applied (see Fig.6.9). Another quantity which is strongly correlated to the vortex pinning is the depinning current, which is always lower than the depairing current and can be determined by fast DC measurements (see section 3.2.3). The depinning current describes the maximal current a superconductor in the vortex state can sustain before a finite resistance develops. The depinning current is reached once the Lorentz force produced by the driving current overcomes the maximal pinning force. The pinning force is proportional to the spatial derivative of the pinning potential. There is an importance difference in the interpretation of inductance and depairing current measurements in the vortex regime. While the inductance measurement is sensitive to the curvature at the bottom of the pinning potential, the depinning current measures the point of maximal slope of the potential. The two quantities are conceptually different and therefore cannot be identical.

Critical currents are determined from DC current-voltage-characteristics. A voltage in the sample is produced by applying fast DC current ramp pulses to one of the wires shown in Fig. 7.1. The voltage drop is amplified with a differential voltage amplifier. The resulting signal is measured with an oscilloscope.

Fig. 7.2 shows an example of the measured IV characteristics from which the critical currents I_c are extracted. For each $B_\perp$-value 50 IV traces are measured and averaged afterwards. As the voltage drop and the voltage applied to a preresistor that defines the current is measured with an oscilloscope, the resolution in both axes are limited which leads to substantial noise in the extracted I_c data. The current resolution is of the order of $6\,\mu$A, the voltage resolution of the order of 4 mV for a single trace. Averaging enhances the voltage resolution.

From IV-data, exemplary shown in Fig. 7.2, I_c is determined by using a threshold condition of $V_{th} \approx 10\,\text{mV}$. This means, I_c is defined as the current needed to produce an absolute voltage of at least V_{th}. I_c is therefore the first point in the IV-trace that lies above (or below if $V < 0$) the threshold voltage upon increasing the current in either direction. As the oscilloscope has only a resolution of 128 points for either positive and

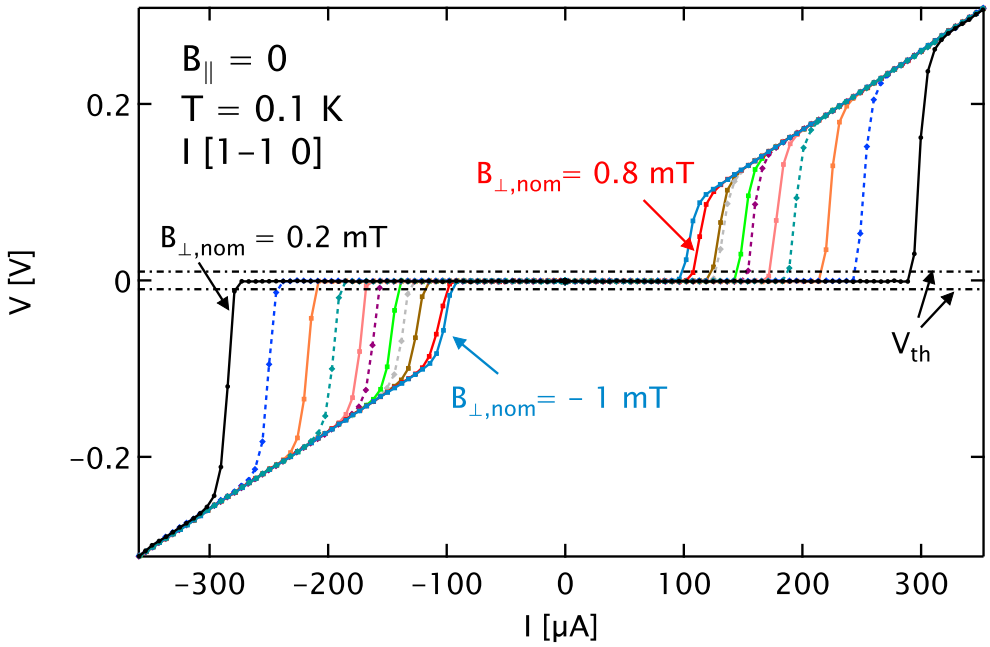

Fig. 7.2.: Exemplary IV characteristics at low temperatures for nominal out-of-plane fields $B_\perp$ ranging from $-1\,\mathrm{mT}$ to $0.8\,\mathrm{mT}$ in steps of $0.2\,\mathrm{mT}$ and $B_\parallel = 0$. The absolute minimum of $B_\perp$ is at a nominal field of $\sim 0.2\,\mathrm{mT}$. Dashed lines correspond to positive fields, solid lines represent negative fields. The horizontal dashed-dotted lines represent the threshold voltage $|V_{th}| = 10\,\mathrm{mV}$, which defines I_c.

negative voltage range of 1 V, only discrete voltage steps of $\sim 8\,\mathrm{mV}$ can be measured. Averaging slightly extends the resolution of measurable voltage values.

7.1.2. Enhancement of Depinning Current in In-Plane Magnetic Fields

In section 6.2.3 a strong decrease of the vortex inductance was observed in the presence of an in-plane field that was aligned perpendicular to the supercurrent direction. This was attributed to an increase of the pinning constant k_p, which is proportional to the curvature at the bottom of the pinning potential. In this section it will be shown that in the presence of an in-plane field not only the curvature of the pinning potential is increased, but also the maximal pinning force.

The maximal pinning force can be determined by the measurement of the critical current in the presence of an out-of-plane field. For that, IV-curves similar to those shown in Fig. 7.2 have been recorded by sweeping $B_\perp$. Additional in-plane fields were applied

perpendicular to the current to identify a possible enhancement of I_c with $B_\parallel$. From the measured IV-curves $I_c(B_\perp)$ is extracted by using the above mentioned threshold criterion.

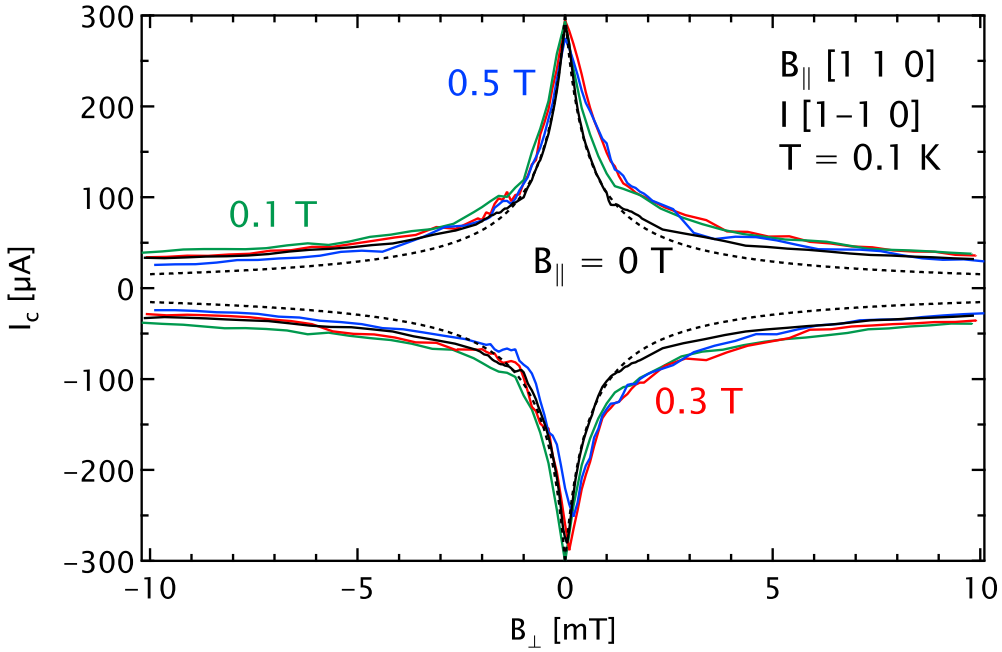

Fig. 7.3.: Positive and negative critical currents in the $[1\bar{1}0]$ direction as a function of $B_\perp$ for transverse in-plane fields $B_\parallel = 0(\text{black}), 0.1(\text{green}), 0.3(\text{red}), 0.5(\text{blue})\,\text{T}$. For $|B_\perp| \leq 1.2\,\text{mT}$ measured data follow the dashed line, which is a fit to eq. 7.2.

In Fig. 7.3 the critical current in the $[1\bar{1}0]$ direction is plotted as a function of perpendicular field for different in-plane fields at low temperatures. $B_\perp$ was swept from negative to positive values and at each point IV traces for both current directions have been performed succesively. Back and forth sweep showed small hysteresis effects (not shown here) that do not alter the qualitative outcome.

The critical current at low temperatures for a superconductor in the dirty limit can be calculated via [77]

$$I_{c0} = wd\frac{8\pi^2\sqrt{2\pi}}{21\zeta(3)e}\left(\frac{(k_B T_c)^3}{\hbar v_F \rho(\rho l)}\right)^{1/2}, \tag{7.1}$$

where w is the width of the sample and $v_F = 1.3 \times 10^6\,\text{m/s}$. With the parameters determined from DC transport measurements (see table 4.1) the expected critical pair-breaking current in zero magnetic field at low temperatures is $\sim 1\,\text{mA}$. Eq. 7.1 is valid

for bulk superconductors. The discrepancy between the theoretically expected and measured $I_{c0} \approx 300\,\mu$A of a factor of ~ 3 might be due to the 2D-character of the Al thin film. As was shown in Fig. 6.2 the superconducting transition is probably BKT-like. Maybe the existance of bound or pinned vortex-antivortex pairs, persistent up to low temperatures, are responsible for the suppression of I_c. In that case the transition to the normal state will not take place at the pair-breaking current, but at the current needed to dissociate or depin the vortex-antivortex pairs, which is always smaller then the depairing current.

For $B_\parallel = 0$, $I_c(B_\perp)$ decreases for $|B_\perp| \leq 1.2\,\mathrm{mT}$ following the empirical equation

$$I_c(B_\perp) = I_{c0}\left(1 + \frac{B_\perp}{\tilde{B}_\perp}\right)^{-1}, \tag{7.2}$$

with $I_{c0} = 302\,\mu$A and characteristic $\tilde{B}_\perp = 0.54\,\mathrm{mT}$. For $|B_\perp| > 1.2\,\mathrm{mT}$ the measured $I_c(B_\perp)$ decreases slower than eq. 7.2. For $B_\parallel > 0$, $I_c(B_\perp)$ for most $B_\perp$ is larger than in the case of zero in-plane field. This tells that the critical depinning current is increased when an in-plane field perpendicular to the current is applied.

To further illustrate the enhancement of $I_c(B_\perp)$ in an orthogonal in-plane field, Fig. 7.4 exemplarily shows the ratio of the depinning current measured for $B_\parallel = 0.1, 0.3\,\mathrm{T}$ and the one for $B_\parallel = 0$ at $B_\perp = 2\,\mathrm{mT}$. Points are calculated from the data shown in Fig. 7.3. For better visibility only the first quadrant is shown.

For $0.5\,\mathrm{mT} < B_\perp < 9\,\mathrm{mT}$ the depinning current is larger for $B_\parallel = 0.1\,\mathrm{T}$ and $0.3\,\mathrm{T}$. The maximal increase of $I_c(B_\perp)$ is of the order of 15% measured at $B_\perp \approx 2.5\,\mathrm{mT}$. For $B_\perp > 2.5\,\mathrm{mT}$ the relatice increase of the depinning current reduces more or less linearly. For $B_\parallel \geq 0.5\,\mathrm{T}$, $I_c(B_\perp = 2\,\mathrm{mT})$ is reduced again below the zero in-plane field I_c (see inset of Fig. 7.4).

Although the data are relatively noisy, a clear trend towards an increase of the depinning current for moderate in-plane fields $B_\parallel \leq 0.5\,\mathrm{T}$ perpendicular to the current can be observed. This indicates that not only the curvature at the bottom of the pinning potentials increase with $B_\parallel$ (see section 6.2.3), but also the maximal pinning force at a distance r_0 away from the center of the pinning potential. Whereas the vortex inductance $L_v(B_\parallel)$ decreases up to a transverse in-plane field of $B_\parallel = 2.5\,\mathrm{T}$, the maximal

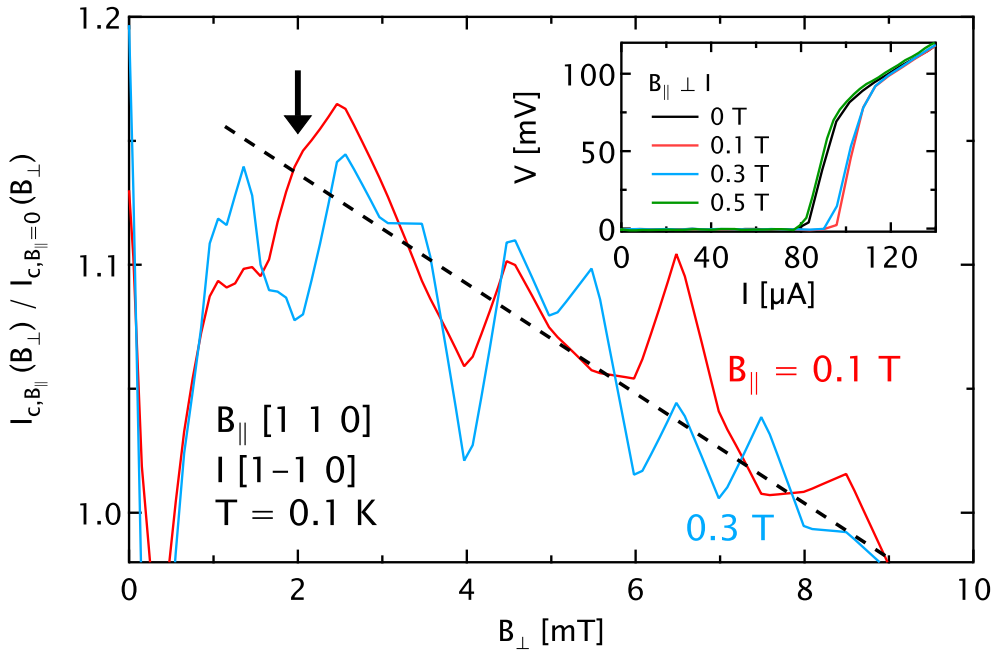

Fig. 7.4.: Critical currents $I_c(B_\perp)$ measured at $B_\parallel = 0.1\,\mathrm{T}$ (red curve) and $B_\parallel = 0.3\,\mathrm{T}$ (light blue curve) normalized with $I_{c,B_\parallel=0}(B_\perp)$ measured in zero in-plane field. Arrow indicates $B_\perp = 2\,\mathrm{mT}$. Dashed line is a guide to the eye indicating linear decrease for $B_\perp > 2\,\mathrm{mT}$ Inset: IV-characteristic at $B_\perp = 2\,\mathrm{mT}$ for in-plane fields of $0, 0.1, 0.3, 0.5\,\mathrm{T}$.

enhancement of the depinning current is already reached at $B_\parallel \approx 0.3\,\mathrm{T}$. The impact of the in-plane field on the curvature in the center of the pinning potential is therefore differently strong than the influence of $B_\parallel$ on the maximal slope of the pinning potential.

7.1.3. Anisotropic Vortex Pinning

So far it was shown, that moderate in-plane fields perpendicular to the current tend to increase the vortex depinning current. In this section the focus will be on the symmetry of the vortex pinning potential under the influence of a magnetic field. At first it will be demonstrated, that pure out-of-plane fields already produce a polarity dependent depinning current, which hints towards asymmetric pinning. This rectification of supercurrent is additionally enhanced by an in-plane field perpendicular to the current.

Fig. 7.5 shows $I_c(B_\perp)$ data measured for $B_\parallel = 0$ in the $[1\bar{1}0]$-direction of sample Al/InAs-S. The same data are used as in Fig. 7.3. The $B_\perp$-dependence of the critical current was already discussed in section 7.1.2. The upper two insets of Fig. 7.5 show small

differences of $|I_c^+|$ and $|I_c^-|$ for $|B_\perp| \leq 2\,\mathrm{mT}$. $|I_c^+|$ appears to be slightly larger than $|I_c^+|$ for most of the $B_\perp$-range. The curves are nearly point symmetrical with respect to the origin. This can be seen by mirroring $I_c^-(B_\perp)$ to $-I_c^-(-B_\perp)$ (lower left panel). After the mirroring, curves for $I_c^+(B_\perp)$ and $-I_c^-(-B_\perp)$ almost coincide.

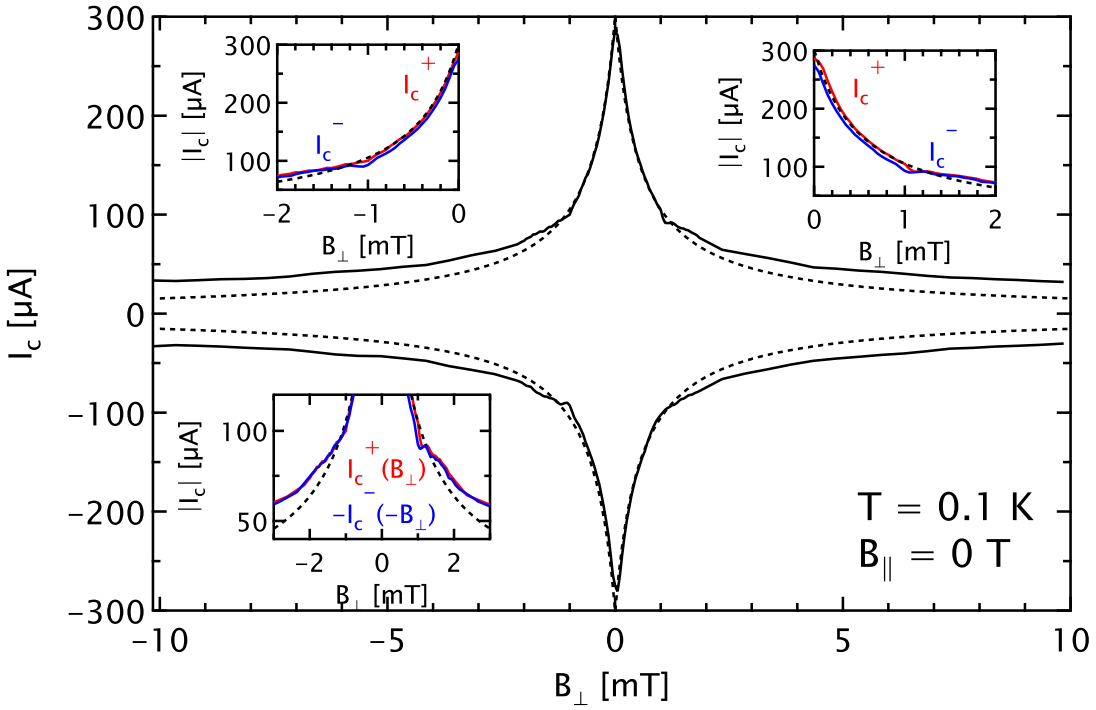

Fig. 7.5.: Main panel: $I_c(B_\perp)$ for $B_\parallel = 0$ at low temperatures. The shown data are the same as in Fig. 7.3. I_c^+ is the critical current measured in the positive direction, I_c^- the one in negative direction. Dashed line is a phenomological fit to eq. 7.2. In the insets I_c^+ is shown in red, I_c^- in blue. Upper insets show zooms into the region of $|B_\perp| \leq 2\,\mathrm{mT}$. In the two upper insets I_c^- has been mirrored to the upper two quadrants for better comparison. Lower left inset shows I_c^+ together with I_c^-, which was point mirrored at the origin.

The measured data shown in Fig. 7.5 look quite similar to results from critical current measurements performed on a superconducting strip with artificial pinning centers (Fig. 7.6) by Yu et al. [85]. In this work polarity dependent depinning currents were measured, which are the consequence of a structural anisotropy. Their sample consists of a two-layer superconductor, where in the upper layer sawtooth-shaped channels perpendicular to the current direction have been etched away. By that, they have created an anisotropic pinning potential in the direction of vortex motion. The differences of $|I_c^+|$ and $|I_c^-|$ measured in the present thesis are much less pronounced compared to [85].

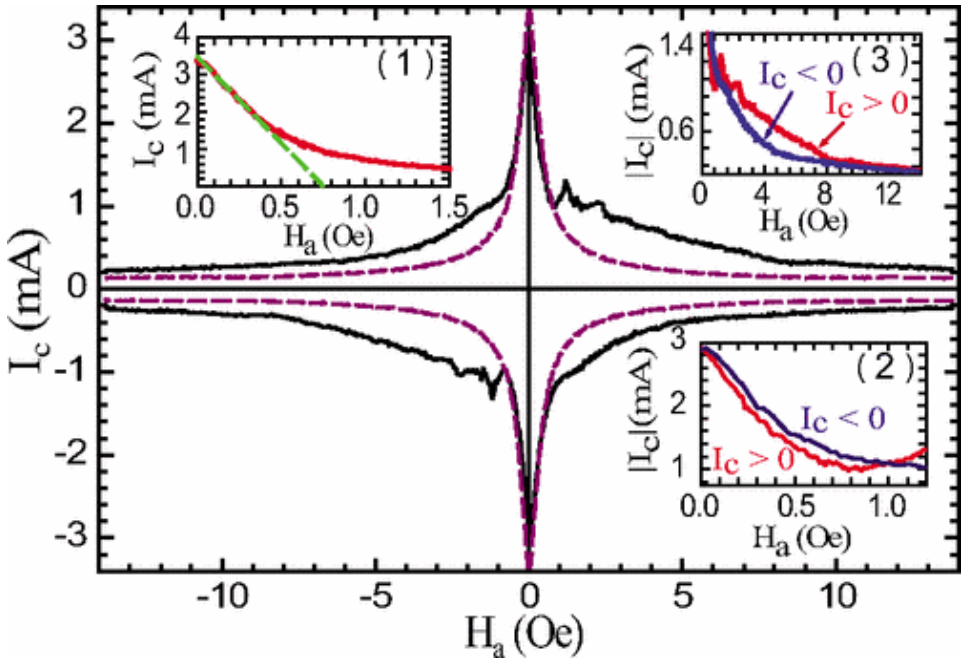

Fig. 7.6.: Main panel: $I_c(B_\perp)$ measured in a superconducting strip with artificial, asymmetric pinning potentials. The curves are point symmetric with respect to the origin. Upper left inset shows a zoom in the low field region of $I_c(B_\perp)$. The two right insets show absolute values of critical currents of both polarities in the 2^{nd} and 3^{rd} quadrant of the main panel. Picture taken from [85].

For better visibility of a polarity-dependent critical current, $\Delta I_c = |I_c^+| - |I_c^-|$ as well as the relative difference defined as

$$\delta I_c = \frac{|I_c{}^+| - |I_c{}^-|}{\frac{1}{2}(|I_c{}^+| + |I_c{}^-|)} \tag{7.3}$$

can be investigated. Data are shown in Fig. 7.7.

The curve seems to be shifted by roughly 1.1 μA to positive ΔI_c indicated by the dashed line. This shift is very likely due to an offset of the zero current line measured by the oscilloscope. The current resolution of this measurement is of the order of $\Delta I = \frac{10\,\mathrm{V}}{26.7\,\mathrm{k\Omega}} = 2.9\,\mu\mathrm{A}$. A constant offset c when subtracting the absolute value of two functions $f_+(x) = |g_1(x) + c|$ and $f_-(x) = |g_2(x) + c|$ can lead to a constant offset in $\Delta f(x)$. For example for $|g_2(x)| > c$ the difference $\Delta f(x)$ is

$$\Delta f(x) = |g_1(x)+c| - |-g_2(x)+c| = g_1(x)+c-(g_2(x)-c) = (g_1(x)-g_2(x))+2c. \tag{7.4}$$

A small offset of the order of μA therefore can be expected considering the given current resolution. In the calculation of $\delta I_c(B_\perp)$, shown on the right side of Fig. 7.7, this offset was subtracted from ΔI_c beforehand. In the following characteristics of $\Delta I_c(B_\perp)$ are therefore to be understood relative to the dashed line, shifted by 1.1 μA with respect to $\Delta I_c = 0$.

Although $\Delta I_c(B_\perp)$ is relatively noisy a basic trend of $\Delta I_c(B_\perp)$ can be observed. In an out-of-plane field regime of $|B_\perp| \lesssim 3\,\mathrm{mT}$, the sign of ΔI_c depends on the sign of $B_\perp$. For $|B_\perp| \lesssim 1\,\mathrm{mT}$, $\Delta I_c(B_\perp)$ increases with $|B_\perp|$. At higher $|B_\perp|$ $\Delta I_c(B_\perp)$ decreases again and becomes unmeasurably small for $|B_\perp| > 3\,\mathrm{mT}$. The maximum of relative anisotropy $\delta I_c(B_\perp)$ is of the order of 5% at $B_\perp \approx 1.1\,\mathrm{mT}$.

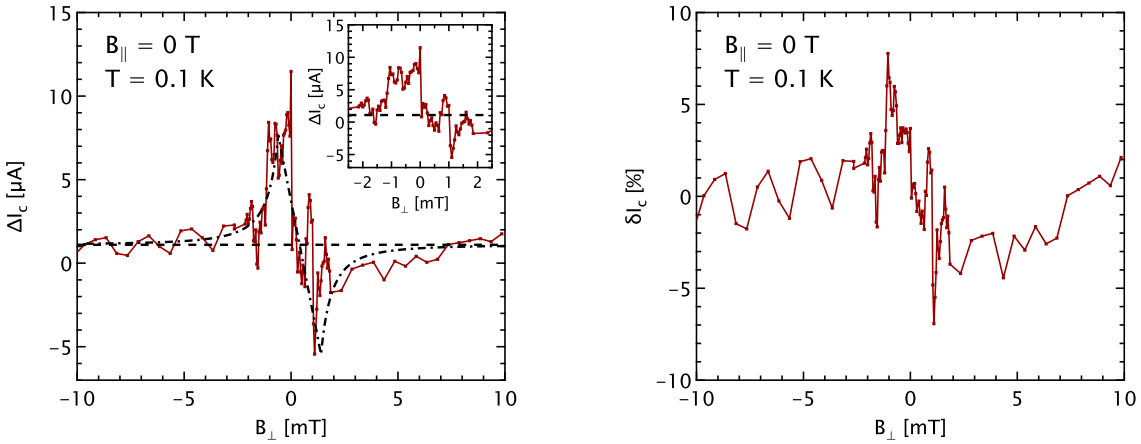

Fig. 7.7.: Left: ΔI_c as a function of $B_\perp$ for $B_\parallel = 0$ at $T = 0.1\,\mathrm{K}$ calculated from the data shown in Fig. 7.5. The dashed line indicates a systematic offset. The dashed dottet line is a guide to the eye. Inset shows a zoom in the low field region $|B_\perp| \leq 2.5\,\mathrm{mT}$. Right: Relative anisotropy $\delta I_c = \frac{|I_c{}^+|-|I_c{}^-|}{\frac{1}{2}(|I_c{}^+|+|I_c{}^-|)}$ as a function of $B_\perp$.

This measurement shows that for small $B_\perp$ the critical current depends on its polarity. This indicates an asymmetric pinning potential. The exact origin for this asymmetry is however unclear. Possibly, spin-orbit fields arise at the Al/InAs interface due to the symmetry breaking of the crystal lattice (see Fig. 3.2). While the InAs (001)-plane is has a cubic unit cell, the Al on top grows in [111]-direction, which has a trigonal structure. This mismatch breaks inversion symmetry at the inferface and hence could probably lead to a spin-orbit field pointing in the out-of-plane direction. Application of $B_\perp$ would then lead to a Zeeman splitting, besides introducing vortices. In trigonal systems such out-of-plane spin textures have already been demonstrated by measuring a polarity dependent resistance in the fluctuation regime of the transition [68][86]. Perhaps

there is an out-of-plane analog to the case of the supercurrent rectification in Rashba superconductors in in-plane magnetic fields [7][8], which arises from the interplay of $B_\parallel$ and the in-plane Rashba fields. For spin-textures that point out-of-plane probably the same mechanism could take place in out-of-plane fields leading to a polaritiy dependent depairing current, which in return affects the vortex depinning current. As will be seen later, measurements performed in the fluctation regime of sample Al/InAs-S indeed show a non-reciprocal resistance in the presence of an out-of-plane field pointing towards an out-of-plane spin component (see section 7.2.2). This hypothesis is affirmed additionally by the fact that a polarity-dependent critical current was also measured at low temperatures in a Josephson junction array produced from the same material (see section A.3.3). In that case, the critical current is not limited by vortex depinning, but by the critical current of the Josephson junction. This shows, that the polarity dependence of the critical current must be, at least partly, a direct consequence of the interplay between $B_\perp$ and the spin-orbit fields of the superconductor. A theoretical analysis of a possible out-of-plane spin-texture at the interface would be desirable at this point.

So far asymmetry of the pinning potential was shown in presence of $B_\perp$ only. Now the impact of an additional in-plane field on the polarity dependence of the critical current should be discussed. From the $I_c(B_\perp)$ at finite in-plane fields perpendicular to the current shown in Fig. 7.3, ΔI_c is calculated. The results are shown in Fig. 7.8.

The polarity of $\Delta I_c(B_\perp)$ clearly depends on the sign of $B_\parallel$ as curves for $B_\parallel = 0.5\,\mathrm{T}$ and $B_\parallel = -0.5\,\mathrm{T}$ show. There is an overall trend that ΔI_c increases with increasing $B_\parallel$. For $|B_\perp| \gtrsim 5\,\mathrm{mT}$ $\Delta I_c(B_\perp)$ is of the order of the noise level and a further interpretation therefore not sensible. A fluctuation pattern showing one main peak and two side peaks, somehow reminiscient of a Fraunhofer-like shape, can be observed. The peaks are indicated by numbers, (2) representing the main peaks, (1) and (3) the side-peaks. The absolute heights of peaks (1) are smaller than those of peaks (3). The peaks look point symmetric with respect to the origin. This becomes even more pronounced when $\Delta I_c(B_\perp)$ for positive $B_\parallel$ is plotted in a graph together with a point-mirrored version of $\Delta I_c(B_\perp)$ measured for negative $B_\parallel$ (lower left inset). After the mirroring, the curves strikingly overlap. Even small features, that look like noise on the first sight, are most likely real. The reason for this oscillation is an open question at the moment.

The maximal $\Delta I_c \approx 58\,\mu\mathrm{A}$ for $B_\parallel = 0.5\,\mathrm{T}$ is measured near $B_\perp = 0$. The relative asymmetry $\delta I_c(B_\perp)$ as defined as in eq. 7.3 reaches values of almost 40% for $|B_\parallel| = 0.5\,\mathrm{T}$

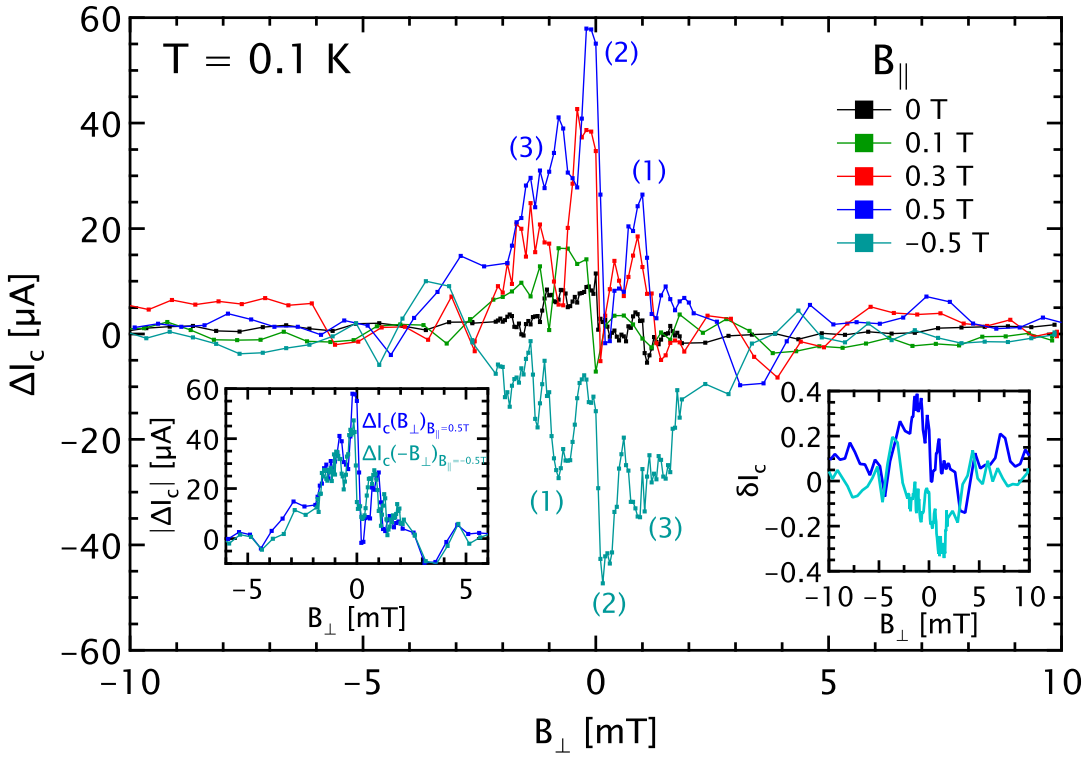

Fig. 7.8.: $\Delta I_c(B_\perp)$ calculated from $I_c(B_\perp)$ data shown in Fig. 7.3 for in-plane fields $B_\parallel = 0, 0.1, 0.3, 0.5, -0.5\,\mathrm{T}$ at low $T = 0.1\,\mathrm{K}$. $B_\perp$ is applied perpendicular to the current. Numbers indicate local maxima. Lower left inset shows $\Delta I_c(B_\perp)$ measured for $B_\parallel = 0.5\,\mathrm{T}$ and $B_\parallel = -0.5\,\mathrm{T}$, where the latter was mirrored at the origin. Lower right inset shows relative asymmetry $\delta I_c(B_\perp)$ as defined as in eq. 7.3 for $B_\parallel = \pm 0.5\,\mathrm{T}$.

(lower right inset) at $|B_\perp| \approx 1.4\,\mathrm{mT}$. For $B_\parallel > 0.5\,\mathrm{T}$ $\Delta I_c(B_\perp)$ becomes much noisier and are therefore not treated here.

This measurement shows that $\Delta I_c(B_\perp)$ not only depends on $B_\perp$ alone, but also even much stronger on $B_\parallel$. The presented data suggest a "8-octant"-problem resulting from presumably odd symmetries in I, $B_\perp$ and $B_\parallel$, which makes analysis challenging. For a more quantitative analysis, measurements with higher resolution in basically all involved quantities (V, I, $B_\perp$) would need to be carried out. A polarity dependent critical current for Rashba superconductors in presence of an in-plane field perpendicular to the current was described theoretically recently [7][8]. So far there is no theoretical work on the behavior of I_c in such systems in presence of an additional out-of-plane field. A more detailed theoretical description would be desirable. In order to investigate the behavior of $\Delta I_c(B_\parallel)$ without even a tiny out-of-plane field would require a dedicated measurement,

which is performed for $B_\perp = 0$ directly after the compensation procedure described in section 3.3.1 without sweeping $B_\perp$.

7.2. Field Induced Non-Reciprocal Transport in Fluctuation Regime

So far the behavior of the critical current at low temperatures in presence of external magnetic fields was investigated. Not only the critical current can become polarity dependent in magnetic fields, but also the resistance can become non-reciprocal in a regime where R is finite (see section 2.3.1). The origins of the two effects occurring at very different temperatures are presumeably closely related. It is the interplay of an in-plane field aligned parallel with the spin-orbit field that leads to the polarity dependent effects. The non-zero resistance can in zero field either result from thermally activated vortex motion (BKT-regime) or from an ohmic contribution (fluctuation regime). With non-zero $B_\perp$ also vortex motion can produce a resistance below T_c, if the current is large enough to depin the vortices.

Non-reciprocal transport effects in these regimes can elegantly be investigated by measuring the second harmonic resistance $R_{2\omega}$ produced by an AC excitation current $I_{AC} \propto \sin(\omega t)$. In symmetric systems the second harmonic is zero, whereas in systems with broken time- and inversion symmetry the signal can become non-zero. The strength of non-reciprocity can then be characterized by the parameter $\gamma_s = \frac{2R_{2\omega}}{R_\omega BI}$ (see eq. 2.48). There have been a large number of publications in which non-reciprocal transport in external magnetic fields in the above mentioned regimes have been demonstrated [6][48][86][87][88][89].
In the Al/InAs heterostructure inversion symmetry is broken in the [001]-direction, which results in a Rashba SOC (see section 2.3.1). An in-plane field in that case should lead to a polarity dependent resistance in the BKT- and fluctuation regime. This effect will be shown to be present in sample Al/InAs-S in the first part of this section.
In section 7.1.3 an indication towards a $B_\perp$-dependent ΔI_c in zero in-plane field was found. As the polarity-dependent critical current and the non-reciprocal resistance seem to be closely related it is intuitive to investigate the impact of a solely out-of-plane field on the 2^{nd}-harmonic response in the BKT- and fluctuation regime. In the second part it will be shown that a small $B_\perp$ indeed leads to a even larger γ_s as in the in-plane field case.

In the third part of this section 2^{nd}-harmonic measurements in combined in- and out-of-plane fields will be discussed.
Temperature dependence of γ_s is discussed at the end of the section. Important experimental details are described in sections 3.3.1 and 3.3.2. Although in most cases not shown in the following, for each $R_{2\omega}(T)$ also a $R_{\omega}(T)$-curve was recorded in the same temperature sweep.

7.2.1. Non-Reciprocal Resistance in In-Plane Fields

First behavior of first (R_{ω}) and second ($R_{2\omega}$) harmonic resistance in the presence of an in-plane field perpendicular to the current directions will be investigated. An in-plane field perpendicular to the current leads to a significant 2ω-resistance signal in an $R(T)$-measurement. Fig. 7.9 shows a typical measurement of the temperature dependence of the first and second harmonic resistance for different current and in-plane field directions (see Fig. 7.1 for current directions). The applied AC current was $I = 500\,\mathrm{nA}$.
For $B_{\parallel} = 0$ (black curves) there is barely any $R_{2\omega}$-signal. Only a some small oscillation can be found for $1.465\,\mathrm{K} < T < 1.48\,\mathrm{K}$ in the regime where $R_{\omega}(T)$ decreases strongly.
In the case where a moderate in-plane field $B_{\parallel} = 0.3\,\mathrm{T}$ is applied perpendicular to the current (red curves) a strong positive $R_{2\omega}$-signal with a peak value of $R_{2\omega,max} = 2.5\,\Omega$ at $T \approx 1.454\,\mathrm{K}$ is found in the range $1.445\,\mathrm{K} < T < 1.465\,\mathrm{K}$. At lower temperatures a negative signal can be observed at $T \approx 1.435\,\mathrm{K}$.
When $B_{\parallel} = 0.3\,\mathrm{T}$ is applied parallel to the current (blue curve) only a small $R_{2\omega}$-signal is measured in the fluctuation regime for $1.45\,\mathrm{K} < T < 1.465\,\mathrm{K}$.

The absolute values of R_{ω} in the normal state for $T > 1.5\,\mathrm{K}$ differ for the shown curves, because they have been measured in several cooldowns with different contact configurations. This figure, however, should only qualitatively show the basic aspects of the experiment and therefore small discrepancies in the absolute values are not important.

It can be seen that only in the case where $B_{\parallel} \perp I$ a significant $R_{2\omega}$ can be measured in the temperature range where $R_{\omega}(T)$ decreases strongly with decreasing temperature. For $B_{\parallel} \parallel I$ and $B_{\parallel} = 0$ only small oscillations can be measured. They are most probably artifacts from not perfectly compensated DC offset currents (see 3.3.2) or out-of-plane fields. As will be seen later, even very small $B_{\perp}$ also produce a strong $R_{2\omega}$ signal. Although great care has been taken to compensate possible offsets of either DC current or $B_{\perp}$, it was never possible to measure absolutely no $R_{2\omega}$ even for $B_{\parallel} = 0$.

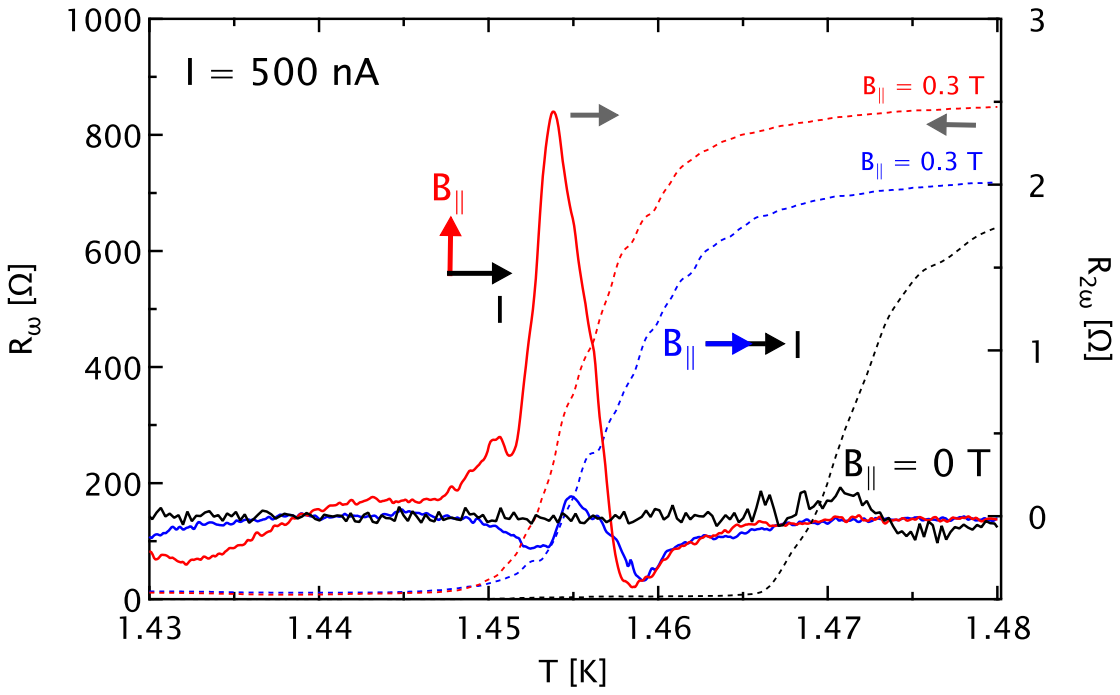

Fig. 7.9.: $R_\omega(T)$ and $R_{2\omega}(T)$ measured for different current and field directions. The applied AC current was 500 nA at a frequency of 117 Hz. Dashed lines represent $R_\omega(T)$, solid lines $R_{2\omega}(T)$. Grey arrows indicate the corresponding y-axes. Black curves have been measured with a current in the $[1\bar{1}0]$-direction in zero in-plane field. Red curves have been recorded with current in the $[1\bar{1}0]$-direction in a field $B_\parallel = 0.3\,\mathrm{T}$ perpendicular to the current. Blue curves have been measured with current in the [110]-direction in a field $B_\parallel = 0.3\,\mathrm{T}$ parallel to the current.

The strong $R_{2\omega}$-signal for $B_\parallel \perp I$ is expected as non-reciprocal transport in Rashba superconductors should only appear when the in-plane field is parallel to the Rashba spin-orbit field [45]. At the temperature where $R_{2\omega}(T)$ is maximal, the linear resistance R_ω is roughly a quarter of the normal state resistance.

In the following the change of $R_{2\omega}(T)$ with varying in-plane fields will be discussed. Fig. 7.10 shows $R_{2\omega}$ as a function of temperature for different in-plane fields perpendicular to the $[1\bar{1}0]$ current direction. For better clarity, $R_\omega(T)$-data are not shown in this graph. The graph shows that the sign of $R_{2\omega}(T)$ depends on the direction of $B_\parallel$. For each field two distinct peaks can be found. With increasing $|B_\parallel|$ peaks are shifted to lower temperatures due to the depression of T_c caused by orbital pair breaking. The largest $R_{2\omega}$ is found for $B_\parallel = 0.3\,\mathrm{T}$. The maximal $R_{2\omega}$ decreases with $|B_\parallel|$ and the width of the $R_{2\omega}(T)$-peaks, especially the one at lower temperatures, broadens in higher fields. For

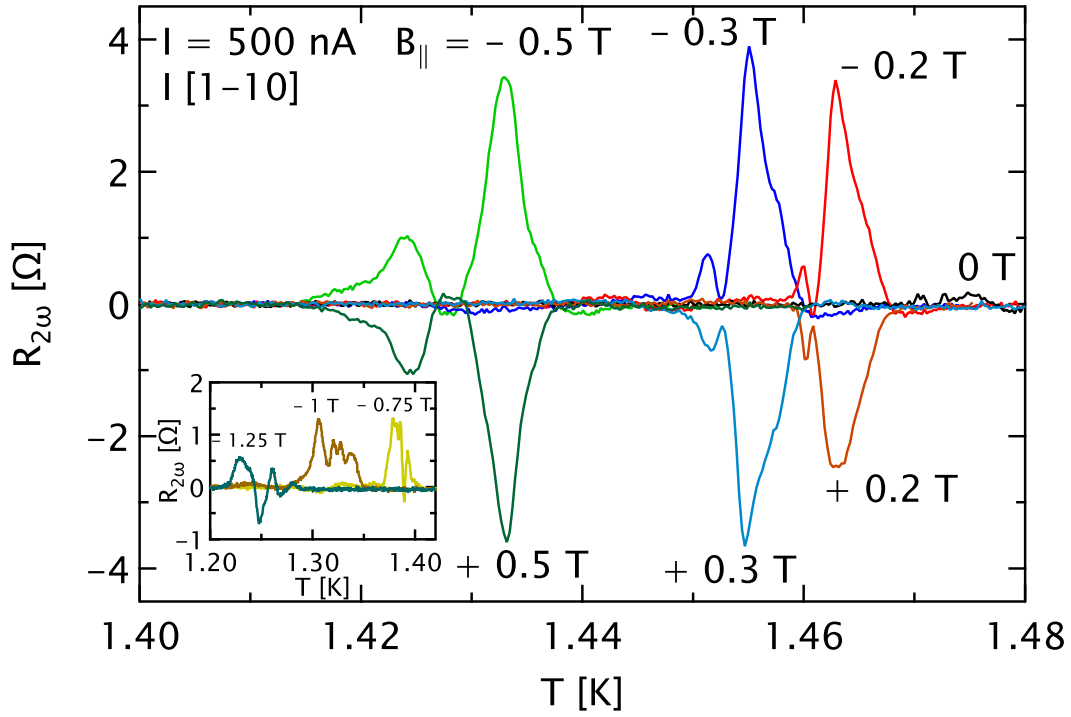

Fig. 7.10.: $R_{2\omega}(T)$ for the $[1\bar{1}0]$ current direction for $B_{\parallel} = -0.5, -0.3, -0.2, 0, 0.2, 0.3, 0.5\,\mathrm{T}$. The in-plane field is perpendicular to the applied AC current $I = 500\,\mathrm{nA}$. Inset shows data measured at $B_{\parallel} = -0.75, -1, -1.25\,\mathrm{T}$

$|B_{\parallel}| > 0.5\,\mathrm{T}$ the signal becomes very irregular (inset of Fig. 7.10).

The characteristics of the non-reciprocal resistance resulting from the interplay of magnetic and spin-orbit field presented here are very similar to the result reported in different systems [6][48][86][87][88][89]. In the given literature it was shown, that $R_{2\omega}$ is only linear for a certain magnetic field range, and reduces for higher fields as it is the case in the present sample, too. The origin of a second peak in the fluctuation regime is still unclear so far. As will be seen later, linearity or $R_{2\omega}$ in I in sample Al/InAs-S is in fact only given up to a current of 100 nA (see 7.2.2). $R_{2\omega}(T)$ measurements in pure in-plane and combined in- and out-of-plane fields unfortunately were only carried out with a current of 500 nA The principle characteristics, nonetheless should be meaningful from the presented data at higher currents.

From the maxima of the $R_{2\omega}(T)$ curves shown in Fig. 7.10 and the corresponding R_{ω}, $\gamma_s = \frac{2R_{2\omega,max}}{R_{\omega}BI}$ can be calculated for the different in-plane fields. Fig. 7.11 shows γ_s as a

function of $B_\parallel$.

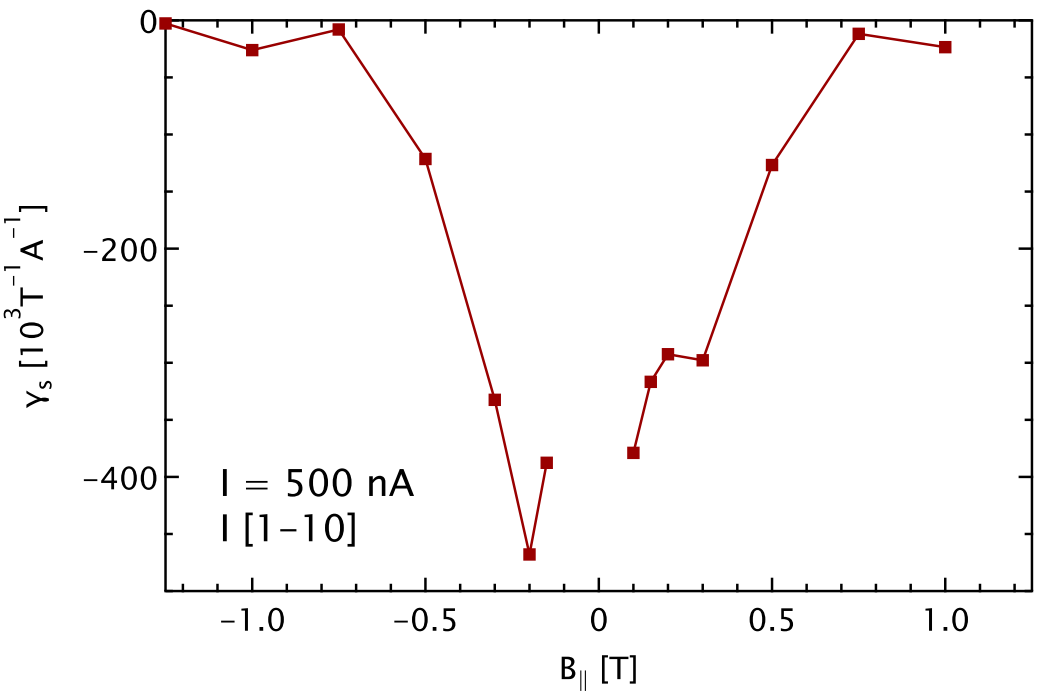

Fig. 7.11.: γ_s calculated from data shown in Fig. 7.10 as a function of in-plane field.

γ_s is maximal for small $|B_\parallel| \approx 0.1 - 0.2\,\mathrm{T}$. The maximum is of the order of $4.5 \times 10^5\,\mathrm{T^{-1}A^{-1}}$. Normalized with respect to the width $w = 2.3\,\mu\mathrm{m}$ of the superconducting strip this gives $w\gamma_s \sim 1\,\mathrm{T^{-1}A^{-1}m}$, which is comparable to other materials ($0.05\,\mathrm{T^{-1}A^{-1}m}$ in [6], $80\,\mathrm{T^{-1}A^{-1}m}$ in [88]). For $B_\parallel > 0.3\,\mathrm{T}$ γ_s decreases very fast.

7.2.2. Non-Reciprocal Vortex Resistance or Unexpected Spin Texture?

Not unexpectedly non-reciprocal transport in the fluctuation regime in sample Al/InAs-S could be measured in the presence of an in-plane field perpendicular to the current direction. This is in accordance with the observation of a polarity dependent critical current at low temperatures in the same field configuration as these two effects probably have the same origin. At low temperatures it was shown that also in pure out-of-plane fields a slightly polarity dependent critical could be measured (see Fig. 7.7). This raises the question if at higher temperatures a non-reciprocal resistance could be also be measured in solely out-of-plane fields.

Similar kind of 2nd-harmonic resistance measurements as in the in-plane field case (see previous section) were performed in small out-of-plane fields for different current directions. An exemplary graph for $R_{2\omega}(T)$ as a function of temperature is shown in Fig. 7.12. Not all measured fields are shown in the graph. The field scales of $B_\perp$, on which non-reciprocal transport can be observed, are of the order of 0.1 mT. This is much less as compared to the in-plane field case (typical field scale $B_\parallel \sim 0.1\,\mathrm{T}$). Again the polarity of $R_{2\omega}(T)$ depends on the sign of $B_\perp$. The peaks of $R_{2\omega}(T)$ are highest for $B_\perp \approx 0.2 - 0.3\,\mathrm{mT}$. The temperature, where $R_{2\omega}(T)$ peaks is shifted to lower temperatures with increasing field due to a slight suppression of T_c. For $B_\perp = 0$ (black curve) almost no signal can be measured. For $B_\perp = \pm 0.5\,\mathrm{mT}$ there is a sign change at $T \approx 1.465\,\mathrm{K}$ (black arrow).

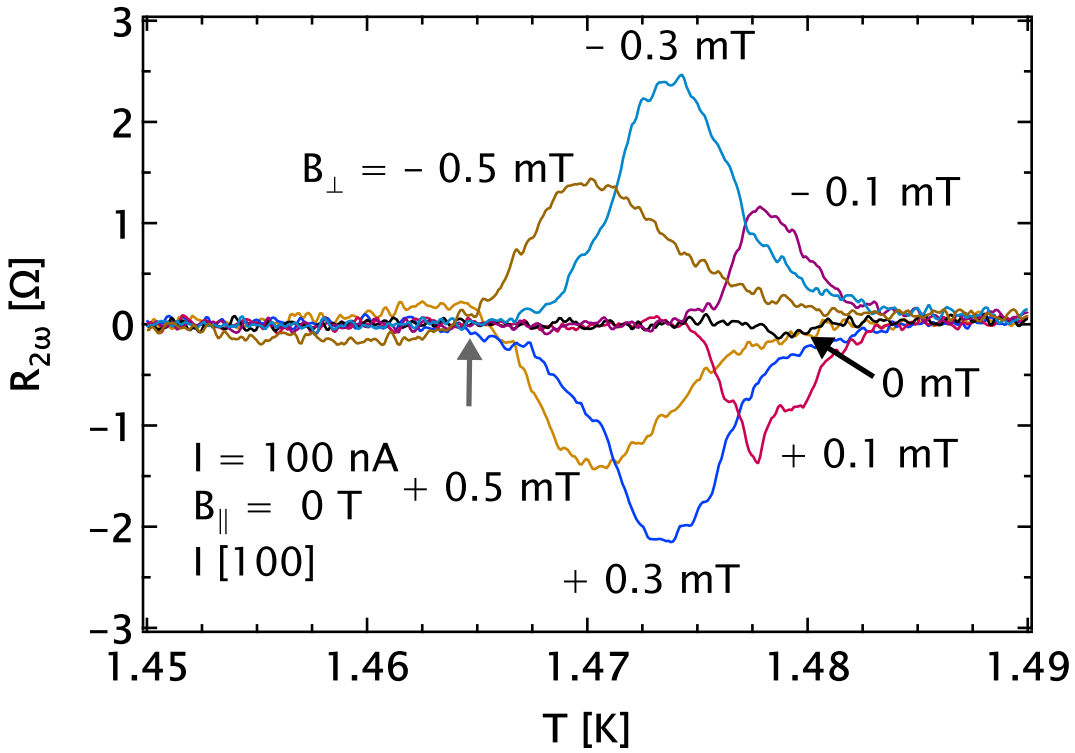

Fig. 7.12.: $R_{2\omega}(T)$ measured in the [100]-direction and a current of 100 nA for $B_\perp = -0.5, -0.3, -0.1, 0, 0.1, 0.3, 0.5\,\mathrm{mT}$. Grey arrow indicates a sign change for $B_\perp = \pm 0.5\,\mathrm{mT}$.

This measurement shows that qualitatively the same characteristic $R_{2\omega}(T)$ can be measured if instead of an in-plane field (Fig. 7.10) an out-of-plane field is applied perpendicular to the current. The field scale, however, is reduced by roughly a factor of 1000. A

non-reciprocal signal in the fluctuation regime of a Rashba superconductor is, however, only expected for in-plane fields perpendicular to the current as the Rashba spin-orbit fields are in-plane [45]. In TMD structures, where the spin-orbit field point out-of-plane, a polarity dependent resistance is expected in the presence of $B_\perp$. It is in principle based on the same mechanism as for Rashba superconductors in an in-plane field. The relevant ingredient is a Zeeman term in the Hamiltonian. The observation of a sizeable $R_{2\omega}(T)$ in an out-of-plane field therefore suggests an unexpected out-of-plane spin texture in the Al/InAs heterostructure.

In Fig. 7.12 it is shown that $R_{2\omega,max}(B_\perp)$ has a maximum for $B_\perp \approx 0.2 - 0.3\,\mathrm{mT}$. In order to check for linearity in $B_\perp$ and I, $R_{2\omega}(T)$-curves for various out-of-plane fields, currents and crystal directions were measured. From all these curves $R_{2\omega,max}$ have been extracted. At first linearity of $R_{2\omega,max}(I)$ as a function of current will be investigated.

Exemplarily for all three investigated crystal directions, Fig. 7.13 shows $R_{2\omega,max}(B_\perp)$ as a function of out-of-plane field for different AC currents, which are extracted from corresponding $R_{2\omega}(T)$-curves similar to Fig. 7.12. Data are shown for the $[1\bar{1}0]$-direction.

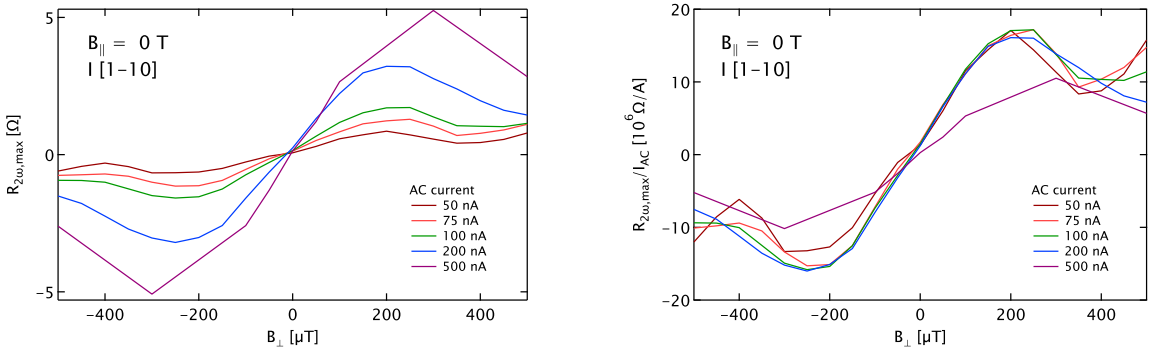

Fig. 7.13.: Left: $R_{2\omega,max}(B_\perp)$ for AC driving currents of $50, 75, 100, 200, 500\,\mathrm{nA}$ in the $[1\bar{1}0]$-direction. Right: same data normalized with the driving current. Up to a current of $200\,\mathrm{nA}$ and $|B_\perp| \leq 200\,\mu\mathrm{T}$ all data lie on a single curve.

Left side of Fig. 7.13 shows linearity of $R_{2\omega,max}(B_\perp)$ for $B_\perp \leq 200\,\mu\mathrm{T}$. Plotting the same data but normalized with the driving current gives information about the linearity of $R_{2\omega,max}$ as a function of I (right side in Fig. 7.13). The different $R_{2\omega,max}(B_\perp)$ collapse to a single curves for $I \leq 200\,\mathrm{nA}$, indicating linearity in this current regime. The same range of linearity in I is found for the other two current directions (not shown here).

For $I > 200\,\mathrm{nA}$ $R_{2\omega,max}$ slightly decreases again.

In the linear current range the influence of the current direction on $R_{2\omega,max}(B_\perp)$ is of peculiar interest as it might give information about the possible out-of-plane spin-orbit field texture in different current (momentum) directions. Fig. 7.14 shows the out-of-plane field dependence of $R_{2\omega,max}(B_\perp)$ for the three different current directions at a current of 100 nA.

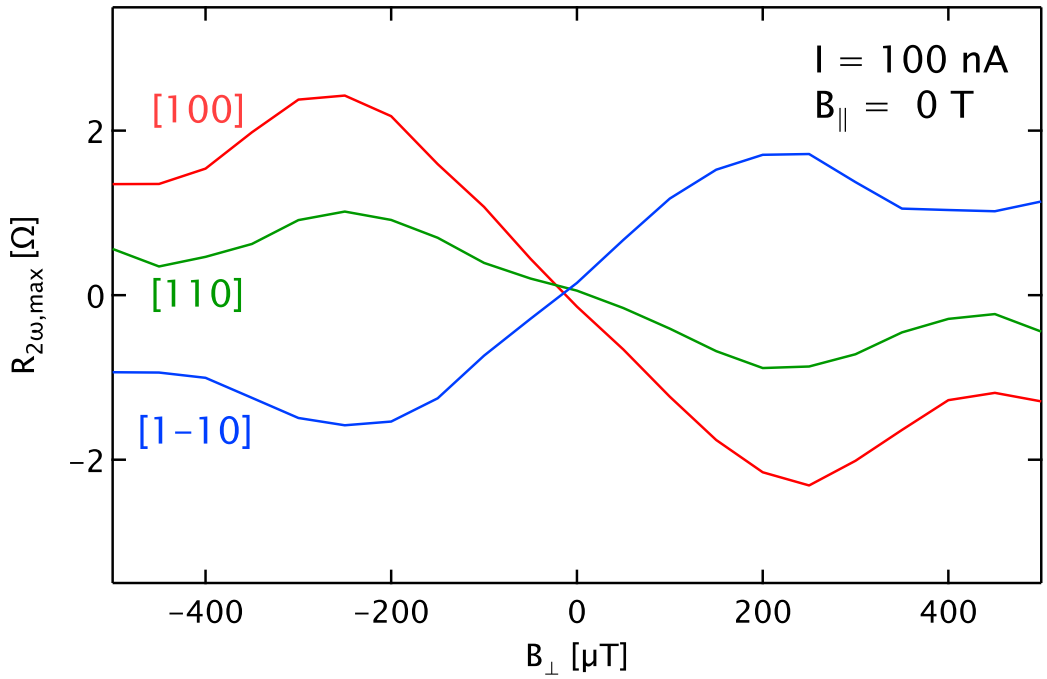

Fig. 7.14.: $R_{2\omega,max}$ as a function of $B_\perp$ for the three investigated current directions and a driving current of 100 nA. Current directions are drawn and labeled with different colors. The signal is linear for out-of-plane fields up to 200 μT in all three directions.

Linearity in $B_\perp$ is given in all three directions up to a field of about 200 μT. At higher fields $R_{2\omega,max}(B_\perp)$ slightly decreases again as it is also the case for currents larger than 200 nA. The curves are different regarding magnitude as well as sign. For the [110] (green) and [100] (red) current-direction $R_{2\omega,max}(B_\perp)$ is positive for negative $B_\perp$ and vice versa. The absolute slope of $R_{2\omega,max}(B_\perp)$ for $|B_\perp| \leq 0.2\,\mathrm{mT}$ is larger for [100] than for [110]. In $[1\bar{1}0]$-direction $R_{2\omega,max}(B_\perp)$ has the opposite with respect to the other directions. The absolute value of the slope for $|B_\perp \leq 0.2\,\mathrm{mT}$ in $[1\bar{1}0]$-direction is somewhere between the corresponding curves for [110] and [100].

Fig. 7.14 shows clearly that the non-reciprocity in presence of $B_\perp$ in the fluctuation regime depends on the current and hence on the momentum direction with respect to the crystal axes. This indicates an anisotropic out-of-plane spin-texture in the Al/InAs heterostructure. Measurements for many more current directions, however, did not yet show a clear systemics regarding the symmetry the anisotropy (see section A.3.2).

The absolute value of $R_{2\omega,max}(B_\perp)$ for small out-of-plane fields is quite comparable to the one measured in the in-plane field case (Fig. 7.10) but the field scale is roughly 3 orders of magnitude smaller. Assuming a similar mechanism responsible for a non-reciprocal resistance in small $B_\perp$ analog to the in-plane field case, $\gamma_s(R_{2\omega,max}) = \frac{2R_{2\omega,max}}{R_\omega B_\perp I}$ can be calculated. This is the same equation as eq. 2.48 with $B_\parallel$ being replaced by $B_\perp$. For this calculation also R_ω data, measured simultaneously with $R_{2\omega}(T)$, are used. $\gamma_s(R_{2\omega,max})$ as a function of $B_\perp$ for the 100-direction, where non-reciprocity is strongest, is shown in Fig. 7.15.

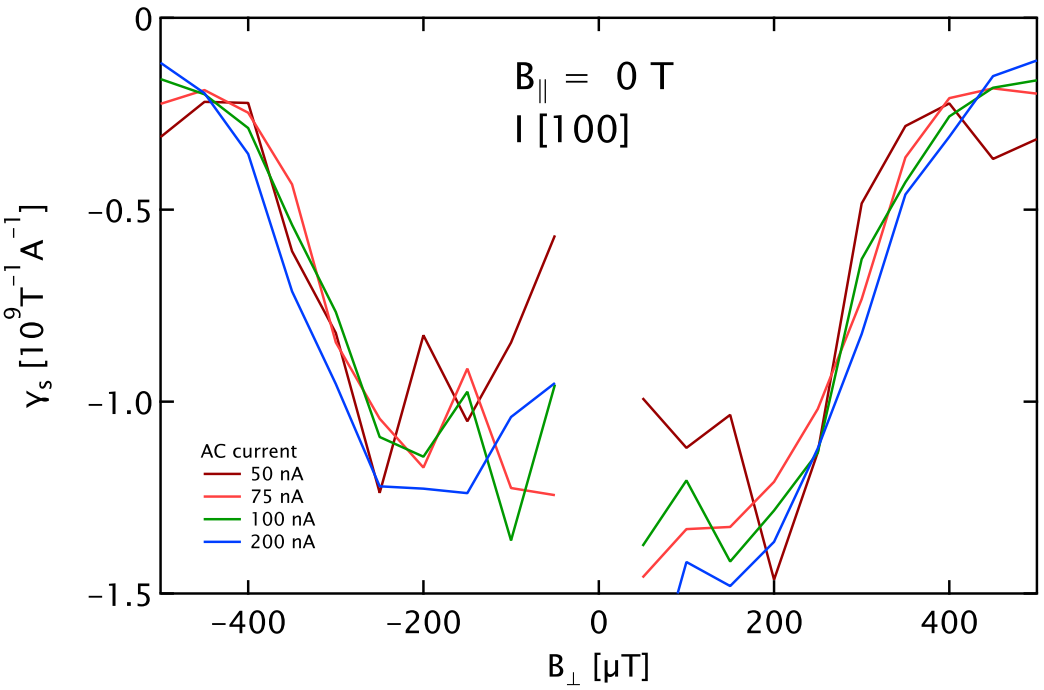

Fig. 7.15.: $\gamma_s(R_{2\omega,max})$ in the fluctuation regime as a function of $B_\perp$ for the [100] current direction and driving currents up to 200 nA. γ is nearly constant for small $B_\perp$ and breaks down for higher fields.

$\gamma_s(B_\perp)$ curves for the other current direction are quite similar. As can be already guessed from Fig. 7.14, $|\gamma_{s,max}|(B_\perp)$ is smaller for [100] and [1$\bar{1}$0] (curves not shown here). The maximum of $\gamma_s(B_\perp)$ is at a field of $0.15 - 0.2mT$ and reaches values as high as $|\gamma_{s,max}| \approx 1.5 \times 10^9\,\mathrm{T^{-1}A^{-1}}$ or normalized with the width $|w\gamma_{s,max}| \approx 3450\,\mathrm{T^{-1}A^{-1}m}$, which is large compared to the in-plane field case ($\gamma_{s,B_\parallel} \sim 1\,\mathrm{T^{-1}A^{-1}}$). This means that, under the assumption of a similar mechanisms responsible for the non-reciprocal resistance in the in- and out-of-plane field case, the associated spin-orbit field directing out-of-plane must be orders of magnitudes larger than in the in-plane case.

7.2.3. Complex Field Dependence of Non-Reciprocal Tranport for Combined In- and Out-of-Plane Fields

So far non-reciprocal transport was studied in both in- and out-of-plane fields. Combining both field directions leads to a polarity dependent critical current at low temperatures resulting in a "8-octant" problem, that was discussed in section 7.1.3. Non-reciprocal resistance at higher temperatures in superimposed in- and out-of-plane fields therefore can be expected.

In the same kind of manner as discussed in sections 7.2.1 and 7.2.2, $R_\omega(T)$ and $R_{2\omega}(T)$ curves have been recorded in various field configurations. The curves were measured before it was found that linearity in of $R_{2\omega}(T)$ in the current is only given up to $I = 200\,\mathrm{nA}$. The shown data are all measured with an AC current of 500 nA and therefore are not in the linear regime anymore. Qualitatively, however, this does not make a big difference. For better comparison, in the following, $R_\omega(T)$ and $R_{2\omega}(T)$ curves recorded for the same $B_\perp$ in different field and current configurations are plotted in the same colors. Curves for $B_\perp = 0$ are drawn in black. Dark blue corresponds to $B_\perp = -2\,\mathrm{mT}$, light blue to $B_\perp = +2\,\mathrm{mT}$. Red curves were recorded for $B_\perp = -5\,\mathrm{mT}$, dark yellow curves for $B_\perp = +5\,\mathrm{mT}$.

In Fig. 7.16 $R_\omega(T)$ and $R_{2\omega}(T)$ in the [1$\bar{1}$0]-direction is shown in out-of-plane magnetic fields $|B_\perp| \leq 5\,\mathrm{mT}$. The transition shifts towards lower temperatures at higher $B_\perp$ due to the suppression of T_c. As was already seen in Fig. 7.12, the sign of $R_{2\omega}(T)$ depends on the polarity of $B_\perp$ and is nearly mirror symmetric with the temperature axis. A not perfectly compensated DC current offset is most probably responsible for the slight

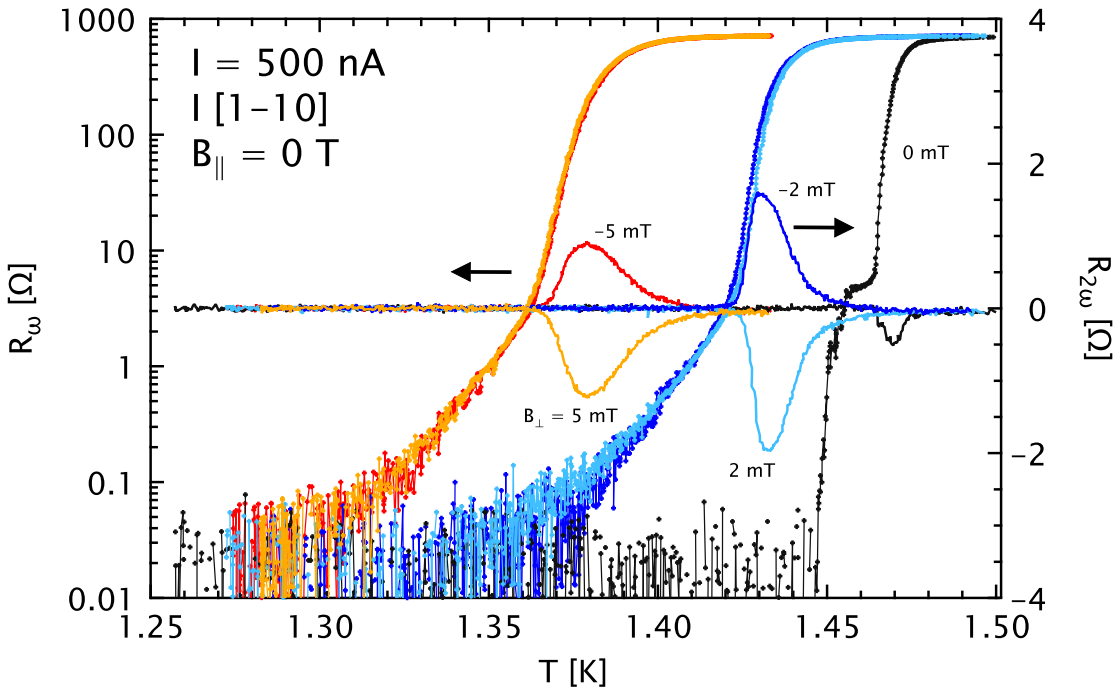

Fig. 7.16.: R_ω,$R_{2\omega}$ as a function of temperature for the $[1\bar{1}0]$ current direction for out-of-plane fields $B_\perp = -5, 2, 0, 2, 5\,\mathrm{mT}$. $R_\omega(T)$ is associated to the left axis, $R_{2\omega}(T)$ to the right axis (indicated by arrows).

asymmetry of $R_{2\omega}(T)$ measured for opposite polarities of $B_\perp$. For the same reason a small $R_{2\omega}(T)$-signal can be measured for $B_\perp = 0$ (black curve). $R_\omega(T)$ for fields of the same magnitude but opposite polarity are on top of each other and therefore are symmetric in $B_\perp$. For $B_\perp = 0$, $R_\omega(T)$ is very sharp with a small shoulder at $T = 1.457\,\mathrm{K}$. The reason for this kink is still unclear. For small $B_\perp$ the onset of $R_\omega(T)$ is linear in a logarithmic scale and therefore indicates an exponential dependence.

Fig. 7.16 so far shows nothing new besides the exponential increase of $R_\omega(T)$ at the onset of resistance most probably caused by thermal activation of pinned vortices. An additional in-plane field, however, strongly changes the observed behavior. Fig. 7.17 shows $R_\omega(T)$ and $R_{2\omega}(T)$ for the same $B_\perp$ as in Fig. 7.16 in an in-plane field of 0.3 T.

In contrast to the zero in-plane field case, $R_\omega(T)$ is not symmetric in $B_\perp$ anymore. For $B_\perp < 0$ the onset of resistance is shifted to lower temperatures. In this case zero resistance is not even reached for $B_\perp = -5\,\mathrm{mT}$. The slope of $R_\omega(T)$ for small resistance is smaller for $B_\perp < 0$ than for $B_\perp > 0$. $R_{2\omega}(T)$-curves for $|B_\perp| \geq 2\,\mathrm{mT}$ are all on the

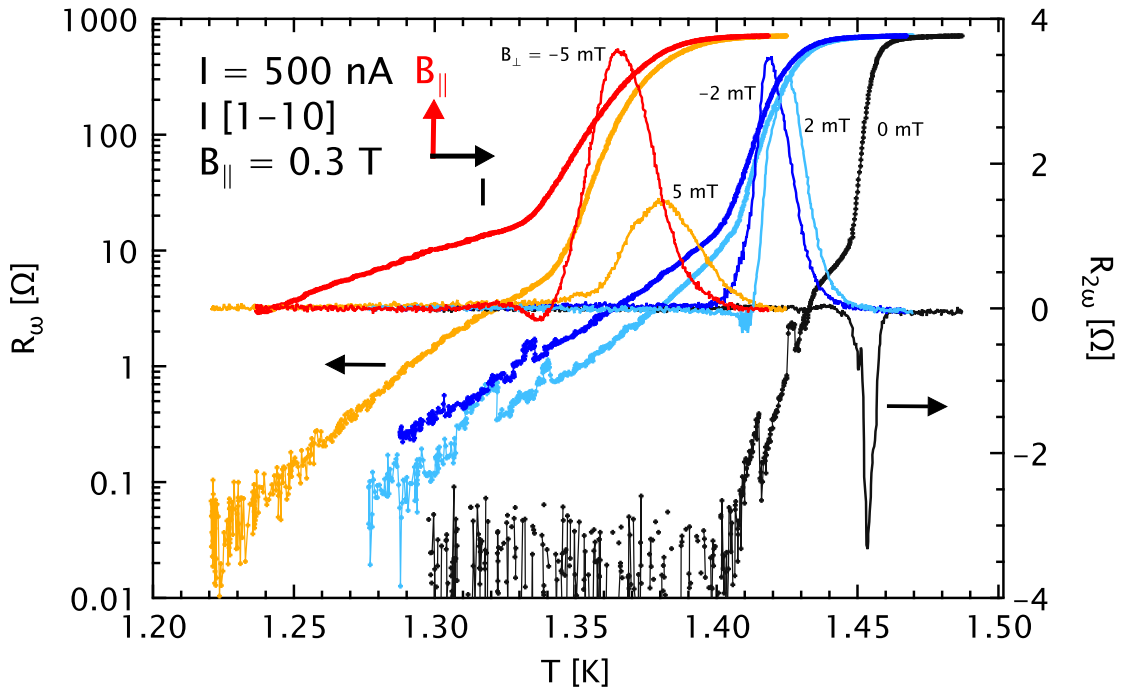

Fig. 7.17.: R_ω, $R_{2\omega}$ as a function of temperature for the $[1\bar{1}0]$ current direction for out-of-plane fields $B_\perp = -5, 2, 0, 2, 5\,\mathrm{mT}$. An in-plane field of $B_\parallel = 0.3\,\mathrm{T}$ is applied perpendicular to the current (indicated in the graph). $R_\omega(T)$ is associated to the left axis, $R_{2\omega}$ to the right axis (indicated by arrows).

positive side of the resistance axis very opposite to the case of zero in-plane field (see Fig. 7.16). The temperatures, where $R_{2\omega}(T)$ is maximal are different for $B_\perp$ of opposite polarities. For $B_\perp < 0$ the peaks are at slightly lower temperatures compared to $B_\perp > 0$. Also the peak heights differ strongly for opposite out-of-plane field directions. For $B_\perp = 0$ their is a peak in the negative direction caused only by the in-plane field as was already seen in section 7.2.1.

Inverting $B_\parallel$ leads to a graph that looks like a version of Fig. 7.17, where $R_{2\omega}(T)$-signals are mirrored to the opposite side of the $R_{2\omega}$-axis and corresponding $B_\perp$ are exchanged with the opposite polarity (see left side of Fig. 7.18). This again shows the complex "8-octant" symmetry of the problem.

On the right side of Fig. 7.18, R_ω and $R_{2\omega}$ are shown in [110]-direction with $B_\parallel$ applied parallel to the current direction as a reference to Fig. 7.17. In this field configuration $R_{2\omega}(T)$ is barely changed compared to the zero in-plane field case (Fig. 7.16). Also the $R_\omega(T)$ curves for opposite $B_\perp$ are only slightly different. These even small differences

most probably arise from a not perfectly perpendicularly oriented in-plane field with respect to the current.

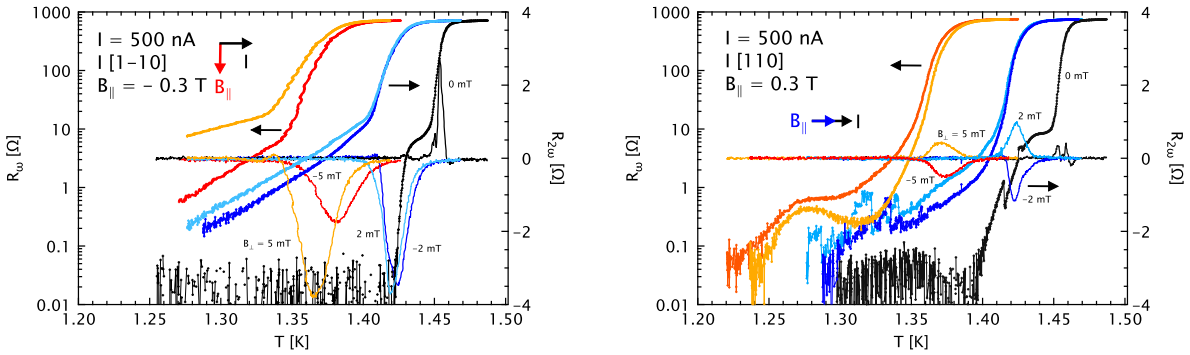

Fig. 7.18.: Left: R_ω, $R_{2\omega}$ as a function of temperature for the $[1\bar{1}0]$ current direction for out-of-plane fields $B_\perp = -5, 2, 0, 2, 5\,\mathrm{mT}$. An in-plane field of $B_\parallel = 0.3\,\mathrm{T}$ is applied perpendicular to the current. Right: R_ω, $R_{2\omega}$ as a function of temperature for the [110] current direction for out-of-plane fields $B_\perp = -5, 2, 0, 2, 5\,\mathrm{mT}$. An in-plane field of $B_\parallel = 0.3\,\mathrm{T}$ is applied parallel to the current.

This measurement shows that there is a complex interplay of the non-reciprocal effects of both in- and out-of-plane magnetic fields. The asymmetry of $R_\omega(T)$ in $B_\perp$ in the presence of an in-plane field again hints towards anisotropic pinning caused by the interplay of Rashba SOC and $B_\parallel$, which is also reflected in the asymmetric $R_{2\omega}(T)$-signal. An in-plane field of 0.3 T is enough to push the asymmetry to one side of the $R_{2\omega}$-axis. This means that the rectification of vortex motion caused by asymmetric pinning is dominated by the in-plane field as was already seen in Fig. 7.8 at low temperatures. A theoretical model would be useful at this point.
Unfortunately only the above shown $B_\perp$ fields were measured in the presence of an additional in-plane field. Investigation of the evolution of the polarity of $R_{2\omega}(T)$ as a function of $B_\perp$ in a fixed in-plane field might reveal further information about the relative strengths of in- and out-of-plane rectification.

7.3. Non-Reciprocal Resistance at the Crossover of Fluctuation and BKT-Regime

So far the behavior of $R_{2\omega}$ and γ_s was mainly studied at the absolute maximum of $R_{2\omega}(T)$ for different magnetic field orientations. It should be noted that, although often seen in literature, this choice of comparing $R_{2\omega,max}$ is kind of arbitrary as the maximum of $R_{2\omega}(T)$ not necessarily coincides with the maximum of $\gamma_s(T)$. In fact, in nearly all cases, even in the fluctuation regime, the two corresponding temperatures differ by some mK. Therefore it is instructive to look at the full $\gamma_s(T)$-dependence for different temperature and field regimes.
In section 2.3.1 different temperature regimes have been discussed theoretically. In 2D systems, where the transition to the superconducting state is of BKT-type, γ_s should diverge as $(T - T_{BKT})^{-3/2}$ for $T \to T_{BKT}$. A second divergence is expected at the mean field critical temperature $\gamma_s \propto (T_c - T)^{-1}$ for $T \leq T_c$ [45]. Considering a right handed coordinate system $\gamma_s(T)$ in this regime has always a positive sign. In the fluctuation regime of the superconductor, however, the sign of $\gamma_s(T)$ depends on the pairing interaction and can also be negative (see eq. 2.49). The ratio of singlet and triplet pairing determines the sign of $\gamma_s(T)$ in the fluctuation regime.

Fig. 7.19 shows $R_{2\omega}(T)$ curves measured in the [100]-direction for several $B_\perp$. This measurement is exemplary and the results are qualitatively the same for the other direction. Similar kind of curves have also been measured with an in-plane field perpendicular to the current instead of $B_\perp$. The discussion is therefore valid for all current directions and for either in- or out-of-plane fields. The current was 500 nA and therefore not in the linear regime. Such a large current was however needed to increase signal to noise-ratio as the noise of $\gamma_s = \frac{2R_{2\omega}}{R_\omega BI}$ is doubled by the measured resistance noise (R_ω and $R_{2\omega}$).

This figure again shows oddness of $R_{2\omega}(T)$ in $B_\perp$. Maximal $R_{2\omega}$ is observed at $|B_\perp| = 0.3\,\mathrm{mT}$. There are sign changes of $R_{2\omega}(T)$ at temperatures always below the highest peak of the corresponding curve. The width of the peaks are broadened with increasing $B_\perp$.

From the data shown in Fig. 7.19 and the corresponding $R_\omega(T)$, $\gamma_s(T) = \frac{2R_{2\omega}(T)}{R_\omega(T)B_\perp I}$ can be calculated. The results are shown in Fig. 7.20. It can be seen that for $|B_\perp| \leq 0.3\,\mathrm{mT}$, $\gamma_s(T)$ has two negative peaks. Two peaks have also been seen in Fig. 7.10 in an in-plane

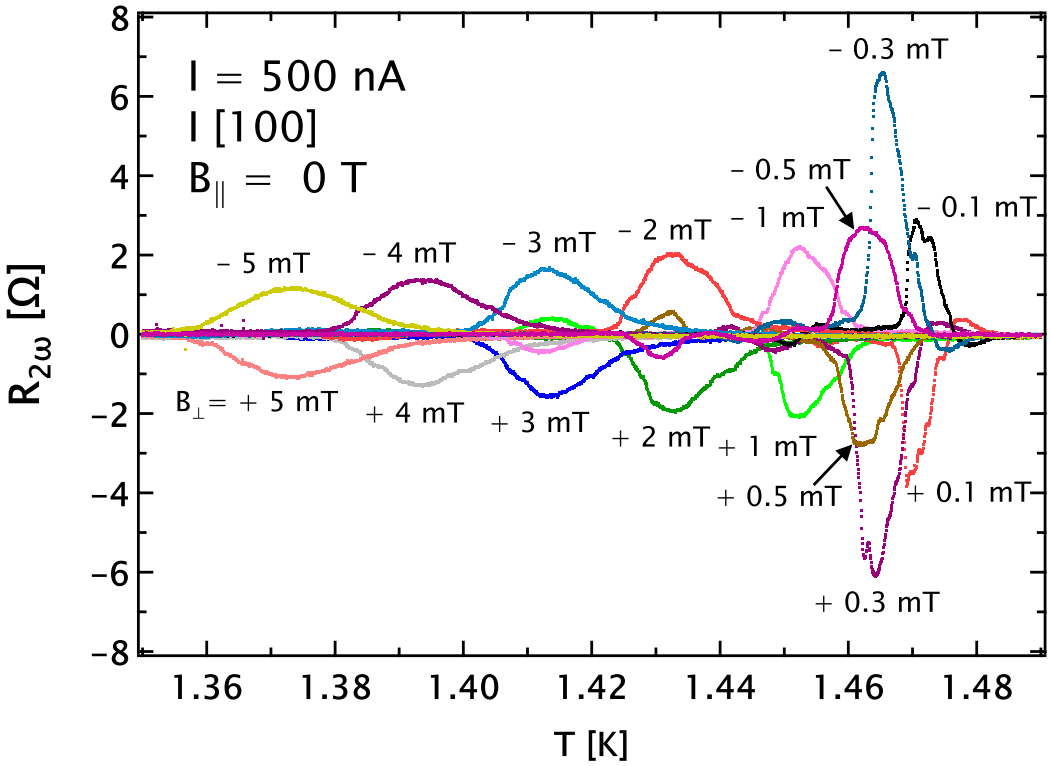

Fig. 7.19.: $R_{2\omega}(T)$ measured in the [100]-direction and a current of 500 nA. The applied out-of-plane fields are $B_\perp = -5, -4, -3, -2, -1, -0.5, -0.3, -0.1, 0, 0.1, 0.3, 0.5, 1, 2, 3, 4, 5$ mT.

field perpendicular to the current. The origin for this two peaks, that one can associate to the fluctuation regime is still unclear. At a temperature range some 10 mK below the main peaks, $\gamma_s(T)$ reverses its sign and diverges. For $|B_\perp| \geq 0.5$ mT the negative peaks decrease strongly and the divergence at lower temperatures also becomes flatter and broader.

This divergence can be attributed to a BKT-like transition, where $\gamma_s(T)$ follows a $(T - T_{KT})^{-3/2}$ dependence near T_{BKT} (eq. 2.55). Strong indications that the transition to the normal state is BKT-like could already be seen in the $R(T)$-dependence of sample Al/InAs-M in zero magnetic field (see Fig. 6.2). This is unexpected as this kind of transition usually is observable only in disordered 2D superconducting systems, where the transition is very broad. In the present material, however, the transition measured in the $R(T)$-dependence is only 10 mK in zero magnetic field. A foot structure at the very onset of the resistance in a $R(T)$ measurement can have various reasons like inhomogeneities in the sample or flux flow due to a finite out-of-plane field. These kind of

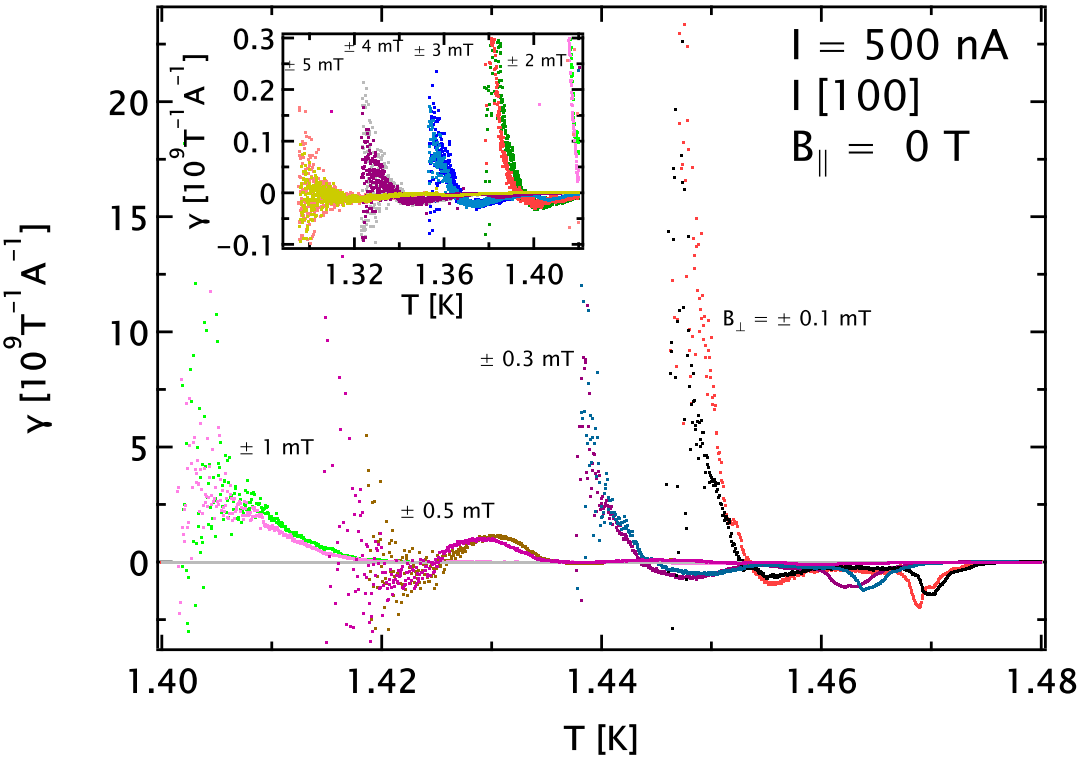

Fig. 7.20.: $\gamma_s(T)$ calculated from data shown in Fig. 7.19. Main panel shows data for $|B_\perp| \leq 1\,\mathrm{mT}$. $\gamma_s(T)$ for higher fields are shown in the inset.

resistances, however, are usually independent of the polarity of the current. The presence or absence of a second harmonic resistance therefore offers a good decision criterion in the discussion of a possible BKT-like transition in a systems with broken time- and inversion symmetry. The observation of a diverging $\gamma_s(T)$ in such systems is a strong indication towards a BKT-like transition.

Because of the continuous crossover from the fluctuation regime for $T > T_c$ to the BKT regime ($T_{BKT} < T < T_c$) it is difficult to fit data properly to the theory, which would be needed for a quantitative analysis. Eq. 2.55 goes to zero at higher temperatures, however a second divergence is expected for $T \to T_c$ (eq. 2.56). This second divergence, however, in reality appears only as a kink in the $\gamma_s(T)$ dependence [88]. For samples, where the sign of $\gamma_s(T)$ is the same in the BKT- and the fluctuation regime for small magnetic field, a fit to Eq. 2.55 can deliver good agreement with the data. This was shown in gated $SrTiO_3$ [88] and for a topological insulator/superconductor heterostructure $SrTiO_3$ [48]. The sign changes in $\gamma_s(T)$ measured in the present sample, however, make a proper

fit to eq. 2.55 or 2.56 impossible as there is no interpolation formula which smoothly interconnects fluctuation and BKT-regime for temperatures $T > T_c \to T_c$. As the sign of $\gamma_s(T)$ in the fluctuation regime depends on the sign and the ratio of the singlet and triplet pairing interaction (eq. 2.49) a detailed analysis of $\gamma_s(T)$ with the support of a theory group could give valuable information on the pairing Hamiltonian and hence the functional form of the order parameter [45].
The broadening of the divergence of $\gamma_s(T)$ with increasing magnetic field was also already seen in the DC $R(T)$ characterization of sample AL/InAs-M (Fig. 6.3). A theoretical treatment of this broadening would be very interesting as so far not much experimental data have been published on the impact of a magnetic field on the BKT-transition characteristics. Of special interest would be in this case the influence of the interplay of SOC and magnetic field on the width of the transition.

8. Discussion and Outlook

Different aspects of the superconducting properties of 2D Al/InAs heterostructures with large Rashba SOC such as anistropic vortex inductance in an in-plane magnetic field or non reciprocal resistance and critical current have been examined and compared with two Al/GaAs reference samples with no SOC. In zero field BCS temperature dependence of the kinetic inductance has been shown. At low temperature small shifts of the resonance frequency have been observed which can be traced back to relatively strong coupling of the Al with two-level-systems in the amorphous AlOx top layer. It may be interesting to compare this effect with measurements on Al thin films with in-situ deposited Al_2O_3 oxide layer, which can be grown at University of Regensburg.

In sample Al/InAs-M an in-plane field decreases the superfluid stiffness, however, artifacts from an inhomogeneous compensation field seem to play a dominant role at higher in-plane fields and hence make it challenging to discriminate them from other features caused by the field (see section A.1.2). A better field homogeneity would be needed to avoid artifacts in the measurement of the $L_s(B_\parallel)$-dependence. Possible improvements of the used setup are discussed in section A.4 in the appendix.
In small out-of-plane fields a very strong inductive response has been measured and was attributed to a vortex inductance produced by the motion of pinned flux lines in the thin film. The large inductance of the order of μH can be tuned continuously with out-of-plain fields of only some mT. This could offer the possibility to design a self-contained electrical component consisting of a tunable inductor in form of a weak-pinning superconductor meander and a small superconducting magnet-coil. Such a nearly dissipation-less, tunable inductor would be a step further towards superconducting electronis.
Counterintuitively, the vortex inductance in the Al/InAs heterostructure decreases with an additional in-plane magnetic field, which could be explained by a strengthening of the pinning force. Furthermore, it was found that this effect is strongly dependent on the relative orientation of in-plane field and current (vortex displacement) direction. Such an anisotropic increase of vortex pinning at low temperatures has not been reported so

far. These findings could be caused by a change of the vortex core shape by the interplay of an in-plane magnetic field and SOC. The reduction of the vortex core size can lead to an increase of the pinning force in both directions, namely parallel and perpendicular to the in-plane field. In a Ginzburg-Landau approach a model was established which captures the main experimental findings. The presented theoretical functional dependence, however, does not yet quantitatively match with experimental data. A revision of the model would be desirable.

The presence of SOC in the Al superconducting film was independently confirmed by measuring signatures of non-reciprocal transport in the fluctuation regime of the superconducting transition. In Rashba superconductors this is explained by the simultaneous presence of singlet and triplet pairing states.

Non-reciprocal transport was not only measured in the fluctuation regime $T > T_c$ but also in the BKT regime. A divergence of $\gamma_s(T)$ in external magnetic field indicates a BKT-like transition [48]. $R(T)$-curves, that were measured in sample Al/InAs-M are nicely reproduced by BKT theory curves and hence also indicate a BKT-like transition 6.2. This shows that despite the good quality of the Al film the transition to the normal state is of BKT-type in that specimen. In-plane magnetic fields lead to a broadening of the BKT transition, which could be measured both in $R(T)$ (Fig. 6.3) and $R_{2\omega}(T)$ (Fig. 7.20) measurements.

In Rashba superconductors only in-plane fields are expected to produce non-reciprocal transport as the field needs to be aligned with the effective spin-orbit fields in order to produce a Zeeman splitting. Transport measurements in finite out-of-plane fields, however, have shown non-reciprocal behavior that is even stronger as in the in-plane case. This indicates the existence of out-of-plane spin-orbit field components in these kind of heterostructures, so far not mentioned in literature for that kind of material. Also in Josephson junction arrays out-of-plane fields lead to non-reciprocal transport indicating an ouf-of-plane spin-orbit field component present in the semiconducting InAs weak link (see section A.3.3). A theoretical model of this finding is still missing.

Similar to the non-reciprocal transport near the superconducting transition, polarity dependence of the critical current was demonstrated in in- and out-of-plane magnetic fields as well as in the combined-fields case at low temperatures. In Rashba superconductors in-plane magnetic fields perpendicular to the current are expected to make the critical current polarity dependent [7][8], which was found in sample Al/InAs-S (see

chapter 7). In small out-of-plane fields strong indication towards asymmetric pinning is found, maybe caused by an out-of-plane spin texture resulting from the different lattice symmetries of the Al and the 2DEG. Critical current measurements in different crystal directions (e.g. on sample Al/InAs-C) in finite $B_\perp$ with higher resolution could shed light on the crystal symmetries. A theoretical modeling of the Al/2DEG interface for different crystal directions could be enlightening.

It was found that there is a polarity dependence and anistropy of the DC resistance and critical current in sample Al/InAs-S in an external magnetic field. A very interesting question would be, if such anisotropies can also be found in the inductive response of the superfluid. For that an asymmetric meander structure with a main current direction would be needed. Asymmetry in such a meander could be achieved by making the aspect ratio of the long segments directing in one direction larger than that of the opposite direction (compare Fig. 6.1). Adding a DC current to the AC excitation would then allow to measure a possible polarity dependence of L_s or L_v in the presence of external magnetic fields, which is not possible for an almost symmetric structure as sample Al/InAs-M. As the vortex lattice in the heterostructure shows a very strong inductive response, polarity dependence and anisotropies of the pinning mechanism at low temperatures could be probed with a high resolution.

Bibliography

[1] F. Flöther, C. Moose, and I. Tavernelli, Experts Insights (2020).

[2] J. Shabani et al., Phys. Rev. B **93**, 155402 (2016).

[3] R. Aguado and L. Kouwenhoven, Phys. Today **73**, 44 (2020).

[4] Y. Oreg, G. Refael, and F. von Oppen, Phys. Rev. Lett. **105**, 177002 (2010).

[5] R. M. Lutchyn, J. D. Sau, and S. D. Sarma, Phys. Rev. Lett. **105**, 077001 (2010).

[6] F. Ando et al., Nature **584**, 373 (2020).

[7] A. Daido, Y. Ikeda, and Y. Yanase, arXiv:2106.03326 (2021).

[8] N. F. Q. Yuan and L. Fu, arXiv:2106.01909 (2021).

[9] R. Meservey and P. M. Tedrow, J. Appl. Phys. **40**, 2028 (1969).

[10] W. Meissner and R. Ochsenfeld, Naturwissenschaften **21**, 787 (1933).

[11] T. Kubo, Phys. Rev. Research **2**, 033203 (2020).

[12] C. Enss and S. Hunklinger, *Tieftemperaturphysik*, volume 1, Springer, 2000.

[13] W. Buckel and R. Kleiner, *Supraleitung*, volume 6, Wiley VCH, 2004.

[14] Y. Ivry et al., Phys. Rev. B **90** (2014).

[15] P. Anderson, J. Phys. Chem. Solids **11**, 26 (1959).

[16] T. I. Baturina and V. M. Vinokur, Ann. Phys. **331**, 236 (2013).

[17] L. Benfatto, C. Castellani, and T. Giamarchi, Phys. Rev. B **80**, 214506 (2009).

[18] J. Pearl, Appl. Phys. Lett. **5**, 65 (1964).

[19] K. Bennemann and J. Ketterson, *The Physics of Superconductors*, 2003.

[20] E. V. Thuneberg, J. Kurkijärvi, and D. Rainer, Phys. Rev. B **29**, 3913 (1984).

[21] E. J.Kramer, J. Nucl. Mater. **72**, 5 (1978).

[22] E. V. Thuneberg, J. Kurkijärvi, and D. Rainer, Phys. Rev. Lett. **48**, 1853 (1982).

[23] D.-H. Wu and S. Sridhar, Phys. Rev. Lett. **65**, 2074 (1990).

[24] G. Blatter et al., Rev. Mod. Phys **66**, 1125 (1994).

[25] C. S. nad T.W. Heitmann et al., Phys. Rev. B **79**, 174512 (2009).

[26] M. W. Coffey and J. R. Clem, Phys. Rev. Lett. **67**, 386 (1991).

[27] M. W. Coffey and J. R. Clem, J. Supercond. **5**, 313 (1992).

[28] M. Golosovsky, M. Tsindlekht, and D. Davidov, Supercond. Sci. Technol. **9**, 1 (1996).

[29] M. Tinkham, *Introduction to Superconductivity*, volume 2, Dover Publications, 2004.

[30] J. Gao, The physics of superconducting microwave resonators.

[31] D. P. Pappas, M. R. Vissers, D. S. Wisbey, J. S. Kline, and J. Gao, IEEE Trans. Appl. Supercond. **21**, 871 (2011).

[32] K. J. G. Götz et al., Nanotechnology **27**, 135002 (2016).

[33] L. Zeng, D. T. Tran, C.-W. Tai, G. Svensson, and E. Olsson, Sci. Rep. **6** (2016).

[34] S. Fritz et al., Sci. Rep. **8** (2018).

[35] J. Lisenfeld et al., Nat. Commun. **6** (2015).

[36] S. Oh et al., Phys. Rev. B **74**, 100502 (2006).

[37] L. Petersen and P. Hedegard, Surf. Sci. **459**, 49 (2000).

[38] G. Dresselhaus, Phys. Rev. **100**, 580 (1955).

[39] E. I. Rashba, Sov. Phys. Solid State **2**, 1109 (1960).

[40] L. Meier et al., Nat. Phys. **3**, 650 (2007).

[41] Y. H. Park et al., Appl. Phys. Lett. **103**, 252407 (2013).

[42] G. L. J. A. Rikken and E. Raupach, Nature **390**, 493 (1997).

[43] G. L. J. A. Rikken and P. Wyder, Phys. Rev. Lett. **94**, 016601 (2005).

[44] G. L. J. A. Rikken, J. Fölling, and P. Wyder, Phys. Rev. Lett. **87**, 236602 (2001).

[45] S. Hoshino, R. Wakatsuki, K. Hamamoto, and N. Nagaosa, Phys. Rev. B **98**, 054510 (2018).

[46] V. Berezinskii, Sov. Phys. JETP **32**, 493 (1971).

[47] J. M. Kosterlitz1 and D. J. Thouless, J. Phys. CB **6**, 1181 (1973).

[48] K. Yasuda et al., Nat. Commun. **10** (2019).

[49] V. M. Edelstein, J. Phys.: Condens. Matter **8**, 339 (1996).

[50] A. A. Abrikosov, JETP **32**, 1442 (1957).

[51] L. P. Gor'kov and E. I. Rashba, Phys. Rev. Lett. **87**, 037004 (2001).

[52] P. W. Anderson, Phys. Rev. Lett. **3**, 325 (1959).

[53] W. Knight, Phys. Rev. **76**, 1259 (1949).

[54] K. Ishida et al., Nature **396**, 658 (1998).

[55] L. A. Openov, Phys. Rev. B **58**, 9468 (1998).

[56] Y. Dalichaouch, M. C. de Andrade, D. A. Gajewski, P. V. R. Chau, and M. B. Maple, Phys. Rev. Lett. **75**, 3938 (1995).

[57] Y. Liu et al., Sci. China Phys. Mech. Astron. **59**, 657402 (2016).

[58] R. Prozorov et al., npj Quantum Mater. **4**, 1 (2019).

[59] Y. Xu and Q. Gu, Solid State Commun. **187**, 68 (2014).

[60] N. Sun, J. Zhao, and X. Yan, Solid State Commun. **197**, 40 (2014).

[61] J. Zhao, X. Yan, and Q. Gu, Int. J. Mod. Phys. B **31**, 1745011 (2017).

[62] M. Ishihara, Y. Amano, M. Ichioka, and K. Machida, Phys. Rev. B **87**, 224509 (2013).

[63] Y. Sera, T. Ueda, H. Adachi, and M. Ichioka, Symmetry **12** (2020).

[64] N. Hayashi and Y. Kato, Phys. Rev. B **66**, 132511 (2002).

[65] N. Hayashi and Y. Kato, J. Low Temp. Phys. **130**, 193 (2003).

[66] T. Wang et al., J. Cryst. Growth **535**, 125570 (2020).

[67] W. L. Sarney, S. P. Svensson, K. S. Wickramasinghe, J. Yuan, and J. Shabani, J. Vac. Sci. Technol. B **36**, 062903 (2018).

[68] P. He et al., Phys. Rev. Lett. **120**, 266802 (2018).

[69] A. F. Hebard and A. T. Fiory, Appl. Phys. Lett. **44**, 291 (1980).

[70] T. R. Lemberger, I. Hetel, J. W. Knepper, and F. Y. Yang, Phys. Rev. B **76** (2007).

[71] M.-S. Kim, J. A. Skinta, T. R. Lemberger, A. Tsukada, and M. Naito, Phys. Rev. Lett. **91**, 087001 (2003).

[72] J. Draskovic et al., Phys. Rev. B **88** (2013).

[73] A. I. Gubin, K. S. Il'in, S. A. Vitusevich, M. Siegel, and N. Klein, Phys. Rev. B **72** (2005).

[74] J. R. Clem and M. W. Coffey, Phys. Rev. B **46**, 14662 (1992).

[75] B. Lv et al., Sci. Rep. **6** (2016).

[76] P. J. Petersan and S. M. Anlage, J. Appl. Phys. **84**, 3392 (1998).

[77] J. Romijn, T. M. Klapwijk, M. J. Renne, and J. E. Mooij, Phys. Rev. B **26**, 3648 (1982).

[78] F. E. Terman, *Radio Engineers Handbook*, McGraw-Hill, 1943.

[79] F. W. Grover, *Inductance Calculations: Working Formulas and Tables*, Dover Phoenix, 2004.

[80] J. Gao et al., Appl. Phys. Lett. **92**, 152505 (2008).

[81] P. Chubov, V. Eremenko, and Y. A. Pilipenko, JETP **28**, 389 (1969).

[82] B. I. Halperin and D. R. Nelson, J. Low Temp. Phys. **36**, 599 (1979).

[83] B. L. T. Plourde et al.

[84] F. S. Bergeret and I. V. Tokatly, Phys. Rev. B Rapid. Commun. **102**, 060056 (2020).

[85] K. Yu et al., Phys. Rev. B Rapid. Commun. **76**, 220507 (2007).

[86] P. He et al., Nat. Phys. **14**, 495 (2018).

[87] E. Zhang et al., Nat. Commun. **11** (2020).

[88] Y. M. Itahashi et al., Sci. Adv. **6** (2020).

[89] J. Lustikova et al., Nat. Commun. **9** (2018).

[90] P. Belova, M. Safonchik, K. B. Traito, and E. Lähderanta, J. Phys.: Conf. Ser. **303** (2011).

[91] J. Bardeen, Rev. Mod. Phys. **34**, 667 (1962).

[92] H. J. Suominen et al., Phys. Rev. B **95**, 035307 (2017).

[93] M. C. Dartiailh et al., Nat. Commun. **12** (2021).

[94] W. Mayer et al., Nat. Commun. **11** (2020).

[95] C. Baumgartner et al., arXiv:2103.06984 (2021).

[96] C. Baumgartner et al., Phys. Rev. Lett. **126**, 037001 (2021).

A. Appendix

In this chapter data worth presenting are shown, which are difficult to explain yet and not the main subject of this thesis. Furthermore, challenges that occured in the laboratory are discussed.

A.1. Inductance Measurements

A.1.1. Artifacts in the Inductive Response

During the measurement process various systematic features and artifacts were observed, which should be discussed in this section. In Fig. A.1 the dependence of the kinetic inductance of sample Al/InAs-M on in-plane fields of different orientations are depicted. At small fields of around 10 mT for all the different field orientations small jumps of about 1.1 nH can be observed, which are probably connected to the increase of geometric inductance at the superconducting to normal transition of the Al bond wires that have a critical field of $\sim 10\,\mathrm{mT}$. In the superconducting state the magnetic field produced by the current through the wire is screened from the interior of the wires and therefore do not contribute to the geometric inductance between. Furthermore there will be some effective mutual inductance due to Meissner expulsion of the magnetic field produced by the current in one wire in a second one. The kinetic inductance of a 1 mm long Al wire of 25 μm diameter is of the order of 1 pH and therefore negligible. In the normal state the magnetic field can penetrate into the wires and store magnetic energy and hence increase the geometric inductance. Also the mutual inductance between two superconducting wires will change when they make a transition to the normal state. As this jump is observed in most of the measurements it is believed to be systematic and therefore can calculated out in the data analysis if accuracy in the nH regime is needed.

In zero magnetic field L should be independent of the rotator position. Inductances from the leads connecting the rest of the cryostat with the sample holder should not

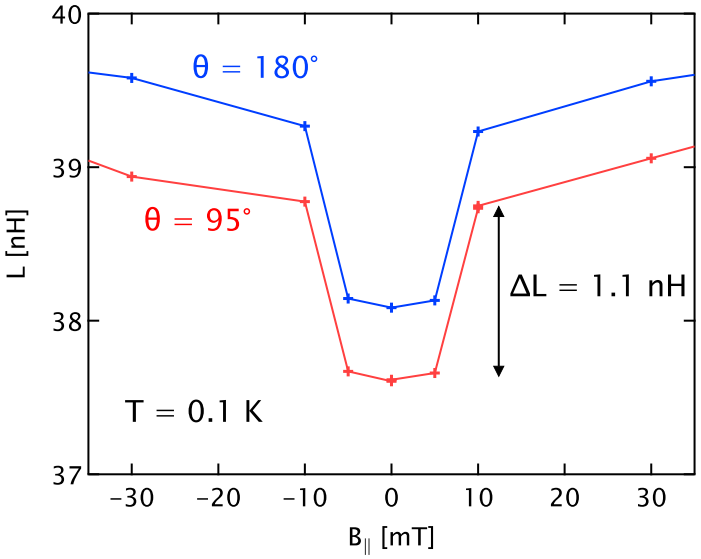

Fig. A.1: L as a function of in-plane field for two almost perpendicular in-plane field directions. Near $|B_{\parallel}| \approx 10\,\mathrm{mT}$ a sharp increase of $\Delta L = 1.1\,\mathrm{nH}$ is observed for both directions probably caused by a transition to the normal state of the Al bond wires ($B_{c,Al} \approx 10\,\mathrm{mT}$.) The minimal value for both directions differs slightly by about 0.6 nH.

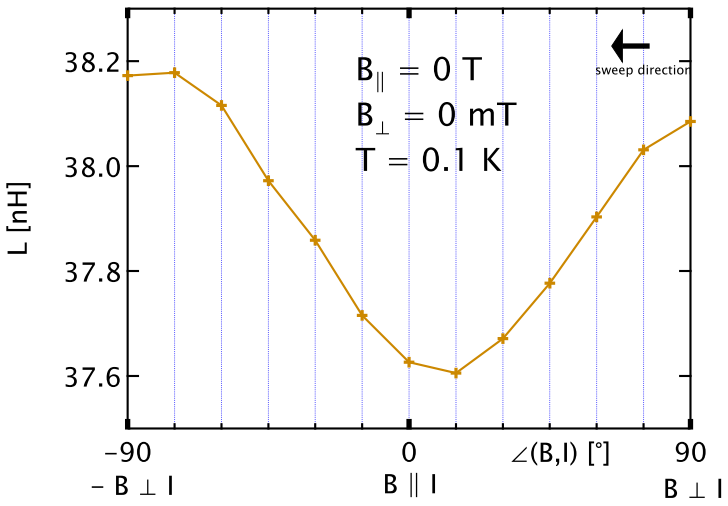

Fig. A.2: L as a function of rotator position in zero magnetic field and low temperatures. Rotation of the sample leads to a continuous variation of the smallest measurable inductance with a peak-to-peak difference of $\sim 0.6\,\mathrm{nH}$ without magnetic field present.

contribute to the RLC parameters as they are decoupled with resistors, which are also mounted directly on the sample holder and move together with the RLC circuit and the sample. It has turned out, however, that the minimal inductance $L(B = 0)$ at constant temperature $T = 0.1\,\mathrm{K}$ varies with the rotator position. Fig. A.2 shows the smallest measurable L as a function of rotation angle. A rotation of 180 ° shows a peak-to-peak spread of L of $\sim 0.6\,\mathrm{nH}$. The reason for this variation is still unclear but must be solely due to geometric changes of the setup during rotation as there is no magnetic field acting on the superconductor. A possible origin could be a small mutual inductance between the RLC circuit and the flexible leads connecting the sample holder and the cryostat that changes when the sample holder is rotated.

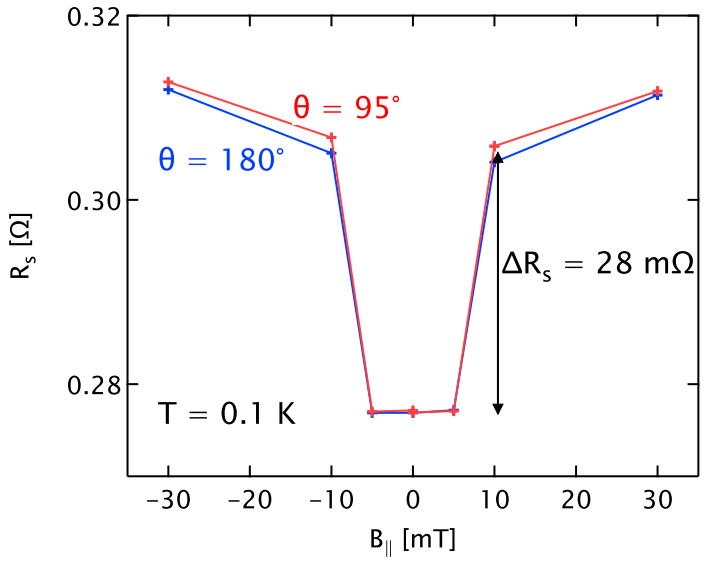

Fig. A.3: R_s as a function of in-plane field for two almost perpendicular in-plane field directions. Near $|B_\parallel| \approx 10\,\mathrm{mT}$ a jump in the resistance of $\Delta R_s = 28\,\mathrm{m\Omega}$ is measured. In contrast to the inductance shown in Fig. A.1 $R_s(B_\parallel = 0)$ is the same for both directions.

Fig. A.1 shows R_s extracted from the width of the resonance curves via eq. 3.8 as a function of in-plane field extracted from the same dataset as in Fig. A.1. The resistance in zero field is the same for both directions and therefore indicates that the variation of L in zero field at different rotator positions comes from a mutual inductance source which does not provide any effective resistance. At the same $|B_\parallel| \approx 10\,\mathrm{mT}$, where a jump is observed in L also a sharp increase of R_s can be observed. The magnitude of the jump $\Delta R_s = 28\,\mathrm{m\Omega}$ is in agreement with an estimate for the bond wire resistance. From the datasheet of the manufacturer "Heraeus" the Al bond wires have a Si content of roughly 1% and a specific resistance of $3\,\mu\Omega\mathrm{cm}$ at room temperature. A wire of 1 mm length and diameter of $25\,\mu\mathrm{m}$ would have a resistance of $61\,\mathrm{m\Omega}$ at room temperature. Considering that few bond wires of several mm length are used for contacting the I_+ and I_- contacts and that the specific resistance of the AlSi probably only decreases slightly with temperature, the magnitude of ΔR_s seems reasonable. Moreover, a change of contact resistance could be considered, as the contacts between the chip carrier and the bond wires change from S-N (superconducting AlSi - gold) to N-N (AlSi - gold). The contact between bond wire and sample also changes from either S-S (superconducting sample - superconducting AlSi) to S-N (superconducting sample - AlSi) if the contact is between the Al thin film and the AlSi bond wire. More likely the bond wires form electrical contact to the semiconductor. In that case the SM-S (semiconducting 2DEG - superconducting AlSi) contact changes to SM-N (semiconducting 2DEG - AlSi) as the AlSi turns normal.

Fig. A.4 shows kinetic inductance L as a function of the angle between field and current

for different fields at low temperatures. For small fields $\leq 0.075\,\mathrm{T}$ there is almost no dependence on the relative orientation of field and current if the systematic oscillatory contribution (see left side of Fig. A.4) is subtracted. For the highest field of 0.3 T there is a peak near $B \parallel I$. At this angle, however, also the misalignment of the sample plane with the magnetic field produced by the large magnet and therefore the field needed to compensated the out-of-plane field component is maximal (see right side of Fig. A.4). It was shown earlier that the compensation field has an inhomogeneity of $\sim 5\%$ measured at two points separated by 0.8 mm. At the point of minimal inductance the out-of-plane field component is compensated as best as possible in the center of the sample. At the outer parts of the sample, however, a compensation field of 4 mT probably leads to an effective out-of-plane field of very roughly $0.05 * 4\,\mathrm{mT} = 0.2\,\mathrm{mT}$. L strongly depends on the absolute value of the out-of-plane field (see Fig. 6.7). Event though only a small part of the sample will experience a finite out-of-plane field component L can increase significantly. With a $\frac{\mathrm{d}L}{\mathrm{d}B_\perp} = 118\,\mathrm{nH/mT}$ and an estimated number of squares of 10% subject to the above calculated out-of-plane field component L increases by 2.4 nH. Although this estimation is very rough uncertainties in L at higher in-plane fields of some nH seem to be realistic.

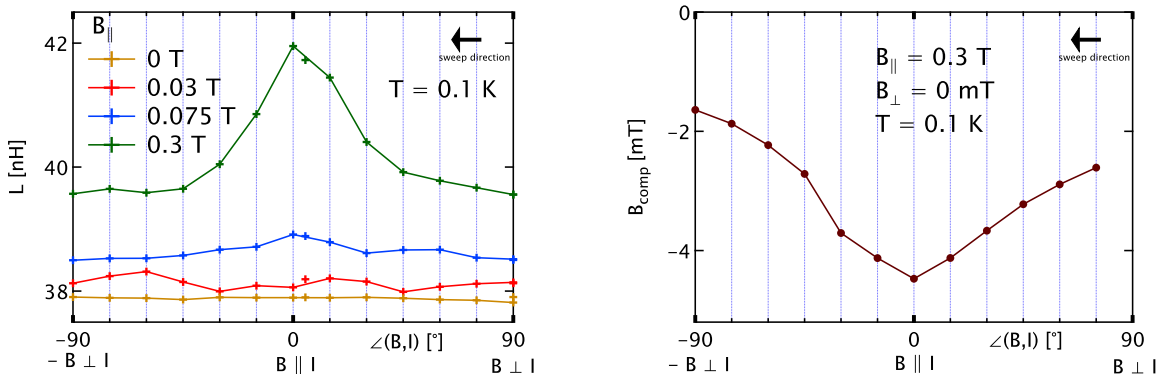

Fig. A.4.: Left: Kinetic inductance L as a function of the angle between field and current for in-plane fields $B_\parallel = 0, 0.03, 0.075, 0.3\,\mathrm{T}$ at $T = 0.1\,\mathrm{K}$. From the raw data the oscillatory contribution to L shown in Fig. A.2 was subtracted. For $B_\parallel > 0$ additionally $\Delta L = 1.1\,\mathrm{nH}$ was subtracted. Right: Out-of-plane field component for $B_\parallel = 0.3\,\mathrm{T}$. Near $B \parallel I$ the measured kinetic inductance as well as the compensation field has a peak.

In Fig. A.5 the out-of-plane field needed to compensate for the parasitic, perpendicular field from the large magnet is shown for three different rotator positions. It shows that the fields needed to compensate an in-plane field in the [110]-direction is significantly larger than in the $[1\bar{1}0]$ orientation. For rotational angle with larger misalignment be-

tween sample plane and $B_\parallel$ higher effective perpendicular field components act on the sample due to the inhomogeneity of the compensation field. For a rotator angle of 245.5 ° the misalignment is minimal. The dependence of $L(B_\parallel)$ for this orientation is quadratic and therefore is in accordance with orbital pair breaking in an in-plane field. The pair breaking parameter Γ for a thin film in a parallel field is quadratic in $B_\parallel$ for moderate fields [11][29]. The superfluid density $n_s(\Gamma) = n_{s0}(1-\Gamma)$ is nearly linear for not too large Γ. The field dependence of $L \propto 1/n_s$ can for moderate in-plane fields be written as

$$L(B_\parallel) \propto \frac{1}{n_s(0)(1-\Gamma)} \propto L(0)/(1 - B_\parallel^2/\tilde{B}_c^2), \tag{A.1}$$

where $\tilde{B}_c$ is a characteristic pair breaking field which depends on sample parameters and should be of the order of $B_{c\parallel}$. In Fig. A.5 only the curve with minimal compensation field is quadratic in $B_\parallel$ whereas in the other cases $L(B_\parallel)$ is more linear probably due to vortex inductance resulting from uncompensated areas of the sample.

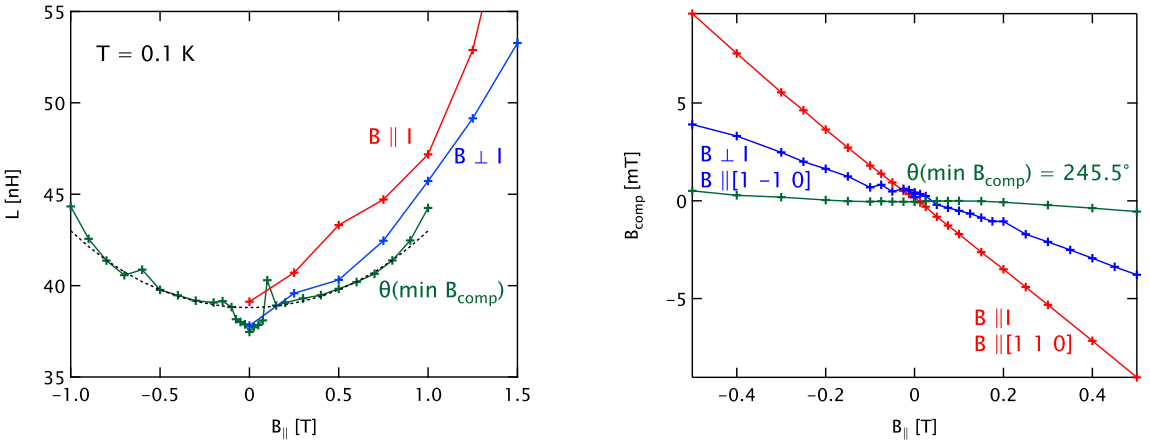

Fig. A.5.: Left: Inductance as a function of the in-plane field for the two main field orientations (red,blue) and at an angle where the compensation field needed to null the out-of-plane field component is minimal (green). The dashed line is a parabola according to pair breaking in moderate in-plane fields with $L_{pb}(B_\parallel) = \tilde{L}(0)/(1 - B_\parallel^2/\tilde{B}_c^2)$, characteristic $\tilde{B}_c = 3.2\,\mathrm{T}$ close to $B_{c,\parallel}$. Red and blue curves are almost linear in $B_\parallel$ Right: Compensation field as a function of in-plane field for the two main relative orientations and at an angle $\theta = 245.5\,°$, where $B_{comp}(B_\parallel)$ is minimal. In the $B \parallel [110]$ configuration much higher fields are needed to compensate the perpendicular component from the in-plane field as in the $[1\bar{1}0]$ orientation. The misalignment angles between sample plane and magnetic field produced by the large magnet are 1.10 ° for $B \parallel [110]$ and 0.45 ° for $B \parallel [1\bar{1}0]$. The misalignment for the green curve is only 0.083 °.

Fig. A.6 shows L as a function of $B_\parallel$ for fields up to 0.5 T. In the case where $B_\parallel \parallel I$,

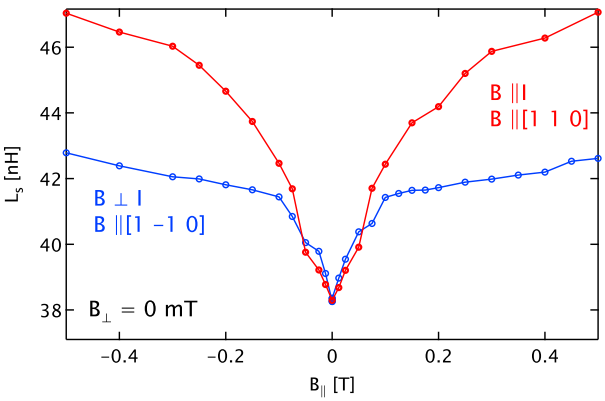

Fig. A.6: Inductance as a function of the in-plane field for the two main field orientations in fields up to 0.5 T. For fields above 0.1 T the curves diverge probably due to vortex contribution to L from only partly compensated areas of the sample. The difference at higher fields result on the one hand from different misalignment angles of field and sample plane which lead to a different number of stray vortices for the two field directions. On the other the enhancement of vortex pinning in an in-plane field is also different for the two orientations.

$L(B_\parallel)$ increases for small fields linearly up to 0.1 T before nearly staying constant. For $B_\parallel \parallel I$ L increases non-linearly up to 0.5 T. The curves diverge above 100 mT. The difference however could be explained by an inductance contribution of vortices due to an incomplete compensation of outer parts of the sample at higher fields. The plateau-like dependence in the case of $B_\parallel \perp I$ can be explained by two competing mechanisms. On the one hand increasing $B_\parallel$ leads to an increased number of vortices at the outer parts of the sample which leads to an increase of L. On the other hand an in-plane field perpendicular to the current direction strongly enhances the pinning of vortices and hence reduce the inductance per vortex (see Fig. 6.10). The enhancement of the pinning strength with $B_\parallel \parallel I$ is much weaker and the misalignment of $B_\parallel$ and sample plane is larger compared with the first case (see Fig. A.5). This leads to a larger number of vortices with a higher inductance per vortex. In sum this can lead to the strong difference between the two curves.

It is not excluded that there are anisotropic effects of $B_\parallel$ on L_s. From the experimental findings, however, it is not sensible to draw definite conclusions. A repetition of the measurement in a more homogeneous out-of-plane field would need to be carried out, in order to exclude artifacts. The same holds for data of $L_s(T)$ measured in moderate in-plane fields, which are discussed in the following section.

A.1.2. Role of In-Plane Magnetic Fields

A commonly accepted feature for proving unconventional pairing with nodes in the gap is a power-law dependence of the superfluid stiffness (or inverse kinetic inductance) on temperature. In zero parallel field no hint towards such a dependence could be found. Application of an in-plane field breaks time reversal symmetry and hence anisotropies of the inductive response could be expected. The appearance of nodes of the superconducting gap in parts of the momentum space, induced by the in-plane field, could result in a non-exponential T-dependence of the kinetic inductance.

The temperature dependence of the kinetic inductance in different in-plane fields perpendicular to the main current direction is depicted in Fig. A.7. The magnetic field increase the low-T saturation value $L(0)$ due to orbital pair-breaking effects and reduces the critical temperature leading to a shift of the divergence of $L_s(T)$ to lower temperatures.
For $B_\parallel \leq 0.3\,\mathrm{T}$, $L_s(T)$ can nicely be reproduced by eq. 2.10. Although eq. 2.10 is strictly only valid in absence of any pair-breaking, it should be valid also for small $B_\parallel = 0.3\,\mathrm{T} \approx 0.1 B_{c\parallel}$. For $B_\parallel \geq 0.75\,\mathrm{T}$, eq. 2.10 grows slower than experimental data. Of course, in the presence of pair breaking, eq. 2.10 does not hold anymore and the functional dependence cannot be solved analytically anymore. Fitting of the data in this cases becomes technically challenging.
As it is known, that the compensation field is inhomogeneous, it is intuitive to check whether there is a signature of a finite out-of-plane at higher in-plane-fields. In this case the pure kinetic inductance would be complemented by a small portion of vortex inductance according to eq. 2.37. Data for $B_\parallel \geq 0.75\,\mathrm{T}$ are fitted to this equation with fixed critical temperatures, determined from DC $R(T)$-measurements (Fig. 6.3). It turns out that experimental data can nicely be reproduced if a hypothetic small vortex inductance of $L_v(0)_{B=0.75\,\mathrm{T}} = 2.46\,\mathrm{nH}$ and $L_v(0)_{B=1\,\mathrm{T}} = 4.2\,\mathrm{nH}$ is taking into account. These contributions would correspond to an effective out-of-plane field of $21\,\mu\mathrm{T}$ and $36\,\mu\mathrm{T}$ respecitvely, which does not seem unrealistic considering an absolute compensation field of the order of few mT (Fig. A.5).
Again, there is no evidence, that there is no unconventional in-plane field dependence of $L_s(T)$. A clear power-law behavior suggesting such an unconventional behavior besides from presumable vortex motion can not be resolved undoubtedly, however.

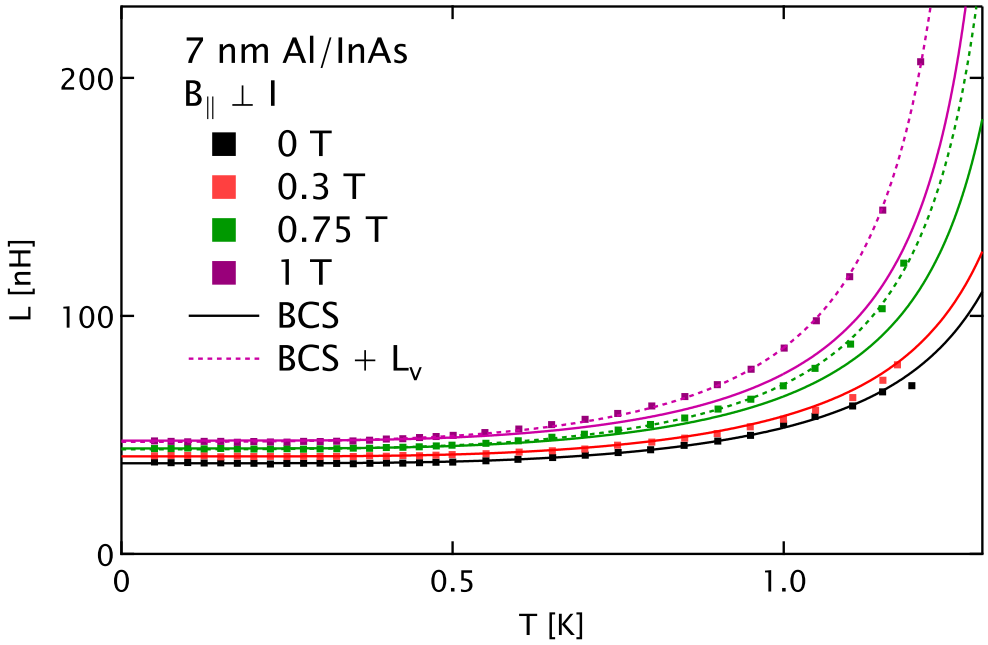

Fig. A.7.: Temperature dependence of the kinetic inductance for in-plane fields of $B_{\parallel} = 0, 0.3, 0.75, 1\,\mathrm{T}$. Solid lines are fits to eq. 2.10 with $T_c(B_{\parallel})$ as determined in Fig. 6.3 with free parameter $\lambda(0)$. For $B_{\parallel} \leq 0.3\,\mathrm{T}$ BCS fits reproduce experimental data. At higher fields experimental L increases faster than BCS curves. Dashed lines correspond to 2-parameter fits to eq. 2.37 with fitting parameters $\lambda(0)$ and $L_v(0)$, which accounts for a vortex contribution to L resulting from uncompensated areas of the sample. The contribution of vortices at low temperatures are $L_v(0)_{B=0.75\,\mathrm{T}} = 2.46\,\mathrm{nH}$ and $L_v(0)_{B=1\,\mathrm{T}} = 4.2\,\mathrm{nH}$ corresponding to an effective out-of-plane field of $21\,\mu\mathrm{T}$ and $36\,\mu\mathrm{T}$ respectively.

A.1.3. Duffing Oscillation for Large Driving Currents

Not only magnetic fields, temperature or DC currents can affect the inductive AC response of the superconducting film but also the AC current itself. In most cases the AC current is kept as high as possible for good signal to noise ratio but small enough not to have an impact on the inductance. A high AC current can increase the inductance either due to pair breaking effects reducing the superfluid stiffness, due to nonlinear displacement of vortices caused by the Lorentz force or because of heating effects.
Fig. A.8 shows spectra measured at low temperatures in zero in-plane field for different AC excitations ranging from 2 nA to 20 μA in a vortex-free and a vortex-carrying state in sample Al/GaAs-M15.

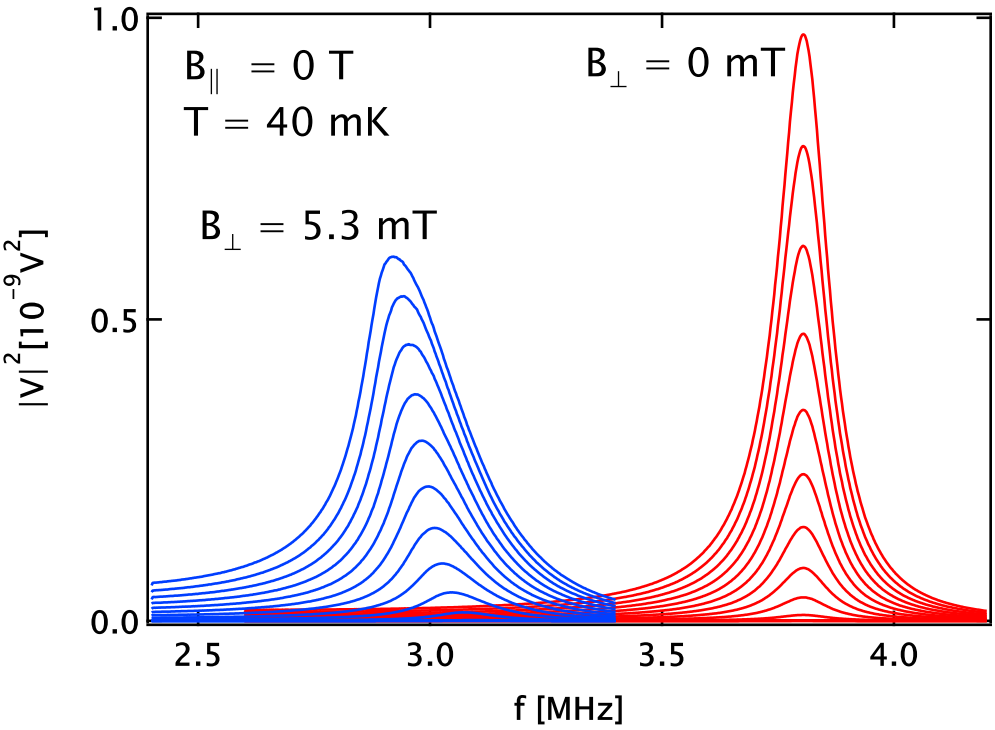

Fig. A.8.: Resonance spectra measured with excitation currents V_{bias}/R_D ranging from 2 μA to 20 μA in steps of 2 μA with (red) and without vortices (blue) present in the sample. The measurement was performed in zero in-plane field at low temperatures. Up to the maximal bias current the shape of the response in the vortex-free state remains harmonic.

For $B_\perp = 0$ the spectrum is only stretched in magnitude but the resonance frequency as well as its width stays constant. In a finite out-of-plane field, where the inductance is dominated by the response of pinned vortices the situation is strongly different. With increasing AC current the curves increase less and less in magnitude due to enhanced

damping and the frequency at which the signal is maximal shifts to lower frequencies due to an enhanced effective inductance due to pair breaking and non-linear vortex displacement. Furthermore the shape of the spectra are tilted towards lower frequencies which is the consequence of the non-constant AC current that flows in the sample branch of the RLC circuit. For $f < f_0$ the AC current increases with frequency peaking at the resonance frequency before decreasing again for high frequencies. If the current itself affects the inductance of the sample this creates a feedback and produces a Duffing-like oscillation, where higher order terms affect the vortex potential.
More in-depth studies on these non-linear effects could indeed be interesting as it could reveal more details of the non-linear pinning potentials in this system. As in this method one is often restricted to currents low enough that no Joule heating is induced in the decoupling resistors, increasing the AC current is a convenient tool for investigation of higher order current effects. This can be advantageous over the use of high DC currents, because the AC current which is flowing through the sample is amplified within the circuit as $I_{res} \approx Q\frac{V_{bias}}{R_D}$, whereas only the current $I_{AC} = V_{bias}/R_D$ heats up the preresistor.

A.1.4. Comparison of Vortex Dynamics in Different Meander Structures

Low-Field Vortex Pinning

The inductance measured at low temperatures as a function of out-of-plane field gives information about the pinning forces and mechanism in the different samples. Fig. A.9 shows $L(B_\perp)$ curves measured on meander structures of the same geometry for the three different Al films. All curves show a kink-like structure at a moderate field B_{kink}, which indicates probably the crossover to a different pinning regime. At this point the slope of $L(B_\perp)$ is reduced, however, maintaining a positive curvature. The corresponding inductance L_{kink} at this crossover point differs for the three curves and therefore an artifact resulting from a wrong data extraction procedure from the RLC resonance at high L can be excluded.

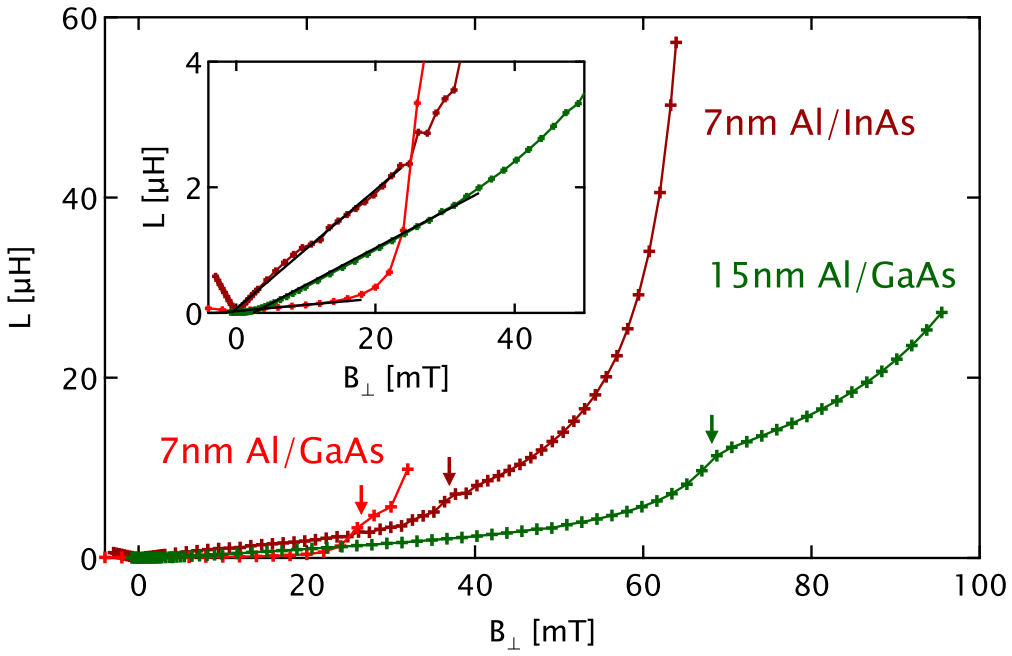

Fig. A.9.: Inductance as a function of $B_\perp$ for the three measured Al films. All three curves start with a linear dependence (inset), which is consistent with an individual pinning model. At higher fields the increase of L with $B_\perp$ increases up to a crossover field where there is a kink. From this point on $L(B_\perp)$ shows again accelerating behavior but with a decreased slope before it diverges near B_{c2}.

From the slopes at low fields pinning constant $k_p = \frac{\phi_0}{d}\left(\frac{\Delta L}{\Delta B_\perp}\right)^{-1}$ can be extracted, which is a measure for the strength of the individual defects in the different films. Dependence

of k_p on film thickness d is shown in Fig. A.10. The pinning constant can be estimated via [28]

$$k_p \approx \chi \frac{B_{c2}^2}{\mu_0}, \tag{A.2}$$

where the prefactor χ depends on the detail of the pinning. For core pinning where the defect size is of the order of the length of the vortex $\chi \approx 0.25$. In that type of pinning regime, the vortex is displaced from its equilibrium position without changing its length. For elastic vortices near strong pinning sites, however, there can be an additional pinning energy associated to the energy needed to deform the vortex and hence elongate it. In this case the vortex is fixed near the defect, while further away in the direction of the magnetic field the vortex is rather unpinned. Then the pinning is governed by the vortex line tension. In that limiting case χ should be much smaller. In general a mixture of both types is expected.

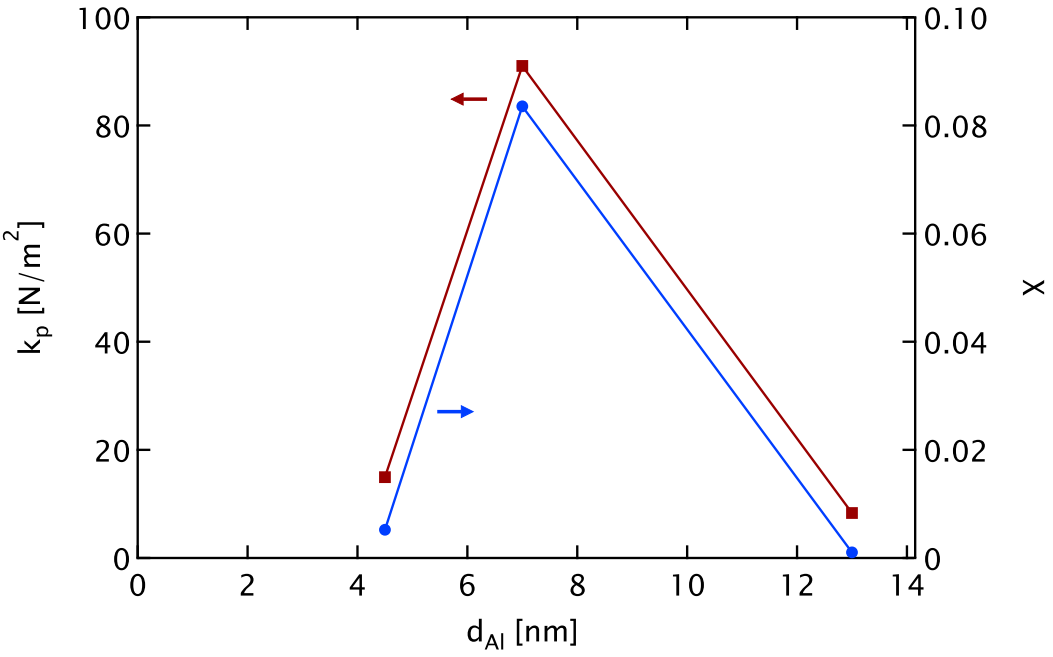

Fig. A.10.: Pinning constant k_p and prefactor χ from eq. A.2 for the different Al films. The thinnest and thickest films show a small χ, which hints towards a pinning mechanism mainly governed by elastic deformation of the vortices, while in the 7 nm film χ is larger and hints towards a stronger contribution from core pinning.

Besides different absolute values for k_p the different Al films show different scaling factors χ used in eq. A.2. The thinnest and thickest Al films have a small value of χ, which can be a hint towards pinning that is mainly controlled by the elasticity of the vortex, while

in the film with intermediate thickness pinning may be mainly governed by core pinning. In the 15 nm thick film it can be understood from small defects that locally pin the vortex while most of the rest of the vortex can be displaced relatively easily. In the thinnest film this should be suppressed strongly. Taking into account, however, that there is a proximitized superconducting layer in the 2DEG underneath the Al the effective length of the vortex can be much longer. While defects are expected to be mainly in the Al layer or at the interfaces to the AlOx or the semiconductor the vortex in the 2DEG can stay relatively unpinned and hence restoring forces due to elastic deformation should be the main source of pinning.

High-Field Vortex Pinning

At higher out-of-plane fields it was shown that there is a crossover to a different pinning regime in the Al/InAs heterostructure which changes the slope of the $L(B_\perp)$-dependence of sample Al/InAs-M (see Fig. A.11). In this regime the impact of an additional in-plane field is strongly different than in the low-$B_\perp$-regime. Whereas the low-field $B_\perp$-dependence is strongly affected by $B_\parallel$, the high-field regime seems to be less affected. For fields $B_\parallel \leq 0.5\,\mathrm{T}$, the $L(B_\perp)$-dependence changes strongly from linear to superlinear, whereas the crossover field is barely altered. At larger $B_\parallel$ the field $B_\perp$ at which L finally diverges is shifted towards lower values. This is consistent with a pair-breaking contribution from the in-plane field, which reduces the superfluid stiffness and thus also B_{c2}.

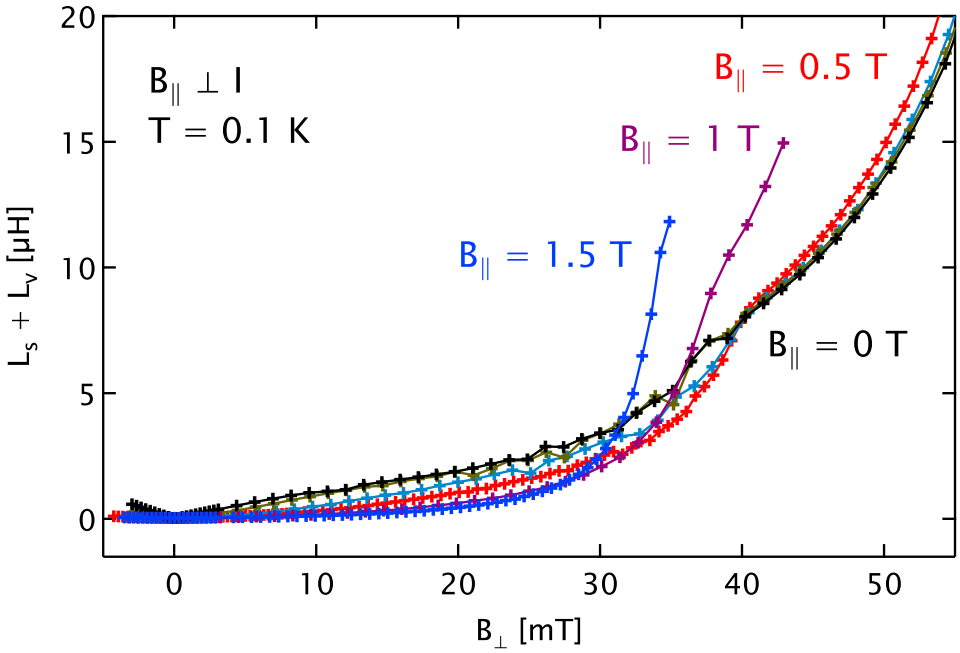

Fig. A.11.: Inductive response of the Al/InAs heterostructure as a function of $B_\perp$ for different in-plane fields perpendicular to the driving current. For moderate $B_\parallel$ high-field $L(B_\perp)$ is nearly uneffected.

One possible explanation would be that at high $B_\perp$ vortex core size $\sim 2\xi$ increases [90] and hence the influence of single defect pinning reduces. Furthermore as $\Lambda = 2\frac{\lambda^2}{d}$ increases at higher fields interaction of vortices with other vortices and Meissner currents at the edges of the sample become stronger, which could eventually become dominant over single defect pinning.

Fig. A.12 shows the dependence of the crossover field B_{kink} normalized with B_{c2} as a function of normalized in-plane field. For $B_{\parallel} = 0$ the crossover field is of the order of $\sim \frac{2}{3}B_{c2}$. In-plane field dependence was measured for the Al/InAs heterostructure and the 15 nm thick Al/GaAs film and seem to more or less have the same dependence.

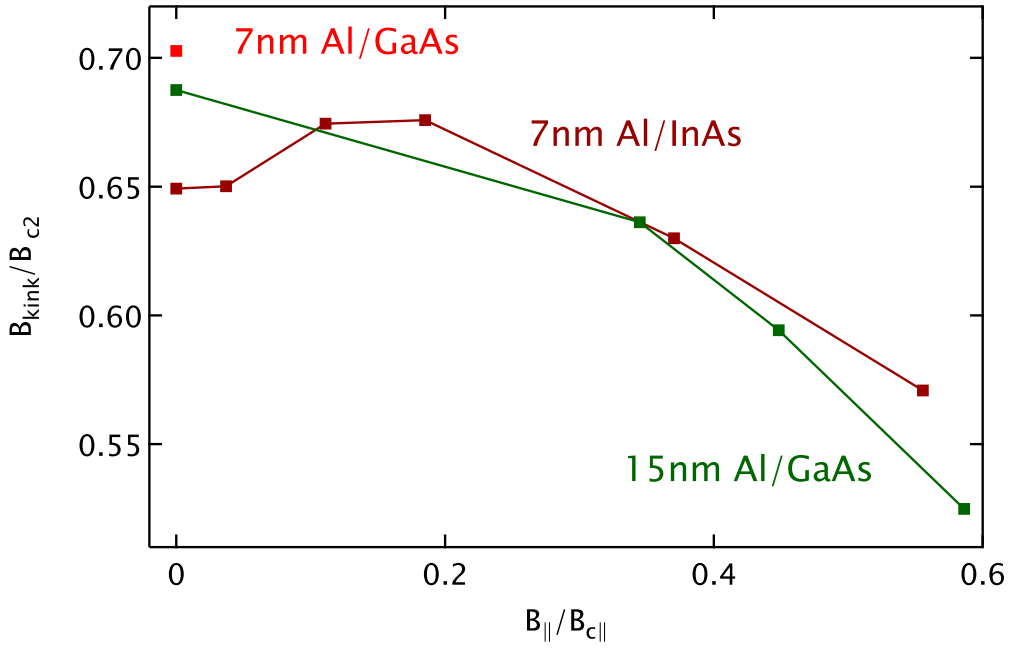

Fig. A.12.: Dependence of crossover field B_{kink} normalized with B_{c2} as a function of normalized in-plane field $B_{\parallel}/B_{c\parallel}$. The curves look similar with a characteristic crossover field of $\sim \frac{2}{3}B_{c2}$ in zero in-plane field.

A.1.5. Stabilization of Vortex Lattice in In-Plane Fields

Another important parameter in the context of superconducting properties is the applied current. A finite current on the one hand accelerates the superfluid which leads to pair breaking effects and hence usually increases the kinetic inductance. On the other hand in the presence of an out-of-plane magnetic field a current produces a finite Lorentz force on the vortices either displacing them from their equilibrium position in the pinning potential or for high enough currents pushing them out of the pinning potential. The presence of vortices in a DC transport measurement can only be cofirmed when there is already a finite resistance. In the dissipationless regime, the presence or absence of vortices cannot be probed in DC. Measurement of the commplex impedance of pinned vortices can only be done with an AC experiment.

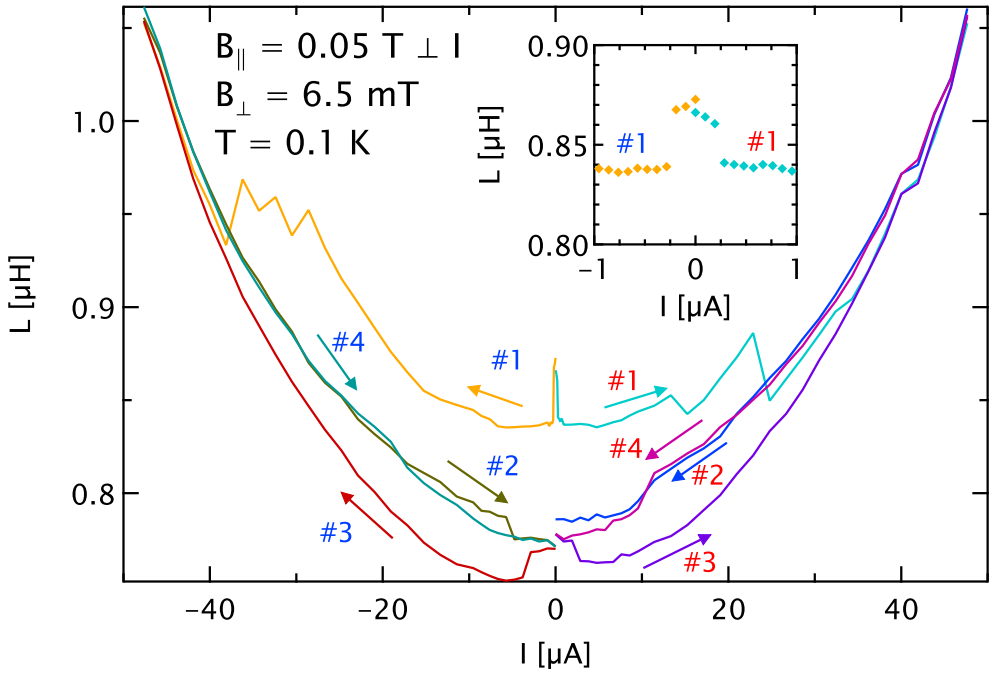

Fig. A.13.: Vortex inductance as a function of superimposed DC current in a transverse in-plane field of 0.05 T. Arrows indicate the sweep direction, curves labeled with the same color of the corresponding number were performed in a single sweep. Numbers 1 to 4 represent consecutive sweep sections. Between the measurements in negative and positive current direction the sample was heated up, the proper field was set before it was cooled down again in absence of any DC or AC bias. On top of a parabolic dependence on the DC bias small jumps to lower inductance values are observable. Inset shows magnified $L(I_{DC})$ at the beginning of the two sweeps.

In order to shine light on the symmetries of the system inductance was measured as

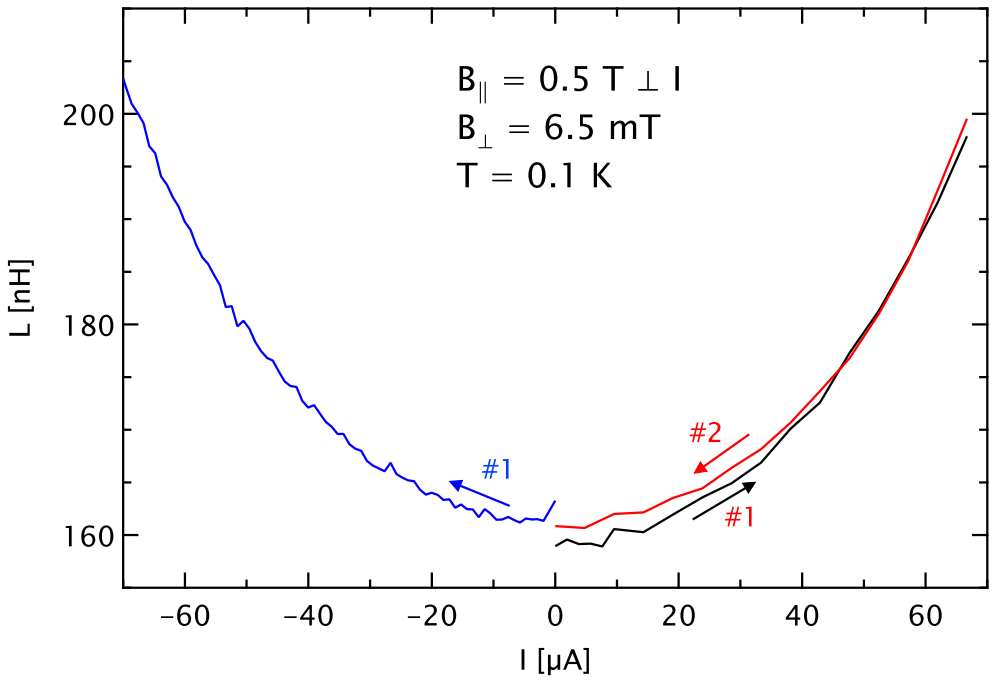

Fig. A.14.: Vortex inductance as a function of superimposed DC current in an in-plane field of 0.5 T perpendicular to the current. Compared with Fig. A.13 the curves are much flatter without big jumps and the relative increase of L_v with DC current is much less.

a function of applied DC current. Non-reciprocal effects of the vortex pinning and/or motion should then be reflected as asymmetries when a DC current is superimposed on the AC excitation. Fig A.13 shows measurements of the vortex inductance in an out-of-plane field of 6.5 mT and an in-plane field perpendicular to the main current direction of 0.05 T. Starting from $I_{DC} = 0$, $L_v(I_{DC})$ at first decreases probably due to hopping of only weakly pinned vortices occupying shallow pinning potentials to pinning sites with deeper potential. A more or less parabolic, monotonic dependence of the vortex inductance on the DC bias follows with distinct jumps to smaller inductance values. These jumps may result from rearrangement of initially stronger pinned vortices to even deeper pinning potentials. Although the curves are not totally symmetric, no clear sign for a non-reciprocal behavior can be found in this measurement. Probably the DC current is simply to large and way above the linear regime of non-reciprocal behavior. Much more importantly the sample is nearly symmetric in the main current direction. In the sample there is only one segment more that carries current in the [110]-direction than segments with current in the opposite direction. This means that non-reciprocal effects that arise from a two-fold antisymmetric effect should cancel out

almost completely..
What this measurement shows, however, is that especially for small in-plane fields and small currents there is a steep decrease of the inductance at the very beginning of the measurement. This reflects again the very unstable vortex lattice in small in-plane fields. This is also consistent with the large run-to-run scattering of the measured inductance values in finite out-of-plane fields and small in-plane fields in Fig. 6.10. Furthermore it shows that increased in-plane field reduces strongly the dependence of L_v on the applied DC current. This shows that not only the inductance produced by the vortex lattice is reduced strongly in the case where vortices sit in the minimum of the pinning potential ($I_{DC} = 0$) but also when vortices are displaced by a DC current.
Fig. A.15 shows the temperature dependence of the mixed vortex and kinetic inductance for constant vortex density ($B_\perp = 10\,\mathrm{mT}$) in an in-plane field of 0.5 T. As already seen, there is a strong reduction of the inductance when the in-plane field is applied perpendicular to the current direction. The overall behavior can nicely be reproduced by eq. 2.37. The data taken with an in-plane field perpendicular to the current is rather flat and therefore pinning is enhanced strongly.

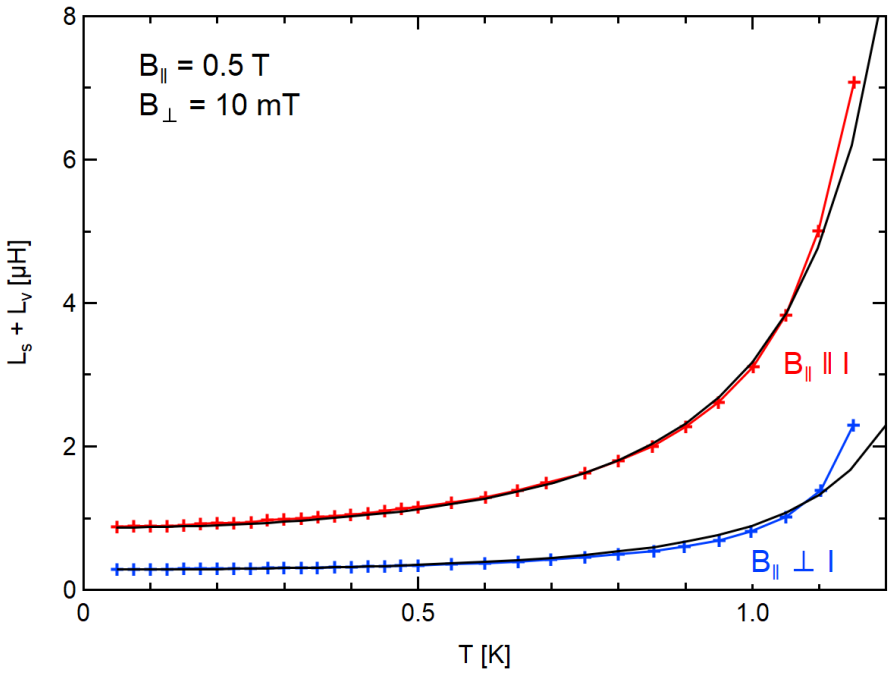

Fig. A.15.: Temperature dependence of vortex inductance for $B_\perp = 10\,\mathrm{mT}$ in an in-plane field of 0.5 T parallel (red) and transverse (blue) to the current direction. Solid lines are fits to eq. 2.37.

A.2. Temperature Dependence of Non-Reciprocal Supercurrent

For a single in-plane field of 0.3 T perpendicular to the $[1\bar{1}0]$ current critical currents were measured for elevated bath temperatures. Fig. A.16 displays $I_c(B_\perp)$ measured for different temperatures. The threshold condition for I_c leads to artifacts when the sample is in the normal state (for high fields or temperatures), because then the normal resistance already is sufficient to produce a voltage larger than V_{th} at a current $I_{sat} = V_{th}/R_n$. At high fields this leads to a saturation of the extracted critical current at I_{sat}. This needs to be kept in mind when further analyzing I_c data.

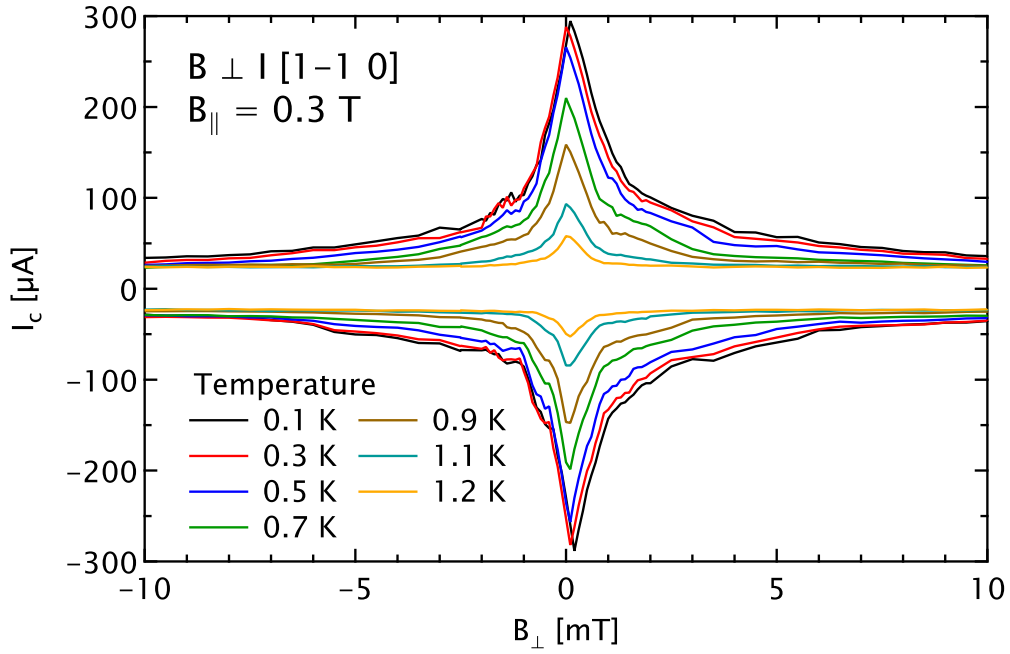

Fig. A.16.: Evolution of critical currents with temperature in an in-plane field of 0.3 T. Measured temperatures were $0.1, 0.3, 0.5, 0.7, 0.9, 1.1, 1.2, 1.3$ K. The critical current was extracted from IV-curves where I_c was defined as the current producing a certain threshold voltage V_{th}.

From the data of Fig. A.16 the critical current for both positive (I_c^+) and negative polarity (I_c^-) can be extracted at $B_\perp$, where $I_c^+(B_\perp)$ is maximal. $I_c(B_\perp)$ for opposite polarities of the current are shown in Fig. A.17. For both polarities I_c decreases with temperature as the critical current depends on the superfluid stiffness which decreases with temperature. $I_c(T)$ roughly follows a T-dependence

$$I_c(T) = I_c(0)\left(1 - T^2/{T_c}^2\right)^{3/2} \tag{A.3}$$

with $I_c(0) = 280\,\mu$A and $T_c = 1.49\,$K proposed by Bardeen [91].

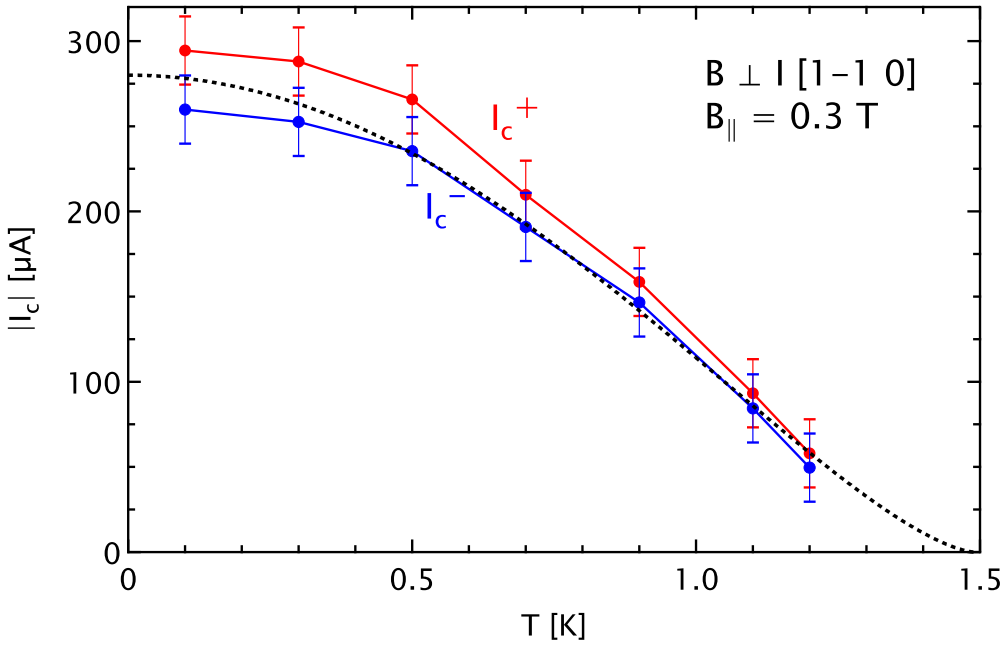

Fig. A.17.: Critical currents as a function of temperature for an in-plane field of 0.3 T perpendicular to the [1$\bar{1}$0] current direction. The dashed line is a phenomenological fit eq. A.3. The inset shows the relative difference of the critical current defined in eq. 7.3.

The absolute and relative differences $\Delta I_c(T)$ and $\delta I_c(T)$ is shown in Fig. A.18. $\Delta I_c(T)$ is highest at low temperatures and initially decreases with increasing temperature. For $T > 0.9\,$K, $\delta I_c(T)$ increases again. Temperature dependence of the rectification of supercurrent in Rashba superconductor exposed to a transverse in-plane field was calculated recently in a clean system and predicts a decrease of $\delta I_c = \frac{\Delta I_c}{|I_c|} \propto \sqrt{1 - \frac{T}{T_c}}$ near T_c [8]. The expected decrease of $\delta I_c(T)$ with temperature is found in the experiment at intermediate temperatures. At higher temperatures, however, the measurements shows a steep upturn. As the transition is probably BKT-like, there could be deviations from the theory near T_{BKT}.

Critical current values and the relative difference for opposite directions for $B_\perp = 0.5, 1\,$mT as a function of temperature are shown in Fig. A.19. $\delta I_c(T)$ decreases with increasing temperature for $B_\perp = 1\,$mT. In the model of Hoshino et al. [45] for a vortex ratchet effect in trigonal systems, a $1/T$ dependence for $T \to 0$ of the non-reciprocal coefficient γ is predicted. Although γ in this case is related to the magnetochiral effect of the resistance, an impact of the in-plane field on the depinning current can be expected.

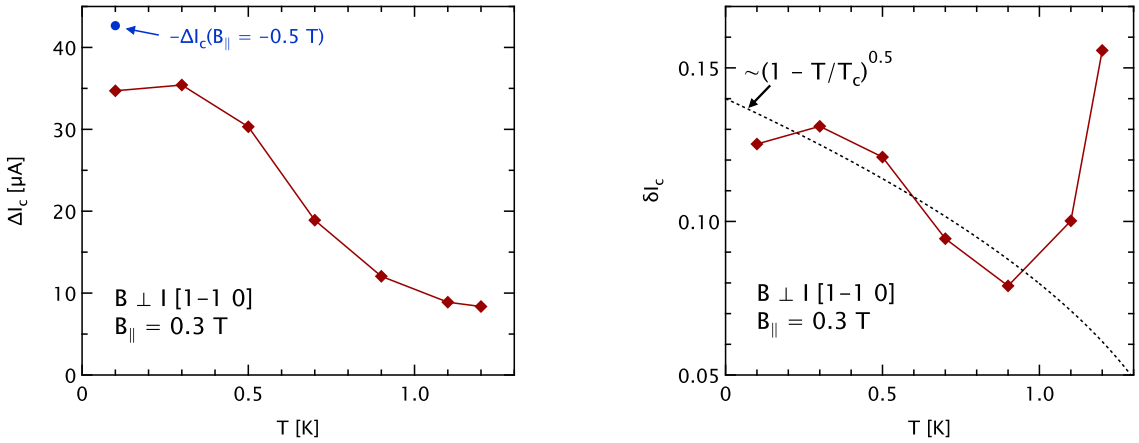

Fig. A.18.: Left: ΔI_c at $B_\perp(I^+_{c,max}) \approx 0$ as a function of temperature. The blue dot was measured as a reference in an in-plane field of $-0.5\,\mathrm{T}$. Right: Normalized $\delta I_c(T)$ as defined in eq. 7.3 in an in-plane field of $B_\parallel = 0.3\,\mathrm{T}$. Dashed line is a Ginzburg-Landau theory curve calculated in [8].

As one probes the point of maximal slope of the pinning potential with the critical current, there is a strong indication that pinning is indeed asymmetric and decreasing with temperature for tranverse in-plane magnetic fields.

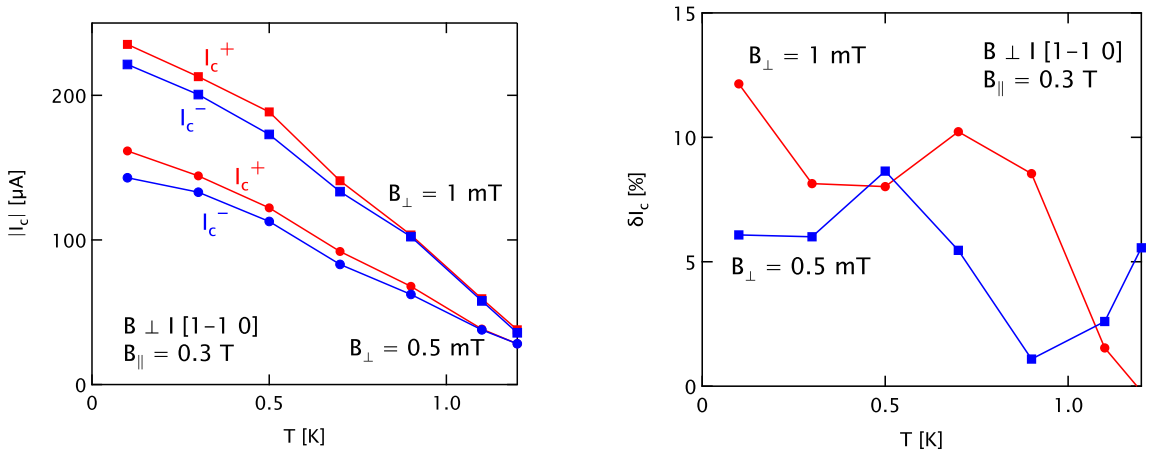

Fig. A.19.: Left: $|I_c|$ as a function of temperature for $B_\parallel = 0.3\,\mathrm{T}$ and $B_\perp = 0.5, 1\,\mathrm{mT}$. Right: Relative anisotropy δI_c as defined in eq. 7.3 as a function of temperature.

A.3. Non-Reciprocal Transport Measurements

A.3.1. Asymmetric Pinning Probed by Slow IV-Measurements at High Temperatures

At higher temperatures due to the much smaller critical current superfluid and vortex dynamics instead of applying fast current ramps can be probed by standard 4-point DC measurements providing the full information of the resistive response to a DC driving current. Fig. A.20 shows IV-characteristics for the $[1\bar{1}0]$ current direction in a transverse in-plane field of $-0.3\,\mathrm{T}$. A constant DC offset of the multimeter of $\sim -1\,\mu\mathrm{V}$ was carefully subtracted for each curve.
For temperatures slightly below the critical temperature $1.42\,\mathrm{K} < T < 1.445\,\mathrm{K}$, a clear signature of magnetochiral anisotropy of the resistance can be found. For temperatures above and below that region the branches for positive and negative branches collapse. This is in good agreement with findings that the γ_s - value, which is responsible for the rectification process, has its maximum near T_{c0} and/or near T_{BKT} in the 2D Rashba systems.

In an additional small out-of-plane field $B_\perp = \pm 2\,\mathrm{mT}$ vortices enter the system. The resistive response is then mainly given by viscous vortex motiont. Corresponding IV-traces are shown in Fig. A.21. There again a strong splitting of the positive and negative branches of the IV-characteristic can be observed. The strongest splitting for both $B_\perp$ directions is at $T = 1.26\,\mathrm{K}$. Again the IV-characteristic depends on the relative orientation of in- and out-of-plane magnetic field. Therefore the two graphs are different under reversal of $B_\perp$. The origin for the splitting could be either non-reciprocal viscous vortex flow when pinning is still weak near T_c or asymmetric pinning [45].
Measured data again are strongly reminiscent of measurements on systems with artificial asymmetric pinning potentials (Fig. A.22) [85].

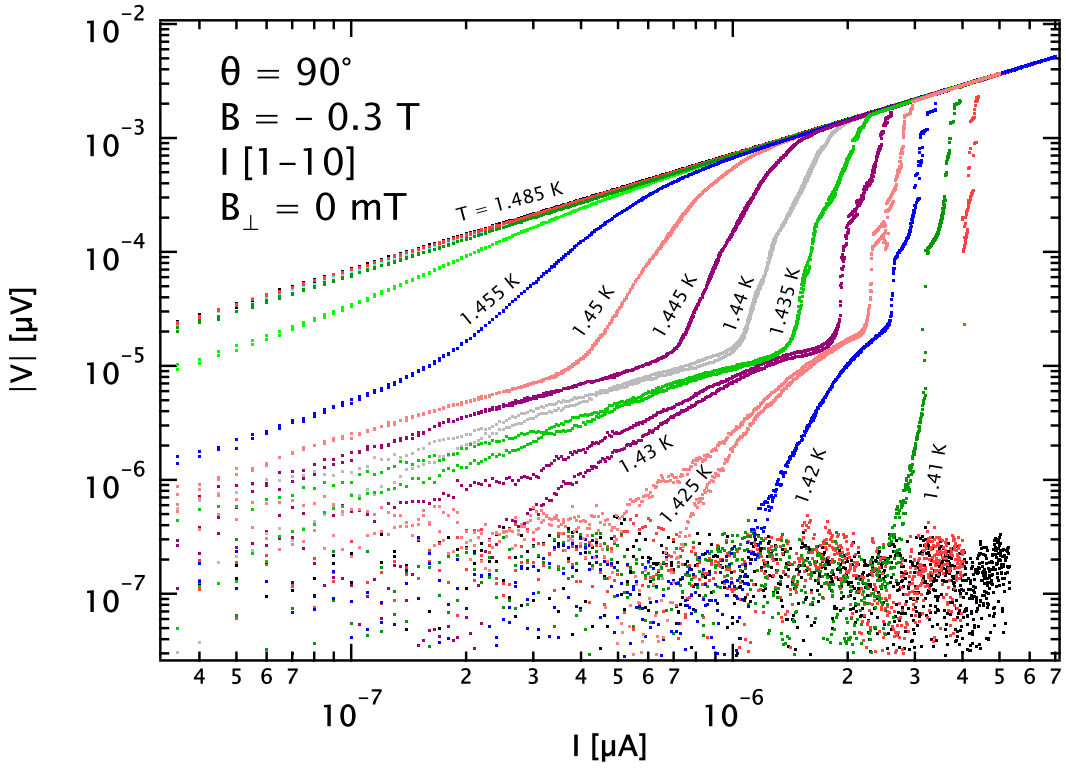

Fig. A.20.: IV-characteristic for the $[1\bar{1}0]$ current direction for different temperatures ranging from 1.4 K to 1.485 K in steps of 0.005 K in an in-plane field of -0.3 T. For comparison negative branches of the IV-curves are mirrored from the third quadrant to the first. The mirrored curves $|V^-|(-I)$ are reaching a constant voltage level systematically at higher currents (on the right side) than $|V^+|(I)$.

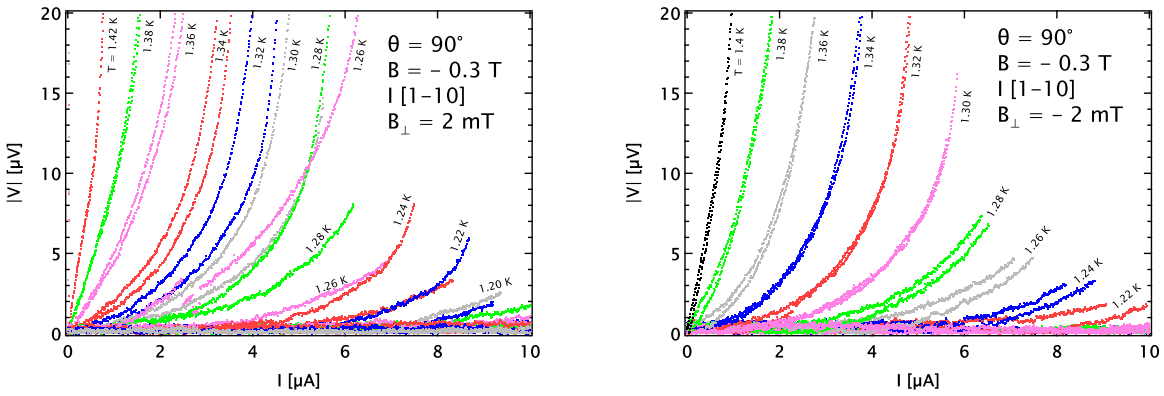

Fig. A.21.: IV-characteristics for mixed in- and out-of-plane magnetic fields for different temperatures ranging from 1.1 K (right) to 1.4 K (left) in steps of 0.02 K. Each color corresponds to a fixed, constant temperature. For better visibility data for the negative current and voltage branch are mirrored into the positive quadrant. For most temperatures not too far away from T_c negative and positive branches are split. The splitting is systematic, i.e. for each temperature the mirrored negative branch of the curve is either left or right of the positive branch. $B_{\parallel} = -0.3\,\mathrm{T}$, $B_{\perp} = 2\,\mathrm{mT}$ in the left graph, $B_{\perp} = -2\,\mathrm{mT}$ in the left graph.

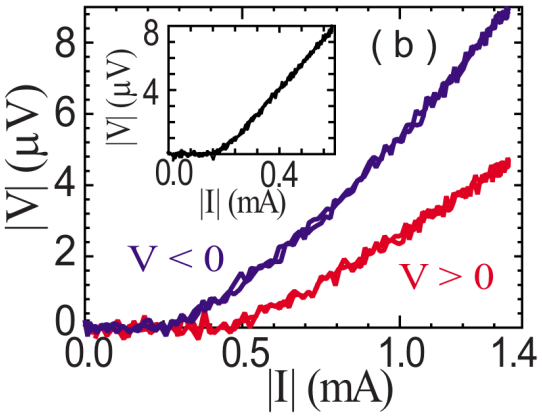

Fig. A.22: IV-characteristics measured in a small out-of-plane field in a superconducting strip with artificial asymmetric pinning potential. Picture taken from [85].

A.3.2. Non-Reciprocal Transport in Al/InAs - Field vs. Crystal Orientation

As was shown in Fig. 7.14, the sign and strength of non-reciprocity in out-of-plane fields depends on the current and therefore crystal direction. For that reason sample Al/InAs-C was designed to measure the dependence of the non-reciprocal transport properties of the material as a function of the relative orientation of current with respect to the crystallographic axes. The sample was again designed and produced by Christian Baumgartner. An optical micrograph of the sample is shown in Fig. A.23. A quite similar sample design as for sample Al/InAs-S was used, however, instead of etching out only three different strips, 21 conducting channels were etched out of the material. Each of the segments has a difference in angle with respect to the neighboring wires of 15 °.

R_ω and $R_{2\omega}$ was measured as a function of temperature and perpendicular field for all the different current directions. Fig. A.24 shows data for an out-of-plane field of 0.2 mT.

There is clear indication that the non-reciprocal signal strongly depends on the relative current direction with respect to the crystal axes. The peaks of the second harmonic resistance show both signs depending on the orientation and also sign changes within one temperature sweeps occur at some angles. Depending on the sign of γ_S for the fluctuation or BKT regime, the $R_{2\omega}$ curve either shows a negative and positive peak or a single extremum with only one peak. As the temperature regimes continuously evolve from one into the other, it is difficult to discriminate one from each other in order to be able to draw a picture of the maximal achievable $R_{2\omega}$ as a function of angle between current and crystal axis.

It can be stated that although it is difficult to draw definite conclusions regarding the symmetries of the system there seems to be some kind of systematics. As for most current directions the shape of the $R_{2\omega}(T)$ curves do not change dramatically from one angle to the next, the curves do not seem to be totally randomn. In the supplementary material of [92] no systematic dependence of the asymmetry of critical current of a Josephson junction on crystal orientations is reported. In this publication, however, critical currents have only be analyzed at the maxima of the Fraunhofer pattern side lobes at rather high $B_\perp > 1\,\mathrm{mT}$ in finite in-plane fields of different orientation. Measurement of the present sample in a more homogeneous out-of-plane field in a vector magnet and better

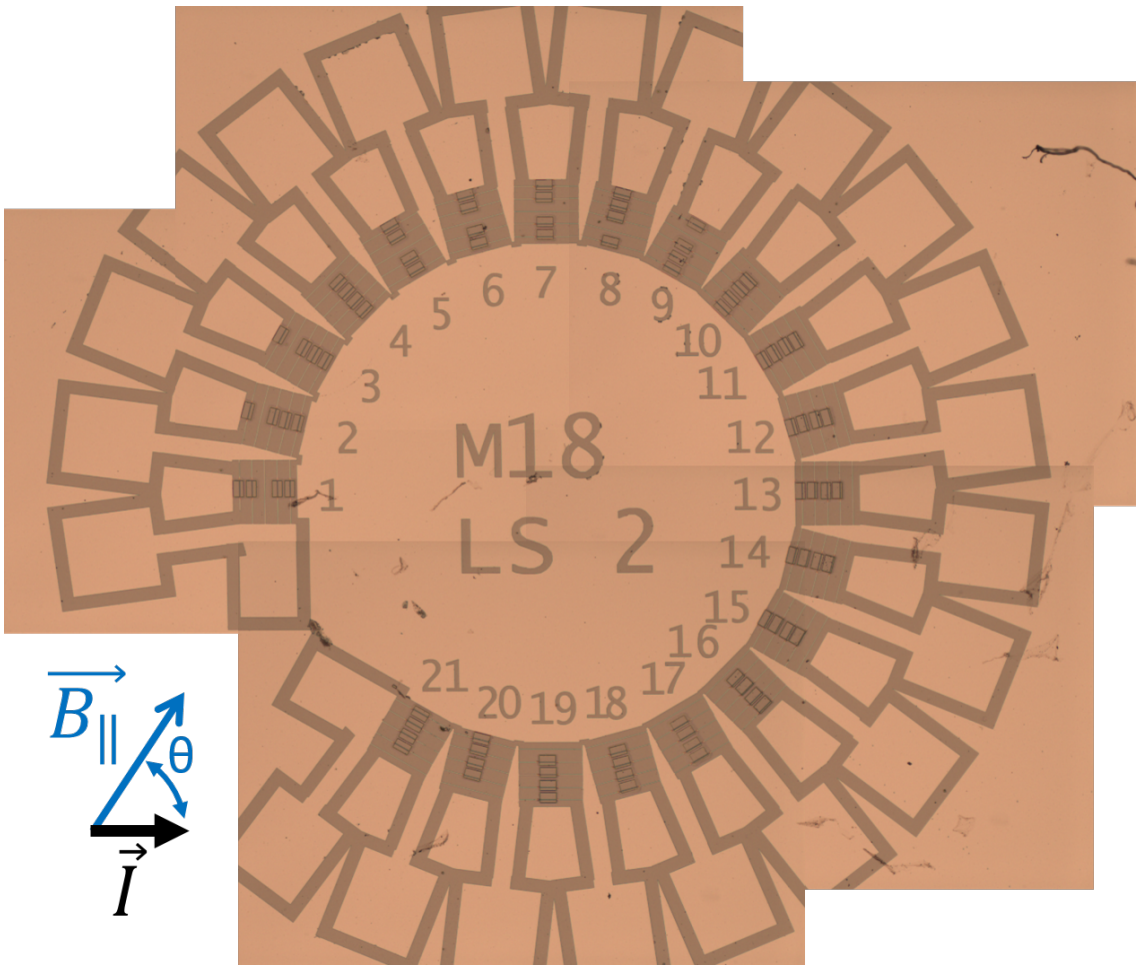

Fig. A.23.: Optical micrograph of sample Al/InAs-C. The bright parts are the pristine film, the darker parts have selectively been etched away. The sample consists of 21 stripes with a length of 200 μm and a width of 2.3 μm. The voltage drop produced by a driving current can be measured for each segment separately. The relative current directions with respect to the crystal axes change by 15 ° from segment to segment covering a total range of 270 °.

temperature control could shine light on the symmetry of the system. Discriminating anisotropic vortex motion or out-of-plane spin components as possible origins of the measured features could be crucial to understand the superconducting properties of the Al/InAs heterostructures. Especially a possible perpendicular spin-texture, so far not treated in literature for this system, could strongly affect interpretation of data collected in devices of this kind of material in out-of-plane fields.

There is one experimental finding that should still be mentioned here. Before measuring the single segments of the sample test measurements were performed, where voltage probes were kept the same while the current was applied to the sample through different contact pads. For example, voltage was measured over segment 15 while for the bias

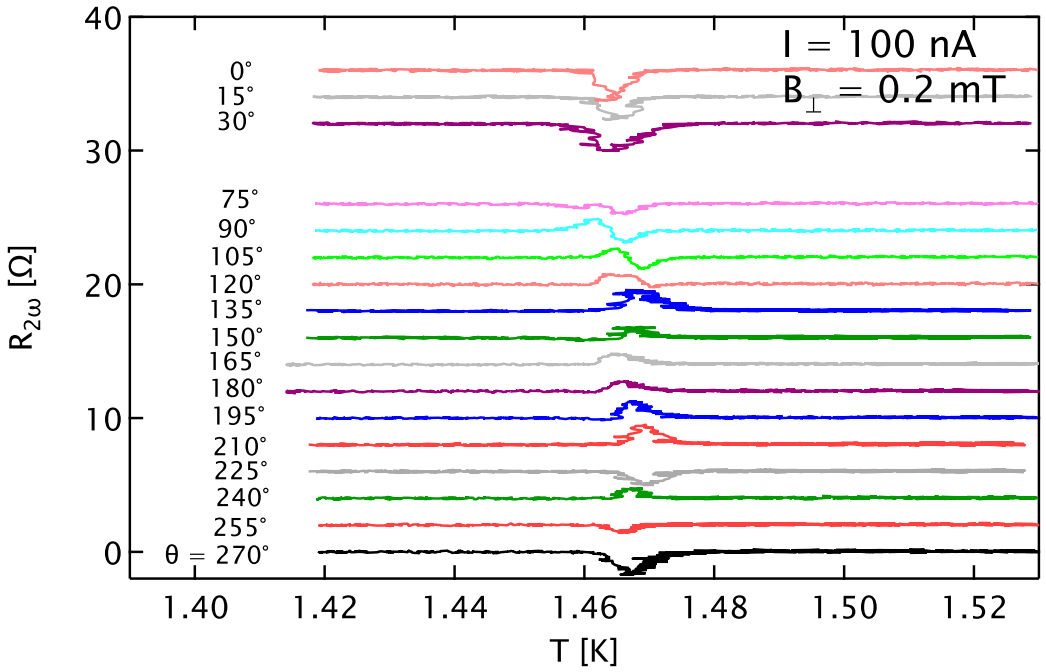

Fig. A.24.: $R_{2\omega}$ as a function of temperature for different current directions in a constant out-of-plane field of 0.2 mT. For clarity the curves have been separated vertically by 2Ω. An angle of 0° corresponds to current in the direction of segment 19 in Fig. A.23 i.e. in the horizontal direction.

current once contacts at the very end of the ring were used. At a subsequent measurement contact pads directly neighboring the voltage probes were used. As expected the R_{ω} signal turned out to be unaffected, $R_{2\omega}$ in contrast was strongly altered. Further measurements revealed that this was due to a change of the DC bias offset current that via frequency mixing strongly affects $R_{2\omega}$. After carefully nulling the DC offset for each single contact configuration similar curves could be recorded. The origin for the different DC current offsets for the different contact configurations are unclear. As the used measurement leads are all of the same material and passing through the same kind of copper powder filters thermal voltages can be excluded.

A.3.3. Out-of-Plane Spin Texture in Josephson Junction Arrays

Polarity dependent critical current and resistance was measured in sample Al/InAs-S in out-of-plane fields at low and high temperatures, respectively. It is assumed that these effects arise from an out-of-plane spin texture resulting from broken crystal symmetries at the interface of Al and 2DEG. As the Al layer alone should not have significant SOC, it is of special interest if the unexpected out-of-plane spin texture has its origin in the 2DEG. In order to probe a possible polarity dependence of resistance or supercurrent in the 2DEG, the natural choice is to measure the 2^{nd}-harmonic resistance of a Josephson junction in a small out-of-plane field, where the resistance and critical current is mainly determined by the semiconducting weak link, which hosts the 2DEG.
Sample 1D_JJ1 was designed and produced by Christian Baumgartner. It consists of a chain of 2250 Al/InAs/Al Josephson junctions made from the same Al/InAs material. The chain is 3.15 μm wide, the single junctions are 100 nm long, which makes them behave as junctions in the short ballistic limit. Fig. A.25 shows a microscopic picture of the sample and a Fraunhofer pattern characterizing the dependence of critical current of the chain on an external out-of-plane field. The sample was intended to measure the effect of an in-plane field on the junction behavior. With the findings in sample Al/InAs-S in mind, however, also a potential emergence of non-reciprocal transport caused by an out-of-plane field could be expected in such kind of structures.

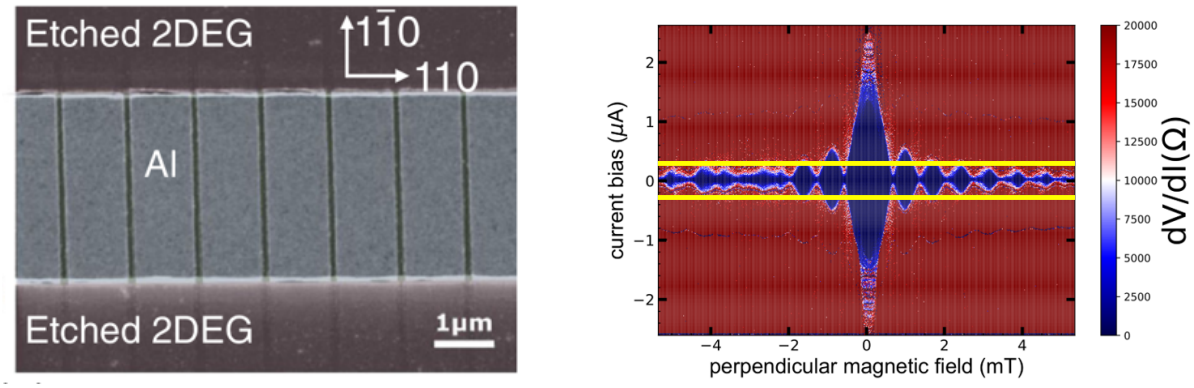

Fig. A.25.: Left: Optical Microcgraph of sample 1D_JJ1 taken by Christian Baumgartner. The structure consists of 2250 Josephson junctions in series that have been etched into the 7 nm thick Al/InAs. The weak link of the junctions consist of 200 nm wide areas of pure InAs where the Al has been etched away selectively. Right: Fraunhofer pattern measured by Christian Baumgartner at low temperatures showing dependence of critical currents of the junction array on an external out-of-plane field. Yellow lines indicate the AC current amplitude used for the measurement of non-reciprocal transport.

After the pre-characterization by recording a Fraunhofer pattern (right side of Fig. A.25)

an AC excitation of 200 nA was applied large enough to overcome the critical current in parts of the investigated $B_\perp$ range. Beforehand the DC offset current was carefully nulled to exclude artifacts in the $V_{2\omega}$ signals (see section 3.3.2). Second harmonic signals resulting from bad DC offset compensation, however, are easily distinguished from field induced asymmetries, because they can be measured even in zero magnetic field. Therefore it is possible to compensate the DC offset by finding the absolute minimum of the second harmonic signal as a function of DC current with an AC current amplitude high enough to overcome I_c in zero field.

First and second harmonic voltage responses as a function of out-of-plane field are shown in Fig. A.26.

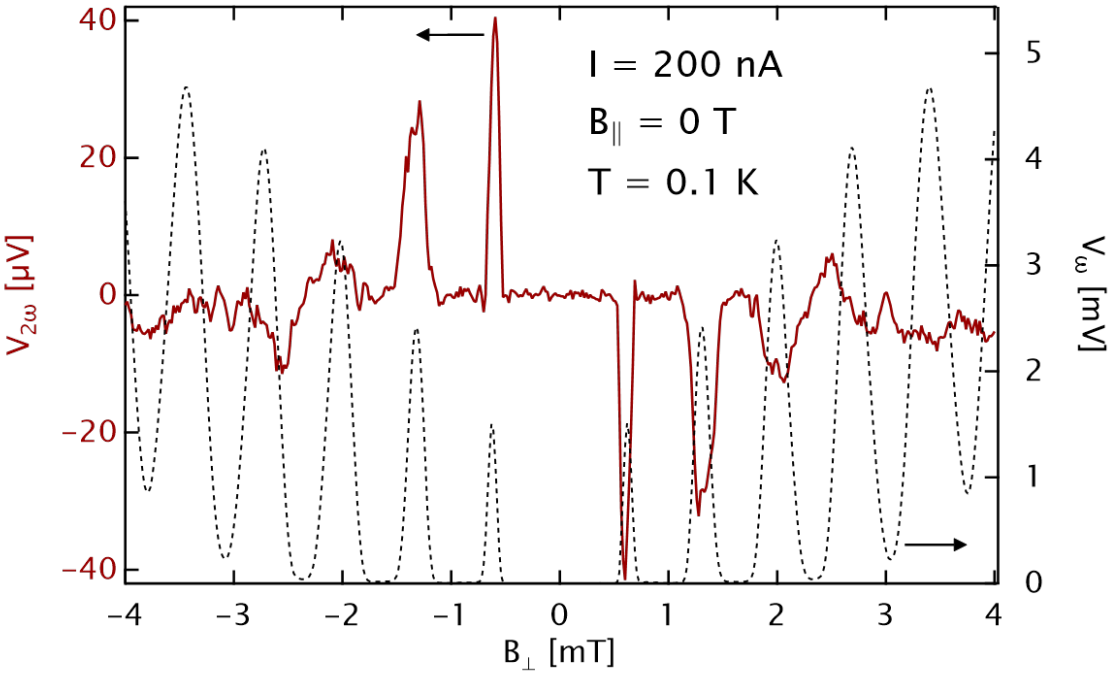

Fig. A.26.: First (V_ω) and second harmonic ($V_{2\omega}$) signals as a function of out-of-plane magnetic field measured at low temperatures. At fields where $I_{AC} > I_c$ finite voltages can be measured as the lock-in amplifier then probes resistive parts of the IV-characteristics. Finite second harmonic signals indicate asymmetries in the IV characteristics sensitive to the field direction.

For out-of-plane fields where $I_{AC} > I_c(B_\perp)$, a finite V_ω is observed due to the finite resistance for currents $> I_c$. $V_\omega(B_\perp)$ shows an oscillating behavior as the $I_c(B_\perp)$ becomes small in the nodes of the Fraunhofer spectrum. $V_\omega(B_\perp)$ is symmetric in $B_\perp$ similar to the Fraunhofer pattern. $V_{2\omega}(B_\perp)$ shows positive and negative peaks whenever also $V_\omega(B_\perp)$

is non-zero. A second harmonic voltage can only be measured if the critical current is polarity dependent. As the sign of $V_{2\omega}(B_\perp)$ depends on the polarity of $B_\perp$, this cannot be an artifact of bad compensation of a DC current offset. This measurement therefore shows evidence for a supercurrent rectification in Josephson junctions in Al/InAs heterostructures induced by an out-of-plane field at low temperatures.

Non-reciprocal transport in purely out-of-plane fields was also reported for a Josephson junction made from a similar heterostructure with a 20 nm thick Al film in [93]. In this work a finite difference of differential resistance $\Delta R = R(+B_\perp) - R(-B_\perp)$ at a fixed DC current for opposite directions of $B_\perp$ is shown, which is another hint towards a non-trivial out-of-plane spin texture. A $B_\perp$-direction dependent differential resistance ΔR in the main lobe of an asymmetric SQUID was also reported in a similar kind of Al/InAs heterostructure with a 10 nm thick Al film [94].

The observations in Fig. A.26 has various consequences. First it shows that the rectifying process is not only present in the fluctuation regime of the superconducting transition (in this case of the transition of the Josepson junctions), that relies on an already finite resistance, but it is directly affecting the critical current making it a 'true' superconducting diode tunable with an out-of-plane field. Second, it proofs that non-reciprocal transport in out-of-plane fields can not only be measured in structures where the 2DEG is covered with Al but also in parts of the material where the InAs is uncovered. In a previous work it was shown that in-plane fields lead to a strong second harmonic signal in the fluctuation regime of the transition of a Josephson junction array due to the large Rashba fields in the semiconductor weak link [95]. As the Josephson effect strongly depends on the properties of the semiconducting weak link and the resistance of the device is dominated by the junction resistances there is strong indication that either ouf-of-plane spin-orbit field components also could exist in the 2DEG itself or that the spin-orbit fields in the Al banks strongly affect the junction behavior. More importantly these findings show that in Josephson junction experiments the role of the out-of-plane field as a pure source of phase difference between the two Al banks has to be complemented by a direct effect of $B_\perp$ on the transport properties of the junction.

A.4. Challenges of Inhomogeneous Compensation Fields

There are several hints towards an inhomogeneous field produced by the pair of small compensation coils. Because the coils are assembled inside the big magnet solenoid they have a small diameter and are far away from being in Helmholtz configuration. This leads to inhomogeneities on the mm scale. For large samples in finite in-plane fields this can become problematic, because then it is not possible to compensate an out-of-plane field component, produced by a small misalignment of the vertical field and sample plane, equally precise over the whole area of the sample. For high-inductance samples like Josephson-Junction arrays or vortex lattices in finite out-of-plane fields this inhomogeneity can be neglected most of the time. However, also in large arrays of Josephson junctions, different effective $B_\perp$ on the sample, can for example lead to a dispersion of higher order lobes when measuring Fraunhofer patterns as in [96].
In this study most of the effects arising from a nominally pure in-plane field can at moderate and high fields be explained by vortex dynamics at parts of the sample where the out-of-plane field component is not compensated perfectly. This makes it nearly impossible to reliably measure small changes of L_s in in-plane fields as the inductance produced by unintendedly introduced vortices is orders of magnitudes larger.
One possibility to reduce the error arising from the inhomogeneous compensation field would be to use compensation coils that are assembled outside of the big magnet with much larger dimensions. Even if in this way Helmholtz configuration cannot be achieved neither, the scale on which the field is inhomogeneous can be increased significantly. Another possibility would be to use a 2D or 3D commercial vector magnet with sufficient homogeneity.

Acknowledgments

During my 6 years as a PhD student a lot of people helped me finding my way through all the struggles one encounters in the lab, in the world of physical theory and in private. I would like to thank in particular

- My advisor Prof. Dr. Strunk. I joined Christoph's workgroup already as a Bachelor student. Superconductivity has always been 'my' topic. I always enjoyed a lot of freedom in which direction my research was heading. Whenever I found something interesting in my data, Christoph supported me in looking closer and closer even if this meant months of measurement time. Although often thinking that this crazy new idea of Christoph would not lead anywhere, each time I was taught better.

- Prof. Dr. Fabian for being the second referee for my thesis.

- Nobel laureate J. Michael Kosterlitz, whom we saw at the 28th International Conference on Low Temperature Physics in Gothenburg, Sweden in 2017, where talked a little about his work on 2D phase transition but much more about mountaineering and the joy of life. He showed me not to forget about the other fine things in life besides work and science.

- Dr. Klaus Kronfeldner, who helped me getting the best out of the dilution cryostat and for all the time spending with me in various bars in Regensburg.

- Christian Baumgartner for producing marvelous samples. His work was eminent for my thesis.

- Dr. Nicola Paradiso for the idea of measuring the inductive response with a simple RLC resonator and his help in the preparation of the manuscripts for the hopefully following publications.

- Dr. Denis Kochan for the theoretical work on the vortex core squeeze.

- Dr. Matthias Kronseder for material supply and gossip in the corridors.
- The electronics workshop. Especially Dieter Riedl for helping out with his expertise on electronics of any kind and Max Simmel for winding the best superconducting coils.
- Out technicians Thomas Haller, Michael Weigel, Cornelia Linz, Daniel Pahl and Uli Gürster for maintenance and upgrade of our measurement and sample preparation equipment.
- Thomas Solleder and Christian Haimerl for the endless support of liquid Nitrogen and Helium.
- The mechanical workshop for producing diverse parts needed for my experiments.
- Our secretaries Elke Haushalter and Claudia Moser for helping with all the administrative challenges.
- My (former) colleagues Dr. Ina Schneider, Dr. Michael Schafberger, Dr. Daniel Steininger, Dr. Stefan Blien, Dr. Alois Dirnaichner, Paul Linsmaier, Christian Bäumel, Thomas Huber and Simon Reinhardt for all the illuminating discussions and beers we had together.
- The "corner boyz" Moritz Frankerl and Andi Haag for the strongly needed distraction on sunny afternoons.
- My parents for always supporting me in doing whatever I do.
- My girlfriend Lena for always listening to my stories from the lab, which must have sounded like from a different planet sometimes and for keeping my back free during intense times of measurement and writing up.
- All people I forgot to mention here. Without you I could not have finished this work.

Subsequent Changes

Following subsequent changes have been made in the presented manuscript:

- In eq. 2.2 a "-" sign was added on the left side of the equation.
- On page 16 the sentence "For the case of very small defects compared with the extension of a vortex ξ..." was changed to "For the case of defects very small compared with the extension of a vortex core ξ...".
- On page 23 the sentence "For bulk and centrosymmetric crystals the electric environment is isotropic and translational invariant and hence SOC is absent." was changed to "For bulk and centrosymmetric crystals the electric environment is relatively isotropic and hence SOC is typically weak.".
- On page 118 the sentence "...much less pronounced as in the reported work." was changed to "...much less pronounced compared to [85]."